

UNIVERSITY OF GRANADA

PHD PROGRAM IN PHYSICS AND MATHEMATICS



UNIVERSIDAD
DE GRANADA

Meson-exchange currents and nuclear correlations in neutrino and electron scattering with nuclei

Submitted by :
Paloma Rodríguez Casalé

In partial fulfillment of the requirements for the degree of Doctor of Philosophy in Physics

Supervised by:
Dr. José Enrique Amaro Soriano

Granada, 2025

UNIVERSIDAD DE GRANADA

PROGRAMA DE DOCTORADO EN FÍSICA Y MATEMÁTICAS



UNIVERSIDAD
DE GRANADA

Corrientes de intercambio de mesones y
correlaciones nucleares en la dispersión
de neutrinos y electrones con núcleos

Memoria presentada por
Paloma Rodríguez Casalé

Para optar al título de Doctora en Física

Bajo la dirección del Dr.
José Enrique Amaro Soriano

Granada, 2025

Agradecimientos

Estos cuatro años de tesis han sido una auténtica aventura, llena de desafíos, aprendizaje y momentos inolvidables. Desde que empecé Física siempre supe que quería doctorarme y ahora que lo he conseguido no puedo sino estar orgullosa de mí misma.

Este trabajo refleja también el apoyo y la generosidad de quienes me han acompañado durante estos años. Quiero agradecer especialmente a mi director de tesis, Quique, por guiarme con paciencia y sabiduría, por nuestros intensos debates llenos de “esa será tu opinión”, que sin duda me han hecho ser mejor física. Pero, sobre todo, por su fe en mí. Porque sin ella nada de esto habría sido posible.

También le estoy agradecida a Nacho, por contratarme por primera vez, dándome la oportunidad de empezar a crecer profesionalmente. A María, Enrique, Victor, Pablo, Maria G, Maria B., Marco, Valerio y Arturo, por su colaboración y apoyo durante el desarrollo de esta tesis.

A Alberto, por aguantarme cuando el cortisol se me disparaba por culpa de la tesis y por escucharme sin descanso mientras practicaba mis charlas una y otra vez. Gracias por estar a mi lado incluso en los días más caóticos.

Y finalmente, a mi familia, mi refugio. Gracias por cada palabra de aliento que me inspiró a seguir mis metas, por enseñarme a no rendirme y por recordarme siempre que los sueños no se cumplen solos y que detrás de cada logro hay esfuerzo, constancia y dedicación.

Resumen

Esta tesis está dedicada al estudio de la dispersión de electrones y neutrinos en núcleos, con especial atención a las corrientes de intercambio de mesones (MEC) y a las correlaciones de corto alcance (SRC) entre pares de nucleones, en procesos de emisión de una partícula.

En el capítulo 2 se mejora el modelo de superscaling con masa efectiva (SuSAM*) mediante la redefinición del tensor hadrónico de un nucleón promediado sobre una distribución de Fermi, en lugar de la extrapolación del gas de Fermi relativista utilizada hasta ahora. Esta formulación elimina la inconsistencia de la negatividad en cinemáticas alejadas del pico cuasielástico. La nueva definición del nucleón efectivo permite extender el formalismo de superscaling para incluir las MEC, que es el foco del capítulo 3.

En el capítulo 3 se hace un análisis de scaling de los datos del ^{12}C incorporando de manera explícita las MEC en el single-nucleon, obteniendo una nueva función de scaling fenomenológica. Con este modelo se estudia el efecto de las MEC en la respuestas electromagnéticas, comparando con el gas de Fermi relativista (RFG) y el modelo de campo medio relativista (RMF).

En el capítulo 4 se analiza en profundidad la interferencia entre las corrientes a un cuerpo (OB) y a dos cuerpos en la respuesta transversal, demostrando con distintos modelos, incluido el de la función espectral, que dicha interferencia resulta siempre negativa en la aproximación de partícula independiente.

El capítulo 5 extiende el estudio de las MEC al caso de la dispersión cuasielástica de neutrinos con corrientes cargadas (CCQE) en los modelos RFG, RMF y SuSAM*. Se encuentra que la interferencia OB-MEC reduce las respuestas transversales y la sección eficaz de neutrinos.

En el capítulo 6 se aborda el estudio de las correlaciones de corto alcance en la función de onda de un par de nucleones en materia nuclear. Para ello, se resuelve la ecuación de Bethe-Goldstone utilizando el potencial nucleón-nucleón desarrollado por el grupo de Granada, lo que permite calcular las componentes de alto momento.

Finalmente, en el capítulo 7 se estudia el efecto conjunto de las MEC y SRC en aproximación de pares independientes, que extiende el gas de Fermi incluyendo las componentes de alto momento de los pares de nucleones sobre los que actúan las MEC. Se encuentra que las SRC generan un aumento de la respuesta transversal, en contraste con lo observado en modelos no correlacionados.

Abstract

This thesis is dedicated to the study of electron and neutrino scattering on nuclei, with special emphasis on meson-exchange currents (MEC) and short-range correlations (SRC) between nucleon pairs in one-particle emission processes.

In chapter 2, the superscaling model with effective mass (SuSAM*) is improved by redefining the single-nucleon hadronic tensor, averaging it over a Fermi distribution instead of using the previous extrapolation from the relativistic Fermi gas. This formulation removes the inconsistency associated with negative contributions in kinematics far from the quasielastic peak. The new definition of the effective nucleon allows extending the superscaling formalism to include MEC, which is the focus of chapter 3.

In chapter 3, a scaling analysis of ^{12}C data is performed incorporating MEC explicitly at the single-nucleon level, leading to a new phenomenological scaling function. Using this model, the effect of MEC on electromagnetic responses is studied and compared with the relativistic Fermi gas (RFG) and the relativistic mean field (RMF) models.

Chapter 4 presents a detailed analysis of the interference between one-body (OB) and two-body currents in the transverse response. It is shown, using several approaches including the spectral function model, that this interference is always negative within the independent-particle approximation.

Chapter 5 extends the study of MEC to the quasielastic charged-current neutrino scattering (CCQE) within the RFG, RMF, and SuSAM* frameworks. It is found that OB-MEC interference reduces both the transverse responses and the neutrino cross section.

Chapter 6 addresses short-range correlations in the wave function of a nucleon pair in nuclear matter. The Bethe-Goldstone equation is solved using the nucleon–nucleon potential developed by the Granada group, allowing for the calculation of high-momentum components.

Finally, chapter 7 studies the combined effect of MEC and SRC in the independent-pair approximation, which extends the Fermi gas by including the high-momentum components of nucleon pairs affected by MEC. It is found that SRC enhance the transverse response, in contrast with what is observed in uncorrelated models.

Contents

1. Introduction	13
2. Improved Superscaling model with relativistic effective mass	19
2.1. Superscaling formalism	19
2.1.1. Electromagnetic response functions	20
2.1.2. Scaling	22
2.1.3. SuSAM*	23
2.2. Averaged single-nucleon response functions	25
2.2.1. RFG extrapolation	25
2.2.2. Alternative to the extrapolated single-nucleon responses	27
2.3. Results	28
2.4. Final remarks	34
3. Improved Superscaling model with Meson Exchange Currents	37
3.1. Meson-exchange currents	40
3.2. Results	43
3.3. Final remarks	59
4. The low momentum OB-MEC interference	61
4.1. Non-relativistic OB-MEC transverse response	61
4.1.1. MEC effective one-body transition currents	66
4.1.2. Interference between one-body and MEC in the transverse response	67
4.1.3. Low-momentum proposition	70
4.2. Results	71
4.2.1. Fermi gas	72
4.2.2. Mean field with Woods-Saxon potential	72

4.2.3. Relativistic mean field	76
4.2.4. SuSAM* model	79
4.2.5. Strong form factor and relativistic effects	79
4.2.6. Plane wave approximation	81
4.2.7. Spectral function model	85
4.2.8. Total interference response.	91
4.3. Final remarks	92
5. CCQE neutrino-nucleus scattering with Meson exchange currents	95
5.1. Charge-changing quasielastic neutrino scattering	95
5.2. Weak CC Meson exchange currents	99
5.3. Non-relativistic interference T-response	103
5.3.1. Non-relativistic weak CC one-body current	104
5.3.2. Non-relativistic weak MEC	104
5.3.3. Effective one-body MEC	106
5.3.4. Non relativistic 1b2b interference single-nucleon responses	107
5.4. Results	109
5.4.1. Cross section	122
5.5. Final Remarks	133
6. Analysis of the SRC with the Bethe-Goldstone equation	135
6.1. The Bethe-Goldstone equation	135
6.2. Multipole expansion of the BG equation	139
6.3. Application to the Granada 2013 potential	140
6.3.1. Solutions in coordinate space	141
6.4. Solutions in momentum space	144
6.4.1. High-momentum distribution	145
6.5. Results	147
6.5.1. Uncoupled waves in coordinate space	147
6.5.2. Coupled waves in coordinate space	151
6.5.3. High-momentum distributions	156
6.6. Final remarks	162

7. Transverse enhancement from MEC and SRC	163
7.1. Formalism	164
7.1.1. Correlated matrix elements	167
7.1.2. High momentum wave functions	171
7.2. Results	173
7.3. Final Remarks	180
8. Conclusions	183
A. Single-nucleon responses	187
B. Isospin Summations in the 1p1h MEC Matrix Element	189
C. Non relativistic reduction of the vector Δ current	193
D. Spin summations in the 1p1h MEC matrix elements	197
E. Spin summations in the interference responses	199
F. Spectral function and hadronic tensor	203
G. Isospin Summations in CCQE matrix element	205
H. Non relativistic reduction of the axial Δ current	209
I. Multipole expansion of the BG equation	211
J. Solution of the Green's Function integral	215

Chapter 1

Introduction

This Thesis is organized in two main parts. The first part is devoted to the study of meson-exchange currents (MEC) in single-nucleon emission reactions induced by electrons and neutrinos in uncorrelated nuclear models. The second part extends the analysis to systems that include short-range correlations (SRC), exploring how their interplay with MEC affects the transverse electromagnetic response, which serves as a necessary step toward a more complete description of neutrino interactions with nuclei.

This analysis is particularly relevant for accelerator-based neutrino experiments, whose increasing precision demands equally accurate theoretical descriptions of neutrino-nucleus interactions [1, 2, 3, 4, 5, 6, 7, 8, 9]. Reliable modeling of these processes is crucial to extract neutrino mixing parameters and understand neutrino oscillations. Thus, providing cross-section predictions for realistic nuclear targets over wide energy ranges is essential [10, 11, 12]. Electron scattering serves as a key benchmark: its abundant data [13, 14] and the link between electromagnetic and weak isovector currents allow nuclear models validated for electrons to be adapted to neutrinos by including an axial current. In the first part of this work, we first examine the case of electron scattering in detail and then extend the analysis to neutrino interactions.

In this context of lepton–nucleus scattering, the general objective of this Thesis is to address two related but distinct problems. The first concerns the role of MEC in the 1p1h nuclear response to electron and neutrino probes, an effect that has not yet been systematically evaluated in the case of neutrino scattering. The second focuses on the influence of SRC on the transverse electromagnetic response in single-particle emission, which are essential to understand the transverse enhancement observed in electron reactions. In this introduction, we develop the context in which this research has been carried out, including the main antecedents, previous models, and calculations relevant to the present work.

Inclusive lepton–nucleus cross sections vary with the energy transferred to the nucleus, which determines the dominant reaction mechanisms across different excitation regions. From elastic and collective excitations at low energies to quasielastic (QE) scattering, resonance production, and deep-inelastic scattering at higher energies, each regime involves distinct nuclear processes. This thesis focuses on the quasielastic region, specifically on 1p-1h excitations, excluding two-nucleon emission, pion production, and other inelastic

channels. Accurate treatment of this domain requires reliable theoretical models and many-body approaches capable of describing the underlying nuclear dynamics [4, 5, 15, 16, 17, 18, 7].

One of the simplest and most widely used approaches to describe quasielastic lepton-nucleus scattering is the relativistic Fermi gas (RFG) model [19, 20, 21]. Although it provides a useful framework for interpreting data, the RFG neglects finite-size effects, nuclear interactions, and correlations. The Relativistic Mean Field (RMF) model [22, 23, 24] improves upon these limitations by including scalar and vector potentials that yield an effective nucleon mass m_N^* and a more realistic relativistic dynamics. Since the RFG assumes a sharp Fermi surface, it also fails to reproduce the the nuclear momentum distribution [25, 26, 27].

To achieve a more realistic description of lepton–nucleus scattering, models beyond the RFG have been developed. These include independent–particle approaches such as the plane–wave impulse approximation (PWIA) and spectral function (SF) methods [28], Dirac Equation Based (DEB) models [29, 30], the shell model with Woods–Saxon potentials [31, 32, 33], and Random Phase Approximation (RPA) frameworks, as well as microscopic approaches like Green’s Function Monte Carlo (GFMC) calculations for light nuclei [34] and coupled–cluster methods [35]. Local Fermi Gas (LFG) models, such as those developed by the Valencia group [36] and by the Lyon group [37], represent sophisticated many–body frameworks, including RPA correlations, effective interactions, and final–state interactions (FSI), and are widely used for describing neutrino–nucleus scattering. Some of these models have been revisited in this thesis, specifically the PWIA, SF, DEB, and shell model with Woods–Saxon potential in chapter 4.

In addition to microscopic and independent-particle approaches, phenomenological scaling models provide an alternative description of the nuclear response. These frameworks, such as the super-scaling approach SuSA, SuSA-v2, and SuSAM* [25, 26, 27] factorize the response into a single-nucleon contribution multiplied by an universal scaling function fitted to electron scattering data. SuSAM* further incorporates medium effects via the relativistic effective nucleon mass inspired by the RMF. In chapter 2, this Thesis employs an improved version of the SuSAM* model, replacing the single-nucleon prefactor previously used in the SuSA approach, which was based on a simple extrapolation of the Fermi gas average. We demonstrate that this extrapolation leads to problems for extreme kinematics outside the Fermi gas region, producing nonphysical negative results in certain cases. This issue is resolved by introducing an alternative averaging procedure, replacing the sharp RFG momentum distribution with a smoother function of Fermi kind. This new definition of the single-nucleon contribution also provides a natural framework to consistently include MEC, as developed in chapter 3.

One of the main objectives of this Thesis is to study in detail the effect of MEC in the 1p-1h channel for both electron and neutrino scattering. MEC naturally arise from the nucleon–nucleon interaction [38], with pion-exchange processes providing the dominant contribution. While MEC are known to play a significant role in the two-particle-two-hole (2p-2h) channel in both electron and neutrino scattering [37, 39, 11], they are typically neglected in the 1p-1h quasielastic response, particularly in the case of neutrino scattering. Previous studies have analyzed MEC effects in electron scattering on medium nuclei using

various models, such as the Fermi gas, RFG, and shell model [40, 41, 33, 42]. Chapter 3 focuses on the consistent inclusion of MEC within the superscaling formalism, a novel development made possible by the approach introduced in chapter 2, which averages the single-nucleon response over a diffused Fermi surface.

In addition to the improved SuSAM*+MEC model developed in chapter 3, independent-particle models, including the RFG, mean-field, and spectral function approaches, typically predict that MEC reduce the transverse response due to partial cancellations among the seagull, Δ , and pion-in-flight contributions. This indicates that MEC alone cannot account for the enhancement observed in experimental data relative to theoretical predictions based solely on one-body currents [33, 43, 44]. However, some studies report results that disagree with these models [45, 46, 47]. These discrepancies motivate the systematic analysis presented in chapter 4, where the interference between one-body and two-body currents is studied in detail using various nuclear models. In particular, in the low-momentum limit, we rigorously demonstrate that within the non-relativistic Fermi gas model, the interference of the Δ and pion-in-flight currents with the one-body current is negative, a result that is consistent with all models examined in the chapter.

As final step of part 1 of this Thesis, in chapter 5 we address the case of neutrino scattering. Building on the formalism developed in the previous chapters, chapter 5 presents the first comprehensive analysis of charged-current quasielastic (CCQE) neutrino scattering that includes MEC in the one-nucleon knockout channel. As previously discussed, the existing neutrino studies have incorporated MEC only in the 2p-2h channel [11, 37, 39], which typically accounts for about 15–20% of the total cross section, depending on the kinematics and on the specific model used [26, 48, 49, 50, 51, 52]. This is particularly relevant since precision in neutrino cross-section modeling is essential for the accurate determination of oscillation parameters. Yet it is also necessary to quantify the effect of MEC in the 1p-1h channel. In this chapter, we perform this analysis for the first time using simple models (RFG, RMF, and SuSAM*). All five response functions relevant to neutrino scattering are computed, including contributions from both one- and two-body axial currents. Special attention is given to the axial current with Δ excitation, which dominates weak MEC, while the seagull axial contribution is found to be negligible—an important difference compared to electron scattering. Finally, the total cross section is also calculated and compared with neutrino experimental data, allowing us to evaluate the relative importance of MEC in the 1p-1h channel compared to the 2p-2h contribution.

In the second part of this Thesis, we go beyond uncorrelated nuclear models and address the case of correlated nuclei. The main motivation, as mentioned above, is to investigate the long-standing problem of the transverse electromagnetic response enhancement, which is the central focus of this part. Meson-exchange currents are widely regarded as the primary mechanism behind the transverse enhancement, a view supported by *ab initio* calculations in light nuclei [53, 54]. However, as demonstrated in the first part of this thesis, single-particle approaches fail to reproduce this enhancement. Instead, they generally predict a negative interference between one- and two-body currents, mainly due to the dominant destructive contribution of the Δ current at higher momentum transfers. An important element absent in these independent-particle frameworks and potentially responsible for the transverse enhancement, as suggested by Fabrocini [35] and Leidemann and Orlandini [55],

are the short-range correlations in the nuclear wave function. Since MEC are two-body operators, it is natural to expect them to be sensitive to the short-distance structure of correlated nucleon pairs, and therefore to investigate whether the enhancement of the 1p1h transverse response may be connected to such correlations. Studying these correlations and quantifying their effect on the 1p1h transverse response is the main goal of chapters 6 and 7, which we address within the simplest possible framework: the independent-pair approximation in nuclear matter.

Short-range correlations, studied in chapter 6, arise when two nucleons interact strongly at short distances within the nuclear medium. These correlations generate high-momentum components in the nuclear wave function that play an essential role in understanding the transverse enhancement discussed above. The interest in SRC has grown substantially in recent years, largely driven by the development of high-energy electron scattering experiments. Facilities such as the Continuous Electron Beam Accelerator Facility (CEBAF) at Jefferson Lab [56] have played a central role in this progress, providing high-intensity, high-resolution electron beams that enable unprecedented exploration of nuclear structure. These experimental advances have opened the way to systematic studies of SRC and have spurred renewed theoretical efforts to understand their role in the nuclear wave function and in various nuclear processes [57, 58].

From a theoretical perspective, SRC play a crucial role in nuclear physics, spanning from fundamental studies to applied contexts. They significantly affect the properties of nuclear matter [59, 60, 61, 62, 63], contribute to the high-momentum components of nuclear wave functions [64, 65, 66, 67, 68, 69], and have important implications in nuclear astrophysics, including the equation of state and evolution of neutron stars [70, 71, 72, 73, 74]. They also impact calculations of symmetry energy and pairing gaps in nuclear and neutron matter [75, 76, 77], modeling of relativistic heavy-ion collisions [78], and nuclear matrix elements relevant for neutrinoless double-beta decay [79, 80]. Moreover, SRCs are essential in describing electron scattering reactions, including (e, e') , $(e, e'N)$, and $(e, e'NN)$ processes [81, 82, 83, 84, 85]. More recently, the universality of N-N SRCs has been explored in connection with factorization properties of nuclear wave functions and momentum distributions, as well as with nuclear contacts [86, 87, 88, 89, 90, 91, 92, 93, 94].

The main approaches traditionally used to address SRC fall into two categories. The first employs Jastrow correlation functions with appropriately tailored short- and long-range behaviors, applied to Slater determinants of single-particle wave functions within variational frameworks [84, 95, 96, 97, 98, 99, 100, 101, 102, 103, 104, 105]. The second is the Brueckner theory of nuclear matter [106, 107, 108], based on solving the Bethe–Goldstone (BG) equation [109, 110, 111] or the effective interaction represented by the G-matrix formalism [112, 113, 114, 115, 116, 117, 118]. Several other powerful methods have also been developed. Similarity renormalization group (SRG) techniques provide phase-equivalent potentials that soften the short-range interaction, thereby circumventing the complications associated with the hard core [119, 120, 121]. In addition, *ab initio* variational Monte Carlo approaches can solve the non-relativistic many-body problem exactly for light nuclei, given a specific nucleon-nucleon interaction [122, 123, 124, 125, 126, 127].

The goal of chapter 6 is to construct the wave function of a correlated nucleon pair and analyze its properties, providing the foundation for the study of combined MEC and

SRC effects in chapter 7. Within the independent-pair approximation [128], SRC are incorporated by solving the Bethe–Goldstone (BG) equation in nuclear matter. This chapter extends the previous work of the Granada group [129, 130] to the case in which the total center-of-mass (CM) momentum of the nucleon pair is non-zero. For this purpose, we employ the realistic coarse-grained Granada 2013 nucleon-nucleon potential, obtained from a partial-wave analysis of nucleon-nucleon scattering below the pion production threshold [131]. The angular average of the Pauli-blocking operator appearing in the BG equation is used, an approximation widely applied in the past [106, 113, 114, 132, 133]. Alternative approaches that solve the BG equation without this angular-average approximation have also been explored [134, 135, 136, 137, 138, 139, 140]. With the Granada 2013 potential and the angular-average approximation, the BG equation simplifies to an algebraic form via a multipole expansion. The resulting correlated radial wave functions are analyzed in both coordinate and momentum space, and their dependence on the CM momentum is studied as a preparatory step for chapter 7.

Finally, in chapter 7, the formalism developed in chapter 6 is applied to incorporate the high-momentum components of the correlated nucleon-pair wave functions into the MEC matrix elements for 1p-1h excitations. These modified matrix elements are then embedded within the response function formalism of the Fermi gas to evaluate the impact of short-range correlations on the transverse nuclear response. Proceeding in this way places us in an optimal position to explore, in a novel and systematic manner, whether SRCs lead to an enhancement of the transverse response. In particular, we aim to investigate whether the high-momentum components of the correlated nucleon pairs can reverse the negative interference effects identified in chapters 3 and 4, potentially changing their sign and producing an enhancement of the transverse channel, as previously observed in the correlated basis function (CBF) calculations of Fabrocini [35].

From the experimental point of view, the enhancement of the transverse response has been clearly established in inclusive electron scattering data. Analyses of world data by Jourdan [43] demonstrated that the transverse response systematically exceeds the predictions of independent-particle models, particularly in the quasielastic region. Similar conclusions were reached by Bodek and Christy [44], who introduced phenomenological scaling functions to reproduce this enhancement across a wide range of nuclei. On the theoretical side, *ab initio* Green’s Function Monte Carlo (GFMC) calculations [53, 141, 54] have confirmed the same trend in light nuclei, showing that two-body currents and correlations lead to an increase of the transverse strength consistent with the experimental findings. These results provide a solid empirical and theoretical motivation for the study of chapter 7, which aims to identify the microscopic origin of the transverse enhancement in terms of short-range correlations and meson-exchange currents within the framework of the Fermi gas.

Objectives and methodology

The objectives of this Thesis, as were presented in the original Thesis project are:

1. Improvement of the SuSAM* model by extending the definition of the averaged single-nucleon response to all values of the scaling variable, thus avoiding unphysical extrapolations and ensuring a more accurate and reliable foundation for the superscaling model.
2. Inclusion of MEC within the superscaling formalism, introducing their interference with one-body currents directly in the single-nucleon prefactor and comparing the results with the Relativistic Fermi Gas and Relativistic Mean Field models for electron and neutrino scattering.
3. Study of short-range correlations, obtained by solving the Bethe–Goldstone equation in nuclear matter using the coarse-grained Granada NN potential to extract high-momentum components of the correlated wave function.
4. Evaluation of one-body–two-body interference in the presence of SRC, to assess their possible role in the enhancement of the transverse response.

The methodology combines well-established nuclear models with several new developments introduced in this work. The SuSAM* model is refined by implementing a realistic Fermi-type momentum distribution and by explicitly including MEC contributions, which are validated through scaling analyses with electron scattering data. Additional theoretical frameworks employed in this thesis include the shell model, the semirelativistic shell model, and the relativistic mean-field (RMF) model with Dirac-equation–based potentials, using existing computational codes. We also analyze the RFG, the RMF in nuclear matter and the spectral function (SF) models.

To compute the flux-integrated neutrino cross sections in chapter 5, including MEC effects, numerical integration were performed on the **PROTEUS** supercomputer at the Instituto Carlos I de Física Teórica y Computacional. The Bethe–Goldstone equation is solved in a partial-wave expansion using the Granada 2013 nucleon–nucleon potential, leading to a system of linear equations that are solved via the Gauss method. The resulting correlated wave functions are obtained in momentum space and then incorporated into the Fermi gas model. Finally, to evaluate the interference between one- and two-body currents in the presence of SRC, a seven-dimensional integral is computed numerically, which can be simplified under the frozen approximation for the spectator nucleon.

Chapter 2

Improved Superscaling model with relativistic effective mass

This chapter focuses on the nuclear quasielastic response in electron scattering, and more specifically, on the superscaling model [142, 143], whose basic theoretical foundations we aim to examine. Scaling assumes that the response factorizes and is expressed as proportional to an average single-nucleon response. The behavior of the single-nucleon responses will be investigated when averaged over a Fermi gas and extrapolated outside of the kinematic range allowed by Pauli blocking. We show that the extrapolation leads to unphysical results in extreme kinematics where the nucleon can not be on shell. We propose a new averaging method that removes the need for extrapolation. This leads to a new definition of the single-nucleon response, averaged over momentum space, with a momentum distribution where the Fermi surface is smeared out instead of using the sharp Fermi gas distribution. This average therefore has a theoretical justification, in contrast to the extrapolation approach [144, 26, 27], and produces results that are similar to those of the traditional superscaling models. This approach provides a solid argument that justifies the choice of the single-nucleon response and does not suffer from the previous issues. It will be shown that the use of the new averaged single-nucleon or the extrapolated one is indifferent in the scaling region, and then this work improves the superscaling formalism from the theoretical point of view by providing a physical justification for its use, which strengthens the applicability of such phenomenological models. See Ref. [145] for more details.

2.1. Superscaling formalism

The theory of the RFG response function and its connection with the theory of superscaling will be briefly reviewed. The scaling variable ψ was first introduced in ref. [146]. The scaling formalism was refined in subsequent works [147, 142, 143] until reaching the most up-to-date version of the SuSA-v2 model [7].

The formalism in this chapter is an extension of the SuSA to the SuSAM* approach based on the equations of nuclear matter interacting with a relativistic mean field (RMF)

[24, 23, 148, 149], which allows for the incorporation of dynamic effects. The simplest approximation in this framework is to introduce scalar and vector potentials with which the nucleons interact. The scalar potential is attractive, while the vector potential is repulsive. The on shell energy is defined as

$$E = \sqrt{m_N^{*2} + p^2}, \quad (2.1)$$

where m_N^* is the relativistic effective mass of the nucleon,

$$m_N^* = m_N - g_s \phi_0 = M^* m_N. \quad (2.2)$$

Here ϕ_0 is the scalar potential energy of the RMF and g_s the corresponding coupling constant. To account for the interaction with the vector potential, a positive energy term needs to be added to the on-shell energy. Therefore, the total energy of the nucleon can be expressed as:

$$E_{RMF} = E + E_v, \quad (2.3)$$

being E_v the called vector energy.

2.1.1. Electromagnetic response functions

We consider the inclusive electron scattering process where an incident electron with energy ϵ scatters off a nucleus with scattering angle θ . The final electron energy is ϵ' . The momentum transfer is q , the energy transfer is ω , and $Q^2 = \omega^2 - q^2 < 0$. The cross section in plane-wave Born approximation with one photon-exchange is written

$$\frac{d\sigma}{d\Omega d\epsilon'} = \sigma_{\text{Mott}}(v_L R_L(q, \omega) + v_T R_T(q, \omega)), \quad (2.4)$$

where Ω is the final electron solid angle, σ_{Mott} is the Mott cross section,

$$\sigma_{\text{Mott}} = \left(\frac{\alpha \cos \theta/2}{2\epsilon \sin^2 \theta/2} \right)^2, \quad (2.5)$$

v_L and v_T are the kinematic factors

$$v_L = \frac{Q^4}{q^4}, \quad v_T = \tan^2 \frac{\theta}{2} - \frac{Q^2}{2q^2}, \quad (2.6)$$

and finally, $R_K(q, \omega)$, $K = L, T$, are the longitudinal and transverse response functions defined below. We focus on the description of the nuclear response functions resulting from the interaction of the electron with the one-body (OB) electromagnetic current, giving rise to one-particle one-hole excitations of the Fermi gas. They are defined in a similar way to the usual RFG formalism [7], with the difference that in our case the nucleons have an effective mass $m_N^* < m_N$.

The hole momentum is \mathbf{h} with $h < k_F$ and on-shell energy $E_h = \sqrt{h^2 + (m_N^*)^2}$. By momentum conservation, the final particle momentum is $\mathbf{p} = \mathbf{h} + \mathbf{q}$ with on-shell energy

$E_p = \sqrt{p^2 + (m_N^*)^2}$. Pauli blocking implies $p > k_F$. The nuclear response functions are then given by

$$R_K^{QE}(q, \omega) = \frac{V}{(2\pi)^3} \int d^3h \frac{(m_N^*)^2}{E_h E_p} 2w_K(\mathbf{p}, \mathbf{h}) \theta(p - k_F) \theta(k_F - h) \delta(E_p - E_h - \omega), \quad (2.7)$$

where w_K are the single-nucleon responses for the 1p1h excitation

$$w_L = w^{00}, \quad w_T = w^{11} + w^{22}, \quad (2.8)$$

corresponding to the single-nucleon hadronic tensor

$$w^{\mu\nu} = \frac{1}{2} \sum_{s_p s_h} j^\mu(\mathbf{p}, \mathbf{h})^* j^\nu(\mathbf{p}, \mathbf{h}) \quad (2.9)$$

and j^μ is the electromagnetic current matrix element

$$j^\mu(\mathbf{p}, \mathbf{h}) = \bar{u}_{s_p}(\mathbf{p}) \left[F_1 \gamma^\mu + i \frac{F_2}{2m_N} \sigma^{\mu\nu} Q_\nu \right] u_{s_h}(\mathbf{h}), \quad (2.10)$$

where F_1 and F_2 , are the Dirac and Pauli form factors of the nucleon. Note that we use the current operator in the vacuum, but the spinors correspond to nucleons with effective mass m_N^* .

To compute the integral (2.7), we change to the variables E_h, E_p, ϕ , with Jacobian $h^2 dh d\cos\theta = (E_h E_p / q) dE_h dE_p$. Then the integral over E_p is made using the Dirac delta. This fixes the angle between \mathbf{q} and \mathbf{h} to the value

$$\cos\theta_h = \frac{2E_h\omega + Q^2}{2hq}, \quad (2.11)$$

and the integration over the angle ϕ gives 2π by symmetry of the responses when \mathbf{q} is on the z -axis [7]. We are left with an integral over the initial nucleon energy

$$R_K^{QE}(q, \omega) = \frac{V}{(2\pi)^3} \frac{2\pi m_N^{*3}}{q} \int_{\epsilon_0}^{\infty} d\epsilon n(\epsilon) 2w_K(\epsilon, q, \omega), \quad (2.12)$$

where $\epsilon = E_h/m_N^*$ is the initial nucleon energy in units of m_N^* , and $\epsilon_F = E_F/m_N^*$ is the (relativistic) Fermi energy in the same units. Moreover we have introduced the energy distribution of the Fermi gas $n(\epsilon) = \theta(\epsilon_F - \epsilon)$. The lower limit, ϵ_0 of the integral in Eq. (2.12) corresponds to the minimum energy for a initial nucleon that absorbs energy ω and momentum q . It can be written as (see Appendix C of ref. [7])

$$\epsilon_0 = \text{Max} \left\{ \kappa \sqrt{1 + \frac{1}{\tau}} - \lambda, \epsilon_F - 2\lambda \right\}, \quad (2.13)$$

where we have introduced the dimensionless variables

$$\lambda = \omega/2m_N^* \quad \kappa = q/2m_N^* \quad \tau = \kappa^2 - \lambda^2. \quad (2.14)$$

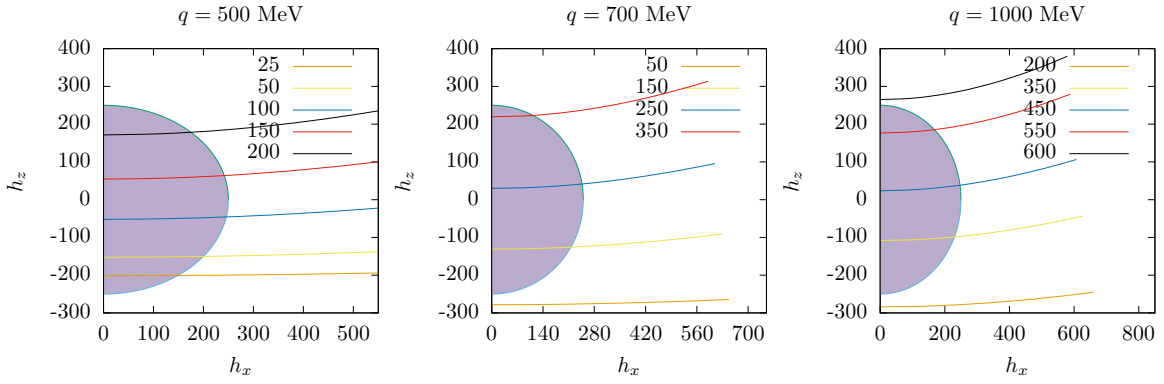


Figure 2.1: Integration path in momentum space of the initial nucleon for different values of the energy transfer ω (indicated in MeV in the key for each panel) and for three values of the momentum transfer.

For a fixed value of ϕ, q, ω , the integral over energy ϵ in Eq. (2.12) corresponds to integrating the single nucleon response over a path in the momentum space of the hole \mathbf{h} , weighted with the momentum distribution. This curve is easily obtained from Eq. (2.11), giving the angle θ_h as a function of the hole energy. Some examples are shown in Fig. 2.1 for three values of q . For each q we plot the integration trajectories in the (h_x, h_z) -plane for several values of ω . The semicircles indicate the moment distribution for $k_F = 250$ MeV. The nuclear response function, $R_K(q, \omega)$, therefore correspond to the integral of the single-nucleon responses along one path. The minimum momentum h_0 , and therefore the minimum energy ϵ_0 , correspond to the intersection of each curve with the h_z axis. The curves for different values of ω do not intersect. The case $h_0 = 0$ only occurs for a certain value of ω , which is precisely the position of the quasielastic peak; this corresponds also to $\epsilon_0 = 1$ (or $\psi^* = 0$ for the scaling variable). For very large or very small ω -values, the curves lie in the region where the momentum distribution is zero, and therefore the corresponding response function is also zero.

2.1.2. Scaling

Scaling is based on the approximated factorization of an averaged single-nucleon response from the nuclear cross section. This factorization is exact in the RMF model with the OB current, where analytical expressions are obtained by explicit integration of the one-body responses [7].

For our purpose, we define a mean value of the single-nucleon responses by averaging with the energy distribution $n(\epsilon)$,

$$\bar{w}_K(q, \omega) = \frac{\int_{\epsilon_0}^{\infty} d\epsilon n(\epsilon) w_K(\epsilon, q, \omega)}{\int_{\epsilon_0}^{\infty} d\epsilon n(\epsilon)}. \quad (2.15)$$

This corresponds to the average of the single-nucleon response $w_K(\epsilon, q, \omega)$ over one of the paths in Fig. 2.1. Using these averaged single-nucleon responses we can rewrite Eq. (2.12)

in the form

$$R_K^{QE}(q, \omega) = \frac{V}{(2\pi)^3} \frac{2\pi m_N^{*3}}{q} 2\bar{w}_K(q, \omega) \int_{\epsilon_0}^{\infty} d\epsilon n(\epsilon). \quad (2.16)$$

This last integral depends only on the variable ϵ_0 , which in turn depends on (q, ω) . In the superscaling approach the ψ^* -scaling variable is used instead of the minimum energy of the nucleon, ϵ_0 . This energy is transformed by a change of variable into the scaling variable, ψ^* , defined as

$$\psi^* = \sqrt{\frac{\epsilon_0 - 1}{\epsilon_F - 1}} \text{sgn}(\lambda - \tau), \quad (2.17)$$

where ψ^* is negative (positive) for $\lambda < \tau$ ($\lambda > \tau$).

The superscaling function is defined as

$$f^*(\psi^*) = \frac{3}{4} \frac{1}{\epsilon_F - 1} \int_{\epsilon_0}^{\infty} n(\epsilon) d\epsilon, \quad (2.18)$$

where $\epsilon_F - 1 \ll 1$ is the kinetic Fermi energy in units of m_N^* . The definition (2.18) is, except for a factor, similar to that of the y -scaling function $f(y)$ [150, 151], where the scaling variable y was the minimum momentum of the initial nucleon.

In RFG and nuclear matter with RMF, Eq. (2.18) is easily evaluated (remember that the RFG is recovered as the particular case $M^* = 1$) as

$$\int_{\epsilon_0}^{\infty} \theta(\epsilon_F - \epsilon) d\epsilon = \theta(\epsilon_F - \epsilon_0)(\epsilon_F - \epsilon_0) = (\epsilon_F - 1)(1 - \psi^{*2})\theta(1 - \psi^{*2}). \quad (2.19)$$

Therefore the scaling function of nuclear matter is

$$f^*(\psi^*) = \frac{3}{4}(1 - \psi^{*2})\theta(1 - \psi^{*2}). \quad (2.20)$$

Note that the scaling function of nuclear matter is zero for $\epsilon_0 > \epsilon_F$, and this is equivalent to $|\psi^*| > 1$. This is a consequence of the maximum momentum k_F for the nucleons in nuclear matter, which implies that $\epsilon_0 < \epsilon_F$.

Using $V/(2\pi)^3 = N/(\frac{8}{3}\pi k_F^3)$ for nuclear matter we can write the response functions (2.16) as

$$R_K^{QE}(q, \omega) = \frac{\epsilon_F - 1}{m_N^* \eta_F^3 \kappa} (Z\bar{w}_K^p(q, \omega) + N\bar{w}_K^n(q, \omega)) f^*(\psi^*), \quad (2.21)$$

where we have added the contribution of Z protons and N neutrons to the response functions, and $\eta_F = k_F/m_N^*$.

2.1.3. SuSAM*

The SuSAM* approach extends the formula (2.21) by replacing $f^*(\psi^*)$ by a phenomenological scaling function obtained from experimental data of (e, e') . In a real, finite nucleus

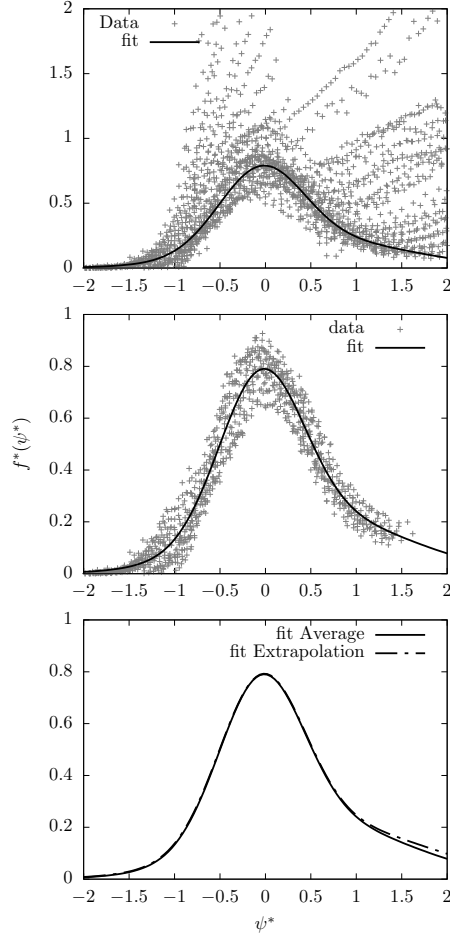


Figure 2.2: Super scaling analysis with relativistic effective mass (SuSAM*) of ^{12}C data. Top panel: experimental scaling data f_{exp}^* plotted against ψ^* . Middle panel: data surviving after cleanup of non-quasielastic sparse points. The black curve is Gaussian fit made in this work, $f_{QE}^*(\psi^*)$. In the bottom panel we compare the two scaling functions obtained with two different definitions of the averaged single-nucleon responses: using the extrapolated Fermi gas responses and performing the average with a Fermi distribution defined in Section 2.2.

the momentum is not limited by k_F (in particular correlated nucleons can greatly exceed the Fermi momentum, see chapter 6). This has the effect that the *phenomenological* super-scaling function is not zero for $|\psi^*| > 1$, and therefore takes into account that the nucleons are not limited by a maximum Fermi momentum.

Several approaches have been used in the past to obtain a phenomenological scaling function. In the original SuSA model, based on the RFG without effective mass, the scaling function was obtained from the longitudinal response data. In the SuSAv2 model, a scaling function for the transverse response was also introduced by means of a RMF theoretical model in finite nuclei. In this chapter we will focus on the SuSAM* model with effective mass where the phenomenological scaling function is obtained directly from the quasielastic data of the inclusive cross section. Different scaling models with effective mass and without effective mass provide different scaling functions, but all may reproduce the quasielastic

cross section reasonably well, since they have been fitted to experimental data.

In the procedure followed in ref [152, 27, 153] the inclusive cross section data are divided by the contribution of the single nucleon. But the SuSAM* model was extended in refs. [154, 155], by subtracting the theoretical contribution of MEC in the 2p2h channel from the experimental data before dividing by the single nucleon, that is

$$f_{exp}^* = \frac{\left(\frac{d\sigma}{d\Omega d\omega} \right)_{exp} - \left(\frac{d\sigma}{d\Omega d\omega} \right)_{2p2h}}{\sigma_M(v_L r_L + v_T r_T)}. \quad (2.22)$$

where

$$r_K = \frac{\epsilon_F - 1}{m_N^* \eta_F^3 \kappa} (Z \bar{w}_K^p(q, \omega) + N \bar{w}_K^n(q, \omega)). \quad (2.23)$$

In Fig. 2.2 these experimental data, f_{exp}^* , are plotted against ψ^* in the interval $-2 < \psi^* < 2$, which largely encompasses the quasielastic domain, extending well beyond the Fermi region $-1 < \psi^* < 1$. It is observed that about half of them roughly collapse forming a thin band around the quasielastic peak. This band constitutes the set of selected data that can be considered QE and we reject the rest, which mainly contribute to inelastic processes. The selected quasielastic data are well parameterized with a sum of two Gaussians, thus obtaining the phenomenological quasielastic function f_{QE}^* , shown also in Fig. 2.2.

2.2. Averaged single-nucleon response functions

One of the most confusing aspects in the superscaling formalism is the definition and meaning of the averaged single-nucleon response functions for $|\psi^*| > 1$ or, equivalently, $\epsilon_0 > \epsilon_F$, i.e., outside the allowed ω -range of the Fermi gas. Traditionally an extrapolation of the Fermi gas formula has often been used. In this section we expose the intrinsic theoretical problems of the Fermi gas extrapolation, and propose an alternative definition that is more satisfactory from the theoretical point of view.

2.2.1. RFG extrapolation

In the traditional superscaling approach, first the averaged single-nucleon responses \bar{w}_K are calculated for $\epsilon_0 < \epsilon_F$ (or $|\psi^*| < 1$) using the Fermi gas momentum distribution,

$$\begin{aligned} \bar{w}_K(q, \omega) &= \frac{\int_{\epsilon_0}^{\infty} w_K(\epsilon, q, \omega) \theta(\epsilon_F - \epsilon) d\epsilon}{\int_{\epsilon_0}^{\infty} \theta(\epsilon_F - \epsilon) d\epsilon} \\ &= \frac{\theta(\epsilon_F - \epsilon_0) \int_{\epsilon_0}^{\epsilon_F} w_K(\epsilon, q, \omega) d\epsilon}{\theta(\epsilon_F - \epsilon_0) \int_{\epsilon_0}^{\epsilon_F} d\epsilon}. \end{aligned} \quad (2.24)$$

Note that this expression is only defined for $\epsilon_0 < \epsilon_F$, in which case the step functions cancel and we obtain

$$\bar{w}_K(q, \omega) = \frac{1}{\epsilon_F - \epsilon_0} \int_{\epsilon_0}^{\epsilon_F} w_K(\epsilon, q, \omega) d\epsilon, \quad (\epsilon_0 < \epsilon_F). \quad (2.25)$$

The function $w_K(\epsilon, q, \omega)$ inside the integral is well defined and positive only if $\epsilon > \epsilon_0$, because it corresponds to the response of a single nucleon with energy ϵ , that absorbs momentum q and energy ω . In the traditional SuSA and SuSAM* approaches the function (2.25) is extended analytically for $\epsilon_0 > \epsilon_F$ in the obvious way. This is called in this work the *extrapolated* single nucleon response function, and it can be written equivalently in the way

$$\bar{w}_K(q, \omega) = \frac{1}{\epsilon_0 - \epsilon_F} \int_{\epsilon_F}^{\epsilon_0} w_K(\epsilon, q, \omega) d\epsilon. \quad (2.26)$$

From this expression it is clear that, for $\epsilon_0 > \epsilon_F$, the function $w_K(\epsilon, q, \omega)$ inside the integral must be evaluated for $\epsilon < \epsilon_0$. But this is not possible for a nucleon on-shell that absorbs (q, ω) , because its minimum energy is ϵ_0 . Therefore it is not guaranteed that the function $w_K(\epsilon, q, \omega)$ inside the integral is positive if is evaluated for $\epsilon < \epsilon_0$. This is a fundamental problem of the single nucleon extrapolation. Next we will study some particular cases where the extrapolated responses are explicitly negative for $\epsilon_0 > \epsilon_F$, that is, for $|\psi^*| > 1$.

Longitudinal single-nucleon response

We use the analytical formulas of the single nucleon responses from Appendix A,

$$w_L = \frac{(G_M^*)^2}{1 + \tau} [\tau(\epsilon + \lambda)^2 - (1 + \tau)\kappa^2] + \frac{(G_E^*)^2}{1 + \tau} (\epsilon + \lambda)^2. \quad (2.27)$$

To better understand the kinematic dependence of this response function it is convenient to express it in terms of the minimal nucleon energy ϵ_0 using

$$\epsilon_0 + \lambda = \kappa \sqrt{\frac{1 + \tau}{\tau}} \implies \kappa^2(1 + \tau) = \tau(\epsilon_0 + \lambda)^2. \quad (2.28)$$

in the regime without Pauli blocking. Then Eq. (A.8) becomes

$$w_L = \frac{(G_M^*)^2 \tau}{1 + \tau} [(\epsilon + \lambda)^2 - (\epsilon_0 + \lambda)^2] + \frac{(G_E^*)^2}{1 + \tau} (\epsilon + \lambda)^2. \quad (2.29)$$

In this equation it is evident that the electric term is always positive. However the magnetic term is positive only for $\epsilon > \epsilon_0$. For this reason, if w_L is calculated using the Fermi gas momentum distribution and then extrapolated to values $\epsilon_0 > \epsilon_F$ (or $\psi^* > 1$), the magnetic term becomes negative. This does not make physical sense because the longitudinal response must be positive, by definition, regardless of the value of the form factors. In fact if we artificially turn off the electric contribution, a negative averaged response \bar{w}_L is obtained for $\epsilon_0 > \epsilon_F$. Let suppose for simplicity that $G_E^* = 0$. Then the extrapolated single-nucleon longitudinal response would be

$$\bar{w}_L = \frac{(G_M^*)^2}{\epsilon_0 - \epsilon_F} \frac{\tau}{1 + \tau} \int_{\epsilon_F}^{\epsilon_0} [(\epsilon + \lambda)^2 - (\epsilon_0 + \lambda)^2] d\epsilon, \quad (2.30)$$

that is negative for $\epsilon_0 > \epsilon_F$.

Transverse single-nucleon response

We find a similar situation in the case of the transverse response from Eq. (A.13) in Appendix A,

$$w_T = 2\tau(G_M^*)^2 + \frac{(G_E^*)^2 + \tau(G_M^*)^2}{1 + \tau} \frac{\tau}{\kappa^2} \left[(\epsilon + \lambda)^2 - \kappa^2 \frac{1 + \tau}{\tau} \right]. \quad (2.31)$$

Again we can rewrite this response as a function of the minimum nucleon energy, ϵ_0 , using $\kappa^2(1 + \tau)/\tau = (\epsilon_0 + \lambda)^2$

$$w_T = 2\tau(G_M^*)^2 + [(G_E^*)^2 + \tau(G_M^*)^2] \left[\left(\frac{\epsilon + \lambda}{\epsilon_0 + \lambda} \right)^2 - 1 \right]. \quad (2.32)$$

Rearranging terms containing G_E^* and G_M^* the single-nucleon transverse response becomes finally

$$w_T = (G_E^*)^2 \left[\left(\frac{\epsilon + \lambda}{\epsilon_0 + \lambda} \right)^2 - 1 \right] + \tau(G_M^*)^2 \left[\left(\frac{\epsilon + \lambda}{\epsilon_0 + \lambda} \right)^2 + 1 \right]. \quad (2.33)$$

Written in this way, it is evident that the magnetic contribution of w_T is always positive. While the electrical term is positive only for $\epsilon > \epsilon_0$. The situation is similar to what we found with the longitudinal response, but in the transverse response it is the electrical term that becomes negative in the extrapolation to $\epsilon_0 > \epsilon_F$. We now turn off the magnetic contribution and suppose that $G_M^* = 0$. Then the averaged T response in RFG would be, with analogy to Eq. (2.30)

$$\bar{w}_T = \frac{(G_E^*)^2}{\epsilon_0 - \epsilon_F} \int_{\epsilon_F}^{\epsilon_0} \left[\left(\frac{\epsilon + \lambda}{\epsilon_0 + \lambda} \right)^2 - 1 \right] d\epsilon. \quad (2.34)$$

From this expression it is clear that the extrapolated \bar{w}_T is negative for $\epsilon_0 > \epsilon_F$ because the function inside the integral is negative, which is not physically acceptable: the transverse response should be positive by definition regardless of the form factors values. In other words, the electrical contribution to the transverse response, although small, cannot be negative.

2.2.2. Alternative to the extrapolated single-nucleon responses

In this work we propose an alternative definition of the averaged single-nucleon responses that solves the extrapolation problem in the superscaling model. As we have seen, the problem is a consequence of the fact that in the Fermi gas there is a maximum momentum for the nucleons. If this momentum is exceeded by extrapolation, i.e. $\epsilon_0 > \epsilon_F$, mathematically this is equivalent to assuming nucleons with energy less than ϵ_0 , which is impossible in the Fermi gas because nucleons are on-shell. Hence results without physical sense, such as negative responses, are obtained if the extrapolated formula is applied.

The proposed solution involves using equation (2.15) for the averaged single-nucleon responses, but introducing a momentum distribution without a maximum momentum, and

that at the same time does not differ much from the Fermi gas distribution, for $h < k_F$. An appropriate function is a distribution of Fermi type

$$n(h) = \frac{a}{1 + e^{(h-k_F)/b}}. \quad (2.35)$$

Where b is a smearing parameter for the Fermi surface, which is no longer restricted to a sphere as in figure 1. Then the integrals by averaging in Eq. (2.15) extend to infinity and therefore there is no longer an upper limit for ϵ_0 , which can take any value up to infinity. The single-nucleon responses of the integrand always are evaluated for $\epsilon > \epsilon_0$ and they are therefore positive definite

In addition, for $\epsilon < \epsilon_F$, the momentum distribution is similar to the Fermi Gas distribution, $\theta(k_F - h)$, and then it is expected that the averaged single-nucleon be similar to that of the RFG. Now, for $\epsilon > \epsilon_F$ the integration in the eq. (2.15) extends in momentum space along one of the paths outside the Fermi sphere of Figure (2.1). Then the average has the physical sense of coming from regions above the Fermi sphere, that is to say, from the high momentum zone that the Fermi gas cannot describe. This is in accordance with the meaning attached to the experimental scaling function for $|\psi^*| > 1$, which comes mainly from high momentum nucleons.

2.3. Results

We present results for the averaged nucleon responses and for the total nuclear responses in the SuSAM* model. The calculations are made for electron scattering off the nucleus ^{12}C with Fermi momentum $k_F = 225$ MeV/c and effective mass $m_N^* = 0.8m_N$. These values were fitted to the quasielastic data of f_{exp}^* to obtain the best possible scaling [152, 27]. We evaluate the validity of the scaling model when using the Fermi gas extrapolation for the nucleon response function. Specifically, the results obtained by averaging the single-nucleon response function over a smeared Fermi momentum distribution, Eq. (2.35) are compared with the extrapolated response function obtained from the Fermi gas model.

In Fig. 2.3 we compare the averaged nucleon responses with the extrapolated ones. The sum of proton plus neutron is shown. The averaged responses have been calculated with a Fermi distribution using a smearing parameter $b = 50$ MeV/c. The responses do not depend much on the precise value of this parameter for small variations. We see that the averaged responses are practically the same as the extrapolated responses of the Fermi gas in the quasielastic scaling region, $-2 < \psi^* < 2$. But both results start to diverge for large ω or $\psi^* > 2$. The extrapolated transverse response becomes negative for $\psi^* > 4, 5$ and 7 , for $q = 500, 700$, and 1000 MeV/c, respectively, very close to the photon line. This is easily explained because in Eq. 2.33, the magnetic term is multiplied by τ . Therefore the w_T response is dominated by the electric term for $\tau \rightarrow 0$, that is, for large ω , and in Eq. 2.34 we have seen that this term is negative when extrapolated to $\epsilon_0 > \epsilon_F$.

More details can be seen in Fig. 2.4 where we show the averaged and extrapolated response functions separated for protons and neutrons, as a function of the scaling variable.

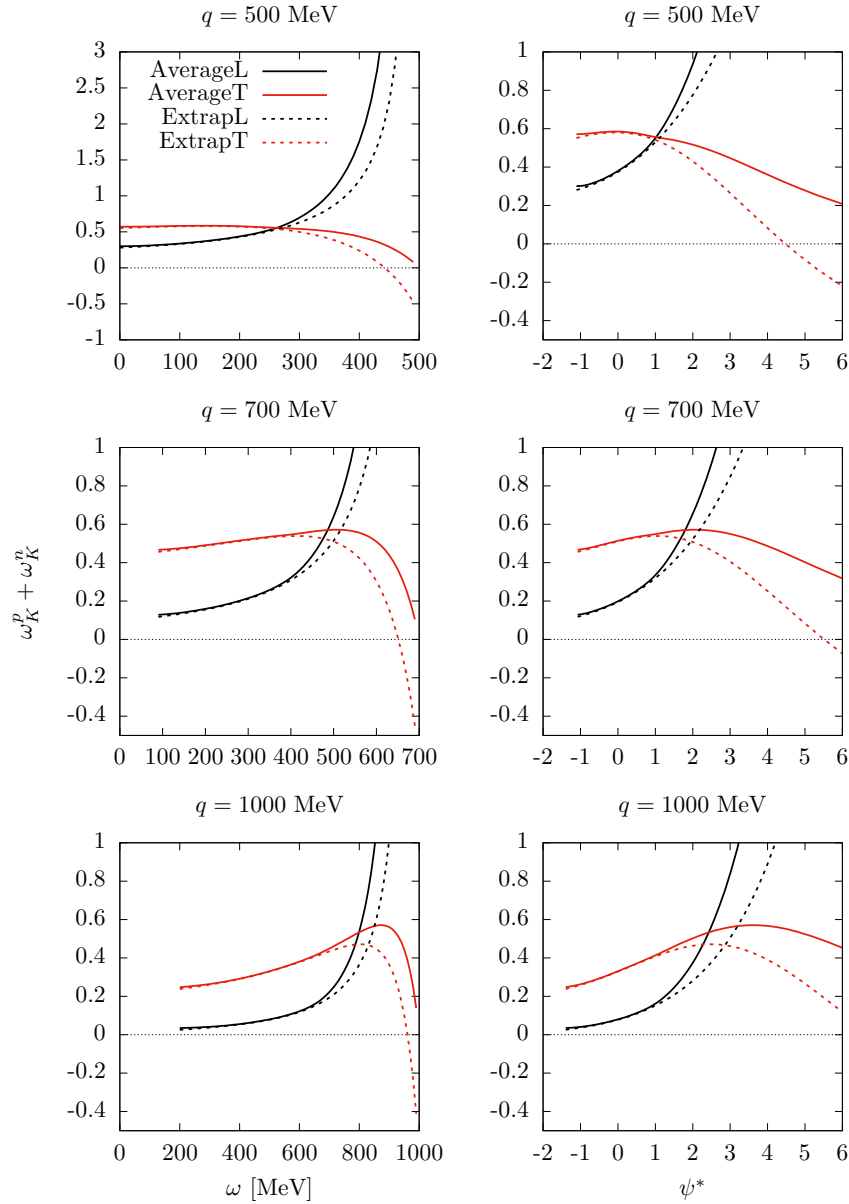


Figure 2.3: Averaged and extrapolated longitudinal and transverse response functions for proton plus neutron, as a function of ω and of the scaling variable ψ^* , for three values of the momentum transfer.

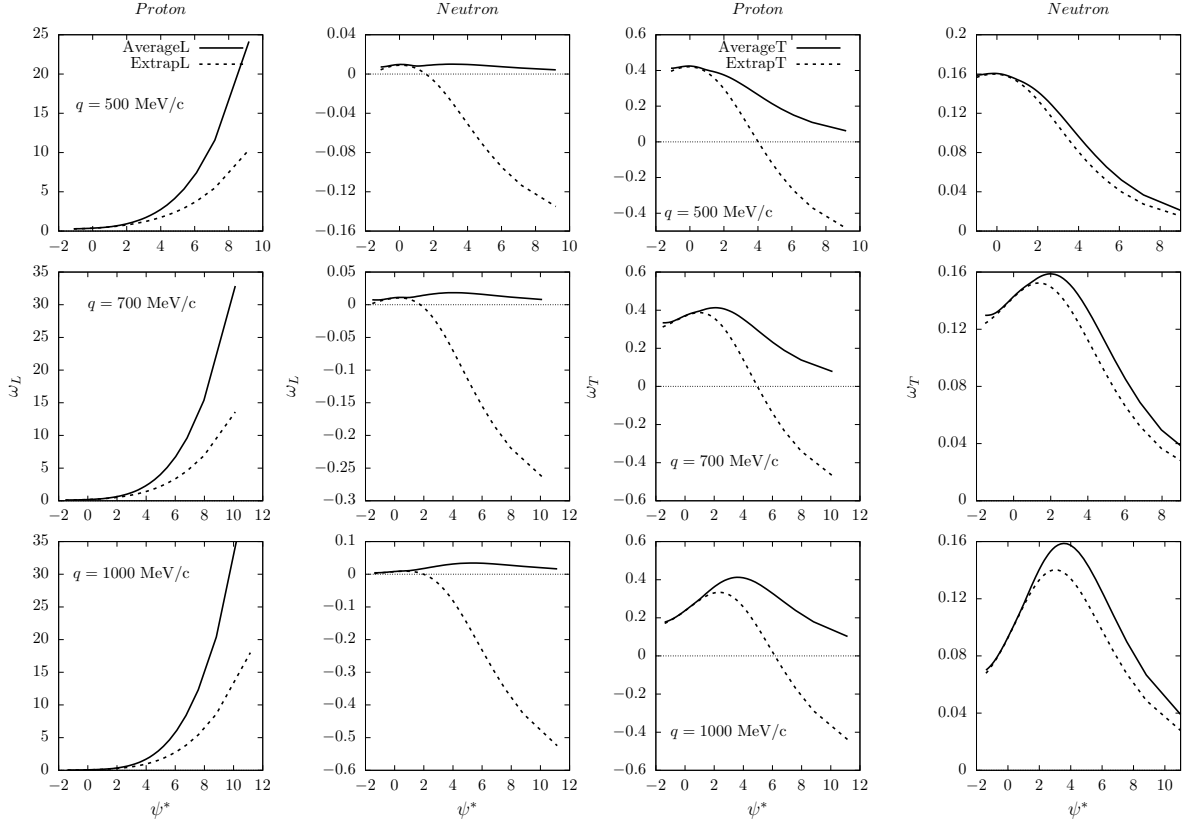


Figure 2.4: Averaged and extrapolated longitudinal and transverse response functions for protons and neutrons, as a function of the scaling variable and for three values of the momentum transfer.

The extrapolated and averaged responses start to differ in the region $\psi^* > 2$ and the discrepancy increases with ψ^* . The extrapolated longitudinal response of neutrons is negative for $\psi^* > 2$. This agrees with what was seen analytically in the previous section, because the extrapolation of the longitudinal magnetic response is negative and the electric form factor of the neutron is negligible. This does not affect the results of the SuSAM* model in the scaling region because the longitudinal response of the neutron is much smaller than that of the proton.

In Fig.2.4 we also can see that the averaged proton transverse response is very similar to the extrapolation in the scaling region and differ for $\psi^* > 2$. They also start to differ in the ψ^* -negative region for $\psi^* < -2$. The extrapolated transverse response of protons is negative from $\psi^* \sim 4\text{--}6$ depending on the value of q . Again this is because the electrical term of the proton dominates this response for large ω since the magnetic term carries a factor τ , which tends to zero for $\omega \rightarrow q$. In contrast the averaged proton transverse responses are always positive.

The averaged transverse neutron response shown in Fig. 2.4 is similar in shape to the Fermi gas extrapolation in the scaling region. But again they differ for $|\psi^*| > 2$, where the averaged one is the largest, and the difference between the two increases with the

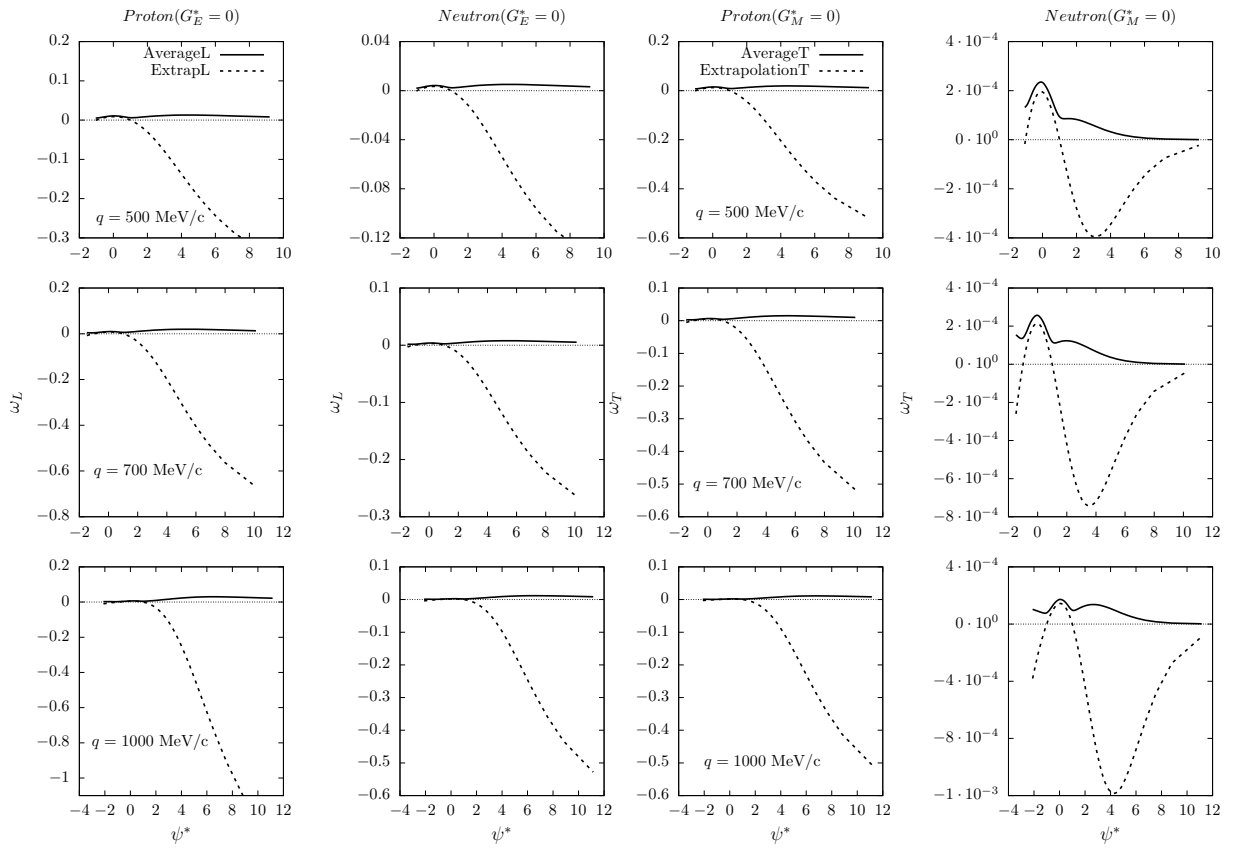


Figure 2.5: Averaged and extrapolated transverse response functions for protons and neutrons, for $G_M^* = 0$, as a function of the scaling variable and for three values of the momentum transfer. Averaged and extrapolated longitudinal response functions for protons and neutrons, for $G_E^* = 0$, as a function of the scaling variable and for three values of the momentum transfer.

momentum transfer.

We have seen in the extrapolation formulas, Eqs.(2.30) and (2.34), that the magnetic contribution to the longitudinal response and the electrical contribution to the transverse response become both negative for $\epsilon_0 > \epsilon_F$. This can be explicitly seen in the results in Fig. 2.5, where we plot the longitudinal responses computed for $G_E^* = 0$ and the transverse responses computed for $G_M^* = 0$, for protons and neutrons. In fact, in all cases of Fig. 2.5 the extrapolated responses are negative for $|\psi^*| > 1$. On the contrary, the averaged responses are always positive.

In Figs. 2.6 and 2.7 we use the superscaling model to investigate the nuclear responses under various inputs for the single-nucleon. The nuclear response is computed from the product of the averaged nucleon-responses and a phenomenological scaling function obtained from the data, using Eq. (2.21).

The results in Figs. 2.6 and 2.7 demonstrate that there are no significant differences in the separate responses of protons and neutrons when computed with the averaged single-

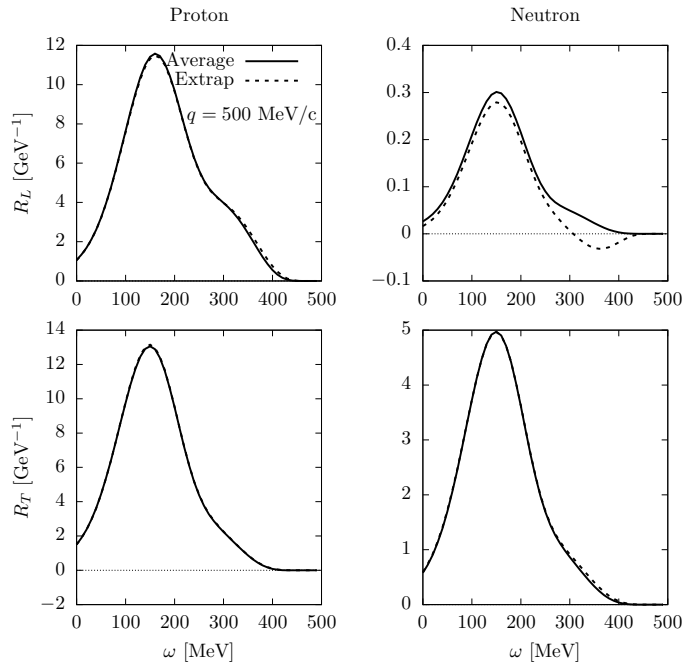


Figure 2.6: Longitudinal and transverse response functions separated for protons and neutrons in the SuSAM* model using the averaged and extrapolated single nucleon responses for $q = 500$ Mev/c

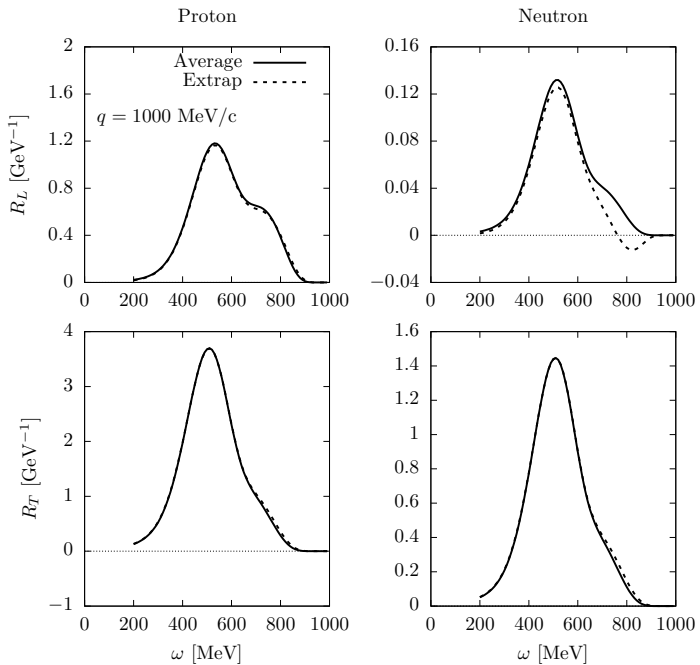


Figure 2.7: The same as in Fig 2.6 for $q = 1000$ MeV/c

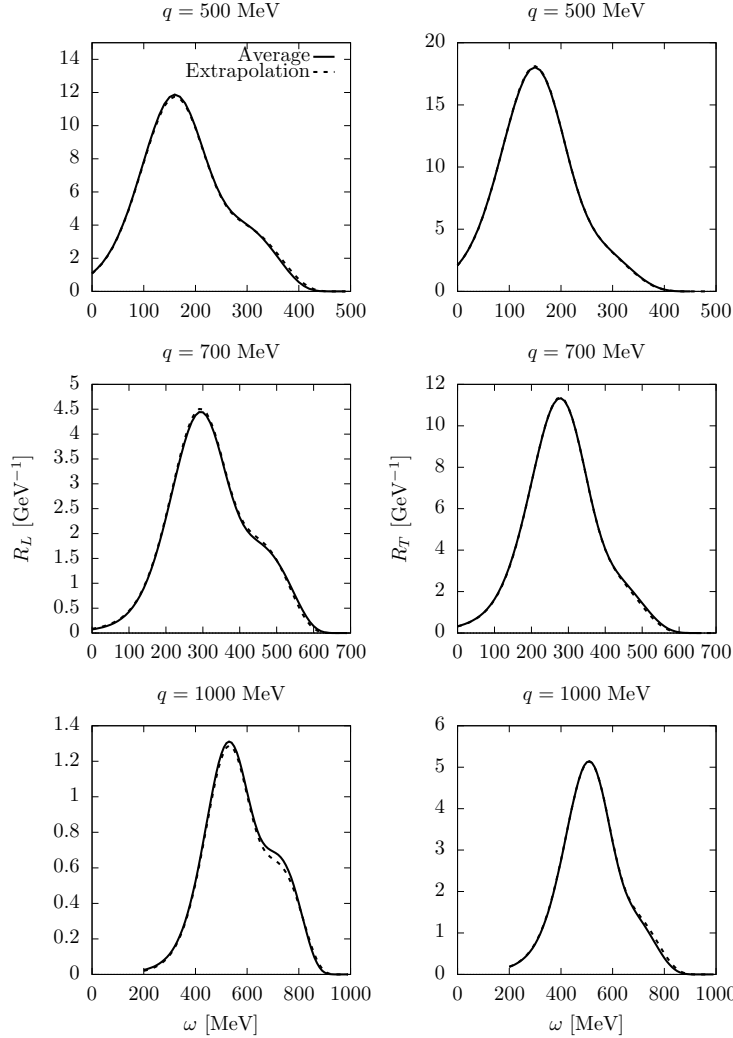


Figure 2.8: Longitudinal and transverse response functions in the SuSAM* model using the averaged and extrapolated single nucleon responses

nucleon compared to the extrapolation. The only difference is seen in the longitudinal neutron response for high ω , which becomes negative in the extrapolated model. However this is not relevant for the total nuclear response, as the neutron contribution is negligible in the longitudinal response as compared to the proton one.

This is verified in the results of Fig. 2.8 for the total responses. Both the averaged and the extrapolated single-nucleon responses give essentially the same result. The results obtained have two important implications. Firstly, they provide support for the validity of using the single-nucleon response extrapolated from the Fermi gas, as this approach yields the same results as using a response averaged with a nuclear momentum distribution that does not have a maximum momentum. Secondly, they justify the use of the averaged response as a means of avoiding the potential issues that we have identified with the extrapolation method.

Finally we have conducted a new scaling analysis of the ^{12}C data using the single-nucleon response averaged with the Fermi distribution. The results, as shown in Figure

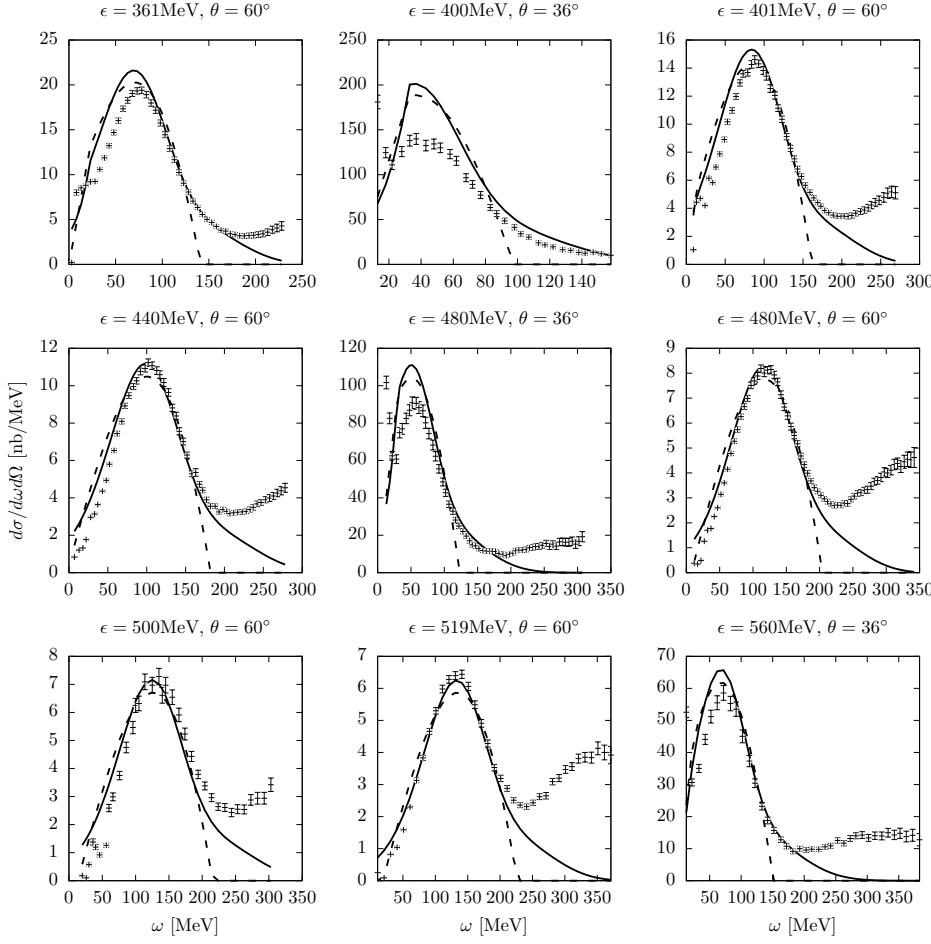


Figure 2.9: Quasielastic (e, e') cross section of ^{12}C as a function of ω for several values of the electron energy, ϵ , and scattering angles θ , computed with the present SuSAM* model (black lines) compared to the RFG with effective mass (dashed lines). Experimental data are from refs. [13, 14]

2.2, demonstrate that the scaling function obtained using this approach is virtually indistinguishable from the one obtained through extrapolation. These findings highlight the robustness of the scaling approach and suggest that using the averaged response may be a viable alternative to extrapolation in certain cases. Furthermore, in Figures 2.9 and 2.10, we compare the cross section of ^{12}C using the SuSAM* model and the RMF model of nuclear matter for a selected set of kinematics. The SuSAM* model still proves to be an excellent method to parameterize the quasielastic cross-section through a single scaling function.

2.4. Final remarks

The findings found in this chapter demonstrate the robustness and versatility of the superscaling models with respect to the choice of the averaged single-responses, and its

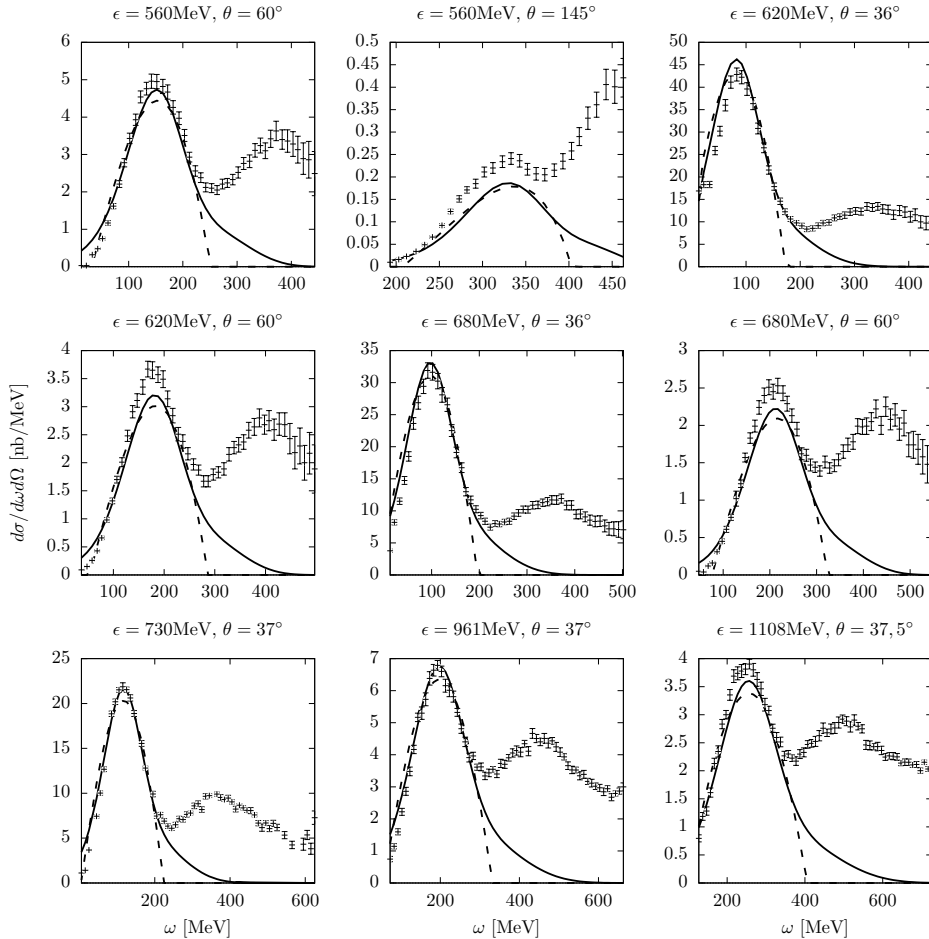


Figure 2.10: Quasielastic (e, e') cross section of ^{12}C as a function of ω for several values of the electron energy, ϵ , and scattering angles θ , computed with the present SuSAM* model (black lines) compared to the RFG with effective mass (dashed lines). Experimental data are from refs. [13, 14]

potential applications in a variety of situations in electron and neutrino scattering. The updated single-nucleon responses provide a well-defined theoretical basis for the scaling function that is compatible with the traditional extrapolation in the scaling region. This reinforces the universality of the scaling function because it is independent of the way in which the average response of the nucleon is defined. This means that the scaling function can be used to describe the electromagnetic response of nucleons in different types of nuclei, regardless of their size or composition.

The averaged single-nucleon model has promising applications in other situations outside the scaling region for high-energy transfer. For instance in two-particle emission reactions, two-particle two-hole (2p2h) excitation can be produced by the one-body current due to nuclear short-range correlations. The electromagnetic interaction with a nucleon belonging to a correlated pair can result in the emission of both nucleons because the correlated nucleons acquire high-momentum components that allow the overlap of the wave function with states above the Fermi momentum. A simple model of emission of two correlated nucleons has been proposed in ref. [156] to explain phenomenologically the tail of the scaling function at high energies.

Another direct application of this method concerns the calculation of the contribution of MEC to the quasielastic 1p1h response in the superscaling model. This calculation was performed in the RFG for instance in Refs. [157, 42] and involves computing an effective one-body current as the sum of one-body plus MEC, 1p1h matrix elements. The traditional scaling model with extrapolation is not trivial to apply in this case, as the single-nucleon responses of the MEC must be computed numerically. However, the averaged single-nucleon responses of the OB+MEC operator can be directly computed as we have done in this work. The analysis of this application constitutes the main content of the next chapter.

Chapter 3

Improved Superscaling model with Meson Exchange Currents

In this chapter, the effect of meson exchange currents will be incorporated consistently into the framework of the relativistic effective mass superscaling model that was discussed in chapter 2. See Ref. [158] for more details.

Until now, an unified model that incorporates 1p1h MEC in the superscaling function had not been proposed. This was primarily due to the violation of scaling properties by MEC, even at the Fermi gas level [159]. Additionally, the 1p1h matrix element of MEC is not easily extrapolated to the $|\psi| > 1$ region outside the range where the Fermi gas response is zero, as nucleons are constrained by the Fermi momentum. In this chapter, we address both of these points by using the new approach where the single nucleon response is averaged with a smeared momentum distribution around the Fermi surface, defined in Eq. (2.35). As a result, the averaged single nucleon responses are well defined for all the values of ψ .

Let us begin by recalling the formalism of QE electron scattering within the RFG model of nuclear matter, now incorporating the MEC effect. In the independent particle models, the main contribution to the hadronic tensor in the quasielastic peak comes from the one-particle one-hole (1p1h) final states. As the transferred energy increases, there are contributions from two-particle two-hole (2p2h) emission, the inelastic contribution of pion emission above the pion mass threshold, and the deep inelastic scattering at higher energies. Therefore, the hadronic tensor can be generally decomposed as the sum of the 1p1h contribution and other contributions:

$$W^{\mu\nu} = W_{1p1h}^{\mu\nu} + W_{2p2h}^{\mu\nu} + \dots \quad (3.1)$$

We focus on the 1p1h response which, in the RFG model, reads

$$W_{1p1h}^{\mu\nu} = \sum_{ph} \langle ph^{-1} | \hat{J}^\mu | F \rangle^* \langle ph^{-1} | \hat{J}^\nu | F \rangle \delta(E_p - E_h - \omega) \theta(p - k_F) \theta(k_F - h) \quad (3.2)$$

where $|p\rangle \equiv |\mathbf{p} s_p t_p\rangle$ and $|h\rangle \equiv |\mathbf{h} s_h t_h\rangle$ are plane wave states for particles and holes, respectively, and $|F\rangle$ is the RFG ground state with all momenta occupied below the Fermi

momentum k_F . The novelty compared to previous chapter is that we start from a current operator that is a sum of one-body and two-body operators. This approach allows us to consider the contributions of both the usual electromagnetic current of the nucleon and the meson-exchange currents to the 1p1h response:

$$\hat{J}^\mu = \hat{J}_{1b}^\mu + \hat{J}_{2b}^\mu, \quad (3.3)$$

where \hat{J}_{1b} represents the OB electromagnetic current of the nucleon and \hat{J}_{2b} is the two-body MEC. Both currents can generate non-zero matrix elements for 1p1h excitation. MEC are two-body operators and they can induce 1p1h excitation due to the interaction of the hit nucleon with a second nucleon acting as a spectator. The many-body matrix elements of these operators are given by

$$\langle ph^{-1} | \hat{J}_{1b}^\mu | F \rangle = \langle p | \hat{J}_{1b}^\mu | h \rangle \quad (3.4)$$

for the OB current and

$$\langle ph^{-1} | \hat{J}_{2b}^\mu | F \rangle = \sum_{k < k_F} \left[\langle pk | \hat{J}_{2b}^\mu | kh \rangle - \langle pk | \hat{J}_{2b}^\mu | kh \rangle \right] \quad (3.5)$$

for the two-body current, where the sum over spectator states (k) is performed over the occupied states in the Fermi gas, considering both the direct and exchange matrix elements. Due to momentum conservation, the matrix element of the OB current between plane waves can be written as

$$\langle p | \hat{J}_{1b}^\mu | h \rangle = \frac{(2\pi)^3}{V} \delta^3(\mathbf{q} + \mathbf{h} - \mathbf{p}) \frac{m_N}{\sqrt{E_p E_h}} j_{1b}^\mu(\mathbf{p}, \mathbf{h}), \quad (3.6)$$

where V is the volume of the system, m_N is the nucleon mass, $E_p = \sqrt{p^2 + m_N^2}$ and $E_h = \sqrt{h^2 + m_N^2}$ are the on-shell energies of the nucleons involved in the process, and $j_{1b}^\mu(\mathbf{p}, \mathbf{h})$ is the OB current (spin-isospin) matrix

$$j_{1b}^\mu(\mathbf{p}, \mathbf{h}) = \bar{u}(\mathbf{p}) \left(F_1 \gamma^\mu + i \frac{F_2}{2m_N} \sigma^{\mu\nu} Q_\nu \right) u(\mathbf{h}), \quad (3.7)$$

being F_1 and F_2 the Dirac and Pauli form factors of the nucleon. In the case of the two-body current, the elementary matrix element can be written in a similar form:

$$\langle p'_1 p'_2 | \hat{J}_{2b}^\mu | p_1 p_2 \rangle = \frac{(2\pi)^3}{V^2} \delta^3(\mathbf{p}_1 + \mathbf{p}_2 + \mathbf{q} - \mathbf{p}'_1 - \mathbf{p}'_2) \frac{m_N^2}{\sqrt{E'_1 E'_2 E_1 E_2}} j_{2b}^\mu(\mathbf{p}'_1, \mathbf{p}'_2, \mathbf{p}_1, \mathbf{p}_2). \quad (3.8)$$

Here $j_{2b}^\mu(\mathbf{p}'_1, \mathbf{p}'_2, \mathbf{p}_1, \mathbf{p}_2)$ is a spin-isospin matrix and it depends on the momenta of the two nucleons in the initial and final state. The two-body current contains the sum of the diagrams shown in Figure 3.1, including the seagull, pionic, and Δ isobar currents. The specific form of the two-body current function will be given later when we discuss the MEC model. By inserting (3.8) into Eq. (3.5) we obtain an expression similar to (3.6) that resembles the matrix element of an effective OB current for the MEC:

$$\langle ph^{-1} | \hat{J}_{2b}^\mu | F \rangle = \frac{(2\pi)^3}{V} \delta^3(\mathbf{q} + \mathbf{h} - \mathbf{p}) \frac{m_N}{\sqrt{E_p E_h}} j_{2b}^\mu(\mathbf{p}, \mathbf{h}). \quad (3.9)$$

The effective OB current generated by the MEC involves a sum over the spectator nucleons and is defined by

$$j_{2b}^\mu(\mathbf{p}, \mathbf{h}) \equiv \sum_{k < k_F} \frac{m_N}{V E_k} [j_{2b}^\mu(\mathbf{p}, \mathbf{k}, \mathbf{h}, \mathbf{k}) - j_{2b}^\mu(\mathbf{p}, \mathbf{k}, \mathbf{k}, \mathbf{h})]. \quad (3.10)$$

Note that in the thermodynamic limit $V \rightarrow \infty$ the above sum will be transformed into an integral over the momenta occupied in the Fermi gas:

$$\frac{1}{V} \sum_{k < k_F} \rightarrow \sum_{s_k t_k} \int \frac{d^3 k}{(2\pi)^3} \theta(k_F - k). \quad (3.11)$$

Finally, we can write the transition matrix element of the total current between the ground state and the 1p1h state as

$$\langle ph^{-1} | \hat{J}^\mu | F \rangle = \frac{(2\pi)^3}{V} \delta^3(\mathbf{q} + \mathbf{h} - \mathbf{p}) \frac{m_N}{\sqrt{E_p E_h}} j^\mu(\mathbf{p}, \mathbf{h}), \quad (3.12)$$

where the effective total current for the 1p1h excitation includes contributions from both the OB current and MEC:

$$j^\mu(\mathbf{p}, \mathbf{h}) = j_{1b}^\mu(\mathbf{p}, \mathbf{h}) + j_{2b}^\mu(\mathbf{p}, \mathbf{h}). \quad (3.13)$$

By inserting (3.12) into Eq. (3.2) and taking the thermodynamic limit, we obtain the following expression for the hadronic tensor:

$$W^{\mu\nu} = \frac{V}{(2\pi)^3} \int d^3 h \delta(E_p - E_h - \omega) \frac{m_N^2}{E_p E_h} 2w^{\mu\nu}(\mathbf{p}, \mathbf{h}) \theta(p - k_F) \theta(k_F - h), \quad (3.14)$$

where $\mathbf{p} = \mathbf{h} + \mathbf{q}$ by momentum conservation after integration over \mathbf{p} . The function $w^{\mu\nu}$ is the effective single-nucleon hadronic tensor in the transition

$$w^{\mu\nu}(\mathbf{p}, \mathbf{h}) = \frac{1}{2} \sum_{s_p s_h} j^\mu(\mathbf{p}, \mathbf{h})^* j^\nu(\mathbf{p}, \mathbf{h}). \quad (3.15)$$

In this equation, we did not include the sum over isospin $t_p = t_h$. Therefore, $w^{\mu\nu}$ refers to the tensor of either proton or neutron emission, and the total tensor would be the sum of the two contributions. Note that the effective single-nucleon tensor $w^{\mu\nu}$ includes the contribution of MEC, thus encompassing an interference between the one-body and two-body currents. Indeed, the relevant diagonal components of the effective single-nucleon hadronic tensor for the longitudinal and transverse responses can be expanded as

$$\begin{aligned} w^{\mu\mu}(\mathbf{p}, \mathbf{h}) &= \frac{1}{2} \sum_{s_p s_h} |j_{1b}^\mu + j_{2b}^\mu|^2 \\ &= \frac{1}{2} \sum |j_{1b}^\mu|^2 + \text{Re} \sum (j_{1b}^\mu)^* j_{2b}^\mu + \frac{1}{2} \sum |j_{2b}^\mu|^2 \\ &\equiv w_{1b}^{\mu\mu} + w_{1b2b}^{\mu\mu} + w_{2b}^{\mu\mu}, \end{aligned} \quad (3.16)$$

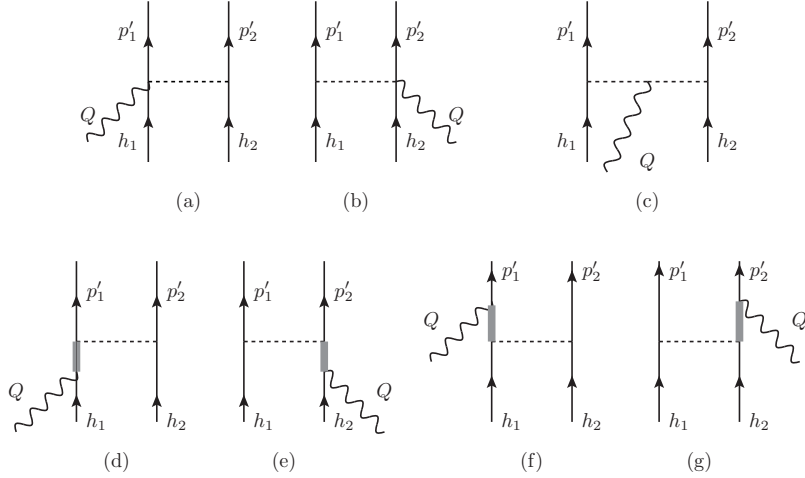


Figure 3.1: Feynman diagrams for the 2p2h MEC model used in this work.

where $w_{1b}^{\mu\mu}$ is the tensor corresponding to the one-body current, $w_{1b2b}^{\mu\mu}$ represents the interference between the one-body and two-body currents, and $w_{2b}^{\mu\mu}$ corresponds to the contribution of the two-body current alone. The one-body part is the leading contribution in the quasielastic peak, while the dominant contribution of the MEC corresponds to the interference with the one-body current [33, 42], being the pure contribution of the two-body current generally smaller.

3.1. Meson-exchange currents

In this section, we present the relativistic meson exchange currents model developed in Ref. [160]. The Feynman diagrams shown in Fig. 3.1 illustrate the different components of the MEC model. Diagrams (a) and (b) correspond to the seagull current, diagram (c) represents the pion-in-flight current, and diagrams (d,e) and (f,g) depict the forward- and backward- $\Delta(1232)$ currents, respectively. The specific treatment of the Δ current is model-dependent, and various versions exist with possible corrections to the off-shell relativistic interaction of the Δ . While these different models may exhibit slight variations and corrections to the Δ off-shell interaction, they generally yield similar results for the dominant transverse response at the quasielastic peak. In particular, in the results section, we will compare our findings with the model presented in Refs. [161, 42], which was previously employed to assess the impact of MEC on the 1p1h response.

In our model the MEC functions defined in Eq. (3.8) correspond to the sum of diagrams of Fig. 3.1

$$j_{2b}^{\mu}(\mathbf{p}'_1, \mathbf{p}'_2, \mathbf{p}_1, \mathbf{p}_2) = j_{sea}^{\mu} + j_{\pi}^{\mu} + j_{\Delta}^{\mu}, \quad (3.17)$$

where the Δ current is the sum of forward and backward terms

$$j_{\Delta}^{\mu} = j_{\Delta F}^{\mu} + j_{\Delta B}^{\mu}. \quad (3.18)$$

These functions are defined by

$$j_{sea}^\mu = i[\boldsymbol{\tau}^{(1)} \times \boldsymbol{\tau}^{(2)}]_z \frac{f^2}{m_\pi^2} V_{s'_1 s_1}(p'_1, p_1) F_{\pi NN}(k_1^2) \bar{u}_{s'_2}(p'_2) F_1^V \gamma^5 \gamma^\mu u_{s_2}(p_2) + (1 \leftrightarrow 2) \quad (3.19)$$

$$j_\pi^\mu = i[\boldsymbol{\tau}^{(1)} \times \boldsymbol{\tau}^{(2)}]_z \frac{f^2}{m_\pi^2} F_1^V V_{s'_1 s_1}(p'_1, p_1) V_{s'_2 s_2}(p'_2, p_2) (k_1^\mu - k_2^\mu) \quad (3.20)$$

$$\begin{aligned} j_{\Delta F}^\mu &= U_F(1, 2)_z \frac{f^*}{m_\pi^2} V_{s'_2 s_2}(p'_2, p_2) F_{\pi N\Delta}(k_2^2) \bar{u}_{s'_1}(p'_1) k_2^\alpha G_{\alpha\beta}(p_1 + Q) \Gamma^{\beta\mu}(Q) u_{s_1}(p_1) \\ &\quad + (1 \leftrightarrow 2) \end{aligned} \quad (3.21)$$

$$\begin{aligned} j_{\Delta B}^\mu &= U_B(1, 2)_z \frac{f^*}{m_\pi^2} V_{s'_2 s_2}(p'_2, p_2) F_{\pi N\Delta}(k_2^2) \bar{u}_{s'_1}(p'_1) k_2^\beta \hat{\Gamma}^{\mu\alpha}(Q) G_{\alpha\beta}(p'_1 - Q) u_{s_1}(p_1) \\ &\quad + (1 \leftrightarrow 2) \end{aligned} \quad (3.22)$$

We will evaluate these matrix elements in the framework of the RMF model, where the spinors $u(p)$ are the solutions of the Dirac equation with relativistic effective mass m_N^* . The four-vectors $k_i^\mu = p_i^\mu - p_i^\mu$ with $i = 1, 2$ are the momenta transferred to the nucleons 1,2. We have defined the following function that includes the πNN vertex, a form factor, and the pion propagator

$$V_{s'_1 s_1}(p'_1, p_1) = F_{\pi NN}(k_1^2) \frac{\bar{u}_{s'_1}(p'_1) \gamma^5 k_1 u_{s_1}(p_1)}{k_1^2 - m_\pi^2}. \quad (3.23)$$

We apply strong form factors at the pion absorption/emission vertices given by [162, 163]

$$F_{\pi NN}(k^2) = F_{\pi N\Delta}(k^2) = \frac{\Lambda^2 - m_\pi^2}{\Lambda^2 - k^2}. \quad (3.24)$$

The charge structure of the Δ current involves the isospin matrix element of the operators

$$U_F(1, 2)_z = \sqrt{\frac{3}{2}} \sum_{i=1}^3 (T_i^{(1)} T_z^{(1)\dagger}) \otimes \tau_i^{(2)}, \quad (3.25)$$

$$U_B(1, 2)_z = \sqrt{\frac{3}{2}} \sum_i (T_z^{(1)} T_i^{(1)\dagger}) \otimes \tau_i^{(2)}, \quad (3.26)$$

where we denote by T_i^\dagger the Cartesian coordinates of the $\frac{1}{2} \rightarrow \frac{3}{2}$ transition isospin operator. This transition can be represented using the Clebsch-Gordan coefficients,

$$\langle \frac{3}{2} t_\Delta | T_\mu^\dagger | \frac{1}{2} t \rangle = \langle \frac{1}{2} t_1 \mu | \frac{3}{2} t_\Delta \rangle \quad (3.27)$$

with T_μ^\dagger being the spherical components of the vector \vec{T}^\dagger . With the aid of the expression $T_i T_j^\dagger = (2/3) \delta_{ij} - \frac{i}{3} \epsilon_{ijk} \tau_k$ and making the summation, we can rewrite the isospin operators in the forward and backward Δ current as

$$U_F(1, 2)_z = \sqrt{\frac{3}{2}} \left(\frac{2}{3} \tau_z^{(2)} - \frac{i}{3} [\boldsymbol{\tau}^{(1)} \times \boldsymbol{\tau}^{(2)}]_z \right) \quad (3.28)$$

$$U_B(1, 2)_z = \sqrt{\frac{3}{2}} \left(\frac{2}{3} \tau_z^{(2)} + \frac{i}{3} [\boldsymbol{\tau}^{(1)} \times \boldsymbol{\tau}^{(2)}]_z \right). \quad (3.29)$$

The $\gamma N \rightarrow \Delta$ transition vertex in the forward Δ current is defined as [164, 165]

$$\Gamma^{\beta\mu}(Q) = \frac{C_3^V}{m_N} (g^{\beta\mu} Q - Q^\beta \gamma^\mu) \gamma_5 \quad (3.30)$$

while for the backward Δ current

$$\hat{\Gamma}^{\mu\alpha}(Q) = \gamma^0 [\Gamma^{\alpha\mu}(-Q)]^\dagger \gamma^0. \quad (3.31)$$

In this vertex we neglect the contributions of order $O(1/m_N^2)$. Note that the $\Gamma^{\beta\mu}$ operator is a spin matrix and depends on the vector form factor C_3^V . In our work, we use the vector form factor in Δ current from Refs. [165]:

$$C_3^V(Q^2) = \frac{2.13}{(1 - \frac{Q^2}{M_V^2})^2} \frac{1}{1 - \frac{Q^2}{4M_V^2}}. \quad (3.32)$$

Various alternative approximations to the propagator have been proposed [166]. However, in the case of the quasielastic peak, the typical kinematics are of the order of 1 GeV, and these issues are not expected to be relevant. They are overshadowed by other more significant nuclear effects that dominate in this energy regime. Here we use the Δ propagator commonly used for the spin-3/2 field

$$G_{\alpha\beta}(P) = \frac{\mathcal{P}_{\alpha\beta}(P)}{P^2 - M_\Delta^2 + iM_\Delta\Gamma(P^2) + \frac{\Gamma(P^2)^2}{4}} \quad (3.33)$$

where M_Δ and Γ are the Δ mass and width respectively. The projector $\mathcal{P}_{\alpha\beta}(P)$ over spin-3/2 on-shell particles is given by

$$\mathcal{P}_{\alpha\beta}(P) = -(\not{P} + M_\Delta) \left[g_{\alpha\beta} - \frac{\gamma_\alpha \gamma_\beta}{3} - \frac{2P_\alpha P_\beta}{3M_\Delta^2} + \frac{P_\alpha \gamma_\beta - P_\beta \gamma_\alpha}{3M_\Delta} \right]. \quad (3.34)$$

Finally, the Δ width $\Gamma(P^2)$ is given by

$$\Gamma(P^2) = \Gamma_0 \frac{m_\Delta}{\sqrt{P^2}} \left(\frac{p_\pi}{p_\pi^{res}} \right)^3. \quad (3.35)$$

In the above equation, p_π is the momentum of the final pion resulting from the Δ decay and p_π^{res} is its value at resonance ($P^2 = m_\Delta^2$), and $\Gamma_0 = 120$ MeV is the width at rest. The width (3.35) corresponds to the Δ in a vacuum, and it is expected to be slightly different in the medium depending on the kinematics.

In the relativistic mean field description used in this work, we consider that Δ also interacts with scalar and vector fields, acquiring an effective mass and vector energy. To treat this case, we make the following substitutions in the Δ propagator for the Δ mass and momentum [149, 167]:

$$M_\Delta \rightarrow M_\Delta^*, \quad P^{*\mu} = P^\mu - \delta_{\mu 0} E_v^\Delta. \quad (3.36)$$

We use the value $M_\Delta^* = 1042$ MeV, taken from [155], and the universal vector coupling $E_v^\Delta = E_v = 141$ MeV.

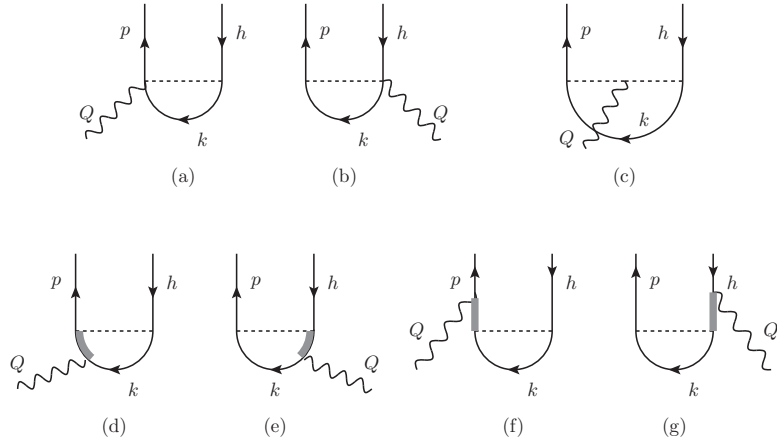


Figure 3.2: Diagrams for the 1p1h MEC matrix elements

With the MEC model defined in Eqs. (3.19)-(3.22), the effective one-body current $j_{2b}^\mu(\mathbf{p}, \mathbf{h})$ is generated by summing over the spin, isospin and momentum of the spectator nucleon, as in Eq. (3.10). Due to the sum over isospin t_k and spin, the direct part is zero and two of the four exchange diagrams contributing to the Δ current in the 1p1h matrix element are zero. Specifically, in the forward Δ current, the diagram containing the isospin operator $U_F(2, 1)$ yields zero (diagram (g) of Fig. 3.2). Similarly, for the backward Δ current, the diagram involving the isospin operator $U_B(1, 2)$ also vanishes (diagram (f) of Fig. 3.2). Therefore only diagrams (d), forward, and (e), backward, contribute in the case of the Δ current. These results are demonstrated in Appendix B.

3.2. Results

In this section, we present results for the effects of MEC on the 1p1h response functions using several models: RFG, the relativistic Fermi gas with effective mass (RMF), and the generalized SuSAM* model of chapter 2. By employing these different models, we take into account relativity and we can analyze the impact of including the relativistic effective mass of the nucleon and the Δ resonance appearing in the MEC. The scaling analysis described in chapter 2 will allow us to study the influence of MEC on the generalized scaling function also in the region $|\psi^*| > 1$ where the RFG and RMF responses are zero. Moreover, we can investigate how the inclusion of MEC affects the 1p1h response functions and compare it with the predictions of the RFG and RMF models.

Unless stated otherwise, we present the results for ^{12}C with a Fermi momentum of $k_F = 225$ MeV/c. We use an effective mass of $M^* = 0.8$, following the same choice of parameters as in reference [154, 155]. The calculation of 1p1h responses involves evaluating the 1p1h matrix element of the MEC, as given by Eq. (3.10). This requires performing a numerical three-dimensional integration to account for the momentum dependence. Subsequently, a one-dimensional integration is carried out to calculate the averaged single-nucleon responses, as described in Eq. (2.15).

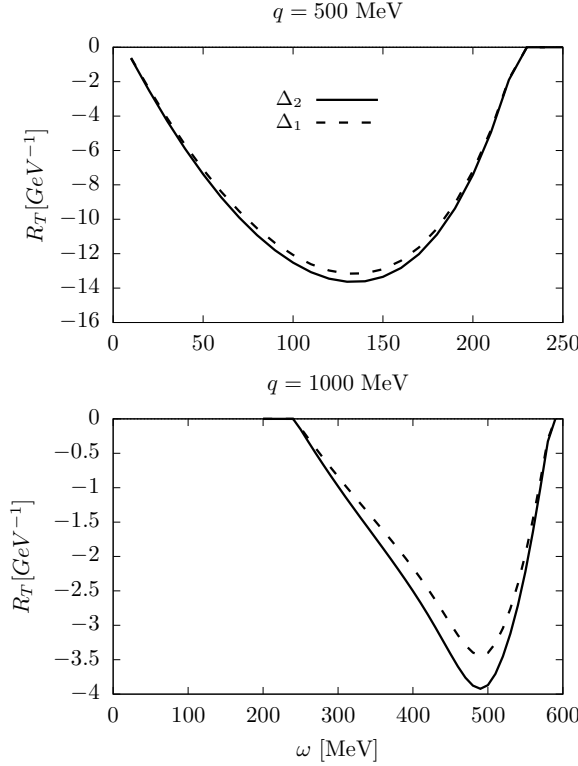


Figure 3.3: Interference OB-MEC in the transverse response of ^{40}Ca for two values of the momentum transfer, with $k_F = 237$ MeV/c. In the graph, the curve labeled Δ_1 corresponds to using the Δ current of the present work in RFG. The curve Δ_2 corresponds to the calculation from reference [42].

First, since this work is an extension of the MEC model from Ref. [42] to the superscaling formalism, we will compare with the OB-MEC interference responses presented in [42] within the framework of the RFG. It should be noted that in [42] a different version of the Δ current was used. The Δ current was obtained from the $\gamma N \Delta$ Lagrangian proposed by Pascalutsa [161]

$$\mathcal{L}_{\gamma N \Delta} = ie \frac{G_1}{2m_N} \bar{\psi}^\alpha \Theta_{\alpha\mu} \gamma_\nu \gamma_5 T_3^\dagger N F^{\nu\mu} + \text{h.c.}, \quad (3.37)$$

plus $O(1/m_N^2)$ terms that give negligible contribution in the quasielastic energy region. The tensor $\Theta_{\alpha\mu}$ may contain an off-shell parameter and another arbitrary parameter related to the contact invariance of the Lagrangian. In this work we use the simplest form

$$\Theta_{\alpha\mu} = g_{\alpha\mu} - \frac{1}{4} \gamma_\alpha \gamma_\mu. \quad (3.38)$$

The coupling constant G_1 was determined in [161] by fitting Compton scattering on the nucleon. However, there is a detail that needs to be clarified: the isospin operator used by Pascalutsa is normalized differently from the standard convention. That is, $T_i^{\text{Pascalutsa}} = \sqrt{\frac{3}{2}} T_i$, where T_i is the operator used in our calculation. This means that if we use the standard T_i in the Lagrangian (3.37), it should be multiplied by $\sqrt{\frac{3}{2}}$. This is equivalent to

multiplying Pascalutsa's coupling constant $G_1 = 4.2$ by the factor $\sqrt{\frac{3}{2}}$. In reference [42], this detail went unnoticed, and the $\sqrt{3/2}$ factor was not included in the calculations.

Using the Lagrangian given by Eq. (3.37), the following Δ current was obtained in [42]

$$\begin{aligned} j_{\Delta F}^\mu &= [(T_i T_3^\dagger) \otimes \tau_i]_{t'_1 t'_2, t_1 t_2} \frac{f f^*}{m_\pi^2} F_\Delta(Q^2) V_{\pi NN}^{s'_2 s_2}(p'_2, p_2) F_{\pi N\Delta}(k_2^2) \\ &\quad \bar{u}_{s'_1}(p'_1) k_2^\alpha \left[\Theta^{\alpha\beta} G_{\beta\rho}(p_1 + Q) \frac{G_1}{2m_N} [\Theta^{\rho\mu} \gamma^\nu - \Theta^{\rho\nu} \gamma^\mu] \gamma_5 Q_\nu \right] u_{s_1}(p_1) + (1 \leftrightarrow 2), \end{aligned} \quad (3.39)$$

and a similar expression for the Δ backward current. This current was used in Ref. [42] to compute the OB-MEC interference with the following form factor

$$F_\Delta(Q^2) = G_E^p(Q^2) \left(1 - \frac{Q^2}{3.5(GeV/c)^2} \right)^{-1/2} \quad (3.40)$$

where G_E^p is the electric form factor of the proton.

In Figure 3.3, we present the interference between the OB and Δ currents in the transverse response of ^{40}Ca . We compare our results with the model of reference [42] in RFG, where the Lagrangian of Pascalutsa was used. The results of [42] have been corrected with the factor of $\sqrt{\frac{3}{2}}$ mentioned earlier. For $q = 500$ MeV/c, there is little difference between the two models. However, for $q = 1$ GeV/c, the difference becomes more noticeable.

The results of Fig. 3.3 show that the Δ current model used in this work does not differ significantly from the model in reference [42], providing similar results. The small differences observed can be attributed to the different form factor and coupling constants, and can be understood as a model dependence in these results. From here on, all the results refer to the Δ current model described in equations (3.21,3.22).

It is expected that any relativistic model should reproduce the results of the well-established non-relativistic model for small values of energy and momentum in the non-relativistic limit [168]. As a check in this regard, in Fig. 3.4 we compare the present model with the non-relativistic Fermi gas model from ref. [33]. The non relativistic Δ current used is taken from [42]. This current is similar to the non relativistic Δ -current of the vector MEC performed in Appendix C. To perform this comparison the same form factors and coupling constants are used in the relativistic and non relativistic models. To take this limit in Fig. 3.4, we follow the procedure as follows: q is small and $k_F = q/2$. We show the comparison between the two models for various values of q ranging from 100 to 500 MeV/c. In the left panels, we present the contribution of the transverse response stemming from the interference OB- π (including seagull and pionic) between the pure pionic MEC (diagrams a–c in Fig. 3.2), and in the right panels, we show the OB- Δ interference (diagrams d–g in Fig. 3.2) for the same values of q . As expected, we observe that for $q = 100$ MeV/c, the relativistic and non-relativistic models practically coincide, demonstrating the consistency between the two models in the non-relativistic limit.

In Fig. 3.4 one can also observe that for low values of q the dominant contributions to the MEC are from the seagull and pion-in-flight diagrams, with the seagull diagram

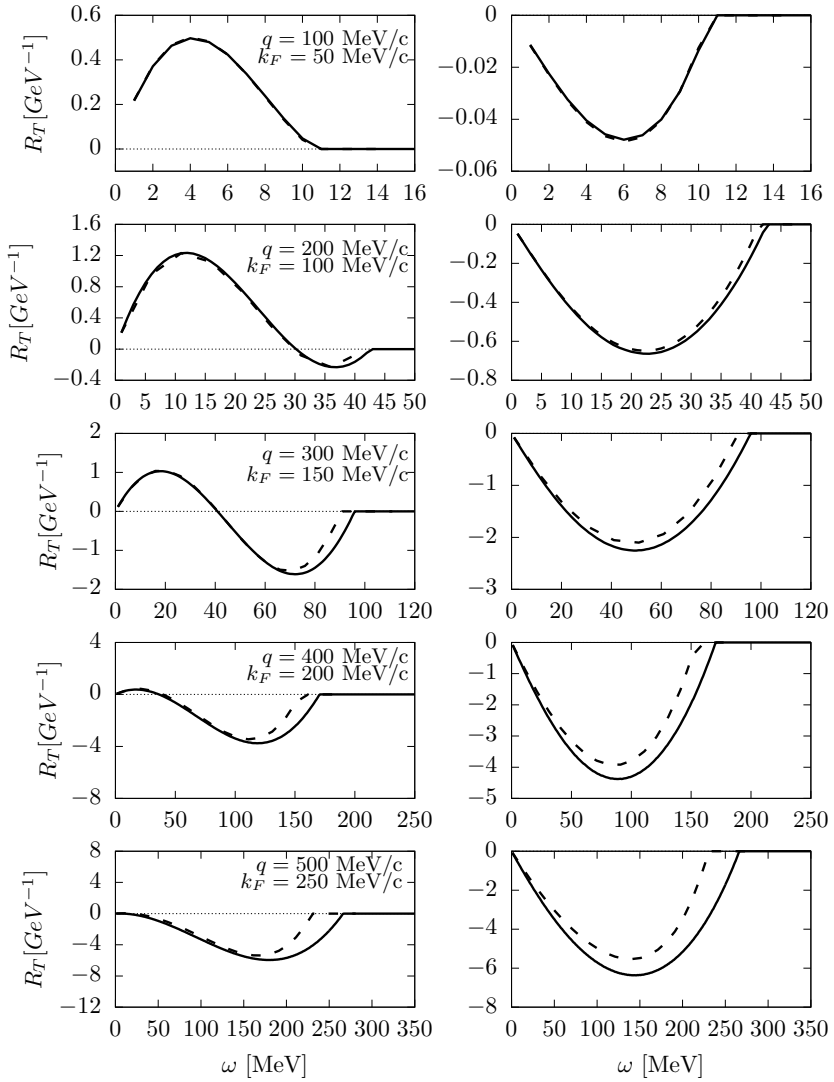


Figure 3.4: Comparison between relativistic and non relativistic MEC transverse responses in ^{12}C . Dashed lines: RFG. Solid lines: non-relativistic Fermi gas. Left panels show the interference OB- π (seagull and pionic), and left panels the interference OB- Δ . In these calculations the strong form factors in the pion vertices are set to one.

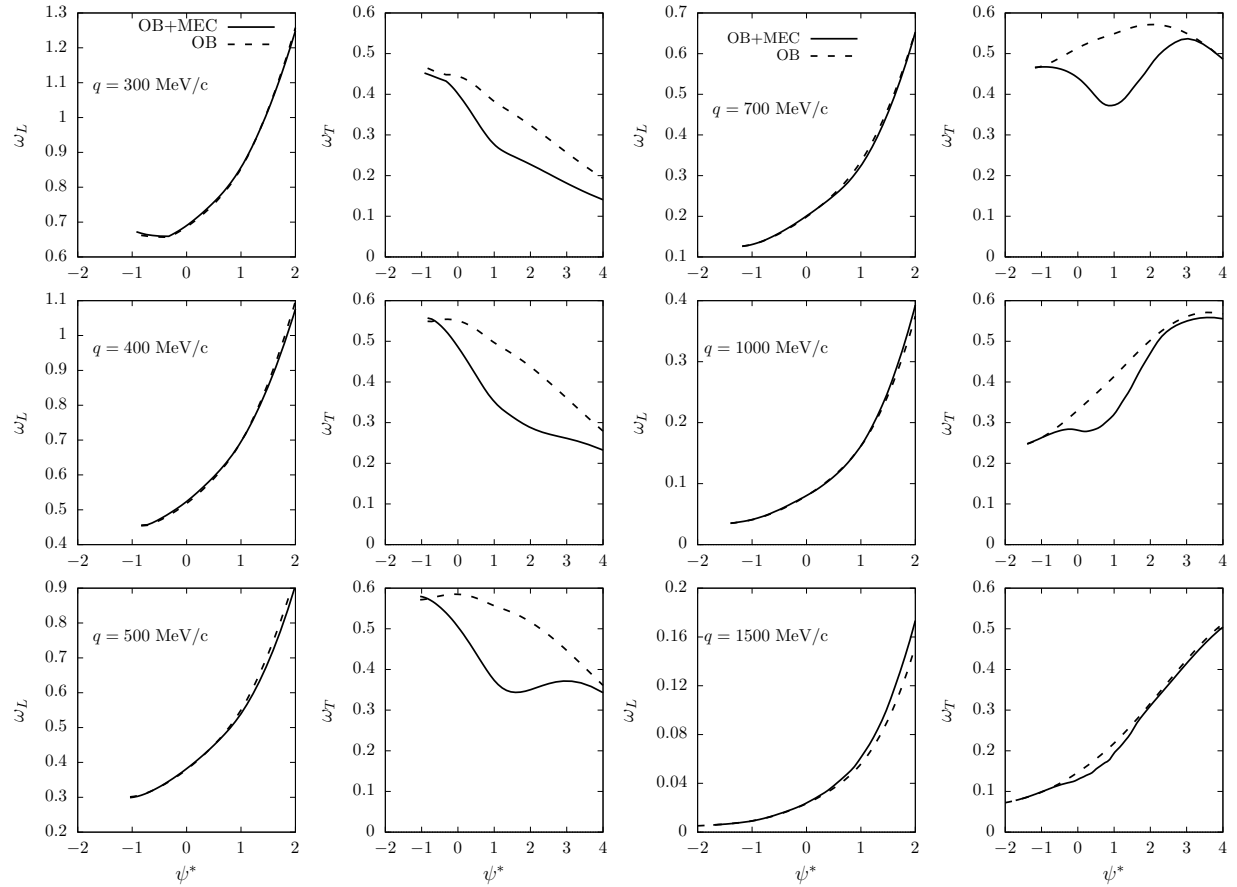


Figure 3.5: Averaged single nucleon responses computed with and without MEC, for several values of the momentum transfer as a function of the scaling variable ψ^* .

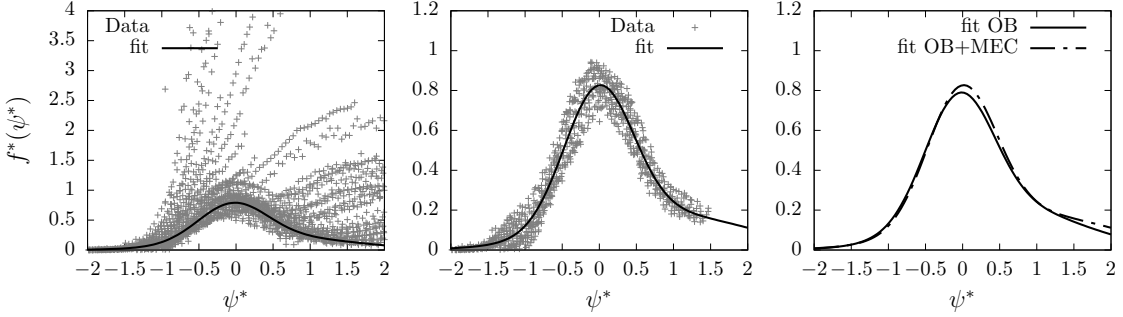


Figure 3.6: Scaling analysis of ^{12}C data including MEC and relativistic effective mass $M^* = 0.8$. The Fermi momentum is $k_F = 225$ MeV/c. In the left panel, we show the data points after scaling, representing the overall distribution. In the middle panel, we display the selected data points, which have been chosen after eliminating those that do not exhibit clear scaling behavior. In the right panel, we present the phenomenological scaling function, which has been fitted to the selected data points, compared to the scaling function obtained in a similar analysis without MEC. Experimental data are taken from Refs. [13, 14].

playing a particularly important role. These diagrams contribute positively to the MEC, enhancing the overall response. On the other hand, the contribution from the Δ resonance is negative. As q increases, the influence of the Δ resonance becomes more significant, and it starts to dominate the MEC contribution for q values around 400 MeV/c.

Before performing the scaling analysis, we examine the averaged single-nucleon responses that will be used to scale the data. In Figure 3.5, we display the longitudinal and transverse effective single-nucleon responses for various values of q as a function of the scaling variable. The calculated responses are shown separately for the OB current and the total responses including the MEC and taking into account the sum of protons and neutrons. The total response, which we have defined in equation (2.21), comes from the product of the single nucleon with the phenomenological scaling function obtained from the (e, e') data as shown below (note that the single-nucleon tensor in equation (2.21) now includes the contribution from meson exchange currents). We have used the Fermi distribution, Eq. (2.35), with a smearing parameter $b = 50$ MeV/c, although the single nucleon responses do not depend much on this specific value. It is observed that the effect of the MEC is negligible in the longitudinal response, as the curves for the OB current and total response overlap. However, in the transverse response, the effect of the MEC becomes appreciable, resulting in a reduction of the w_T response compared to the OB current. This reduction can be attributed to the interference between the one-body and two-body currents, which leads to a modified transverse response. Note that the center of the quasielastic peak corresponds to $\psi^* = 0$, where the energy and momentum can be transferred to a nucleon at rest. We see that MEC have a larger impact in the region $\psi^* > 0$, that is, the right-hand side of the peak, corresponding to higher energy transfers.

In Figure 3.6, we present the scaling analysis of the ^{12}C data using the formalism of scaling explained in the previous chapter but including MEC in the single-nucleon prefactors. In the left panel, the experimental data, f_{exp}^* , are plotted against ψ^* in the interval

$-2 < \psi^* < 2$. Experimental data are from Refs. [13, 14] and cover a wide electron energy range, from 160 MeV up to 5.8 GeV. We observe, as in chapter 2, a significant dispersion of many data points, indicating a wide range of inelastic scattering events. However, we also notice that a portion of the data points cluster together and collapse into a thick band. These data points can be considered as associated to quasielastic (1p1h) events. To select these quasielastic data, we apply a density criterion. For each point, we count the number of points, n , within a neighborhood of radius $r = 0.1$, and eliminate the point if n is less than 25. Points that have been disregarded are likely to correspond to inelastic excitations and low energy processes that violate scaling and cannot be considered within quasielastic processes. We observe that the remaining selected points, about half of the total, shown in the middle panel of Fig. 3.6, form a distinct thick band. These points represent the ones that best describe the quasielastic region and approximately exhibit scaling behavior. The black curve represents the phenomenological quasielastic function $f^*(\psi^*)$, that provides the best fit to the selected data using a sum of two Gaussian functions:

$$f^*(\psi^*) = a_3 e^{-(\psi^* - a_1)^2 / (2a_2^2)} + b_3 e^{-(\psi^* - b_1)^2 / (2b_2^2)}. \quad (3.41)$$

The parameters found are shown in table 3.1.

In the right panel of Fig. 3.6 we compare the scaling function obtained in our analysis with the scaling function obtained without including the MEC contributions in chapter 2. When including the MEC, the scaling function appears slightly higher since the single-nucleon response with MEC is slightly smaller than without them. However, both analyses provide a similarly acceptable description of the data. This suggests that while the MEC do have an impact on the scaling behavior, their effect is relatively small and does not significantly alter the overall scaling pattern observed in the data.

Now that we have obtained the phenomenological scaling function through the scaling analysis, we can utilize this function to calculate the response functions of the model beyond the RMF. By multiplying the scaling function by the averaged single nucleon responses, as stated in Eq. (2.21), we can extend our calculations to different kinematic regimes and explore the behavior of the responses beyond the relativistic mean field description. This allows us to investigate the influence of various factors, such as the MEC and relativistic effects, on the response functions and cross sections.

In Figures 3.7-3.10, we present the interference's of the OB-MEC in the response functions for different values of q (500, 700, 1000, and 1500 MeV/c). We separate the interferences into OB-seagull, OB-pionic, and OB- Δ contributions for both the longitudinal and transverse responses as functions of ω . Each panel displays three curves corresponding to the free RFG (with effective mass $M^* = 1$), the RMF (with effective mass $M^* = 0.8$), and the present SuSAM* model. These figures allow us to analyze the relative contributions of the different OB-MEC interferences in the response functions at various kinematic regimes.

a_1	a_2	a_3	b_1	b_2	b_3
-0.01015	0.46499	0.69118	0.86952	1.16236	0.17921

Table 3.1: Table of fitted parameters of the scaling function.

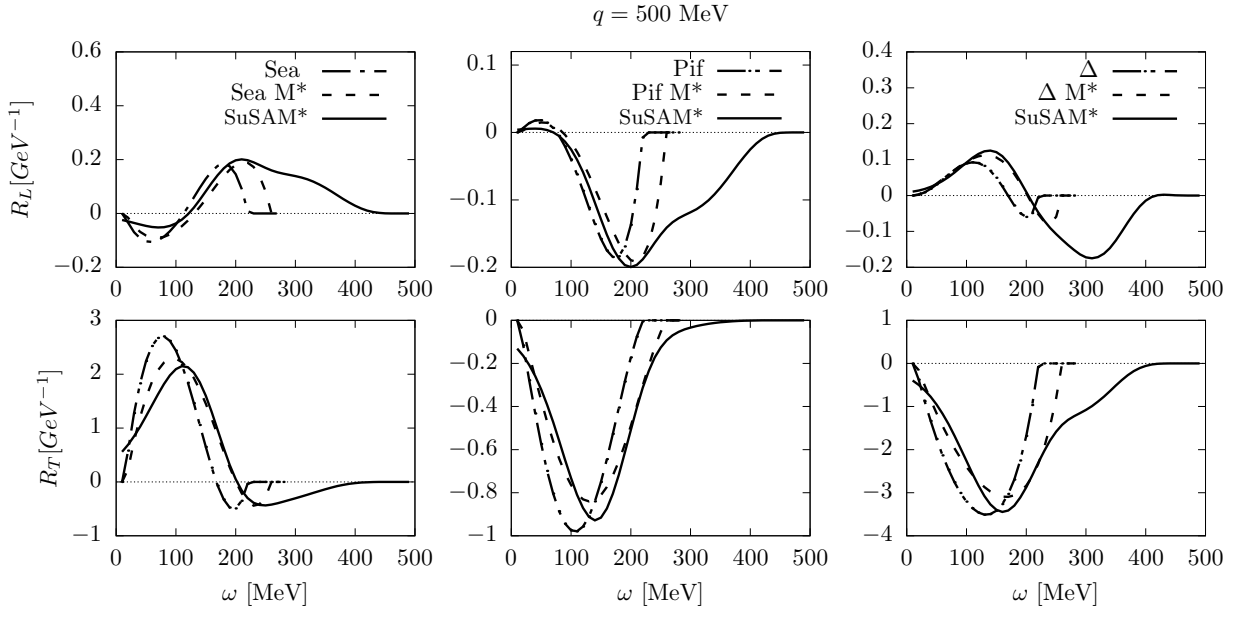


Figure 3.7: Interference OB-MEC responses separated in seagull, pion-in-flight, and Δ contributions for ^{12}C and $q = 500$ MeV/c. In each panel we compare the results of RFG (with $M^* = 1$, dot-dashed), with the RMF (with $M^* = 0.8$, dashed) and the SuSAM* model (solid).

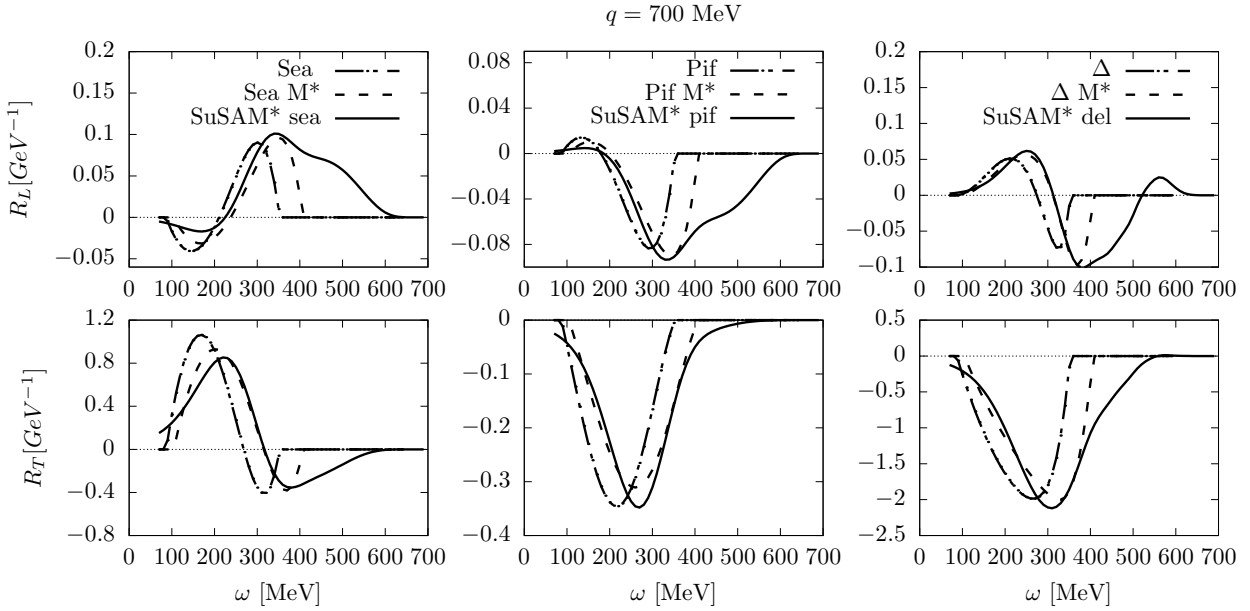
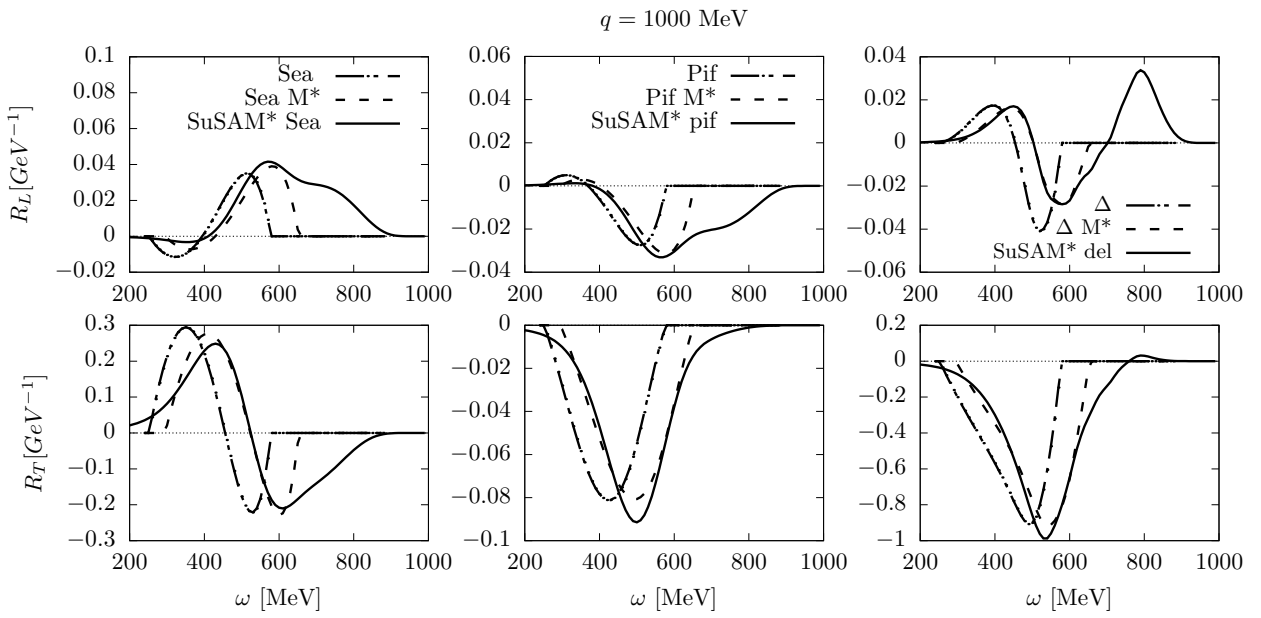
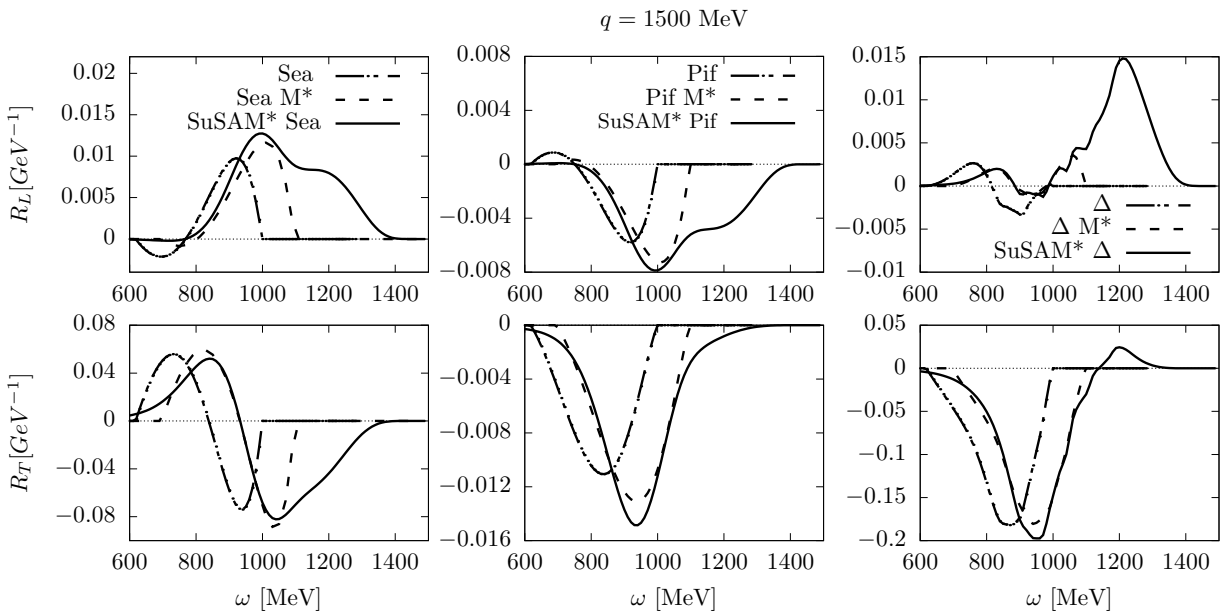


Figure 3.8: The same as Fig. 7 for $q = 700$ MeV/c.

Figure 3.9: The same as Fig. 7 for $q = 1000$ MeV/c.Figure 3.10: The same as Fig. 7 for $q = 1500$ MeV/c.

By comparing the results obtained from the RFG, RMF, and SuSAM* models, we can observe the effects of including the relativistic interaction through the effective mass and the scaling function on the interferences.

First we observe that the introduction of the effective mass $M^* = 0.8$ shifts the responses to the right, towards higher energy values. The effective mass takes into account the binding of the nucleon in the nucleus, which causes the quasielastic peak to approximately coincide with the maximum of the experimental cross section. In the RFG, this is traditionally taken into account by subtracting a binding energy of approximately 20 MeV from ω to account for the average separation energy of the nucleons. In the RMF, this is automatically included by considering the effective mass of the nucleon, $M^* = 0.8$, which was adjusted for ^{12}C precisely to achieve this effect.

In the transition from the RMF to the SuSAM* model, we replace the scaling function of the RFG with the phenomenological scaling function that we have adjusted. This new scaling function extends beyond the region of $-1 < \psi^* < 1$, where the RFG scaling function is zero. As a result, we observe in Figures 3.7-3.10 that the interferences acquire a tail towards high energies, similar to the behavior of the scaling function. The tail effect is more pronounced in the longitudinal responses because the single-nucleon longitudinal response, as shown in Figure 3.5, increases with ω . This amplifies the tail when multiplied by the scaling function. However, it is important to note that the contribution of the MEC to the longitudinal response is relatively small compared to the dominant transverse response. Therefore, while the tail effect is observed in the longitudinal responses, its impact on the cross section is not as significant as in the transverse channel, if not negligible.

In the dominant transverse response, the seagull contribution from the MEC is positive, leading to an enhancement of the response, while the pionic and Δ contributions are negative, causing a reduction in the overall response when including the MEC. This is in line with pioneering calculations by Kohno and Otsuka [40] and by Alberico *et al.* [41] in the non-relativistic Fermi gas. Moreover, in shell model calculations, similar results have been obtained [33]. It is worth noting that the relative importance of the MEC contributions depend on the momentum transfer q and the energy transfer ω . For the values considered in Figures 3.7-3.10, the Δ current is found to be the dominant contribution, leading to a net negative effect from the MEC.

The observation in Fig. 3.10 of a sign change and a small bump in the OB- Δ transverse response for high values of ω is indeed interesting. The change of sign is already observed for $q=1$ GeV/c in Fig. 3.9. This connects with the findings in reference [169], where a pronounced bump and sign change were reported in a semi-relativistic shell model calculation based on the Dirac equation with a relativistic energy-dependent potential. In the present calculation the bump is observed but it is very small compared to the results of Ref. [169]. Note that, in the present work, the fully relativistic SuSAM* approach is employed, which takes into account the dynamical properties of both nucleons and the Δ , as well as the scaling function. This differs from the approach in reference [169], where a static propagator for the Δ was used. To definitively clarify the difference with the present results, a fully relativistic calculation in finite nuclei, considering the dynamical properties of the Δ would be necessary.

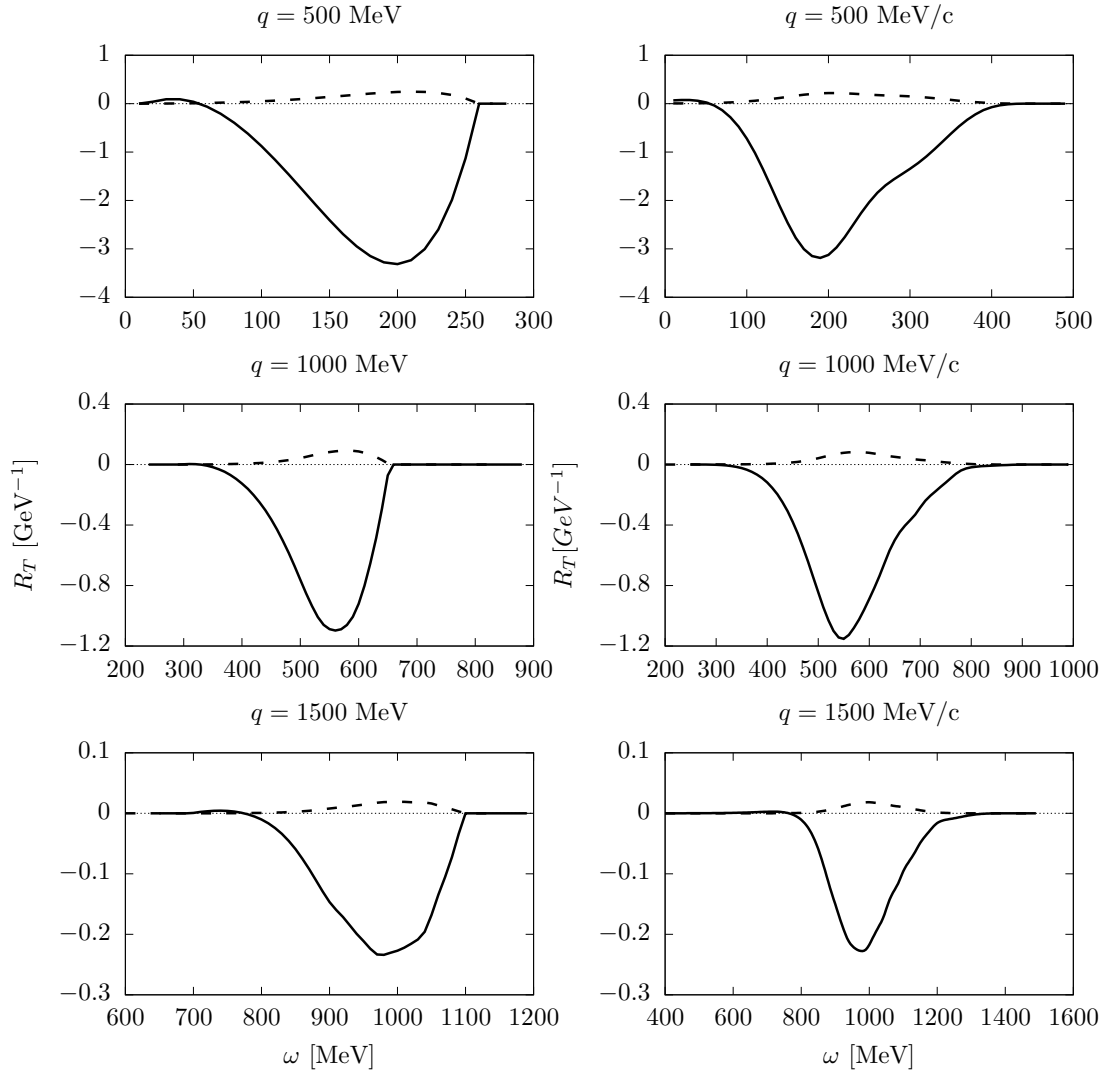


Figure 3.11: Left panel: Comparison of OB-MEC interference in the transverse response (black lines) with the pure MEC transverse response (dashed lines) for several values of q in the RMF model. Right panel: The same but in the SuSAM* model.

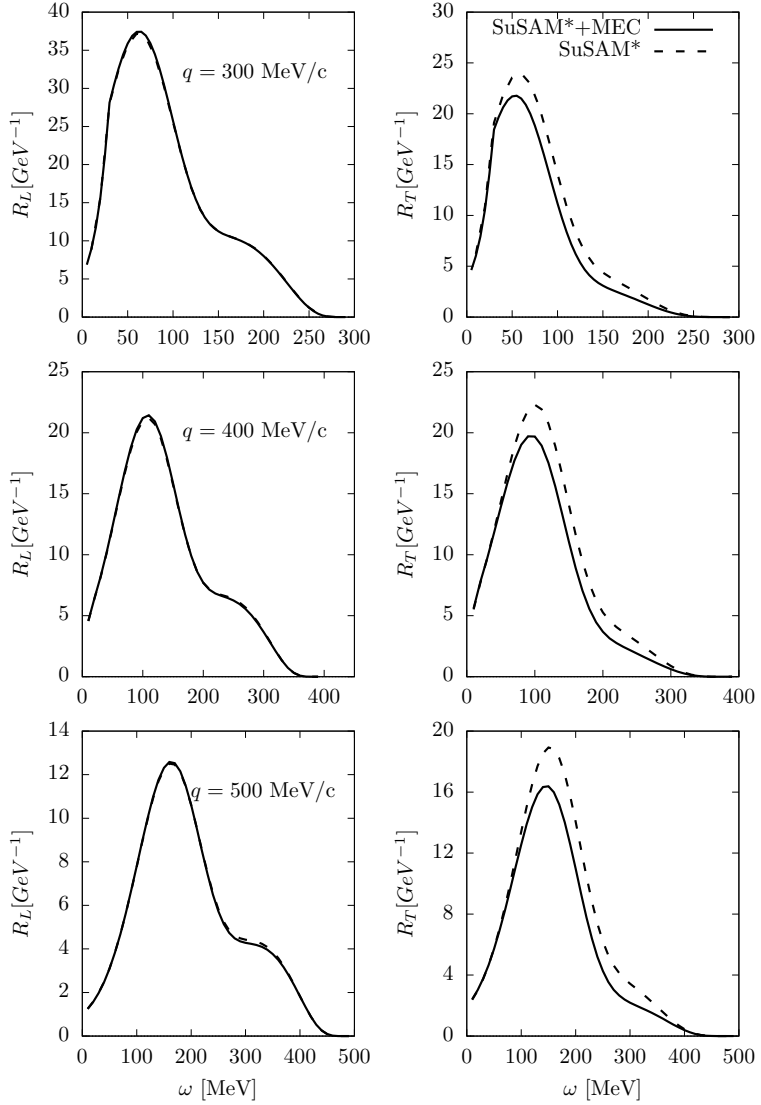


Figure 3.12: Response functions calculated in the generalized SuSAM* model (black curves) for $q = 300, 400, 500$ MeV/c. The dashed curves do not include the MEC.

The comparison of the OB-MEC interference with the MEC contribution alone (represented by $w_{1b2b}^{\mu\nu}$ and $w_{2b}^{\mu\nu}$, respectively in Eq. (3.16) in the transverse response is shown in Fig. 3.11. We observe that the MEC contribution alone represents a small and almost negligible contribution to the transverse response. This justifies the previous calculations that focused only on the OB-MEC interference (e.g., the semi-analytical calculations in references [32, 33] for the non-relativistic Fermi gas), as it provides an excellent approximation. This observation holds true for both the RMF model and the SuSAM* model in Fig. 3.11. It highlights the fact that the dominant contribution to the transverse response arises from the interference between the OB and MEC, while the pure MEC contribution is relatively small.

In Fig. 3.12 and 3.13, we present the total responses of ^{12}C computed using the generalized SuSAM* model. These responses are obtained by multiplying the phenomenological

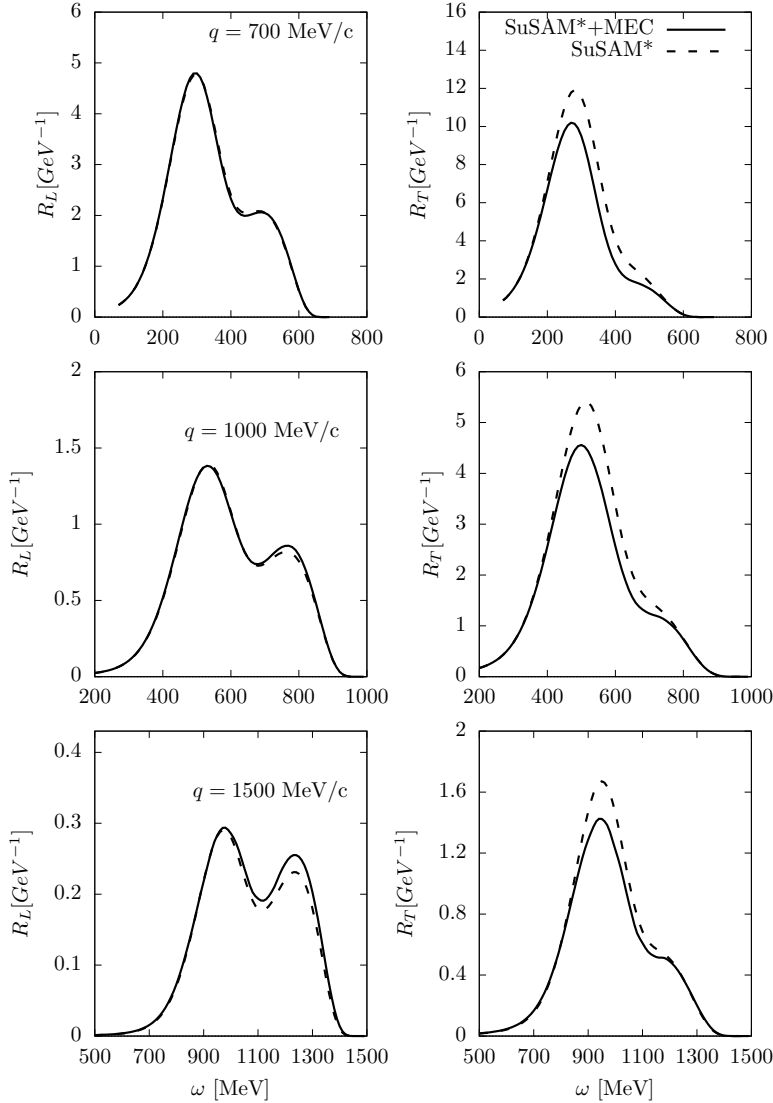


Figure 3.13: Response functions calculated in the generalized SuSAM* model (black curves) for $q = 700, 1000, 1500$ MeV/c. The dashed curves do not include the MEC.

scaling function by the averaged single-nucleon response and summing over protons and neutrons, as given by Eq. (2.21). The responses are shown for different values of q as a function of ω . In the same figure, we also show the results without including the MEC contributions, which corresponds to setting the terms $w_{1b2b} + w_{2b}$ associated with the two-body current (Eq. (3.16)) to zero.

Comparing the results with and without MEC, we observe that the impact of MEC is more significant in the transverse response compared to the longitudinal response. This is expected since the corrections due to MEC in the longitudinal response are higher-order effects in a non-relativistic expansion in powers of v/c , as known from previous studies [38]. Therefore, the MEC contributions to the longitudinal response are minimal and only start to become noticeable for $q \geq 1.5$ GeV in the high-energy region. However, this high-energy region is dominated and overshadowed by pion emission and inelastic processes, making it

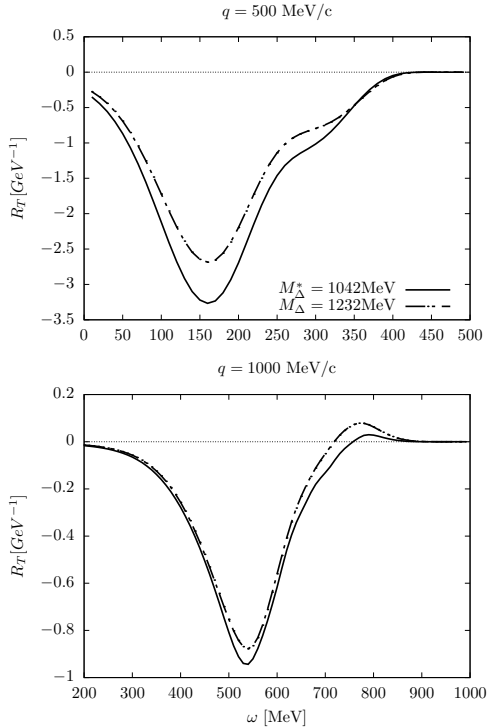


Figure 3.14: Comparison of the transverse interference OB- Δ computed in the generalized SuSAM* model with and without relativistic effective mass and vector energy for the Δ .

difficult to isolate the 1p1h longitudinal response.

The inclusion of MEC in the single-nucleon leads to a reduction of the transverse response by around 10% or even more for all studied values of q . This is consistent with previous calculations in RFG and the shell model [33, 35, 42, 169, 170]. These calculations have consistently shown that MEC in the 1p1h channel tend to decrease the transverse response compared to the contribution from the one-body current. Note that this reduction in the transverse response is a direct consequence of the destructive interference between the one-body current and MEC. The contribution of MEC to the transverse response is negative because the direct two-body matrix element is zero (in symmetric nuclear matter, $N = Z$) or almost zero (in asymmetric nuclear matter, $N \neq Z$, or in finite nuclei) after summing over isospin.

The treatment of the Δ resonance in the medium is subject to various ambiguities and uncertainties. In our generalized SuSAM* model, we have assumed that the Δ resonance acquires an effective mass M_Δ^* and vector energy E_v^Δ due to its interaction with the RMF. This requires modifying the propagator according to the formalism proposed in references [149, 167]. To estimate the effect of this treatment, in Fig. 3.14 we compare the transverse response for the OB- Δ interference calculated assuming that the Δ remains unchanged in the medium, i.e., setting $M_\Delta^* = M_\Delta$ and $E_v^\Delta = 0$. The response with the free Δ without medium modifications is slightly smaller in absolute value, around 10% depending on the momentum transfer. This can be seen as an estimation of the uncertainty associated with the Δ interaction in the medium.

Another related issue is the modification of the Δ width in the medium, which we

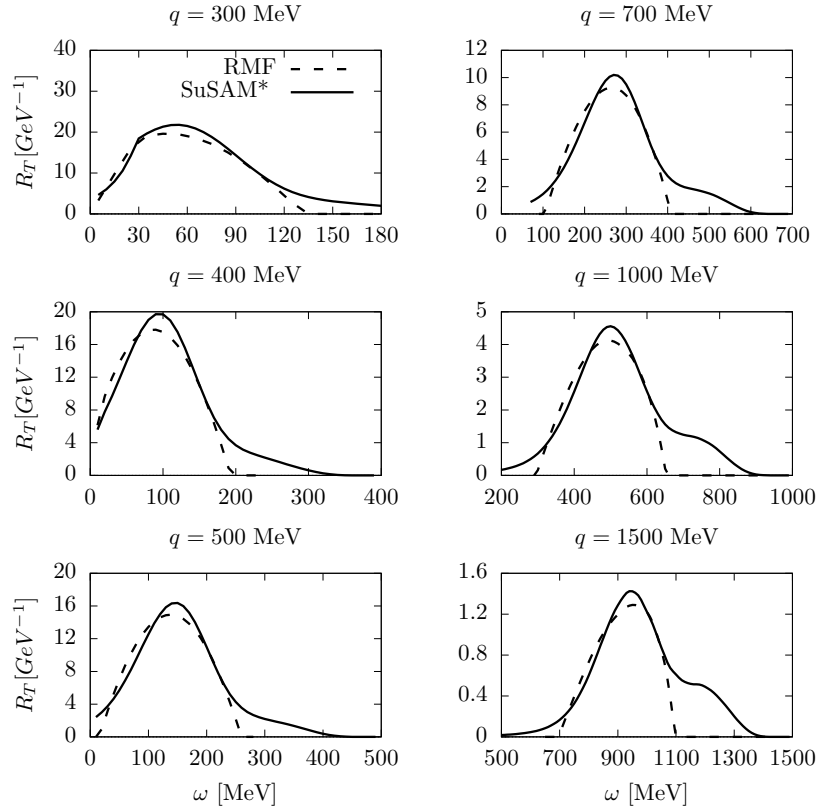


Figure 3.15: Total transverse responses for ^{12}C including MEC in the RMF model with $M^* = 0.8$ compared to the generalized SuSAM* model.

have not considered here assuming the free width (3.35). This effect can also influence the results, but it is expected to be of the same order as the observed effect in Fig. 3.14. The treatment of the Δ resonance in the medium is a complex topic, and further investigations and refinements are needed to fully understand its effects and uncertainties.

In Fig. 3.15, we compare the total transverse response calculated in the RMF model with an effective mass of $M^* = 0.8$ to the results obtained in the generalized SuSAM* approach for various momentum transfers, ranging from $q = 300 \text{ MeV}/c$ to $q = 1500 \text{ MeV}/c$. Both calculations include the effects of MEC. One notable difference between the two approaches is the presence of a pronounced tail at high energy transfer rates in the SuSAM* results. This tail extends well beyond the upper limit of the RFG responses, reflecting the effect of the phenomenological scaling function used in the SuSAM* approach. Similar effects are found in the longitudinal response. Additionally, it is worth noting that the peak height of the transverse response in the SuSAM* approach is generally higher compared to the RMF model.

Finally, in Fig. 3.16, we present the results for the (e, e') double differential cross-section of ^{12}C calculated with the generalized SuSAM* model including MEC, compared to experimental data for selected kinematics. We also compare these with the same model but assuming that only the single-nucleon contribution is present, i.e., setting the MEC to zero. We observe that the inclusion of MEC in this model leads to a small reduction in

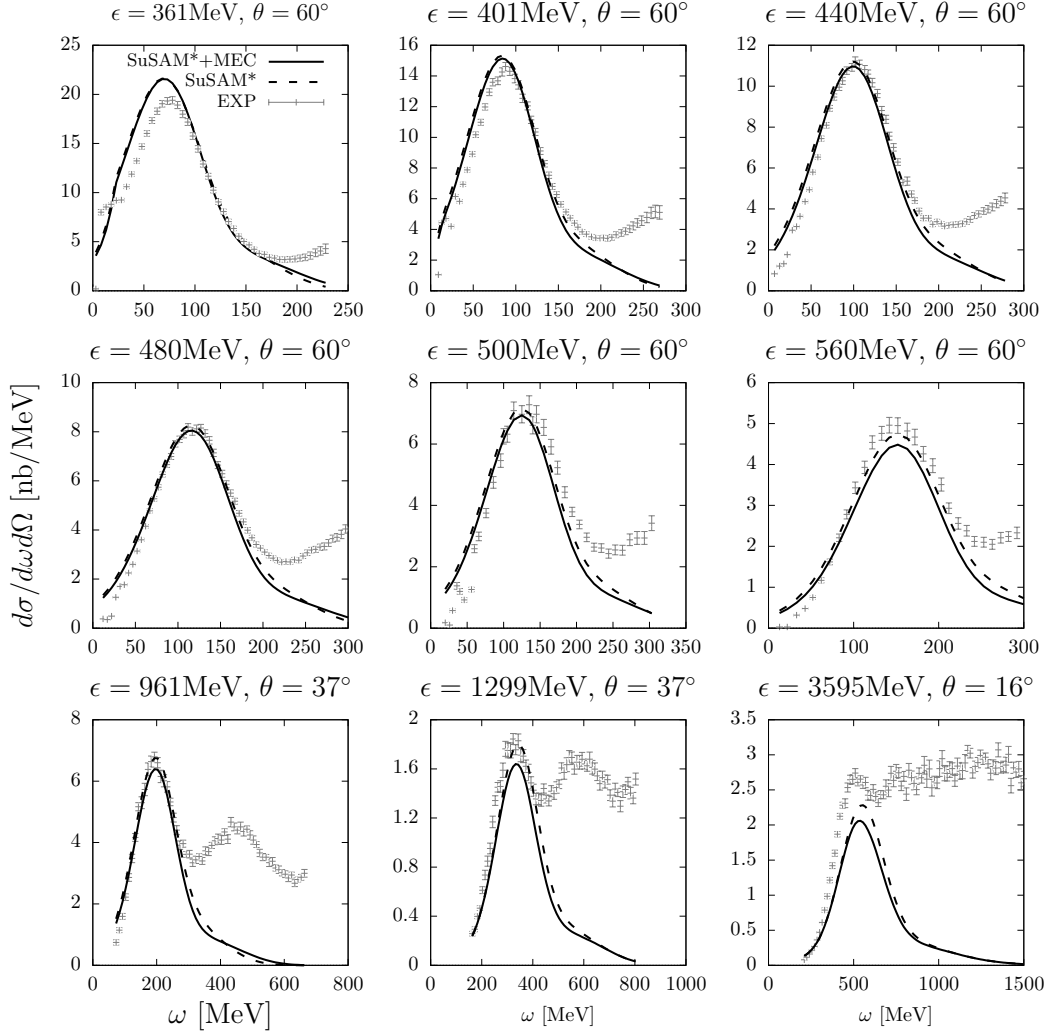


Figure 3.16: Cross section of ^{12}C for several kinematics computed with the generalized SuSAM* model, including MEC, compared with the same calculation without MEC. Experimental data are from Refs. [13, 14].

the cross-section compared to the case without MEC. This reduction is a consequence of the decrease in the transverse response due to the presence of MEC.

Figure 3.16 also provides an illustrative example of the averaged description of the global (e, e') cross-section data. Considering the scaling violation uncertainty (the scatter of the points in the scaling band is larger than 20 %) significant deviations from the QE data are expected for certain kinematic conditions. In some cases, the predicted cross-section is above the data, while in others, it is below. Note that the phenomenological scaling function is obtained by excluding data points that significantly deviate from scaling behavior. Specifically, kinematics involving substantial contributions from pion emission are excluded as non-quasielastic. Consequently, in these cases, the predicted cross-section falls below the experimental data.

This work does not include comparisons with separate response function experimental data or the Coulomb sum rule. While the scaling band results from the clustering of data points with varying momentum and energy transfers, the faithful reproduction of separate response functions by a model is not necessarily guaranteed. To ensure the accuracy of a scaling-based approach in describing response functions, it would be imperative to somehow incorporate experimental information about these response functions into the scaling analysis. This is an endeavor that requires further investigation beyond the scope of this chapter, which primarily serves to illustrate how to modify the scaling approach to incorporate MEC within the single-nucleon framework. The study of the response functions will be addressed in chapter 7, in connection with MEC and short-range correlations.

3.3. Final remarks

This chapter focused on the inclusion of meson exchange currents within the framework of the superscaling analysis with effective mass, presented in chapter 2. From the results, we observed that, in all the models considered, the transverse response decreases when including MEC in the 1p1h channel. This result is consistent with previous independent calculations performed in the relativistic and non-relativistic Fermi gas models as well as in the non-relativistic and semi-relativistic shell models. The result is a consequence of the fact that the main contribution arises from the interference of the OB and Δ currents, in particular through the exchange diagram, carrying a minus sign. The contribution from the direct part of the MEC matrix element is zero in the Fermi gas, and this is one of the reasons for the negative contribution.

We anticipate that the landscape may undergo transformation with the development of a more realistic averaged single-nucleon framework, possibly incorporating a Fermi gas description enhanced by short-range correlations. In such a scenario, the meson-exchange currents are expected to exert a more substantial influence, potentially leading to a significant increase in the transverse response. This issue will be addressed in chapters 6 and 7, where the high-momentum components arising from SRC are explicitly calculated [171], and subsequently incorporated into our quasielastic scattering model.

Chapter 4

The low momentum OB-MEC interference

Until now, we have studied the QE nuclear responses, first focusing on the one-body current and later incorporating meson exchange currents. Both cases have been examined within the framework of an improved scaling model based on a mean value of the single-nucleon tensor, which is averaged with the energy distribution $n(\epsilon)$.

In this chapter, we study in more detail the interference responses with MEC at low momentum, with a particular focus on the low-momentum proposition for single-particle emission. This proposition states that, in the Fermi gas, the transverse interference response between the OB current and the Δ and pionic currents is negative, resulting in a partial cancellation with the seagull current. To further investigate this behavior, we have compared our results with several models, both relativistic and non-relativistic, and our findings indicate that they all satisfy the proposition.

The motivation behind this study arises from the conflicting results reported in previous works concerning the sign of the Δ interference response. In those cases, the calculations that use independent-particle models [46, 47], have reported a large and positive interference of one-body and two-body currents in the transverse response. These results contradict previous calculations, including those presented in chapter 3, and their origin is not entirely understood, necessitating further clarification. While a close examination of [46, 47] suggest a Δ current with the opposite sign to the commonly employed Δ current adopted in our work [38], a detailed study, such as the one presented in this chapter, is required to systematically analyze the theoretical foundations of the interference response and to assess whether the observed discrepancies arise from fundamental differences in the modeling of nuclear dynamics or from specific approximations used in these calculations. More details can be found in Ref. [172].

4.1. Non-relativistic OB-MEC transverse response

In this section we calculate in detail the OB-MEC interference in the T-response in the Fermi model, where we perform analytically the spin-isospin sums. We provide detailed

expressions from which the low-momentum theorem follows trivially. First, we present the non-relativistic (NR) reduction of the one-body, Eq.(3.7) and two-body relativistic currents, Eqs.(3.19)-(3.22). Since one of the main objectives in this chapter is to demonstrate the low-momentum proposition, we will first verify that the NR limit of our current operators are consistent with the well-known NR currents of Riska [38], which are the standard operators typically used in calculations including seagull, pion-in-flight, and Δ currents. The one-body operator, which corresponds to a transverse current, will be expressed as the sum of a magnetization term \mathbf{j}_M and a convection term \mathbf{j}_C

$$\mathbf{j}_{1b}(\mathbf{p}, \mathbf{h}) = \mathbf{j}_M(\mathbf{p}, \mathbf{h}) + \mathbf{j}_C(\mathbf{p}, \mathbf{h}), \quad (4.1)$$

$$\mathbf{j}_M(\mathbf{p}, \mathbf{h}) = -\delta_{t_p t_h} \frac{G_M^h}{2m_N} i\mathbf{q} \times \boldsymbol{\sigma}_{s_p s_h}, \quad (4.2)$$

$$\mathbf{j}_C(\mathbf{p}, \mathbf{h}) = \delta_{t_p t_h} \delta_{s_p s_h} \frac{G_E^h}{m_N} \left(\mathbf{h} + \frac{\mathbf{q}}{2} \right). \quad (4.3)$$

with $\mathbf{q} = \mathbf{p} - \mathbf{h}$ by momentum conservation. Here G_M^h (G_E^h) is the magnetic (electric) form factor of the nucleon with isospin t_h . In the quasielastic peak the convection current contribution is much smaller than the magnetization and can be neglected.

For the NR reduction of the meson exchange currents, the treatment is deliberately didactic, to ensure that our results are easily reproducible. We aim to leave no ambiguous or unclear steps in the derivation process. We will take the static limit in which the momenta of the initial and final nucleons are very small.

In the NR limit, the lower component of the Dirac spinors is neglected, and the 4×4 Dirac matrices reduce to 2×2 Pauli matrices acting on the upper components. Additionally, we will only consider the NR reduction of the transverse current, i.e., J^i for $i = 1, 2$, as this is the dominant contribution in this limit. The contribution of MEC to the longitudinal response is neglected as we have seen in chapter 3. The NR approximation is further justified by numerical calculations.

To achieve this reduction, we apply the following rules:

$$\gamma^0 \rightarrow 1, \quad \gamma^i \rightarrow 0, \quad \gamma_5 \gamma^0 \rightarrow 0, \quad (4.4)$$

$$\gamma_5 \gamma^i \rightarrow -\sigma_i, \quad \gamma^i \gamma^j \rightarrow -\sigma_i \sigma_j, \quad \gamma^0 \gamma^j \rightarrow 0. \quad (4.5)$$

For a nucleon momentum:

$$p^\mu \rightarrow (m_N, p^i), \quad \not{p} \rightarrow p_0. \quad (4.6)$$

For the momentum transfer to nucleon i :

$$k^\mu \rightarrow (0, k^i), \quad \gamma_5 \not{k} \rightarrow \mathbf{k} \cdot \boldsymbol{\sigma}. \quad (4.7)$$

To simplify the writing at this stage, we do not explicitly include the strong form factors. These can be applied later on to the NR currents. Most of the results will be obtained with these form factors set to one, and we will see that the effect of including them is small for the low momentum transfer values considered here. Additionally, their inclusion does not alter the general result of the proposition, which is our main objective.

The V -function defined in Eq. (3.23),

$$V_{s'_1 s_1}(p'_1, p_1) = F_{\pi NN}(k_1^2) \frac{\bar{u}_{s'_1}(p'_1) \gamma^5 \not{k}_1 u_{s_1}(p_1)}{k_1^2 - m_\pi^2}. \quad (4.8)$$

is directly obtained in this limit

$$V_{s'_1 s_1}(p'_1, p_1) \longrightarrow -\frac{\mathbf{k}_1 \cdot \boldsymbol{\sigma}^{(1)}}{\mathbf{k}_1^2 + m_\pi^2} \quad (4.9)$$

where a matrix element between initial and final spin states is understood, i.e. $\langle s'_1 | \cdot | s_1 \rangle$, but is not explicitly written for simplicity. The spin states $|s\rangle$ are NR, two-component spinors, corresponding to the upper component of the Dirac spinors.

Seagull current

In the seagull current, we start by using a notation to separate the isospin part, which does not change in the NR limit,

$$j_s^\mu = i[\boldsymbol{\tau}^{(1)} \times \boldsymbol{\tau}^{(2)}]_z j_{s3}^\mu \quad (4.10)$$

Here the function j_{s3}^μ is independent on isospin and is defined by

$$j_{s3}^\mu(1', 2', 1, 2) = \frac{f^2}{m_\pi^2} V_{s'_1 s_1}(p'_1, p_1) \bar{u}_{s_2}(p'_2) F_1^V \gamma^5 \gamma^\mu u_{s_2}(p_2) + (1 \leftrightarrow 2) \quad (4.11)$$

where in the $(1 \leftrightarrow 2)$ term we have used the property

$$[\boldsymbol{\tau}^{(2)} \times \boldsymbol{\tau}^{(1)}] = -[\boldsymbol{\tau}^{(1)} \times \boldsymbol{\tau}^{(2)}]. \quad (4.12)$$

The NR reduction is directly obtained using Eqs. (4.5) and (4.9). Therefore the seagull current j_{s3}^i in the NR limit becomes

$$\mathbf{j}_{s3} \rightarrow \frac{f^2}{m_\pi^2} F_1^V \left(\frac{\mathbf{k}_1 \cdot \boldsymbol{\sigma}^{(1)}}{\mathbf{k}_1^2 + m_\pi^2} \boldsymbol{\sigma}^{(2)} - \frac{\mathbf{k}_2 \cdot \boldsymbol{\sigma}^{(2)}}{\mathbf{k}_2^2 + m_\pi^2} \boldsymbol{\sigma}^{(1)} \right) \quad (4.13)$$

Pionic current

The pion-in-flight current can be written similarly to the seagull current as

$$j_\pi^\mu = i[\boldsymbol{\tau}^{(1)} \times \boldsymbol{\tau}^{(2)}]_z j_{\pi3}^\mu \quad (4.14)$$

where $j_{\pi3}^\mu$ is independent on isospin and is defined by

$$j_{\pi3}^\mu(1', 2', 1, 2) = \frac{f^2}{m_\pi^2} F_1^V V_{s'_1 s_1}(p'_1, p_1) V_{s'_2 s_2}(p'_2, p_2) (k_1^\mu - k_2^\mu) \quad (4.15)$$

The NR reduction of the pionic current is directly obtained from Eq. (4.9)

$$\mathbf{j}_{\pi3} \rightarrow \frac{f^2}{m_\pi^2} F_1^V \frac{\mathbf{k}_1 \cdot \boldsymbol{\sigma}^{(1)}}{\mathbf{k}_1^2 + m_\pi^2} \frac{\mathbf{k}_2 \cdot \boldsymbol{\sigma}^{(2)}}{\mathbf{k}_2^2 + m_\pi^2} (\mathbf{k}_1 - \mathbf{k}_2) \quad (4.16)$$

It is straightforward to verify that the NR reduction of the seagull plus pionic currents coincide with the usual expressions found in the literature [38].

Δ current

The NR reduction of the Δ current is somewhat more involved due to its more complex spin and isospin structure. In order to simplify the NR reduction, it is convenient to write the Δ current in an abbreviated form

$$j_{\Delta F}^\mu = U_F K_F^\mu + (1 \leftrightarrow 2) \quad (4.17)$$

$$j_{\Delta B}^\mu = U_B K_B^\mu + (1 \leftrightarrow 2) \quad (4.18)$$

where a matrix element is assumed to be taken between the initial and final isospin states $\langle t'_1 t'_2 | \cdot | t_1 t_2 \rangle$, but we do not explicitly write this to simplify the notation.

The functions K_F^μ and K_B^μ are independent on isospin and can be written as

$$K_F^\mu = \frac{ff^*}{m_\pi^2} V_{s'_2 s_2}(p'_2, p_2) A^\mu, \quad (4.19)$$

$$K_B^\mu = \frac{ff^*}{m_\pi^2} V_{s'_2 s_2}(p'_2, p_2) B^\mu. \quad (4.20)$$

where A^μ and B^μ are defined

$$A^\mu = \bar{u}_{s_1}(p'_1) k_2^\alpha G_{\alpha\beta}(p_1 + Q) \Gamma^{\beta\mu}(Q) u_{s_1}(p_1) \quad (4.21)$$

$$B^\mu = \bar{u}_{s_1}(p'_1) k_2^\beta \Gamma^{\alpha\mu}(-Q) G_{\alpha\beta}(p'_1 - Q) u_{s_1}(p_1). \quad (4.22)$$

The NR reduction of the spatial components of the Δ current requires the NR reduction of the components A^i and B^i . This detailed reduction process is carried out in Appendix C. The result is

$$\mathbf{A} \rightarrow g_\Delta \mathbf{q} \times \left[\frac{2}{3} i \mathbf{k}_2 - \frac{1}{3} \mathbf{k}_2 \times \boldsymbol{\sigma}^{(1)} \right] \quad (4.23)$$

$$\mathbf{B} \rightarrow g_\Delta \mathbf{q} \times \left[\frac{2}{3} i \mathbf{k}_2 + \frac{1}{3} \mathbf{k}_2 \times \boldsymbol{\sigma}^{(1)} \right] \quad (4.24)$$

where we have defined the coefficient

$$g_\Delta \equiv \frac{C_3^V}{m_N} \frac{1}{m_\Delta - m_N}. \quad (4.25)$$

Therefore

$$\mathbf{K}_F \rightarrow -\frac{ff^*}{m_\pi^2} \frac{\mathbf{k}_2 \cdot \boldsymbol{\sigma}^{(2)}}{\mathbf{k}_2^2 + m_\pi^2} \mathbf{A} \quad (4.26)$$

$$\mathbf{K}_B \rightarrow -\frac{ff^*}{m_\pi^2} \frac{\mathbf{k}_2 \cdot \boldsymbol{\sigma}^{(2)}}{\mathbf{k}_2^2 + m_\pi^2} \mathbf{B} \quad (4.27)$$

as before a matrix element is assumed to be taken between the initial and final spin states, $\langle s'_1 s'_2 | \cdot | s_1 s_2 \rangle$, but we do not explicitly write this to simplify the notation.

Using the result

$$T_i T_j^\dagger = \frac{2}{3} \delta_{ij} - \frac{i}{3} \epsilon_{ijk} \tau_k = \delta_{ij} - \frac{1}{3} \tau_i \tau_j \quad (4.28)$$

the forward and backward isospin operators can be written as

$$U_F(1, 2) = \frac{1}{\sqrt{6}} (2\tau_z^{(2)} - i[\boldsymbol{\tau}^{(1)} \times \boldsymbol{\tau}^{(2)}]_z) \quad (4.29)$$

$$U_B(1, 2) = \frac{1}{\sqrt{6}} (2\tau_z^{(2)} + i[\boldsymbol{\tau}^{(1)} \times \boldsymbol{\tau}^{(2)}]_z). \quad (4.30)$$

Hence the Δ current can be written as

$$\mathbf{j}_\Delta = \mathbf{j}_{\Delta F} + \mathbf{j}_{\Delta B} = \frac{2}{\sqrt{6}} \tau_z^{(2)} [\mathbf{K}_F + \mathbf{K}_B] + \frac{1}{\sqrt{6}} i[\boldsymbol{\tau}^{(1)} \times \boldsymbol{\tau}^{(2)}]_z [\mathbf{K}_B - \mathbf{K}_F] + (1 \leftrightarrow 2). \quad (4.31)$$

We see that the isospin operators in the Δ current, $\tau_z^{(2)}$ and $[\boldsymbol{\tau}^{(1)} \times \boldsymbol{\tau}^{(2)}]_z$, are multiplied by the sum and the difference between the backward and forward functions, \mathbf{K}_B and \mathbf{K}_F , given in the NR limit by

$$\mathbf{K}_F + \mathbf{K}_B = -\frac{ff^*}{m_\pi^2} \frac{\mathbf{k}_2 \cdot \boldsymbol{\sigma}^{(2)}}{\mathbf{k}_2^2 + m_\pi^2} (\mathbf{A} + \mathbf{B}) \quad (4.32)$$

$$\mathbf{K}_B - \mathbf{K}_F = -\frac{ff^*}{m_\pi^2} \frac{\mathbf{k}_2 \cdot \boldsymbol{\sigma}^{(2)}}{\mathbf{k}_2^2 + m_\pi^2} (\mathbf{B} - \mathbf{A}). \quad (4.33)$$

From Eqs. (4.23) and (4.24),

$$\mathbf{A} + \mathbf{B} = \frac{4}{3} g_\Delta i \mathbf{q} \times \mathbf{k}_2 \quad (4.34)$$

$$\mathbf{B} - \mathbf{A} = \frac{2}{3} g_\Delta \mathbf{q} \times (\mathbf{k}_2 \times \boldsymbol{\sigma}^{(1)}) \quad (4.35)$$

Inserting this result into Eqs. (4.32) and (4.33) we have

$$\mathbf{K}_F + \mathbf{K}_B = -\frac{4}{3} g_\Delta \frac{ff^*}{m_\pi^2} \frac{\mathbf{k}_2 \cdot \boldsymbol{\sigma}^{(2)}}{\mathbf{k}_2^2 + m_\pi^2} i \mathbf{q} \times \mathbf{k}_2, \quad (4.36)$$

$$\mathbf{K}_B - \mathbf{K}_F = -\frac{2}{3} g_\Delta \frac{ff^*}{m_\pi^2} \frac{\mathbf{k}_2 \cdot \boldsymbol{\sigma}^{(2)}}{\mathbf{k}_2^2 + m_\pi^2} \mathbf{q} \times (\mathbf{k}_2 \times \boldsymbol{\sigma}^{(1)}). \quad (4.37)$$

Using these results in Eq. (4.31), it is straightforward to obtain the following expression for the NR Δ current

$$\begin{aligned} \mathbf{j}_\Delta = & i \sqrt{\frac{3}{2}} \frac{2ff^*}{9} \frac{C_3^V}{m_\pi^2 m_N} \frac{1}{m_\Delta - m_N} \left\{ \frac{\mathbf{k}_2 \cdot \boldsymbol{\sigma}^{(2)}}{\mathbf{k}_2^2 + m_\pi^2} [4\tau_z^{(2)} \mathbf{k}_2 + [\boldsymbol{\tau}^{(1)} \times \boldsymbol{\tau}^{(2)}]_z \mathbf{k}_2 \times \boldsymbol{\sigma}^{(1)}] \right. \\ & \left. + \frac{\mathbf{k}_1 \cdot \boldsymbol{\sigma}^{(1)}}{\mathbf{k}_1^2 + m_\pi^2} [4\tau_z^{(1)} \mathbf{k}_1 - [\boldsymbol{\tau}^{(1)} \times \boldsymbol{\tau}^{(2)}]_z \mathbf{k}_1 \times \boldsymbol{\sigma}^{(2)}] \right\} \times \mathbf{q} \end{aligned} \quad (4.38)$$

One can, in fact, verify that this expression coincides with the Δ current appearing in the literature, particularly the expression given in Refs. [38, 173], that we use as reference, except for the precise values of the coupling constants and form factors. This assures us that the relativistic and NR calculations in the low-momentum and low-energy limit should coincide if identical values of coupling and form factors are used.

4.1.1. MEC effective one-body transition currents

With the NR MEC current obtained in the last section, in the NR limit, the effective one-body transition current $\mathbf{j}_{2b}(\mathbf{p}, \mathbf{h})$ in the Fermi gas is obtained by summing over spin, isospin, and integrating over the momentum k of the spectator nucleon. At leading order, only the spatial part of the MEC survives, affecting solely the transverse response, which is perpendicular to the transferred momentum \mathbf{q} . From Eq. (3.10) in the limit $V \rightarrow \infty$ this current is

$$\mathbf{j}_{2b}(\mathbf{p}, \mathbf{h}) = \int \frac{d^3 k}{(2\pi)^3} \sum_{t_k s_k} [\mathbf{j}_{2b}(p, k, h, k) - \mathbf{j}_{2b}(p, k, k, h)]. \quad (4.39)$$

Sum over isospin

We begin by showing that the direct term in Eq. (4.39) is zero. Previously, we note that the MEC can be expanded in terms of the isospin operators $\tau_z^{(1)}$, $\tau_z^{(2)}$ and $[\boldsymbol{\tau}^{(1)} \times \boldsymbol{\tau}^{(2)}]_z$

$$\mathbf{j}_{2b} = \tau_z^{(1)} \mathbf{j}_1 + \tau_z^{(2)} \mathbf{j}_2 + i[\boldsymbol{\tau}^{(1)} \times \boldsymbol{\tau}^{(2)}]_z \mathbf{j}_3 \quad (4.40)$$

where \mathbf{j}_1 , \mathbf{j}_2 , \mathbf{j}_3 are independent on isospin.

We first perform the sum over isospin index t_k . The direct term is

$$\begin{aligned} \sum_{t_k} \mathbf{j}_{2b}(p, k, h, k) &= \sum_{t_k} \langle t_p t_k | \tau_z^{(1)} \mathbf{j}_1 + \tau_z^{(2)} \mathbf{j}_2 + i[\boldsymbol{\tau}^{(1)} \times \boldsymbol{\tau}^{(2)}]_z \mathbf{j}_3 | t_h t_k \rangle \\ &= \delta_{t_p t_h} 4t_h \mathbf{j}_1(p, k, h, k), \end{aligned} \quad (4.41)$$

where we have used the elementary isospin sums performed in Appendix B, Eqs. (B.5–B.7). Therefore the direct term in the matrix element (4.39) is proportional to $\mathbf{j}_1(p, k, h, k)$, which turns out to be zero. Indeed, \mathbf{j}_1 can be obtained from equation (4.38) as

$$\mathbf{j}_1 = iC_\Delta \frac{\mathbf{k}_1 \cdot \boldsymbol{\sigma}^{(1)}}{\mathbf{k}_1^2 + m_\pi^2} 4\mathbf{k}_1 \times \mathbf{q}, \quad (4.42)$$

with

$$C_\Delta \equiv \sqrt{\frac{3}{2}} \frac{2}{9} \frac{f f^*}{m_\pi^2} \frac{C_3^V}{m_N} \frac{1}{m_\Delta - m_N} \quad (4.43)$$

and $\mathbf{k}_1 = \mathbf{p} - \mathbf{h} = \mathbf{q}$. Therefore

$$\sum_{t_k} \mathbf{j}_{2b}(p, k, h, k) = 0. \quad (4.44)$$

This results follows because the Δ current is transverse, i.e., perpendicular to \mathbf{q} . In the relativistic case, a similar situation occurs, and the direct term is zero although the demonstration is more involved. It requires summing over the spin of \mathbf{k} and handling a large number of terms that involve many γ matrices.

The sum over isospin in the exchange part is obtained using the isospin sums performed in Appendix B, Eqs (B.8–B.10)

$$\begin{aligned} \sum_{t_k} \mathbf{j}_{2b}(p, k, k, h) &= \sum_{t_k=\pm 1/2} \langle t_p t_k | \tau_z^{(1)} \mathbf{j}_1 + \tau_z^{(2)} \mathbf{j}_2 + i[\boldsymbol{\tau}^{(1)} \times \boldsymbol{\tau}^{(2)}]_z \mathbf{j}_3 | t_k t_h \rangle \\ &= \delta_{t_p t_h} 2t_h [\mathbf{j}_1(p, k, k, h) + \mathbf{j}_2(p, k, k, h) - 2\mathbf{j}_3(p, k, k, h)] \end{aligned} \quad (4.45)$$

Thus, in symmetric nuclear matter the direct matrix element of the MEC vanishes, and only the exchange term survives in the 1p1h matrix element. Therefore, the many-body diagrams that contribute to the MEC in the 1p1h channel are those shown in chapter 3 in Fig. 3.2. Next, we proceed to perform the spin sums for the different terms of the current.

Sum over spin

The resulting 1p1h matrix elements of the 2b current are computed as

$$\mathbf{j}_{2b}(p, h) = - \int \frac{d^3 k}{(2\pi)^3} \sum_{t_k s_k} \mathbf{j}_{2b}(p, k, k, h) = \mathbf{j}_s(p, h) + \mathbf{j}_\pi(p, h) + \mathbf{j}_\Delta(p, h), \quad (4.46)$$

where only the exchange part contributes. The sums over spin index s_k are performed in Appendix D. The results are the following for the three MEC, seagull, pionic and Δ currents

$$\mathbf{j}_s(p, h) = 4t_h \delta_{t_p t_h} \frac{f^2}{m_\pi^2} F_1^V \int \frac{d^3 k}{(2\pi)^3} \left(\frac{\delta_{s_p s_h} \mathbf{k}_1 + i\boldsymbol{\sigma}_{ph} \times \mathbf{k}_1}{\mathbf{k}_1^2 + m_\pi^2} - \frac{\delta_{s_p s_h} \mathbf{k}_2 + i\mathbf{k}_2 \times \boldsymbol{\sigma}_{ph}}{\mathbf{k}_2^2 + m_\pi^2} \right) \quad (4.47)$$

$$\mathbf{j}_\pi(p, h) = 4t_h \delta_{t_p t_h} \frac{f^2}{m_\pi^2} F_1^V \int \frac{d^3 k}{(2\pi)^3} \frac{\delta_{s_p s_h} \mathbf{k}_1 \cdot \mathbf{k}_2 + i(\mathbf{k}_1 \times \mathbf{k}_2) \cdot \boldsymbol{\sigma}_{ph}}{(\mathbf{k}_1^2 + m_\pi^2)(\mathbf{k}_2^2 + m_\pi^2)} (\mathbf{k}_1 - \mathbf{k}_2) \quad (4.48)$$

$$\mathbf{j}_\Delta(p, h) = 4it_h \delta_{t_p t_h} C_\Delta \mathbf{q} \times \int \frac{d^3 k}{(2\pi)^3} \left(\frac{\mathbf{k}_1^2 \boldsymbol{\sigma}_{ph} + (\boldsymbol{\sigma}_{ph} \cdot \mathbf{k}_1) \mathbf{k}_1}{\mathbf{k}_1^2 + m_\pi^2} + \frac{\mathbf{k}_2^2 \boldsymbol{\sigma}_{ph} + (\boldsymbol{\sigma}_{ph} \cdot \mathbf{k}_2) \mathbf{k}_2}{\mathbf{k}_2^2 + m_\pi^2} \right) \quad (4.49)$$

with $\mathbf{k}_1 = \mathbf{p} - \mathbf{k}$ and $\mathbf{k}_2 = \mathbf{k} - \mathbf{h}$.

4.1.2. Interference between one-body and MEC in the transverse response

In this section, we give the MEC contribution to the effective single-nucleon transverse response, focusing exclusively on the interference between the MEC and OB currents. The pure MEC responses have been previously computed in chapter 3 and have been found negligible, allowing them to be safely disregarded. Here, we describe the interference terms separately for the different MEC components: Seagull, pionic, and Δ , in combination with the magnetization and convection terms of the OB currents. This separation is essential to analyze the relative contributions of each component to the overall response.

It should be clarified that here we are computing the single-nucleon response corresponding to either a proton or a neutron, with the requirement that the isospin of p and h must be the same $t_p = t_h$. At the end of the calculation, the contributions from protons and neutrons must be summed to obtain the total response.

We recall the effective single-nucleon tensor defined in chapter 3 that incorporates the square of the sum of the 1b and 2b currents and can be expanded as

$$\begin{aligned} w^{\mu\mu}(\mathbf{p}, \mathbf{h}) &= \frac{1}{2} \sum_{s_p s_h} |j_{1b}^\mu(\mathbf{p}, \mathbf{h}) + j_{2b}^\mu(\mathbf{p}, \mathbf{h})|^2 \\ &= w_{1b}^{\mu\mu} + w_{1b2b}^{\mu\mu} + w_{2b}^{\mu\mu}. \end{aligned} \quad (4.50)$$

where

$$w_{1b}^{\mu\mu} = \frac{1}{2} \sum_{s_p s_h} |j_{1b}^\mu|^2, \quad (4.51)$$

$$w_{1b2b}^{\mu\mu} = \operatorname{Re} \sum_{s_p s_h} (j_{1b}^\mu)^* j_{2b}^\mu, \quad (4.52)$$

$$w_{2b}^{\mu\mu} = \frac{1}{2} \sum_{s_p s_h} |j_{2b}^\mu|^2. \quad (4.53)$$

The first term, $w_{1b}^{\mu\mu}$, is the tensor corresponding to the one-body current alone, $w_{1b2b}^{\mu\mu}$ is the interference between 1b and 2b currents, and $w_{2b}^{\mu\mu}$ represents the contribution of the two-body current alone that is neglected.

The magnetization-seagull (ms) interference is given by Eq. (4.52)

$$w_{ms}^T = w_{ms}^{11} + w_{ms}^{22} = \operatorname{Re} \sum_{s_p s_h} \mathbf{j}_m(p, h)^* \cdot \mathbf{j}_s(p, h), \quad (4.54)$$

where we use that the magnetization current is perpendicular to \mathbf{q} and it has only x, y components. Using Eq. (4.2) for the magnetization current we can write

$$\begin{aligned} w_{ms}^T &= \delta_{t_p t_h} \operatorname{Re} \sum_{s_p s_h} \left(-\frac{G_M^h}{2m_N} i \mathbf{q} \times \boldsymbol{\sigma}_{s_p s_h} \right)^* \cdot \mathbf{j}_s(p, h) \\ &= \sum_{s_p s_h} \frac{G_M^h}{2m_N} i (\mathbf{q} \times \boldsymbol{\sigma}_{s_h s_p}) \cdot \mathbf{j}_s(\mathbf{p}, \mathbf{h})_{s_p s_h}. \end{aligned} \quad (4.55)$$

We have utilized the fact that the spin sum already yields a real number, as will be shown later, making it unnecessary to explicitly take the real part.

By following the same procedure, we express the various interferences required between the convection and magnetization currents with the seagull, pionic, and Δ operators, as

follows:

$$w_{cs}^T = \operatorname{Re} \sum_{s_p s_h} \mathbf{j}_c^T(p, h)^* \cdot \mathbf{j}_s(p, h) = \sum_{s_p s_h} \frac{G_E^h}{m_N} \delta_{s_h s_p} \mathbf{h}_T \cdot \mathbf{j}_s(\mathbf{p}, \mathbf{h})_{s_p s_h}, \quad (4.56)$$

$$w_{m\pi}^T = \operatorname{Re} \sum_{s_p s_h} \mathbf{j}_m(p, h)^* \cdot \mathbf{j}_\pi(p, h) = \sum_{s_p s_h} \frac{G_M^h}{2m_N} i(\mathbf{q} \times \boldsymbol{\sigma}_{s_h s_p}) \cdot \mathbf{j}_\pi(\mathbf{p}, \mathbf{h})_{s_p s_h}, \quad (4.57)$$

$$w_{c\pi}^T = \operatorname{Re} \sum_{s_p s_h} \mathbf{j}_c^T(p, h)^* \cdot \mathbf{j}_\pi(p, h) = \sum_{s_p s_h} \frac{G_E^h}{m_N} \delta_{s_h s_p} \mathbf{h}_T \cdot \mathbf{j}_\pi(\mathbf{p}, \mathbf{h})_{s_p s_h}, \quad (4.58)$$

$$w_{m\Delta}^T = \operatorname{Re} \sum_{s_p s_h} \mathbf{j}_m(p, h)^* \cdot \mathbf{j}_\Delta(p, h) = \sum_{s_p s_h} \frac{G_M^h}{2m_N} i(\mathbf{q} \times \boldsymbol{\sigma}_{s_h s_p}) \cdot \mathbf{j}_\Delta(\mathbf{p}, \mathbf{h})_{s_p s_h}, \quad (4.59)$$

$$w_{c\Delta}^T = 0. \quad (4.60)$$

Note that only the transverse component of the convection current appears that is proportional to the transverse nucleon momentum, $\mathbf{h}_T = \mathbf{h} - \frac{\mathbf{h} \cdot \mathbf{q}}{q^2} \mathbf{q}$, thereby selecting the x and y components in the transverse response. The convection- Δ interference is zero because the convection current is spin-independent, while the Δ current is linear in the σ operators.

The sums over spin in Eqs. (4.55–4.59) are performed in Appendix E. The result is

$$\begin{aligned} w_{ms}^T(p, h) &= 4t_h \frac{f^2}{m_\pi^2} F_1^V \frac{G_M^h}{2m_N} \int \frac{d^3 k}{(2\pi)^3} \left(\frac{4\mathbf{q} \cdot \mathbf{k}_1}{\mathbf{k}_1^2 + m_\pi^2} + \frac{4\mathbf{q} \cdot \mathbf{k}_2}{\mathbf{k}_2^2 + m_\pi^2} \right) \\ &\equiv 4t_h \frac{f^2}{m_\pi^2} F_1^V \frac{G_M^h}{2m_N} \mathcal{I}_{ms}(\mathbf{p}, \mathbf{h}) \end{aligned} \quad (4.61)$$

$$\begin{aligned} w_{cs}^T(p, h) &= 4t_h \frac{f^2}{m_\pi^2} F_1^V \frac{G_E^h}{m_N} \int \frac{d^3 k}{(2\pi)^3} \left(\frac{2\mathbf{h}_T \cdot \mathbf{k}_1}{\mathbf{k}_1^2 + m_\pi^2} - \frac{2\mathbf{h}_T \cdot \mathbf{k}_2}{\mathbf{k}_2^2 + m_\pi^2} \right) \\ &\equiv 4t_h \frac{f^2}{m_\pi^2} F_1^V \frac{G_E^h}{m_N} \mathcal{I}_{cs}(\mathbf{p}, \mathbf{h}) \end{aligned} \quad (4.62)$$

$$\begin{aligned} w_{m\pi}^T(p, h) &= -4t_h \frac{f^2}{m_\pi^2} F_1^V \frac{G_M^h}{2m_N} \int \frac{d^3 k}{(2\pi)^3} \frac{4(\mathbf{q} \times \mathbf{k}_2)^2}{(\mathbf{k}_1^2 + m_\pi^2)(\mathbf{k}_2^2 + m_\pi^2)} \\ &\equiv -4t_h \frac{f^2}{m_\pi^2} F_1^V \frac{G_M^h}{2m_N} \mathcal{I}_{m\pi}(\mathbf{p}, \mathbf{h}) \end{aligned} \quad (4.63)$$

$$\begin{aligned} w_{c\pi}^T(p, h) &= -4t_h \frac{f^2}{m_\pi^2} F_1^V \frac{G_E^h}{m_N} \int \frac{d^3 k}{(2\pi)^3} \frac{4(\mathbf{q} \cdot \mathbf{k}_2 - \mathbf{k}_2^2) \mathbf{h}_T \cdot \mathbf{k}_2}{(\mathbf{k}_1^2 + m_\pi^2)(\mathbf{k}_2^2 + m_\pi^2)} \\ &\equiv -4t_h \frac{f^2}{m_\pi^2} F_1^V \frac{G_E^h}{m_N} \mathcal{I}_{c\pi}(\mathbf{p}, \mathbf{h}) \end{aligned} \quad (4.64)$$

$$\begin{aligned} w_{m\Delta}^T(p, h) &= -4t_h C_\Delta \frac{G_M^h}{2m_N} \int \frac{d^3 k}{(2\pi)^3} 2 \left(\frac{3q^2 k_1^2 - (\mathbf{q} \cdot \mathbf{k}_1)^2}{\mathbf{k}_1^2 + m_\pi^2} + \frac{3q^2 k_2^2 - (\mathbf{q} \cdot \mathbf{k}_2)^2}{\mathbf{k}_2^2 + m_\pi^2} \right) \\ &\equiv -4t_h C_\Delta \frac{G_M^h}{2m_N} \mathcal{I}_{m\Delta}(\mathbf{p}, \mathbf{h}), \end{aligned} \quad (4.65)$$

where C_Δ is defined in Eq. (4.43), $\mathbf{k}_1 = \mathbf{p} - \mathbf{k}$, and $\mathbf{k}_2 = \mathbf{k} - \mathbf{h}$. In Eqs. (4.61–4.65) we have defined the integrals $\mathcal{I}_{ab}(\mathbf{p}, \mathbf{h})$, that are spin independent.

Finally, the total interference between the one-body and two-body currents is given by the sum of the individual interferences between the different terms of the currents, namely the seagull, pionic, and Δ contributions with magnetization and convection currents.

$$w_{1b2b}^T = w_{ms}^T + w_{cs}^T + w_{m\pi}^T + w_{c\pi}^T + w_{m\Delta}^T. \quad (4.66)$$

4.1.3. Low-momentum proposition

Proposition 1 *The transverse interference response between the Δ current and the OB current is negative in the Fermi gas model: $w_{m\Delta}^T < 0$.*

The low-momentum proposition is applicable, specifically at moderate momentum and energy transfers. Moderate in this context refers to values small compared to the nucleon mass.

To demonstrate the proposition, we first need to express the total single-nucleon interference responses as the sum of the contributions from protons and neutrons.

$$w_{ms}^T(\mathbf{p}, \mathbf{h}) = \frac{f^2}{m_\pi^2} F_1^V \frac{G_M^p - G_M^n}{m_N} \mathcal{I}_{ms}(\mathbf{p}, \mathbf{h}) \quad (4.67)$$

$$w_{cs}^T(\mathbf{p}, \mathbf{h}) = 2 \frac{f^2}{m_\pi^2} F_1^V \frac{G_E^p - G_E^n}{m_N} \mathcal{I}_{cs}(\mathbf{p}, \mathbf{h}) \quad (4.68)$$

$$w_{m\pi}^T(\mathbf{p}, \mathbf{h}) = -\frac{f^2}{m_\pi^2} F_1^V \frac{G_M^p - G_M^n}{m_N} \mathcal{I}_{m\pi}(\mathbf{p}, \mathbf{h}) \quad (4.69)$$

$$w_{c\pi}^T(\mathbf{p}, \mathbf{h}) = -2 \frac{f^2}{m_\pi^2} F_1^V \frac{G_E^p - G_E^n}{m_N} \mathcal{I}_{c\pi}(\mathbf{p}, \mathbf{h}) \quad (4.70)$$

$$w_{m\Delta}^T(\mathbf{p}, \mathbf{h}) = -\sqrt{\frac{3}{2}} \frac{2ff^*}{9} \frac{C_3^V}{m_\pi^2} \frac{G_M^p - G_M^n}{m_\Delta - m_N} \mathcal{I}_{m\Delta}(\mathbf{p}, \mathbf{h}). \quad (4.71)$$

It suffices to verify that the single-nucleon interference response $w_{m\Delta}^T < 0$ in Eq (4.71). On the one hand, $w_{m\Delta}^T$ is proportional to the integral $\mathcal{I}_{m\Delta}$, which contains the pion propagator multiplied by a factor that is always positive. The term in question can be seen inside the integral of Eq. (4.65), given by

$$3q^2 k_i^2 - (\mathbf{q} \cdot \mathbf{k}_i)^2 \geq 0, \quad (4.72)$$

with $i = 1, 2$. This ensures that the integral $\mathcal{I}_{m\Delta} \geq 0$. On the other hand, $w_{m\Delta}^T$ is also proportional to $G_M^p - G_M^n$, which is positive as well. Therefore, since $w_{m\Delta}^T$ includes an overall negative sign, the final result is negative, completing the proof.

Typically, the proposition is valid for momentum transfers below approximately 500 MeV, where the interference response $m\Delta$ is explicitly negative. For momentum transfers above this threshold, relativistic effects become increasingly significant. In this regime, the explicit determination of the sign is no longer straightforward due to the complexity of the spin sum in the relativistic case. The analysis requires numerical computations to verify the sign of the interference, as the NR proposition no longer applies directly.

From Eq. (4.63), we can also establish the following proposition for the magnetization-pionic response:

Proposition 2 *The transverse interference response between the pionic current and the magnetization current is negative in the Fermi gas model: $w_{m\pi}^T < 0$*

The proof of this proposition follows similarly to proposition 1, by noticing that the integral $\mathcal{I}_{m\pi}$ is positive, as it contains the square of $\mathbf{q} \times \mathbf{k}_2$, as seen in Eq. (4.63). Then, according to Eq. (4.69), we conclude that $w_{m\pi}^T < 0$.

The convection-pionic interference does not generally have a well-defined sign, but its contribution is much smaller than the magnetization interference. Therefore, proposition 2 can be approximately extended to the total pionic-OB interference.

For the seagull-magnetization interference, a rigorous result is also difficult to establish. However, certain particular cases suggest a trend. For instance, in the case $\mathbf{h} = 0$, it can be demonstrated that $w_{ms}^T > 0$. Additionally, by analyzing the integrand of \mathcal{I}_{ms} for $\mathbf{k} = 0$, we observe that it remains positive below the quasielastic peak and changes sign for $\omega > (q^2/2m_N)(1 + (2m_\pi/q)^2)^{1/2}$. This suggests a general tendency: the interference starts positive at small ω and eventually changes sign at some point beyond the quasielastic peak, though the precise location cannot be determined analytically.

The integrands and signs in the equations for the ms , $m\pi$, and $m\Delta$ transverse responses are consistent with those in the pioneering work of Kohno and Ohtsuka [40], which was among the first to compute 1b-2b interferences using Riska's currents. Similar expressions were also obtained in [32, 174], although written in a different form. One of the key contributions and novelties of the present chapter is the observation that the signs of the $m\Delta$ and $m\pi$ contributions are evidently negative, which follows trivially from Eqs. (98) and (100), as established in our propositions.

4.2. Results

Here we present results for the transverse response functions due to the interference between the MEC and OB current in the 1p1h channel. As discussed in the previous sections, these interferences are expressed as an integral of an effective single-nucleon interference. In the NR Fermi gas, which we have examined in great detail, the single-nucleon interferences are represented through relatively complex integrals after analytically computing the spin traces. In the case of the seagull and Δ currents, these integrals are analytical. For the Δ current, it has been proven that the associated interference response is always negative for all values of q and ω (Proposition 1). In this results section, we calculate the interference transverse responses for various values of $q = 300, 400, 550$ MeV/c, and show the results as a function of ω for ^{12}C . We employ several nuclear models to compare the responses, primarily aiming to observe if the results deviate or not from the Fermi gas significantly. The nuclear models we use include: non-relativistic Fermi gas, relativistic Fermi gas, mean-field models, semi-relativistic models (both Fermi gas and mean field), and the

spectral function model. Relativistic mean field and superscaling models with effective nucleon mass are also considered. The mean-field models include the Woods-Saxon potential, Dirac-equation-based potential, and the plane wave approximation. Many of these models have been previously applied in calculations for the study of electron scattering. Our results show approximate agreement in both magnitude and sign of the different MEC contributions. In particular, all examined models verify the proposition that the effect of the Δ current is negative for these values of momentum transfer, and the total MEC effect is small and predominantly negative. This supports the consensus that models without NN correlations, such as single-particle models or models based on one-hole spectral function do not produce an enhancement of the transverse response.

4.2.1. Fermi gas

We begin by presenting in Fig. 4.1 results for the non-relativistic Fermi gas, with $k_F = 225$ MeV/c. We show the interference of the seagull and pionic currents with the magnetization and convection currents. This is done to demonstrate that the contribution of the convection current in the MEC-OB interference is very small, particularly in the case of the pionic current. As a result, the magnetization current is dominant in the interference for these low to intermediate momentum transfer values. Specifically, we can conclude that, according to proposition 2, the contribution of the pionic current is negative if the small convection contribution is disregarded.

Taking this into account, it is worth mentioning the calculation performed by Alberico et al. [41]. In that reference, a positive result was obtained for the pionic-OB interference, which clearly points to an error in the calculation, as it also considered a Fermi gas model. The proposition establishes that this interference is negative when convection is neglected. In fact, by inspecting Eq. (2.41) of Ref. [41], it can be observed that the contribution of the pionic current is positive in that reference, indicating a possible error in performing the spin summation.

In Fig. 4.2, we present the interferences of the separate MEC components—seagull, pionic, and Δ —with the OB current in the transverse response. Here, we compare the non-relativistic Fermi gas to the relativistic Fermi gas. Both models yield similar results, with increasing differences as the momentum transfer increases, primarily due to the different kinematics. In fact, in chapter 3 we have checked that the relativistic result converges numerically to the NR one when both the momentum transfer q and the Fermi momentum approach zero [158]. NR responses extend to higher values of ω , due to the kinematics. We observe that both propositions 1 and 2 remains valid in the relativistic case, even though it was proven in the NR limit.

4.2.2. Mean field with Woods-Saxon potential

In Fig. 4.3, we compare the Fermi gas results to those of the mean field model for finite nuclei, using a Woods-Saxon (WS) potential [32, 174]. In this model, the initial and final

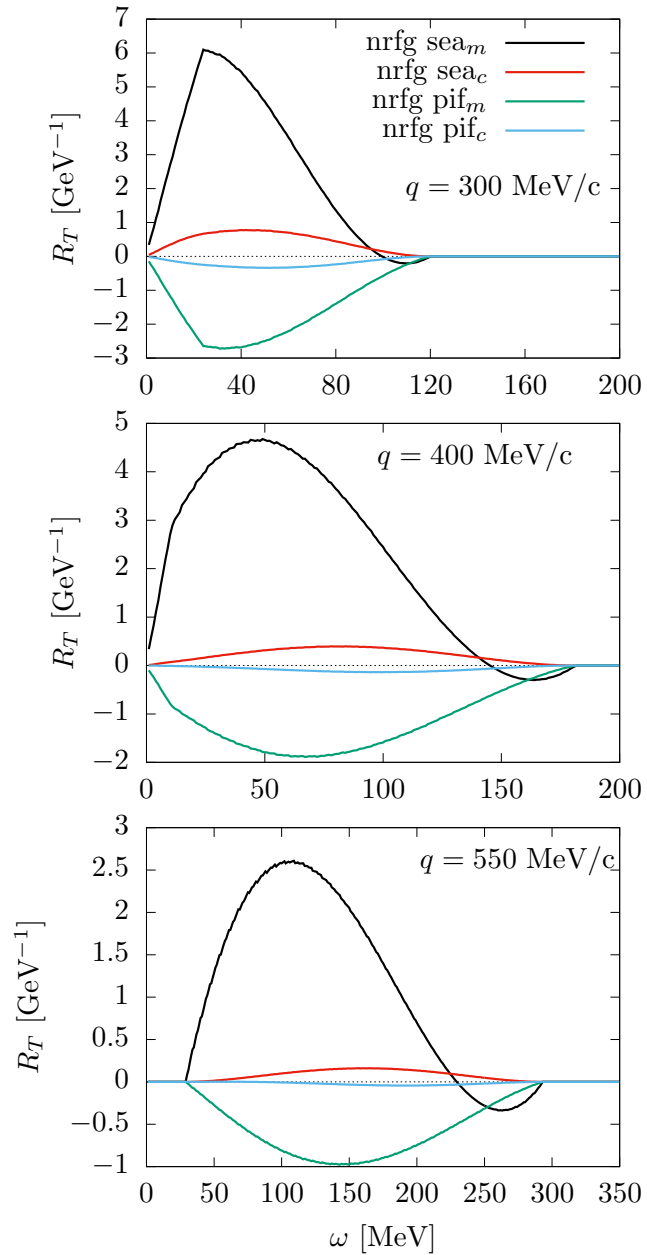


Figure 4.1: Interferences between the components of the one-body current and the MEC in the 1p1h transverse response. Specifically, we represent the magnetization-seagull (ms), convection-seagull (cs), magnetization-pionic ($m\pi$), and convection-pionic ($c\pi$) interferences for different values of q .

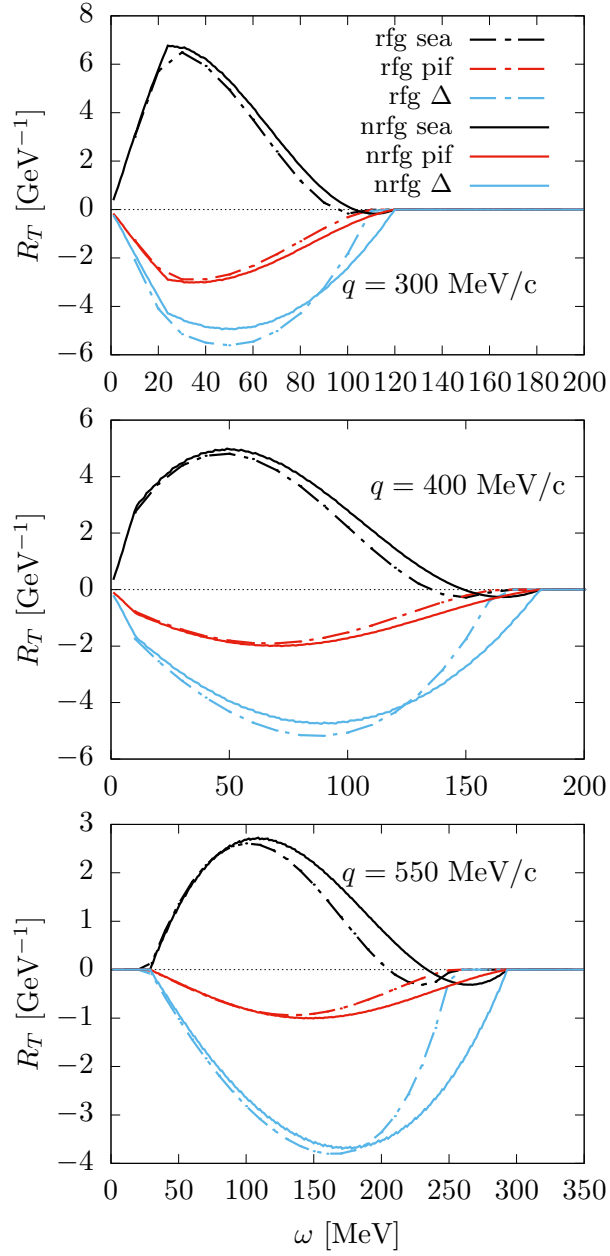


Figure 4.2: Interference between one-body and two-body currents in the transverse response, separated into seagull, pion-in-flight, and Δ currents. We compare the non-relativistic Fermi Gas (NRFG) with the Relativistic Fermi Gas (RFG) for three values of the momentum transfer in the C12 nucleus. The Fermi momentum is $k_F = 225$ MeV/c. Diagrams for the 1p1h MEC matrix elements

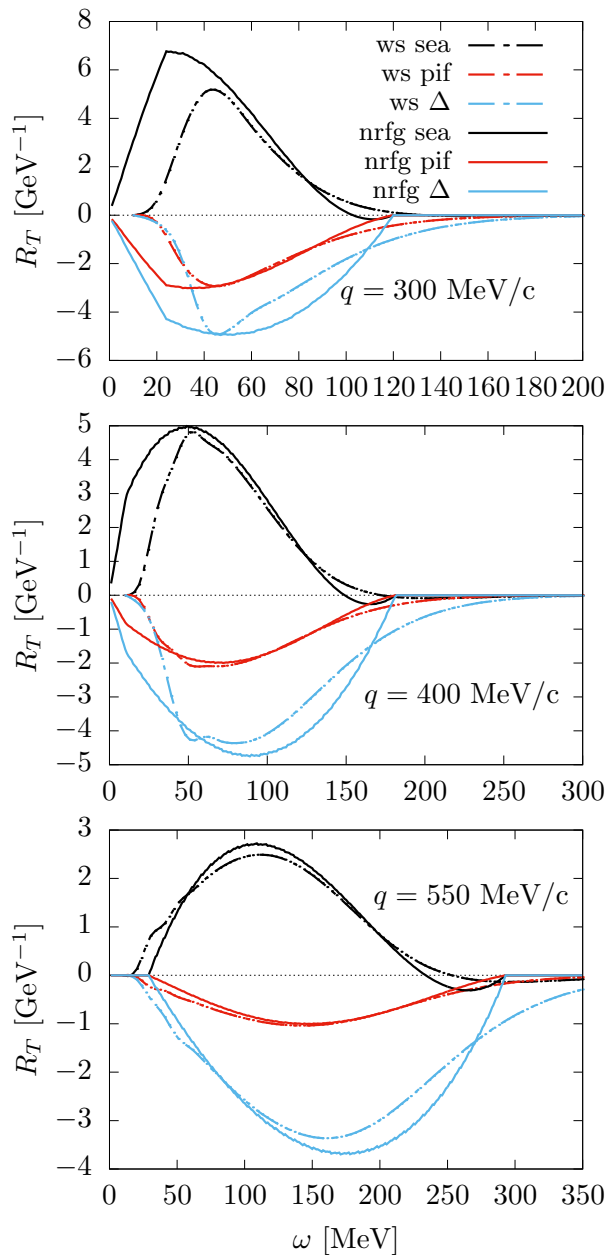


Figure 4.3: The same as Fig. 4.2, comparing between two models: the mean field with Woods-Saxon potential (ws) and the non-relativistic Fermi Gas (nrfg) for different values of momentum transfer q with $k_F = 225$ MeV/c.

Table 4.1: Parameters of the Woods-Saxon potential used in this work for the nucleus ^{12}C .

	V_0 [MeV]	V_{ls} [MeV]	a [fm]	R [fm]
protons	62	3.2	0.57	2.86
neutrons	60	3.15	0.57	2.86

nucleon states are solutions to the Schrödinger equation

$$\left[-\frac{1}{2m_N} \nabla^2 + V(r) \right] \psi(\mathbf{r}) = \epsilon \psi(\mathbf{r}), \quad (4.73)$$

for positive and negative values of the energy ϵ . The WS potential is given by

$$V(r) = -V_0 f(r) + \left(\frac{\hbar}{m_\pi c} \right)^2 \frac{\mathbf{1} \cdot \boldsymbol{\sigma}}{r} \frac{df}{dr} + V_C(r), \quad (4.74)$$

where the function $f(r)$ is the standard Woods-Saxon shape function

$$f(r) = \frac{1}{1 + e^{(r-R)/a}}, \quad (4.75)$$

and $V_C(r)$ is the Coulomb potential of a homogeneously charged sphere with radius R . For ^{12}C we use the WS parameters for ^{12}C given in Table 4.1.

For ^{12}C , the initial states include nucleons in the occupied shells $1s_{1/2}$ and $1p_{3/2}$. More details can be found in Refs. [32, 174]. Note that there is a typographic error in Ref. [32] regarding the relative sign between the central and spin-orbit potentials. This is merely a mistake in the written formula and does not affect the results. The energy of the $1p_{3/2}$ state is lower than that of the $1p_{1/2}$ state because the spin-orbit potential is negative for the $1p_{3/2}$ state and positive for the $1p_{1/2}$ state.

The mean-field approach accounts for some effects of the final-state interaction (FSI) in the response functions. Additionally, unlike the Fermi gas model, it incorporates finite-size effects along with surface effects of the nucleus. In Fig. 4.3 we observe some differences between the WS model and the Fermi gas, particularly at low momentum transfer and low energy, where Pauli blocking affects the Fermi gas more significantly. The WS response shows a slight tail extending to higher energies, unlike the Fermi gas. However, at $q = 550$ MeV/c, the two models become more similar, except for the high-energy tail seen in the WS model. A possible explanation for this similarity at intermediate momentum is that the wavelength of the exchanged photon is small compared to both the nuclear surface and the extent of the nucleon orbits or wave functions in the occupied shells.

4.2.3. Relativistic mean field

In Fig. 4.4 we present the interference responses for two relativistic mean field models: the Dirac-equation based (DEB) model and the relativistic mean field of nuclear matter with effective mass.

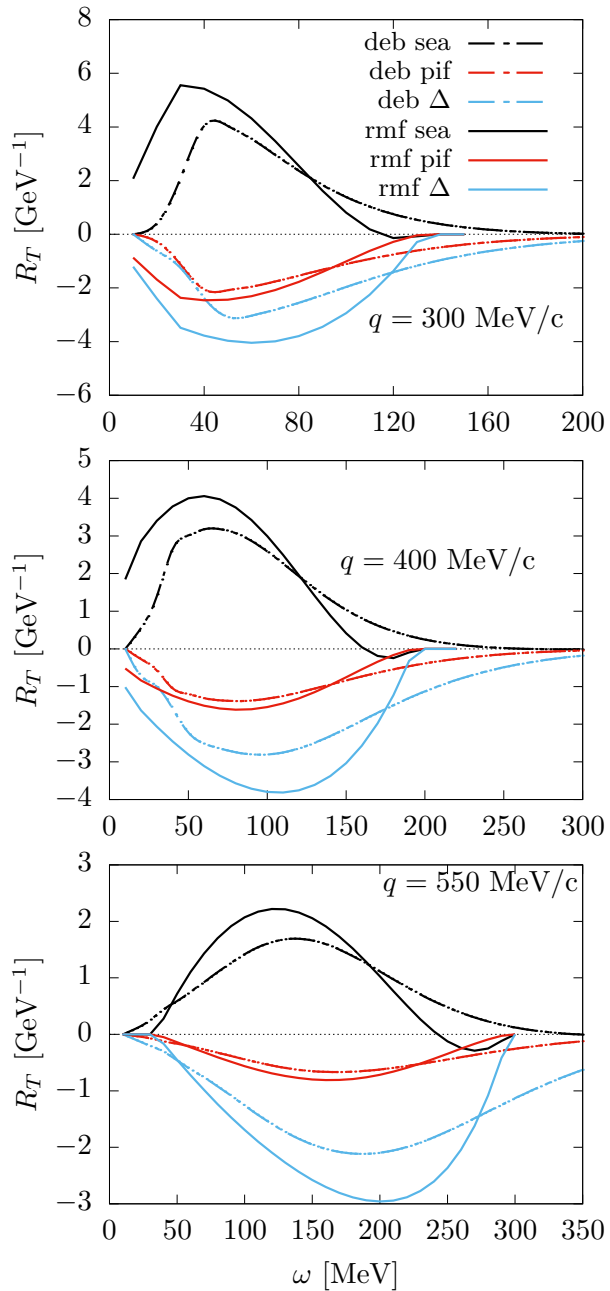


Figure 4.4: The same as Fig. 4.2. Results are compared between two models: the relativistic mean field with DEB potential (deb) and the relativistic mean field of nuclear matter (rmf) with effective mass $M^* = 0.8$, for different values of momentum transfer q .

In the RMF model nucleons move in the presence of scalar $U_S(\mathbf{r})$ and vector $U_V(\mathbf{r})$ potentials, and satisfy a Dirac-like equation for the four-component nucleon wave function $\Psi(\mathbf{r})$:

$$[\gamma^0 (E - U_V(\mathbf{r})) - \boldsymbol{\gamma} \cdot \mathbf{p} - (M + U_S(\mathbf{r}))] \Psi(\mathbf{r}) = 0. \quad (4.76)$$

where Ψ has up and down components

$$\Psi(\mathbf{r}) = \begin{pmatrix} \psi_u(\mathbf{r}) \\ \psi_d(\mathbf{r}) \end{pmatrix} \quad (4.77)$$

The DEB potential is obtained by rewriting the Dirac equation (4.76) as a Klein-Gordon equation for the upper component of the wave function. In this reduction, the upper component is written in the form

$$\Psi_u(\mathbf{r}) = A^{1/2}(r, E) \phi(\mathbf{r}), \quad (4.78)$$

where E is the energy in the final state and $A(r, E)$ is the Darwin term

$$A(r, E) = 1 + \frac{U_S(r) - U_V(r)}{E + M}. \quad (4.79)$$

With this definition the function $\phi(\mathbf{r})$ verifies the equation

$$\left[-\frac{1}{2m_N} \nabla^2 + U_{DEB}(r, E) \right] \phi(\mathbf{r}) = \frac{E^2 - m_N^2}{2m_N} \phi(\mathbf{r}). \quad (4.80)$$

The DEB potential is given by [29, 30]

$$V_{DEB} = V_C + V_{so} \boldsymbol{\sigma} \cdot \mathbf{l} + V_D + V_{coul} \quad (4.81)$$

where the central, spin-orbit and Darwin potentials are given by

$$\begin{aligned} V_C(r, E) &= 2m_N U_S(r) + 2E U_V(r) + U_S(r)^2 - U_V(r)^2 \\ V_{so}(r, E) &= -\frac{1}{rA} \frac{\partial A}{\partial r} \\ V_D(r, E) &= \frac{3}{4A^2} \left(\frac{\partial A}{\partial r} \right)^2 - \frac{1}{rA} \frac{\partial A}{\partial r} - \frac{1}{2A} \frac{\partial^2 A}{\partial r^2}, \end{aligned}$$

and V_{coul} is the Coulomb potential of a homogeneously charged sphere with nuclear radius R .

In Fig. 4.4 we present the results of the interference 1b-2b transverse response using the DEB potential within the semi-relativistic model of Refs. [175, 176]. It is observed that the contribution from the Δ current is negative, as is the contribution from the pion-in-flight current. Consequently, this model verifies the low momentum propositions.

In the same Figure 4.4, the results using the DEB potential are compared with those obtained from the RMF of nuclear matter computed in chapter 3. In this model, the scalar

and vector potentials are constant, making it similar to the RFG but with the nucleon mass replaced by an effective mass $m_N^* = m_N + U_S$ and the energy increased by a constant vector energy $E_V = U_V$. For the ^{12}C case shown in Fig. 4.4, the values used are $m_N^* = 0.8 m_N$ and $E_V = 141$ MeV. More details of the RMF nuclear matter model with MEC can be found in Ref. [154]. As seen in Figure 4.4, both the DEB model and the RMF model with effective mass yield qualitatively similar results, with the peaks of the interference responses largely coinciding. This similarity arises because both models incorporate final-state interaction effects. However, the absolute values obtained with the DEB model are smaller. This is a consequence of the fact that, in the DEB model, the effective mass depends on r , leading to responses that exhibit a tail extending much further than those in the shell model or nuclear matter. Essentially, it appears as if the strength is spread over a wider energy interval. In any case, it is remarkable that the low momentum propositions remain verified in the models presented in Figure 4.4: the 1b- Δ interference is negative and the 1b-pionic one is negative.

4.2.4. SuSAM* model

In this section we present the results obtained with the SuSAM* model for low momentum transfer. This model was introduced in chapter 2 and later extended in chapter 3. In the first step, the single-nucleon prefactor of the superscaling model was modified by computing an averaged value with a Fermi momentum distribution, instead of using the direct extrapolation of the RFG result. In chapter 3, this averaging procedure was further employed to include MEC consistently within the same framework. For a detailed description of the formalism and its derivation, the reader is referred to those chapters.

In Fig. 4.5 we show the interference transverse responses of ^{12}C between the one-body current and the separate MEC contributions (seagull, pionic, and Δ) for momentum transfers $q = 300, 400$, and 550 MeV/ c . This figure complements Figs. 3.7–3.10, where the individual interferences were displayed for higher momentum transfers. Here, the SuSAM* results are compared with those of the RMF model with an effective mass $M^* = 0.8$.

As in chapter 3, both models produce very similar results except for the high- ω tail, where the SuSAM* responses extend slightly beyond the RMF ones due to the phenomenological scaling function inherent to the scaling approach. The overall behavior of the different interference terms remains consistent with that found in the RMF: the seagull contribution is positive, while the pionic and Δ terms are negative. These results confirm that the SuSAM* model also verifies the low-momentum propositions, reproducing the same qualitative features of the RMF calculation. Both frameworks are relativistic and include the effects of an effective nucleon mass.

4.2.5. Strong form factor and relativistic effects

In Fig. 4.6, we show the effect of including the πNN and $\pi N\Delta$ form factors. In our non-relativistic Fermi gas equations and in the low- q propositions, we have omitted these form factors for simplicity. These form factors are multiplicative factors that would be included

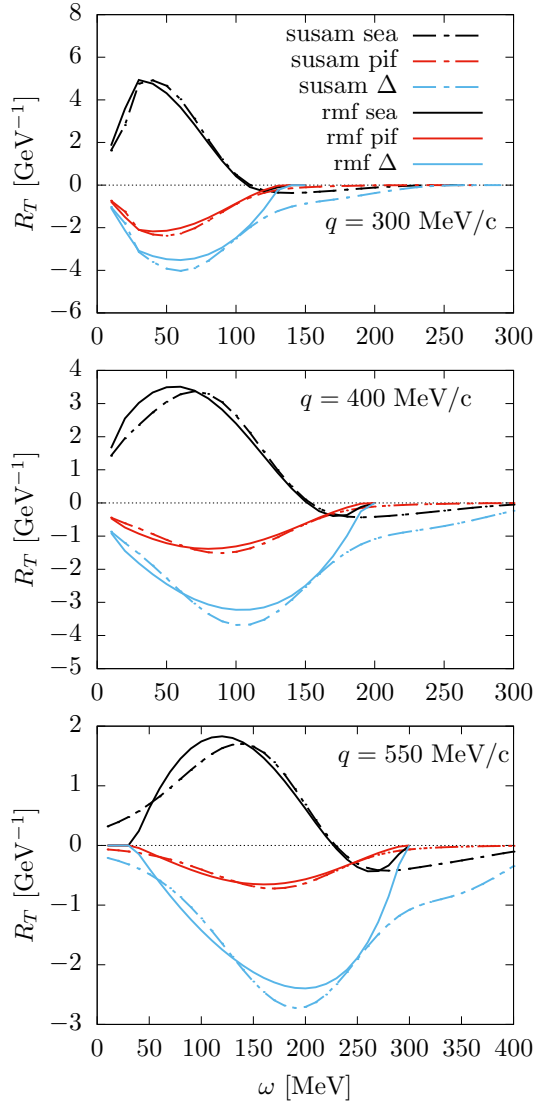


Figure 4.5: The same as Fig. 4.2. Results are compared between two models: the superscaling model with relativistic effective mass and the relativistic mean field of nuclear matter (rmf) with effective mass $M^* = 0.8$, for different values of momentum transfer q .

inside the internal integrals over the intermediate nucleon momentum \mathbf{k} . Their inclusion does not affect the low momentum propositions since these form factors are positive and do not alter the sign of the interference. Moreover, in the NR calculation, some integrals can be evaluated analytically without the form factors, which further simplifies the computation. Given that we are considering small momentum transfers, the effect of the form factors is minimal, as demonstrated in Fig. 4.6, where the relativistic Fermi gas results are compared with and without the strong form factor. As the form factor is less than one, the inclusion produces a reduction of the maximum in absolute value.

The relativistic Fermi gas can be compared with the semirelativistic Fermi gas model (SRFG) developed in [42]. The SRFG model starts from the non-relativistic Fermi gas, incorporating relativistic kinematics and replacing the NR current with a semirelativistic expansion in powers of the initial nucleon momentum divided by the nucleon mass (h/m), while preserving the exact dependence on the final momentum. This approach was extended to include MEC [159] and also applied to the Δ current, although in the latter case the semirelativistic correction is not exact due to the use of a static Δ propagator. The semirelativistic current is obtained from the relativistic one by multiplying by a factor $1/\sqrt{1+\tau}$.

In Fig. 4.7, the SRFG model is compared with the exact RFG for the interference between the MEC and the one-body current. For the seagull and pionic contributions, the SRFG model agrees very well with the relativistic one. However, for the Δ contribution, the approximation is less accurate because the static Δ propagator limits the effectiveness of the semirelativistic factor. In addition, the semirelativistic model was extended to be applied in conjunction with the Woods-Saxon mean field model [176]. This extended model can be directly compared with the DEB model. In fact, the DEB model also incorporates semirelativistic MEC currents, but these currents are further modified because the pion propagator in the DEB model is made dynamic by including the pion energy as the difference in energy between the nuclear states of the mean field model. The comparison between these two models, DEB and SRWS, as shown in Fig. 4.8, reveals significant differences in both the width and the height of the interference response peak. Specifically, the DEB model extends to higher energies and exhibits a broader peak, which is attributed to the fact that the DEB potential is much stronger than the Woods-Saxon potential.

4.2.6. Plane wave approximation

In the shell model with a Woods-Saxon potential, the plane wave approximation (PWA) assumes that the final nucleon with momentum \mathbf{p} is described by a plane wave, meaning it is a solution of the Schrödinger equation without final-state interactions. Therefore, in this approach, the plane wave approximation is applied only to the final outgoing particle state, while the initial state nucleons remain described by the bound shell model wave functions.

Results using this model are presented in Fig. 4.9, where they are compared with the Woods-Saxon mean-field calculations for the 1b-2b interference responses. The observed effect is similar to that seen in the 1b response within the Plane Wave Impulse Approximation (PWIA) [175]. The impact of final-state interactions appears as a shift in the response.

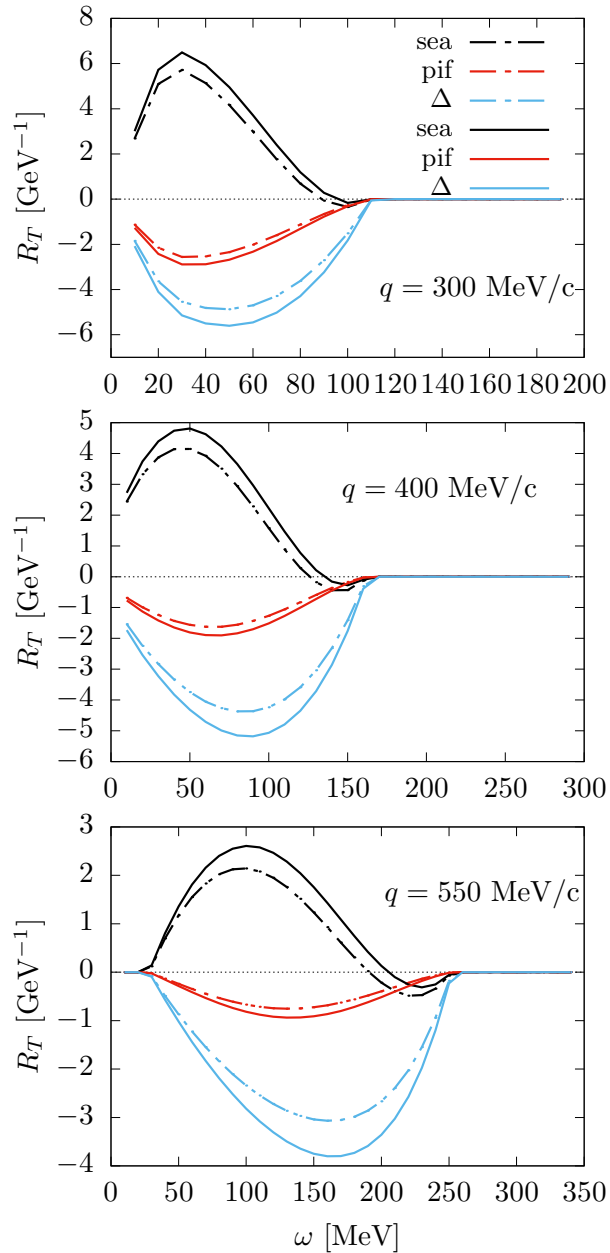


Figure 4.6: The same as Fig. 4.2 but calculated with RFG, with and without the strong πNN form factor. The dashed line represents the results with the form factor, while the solid line represents the results without it.

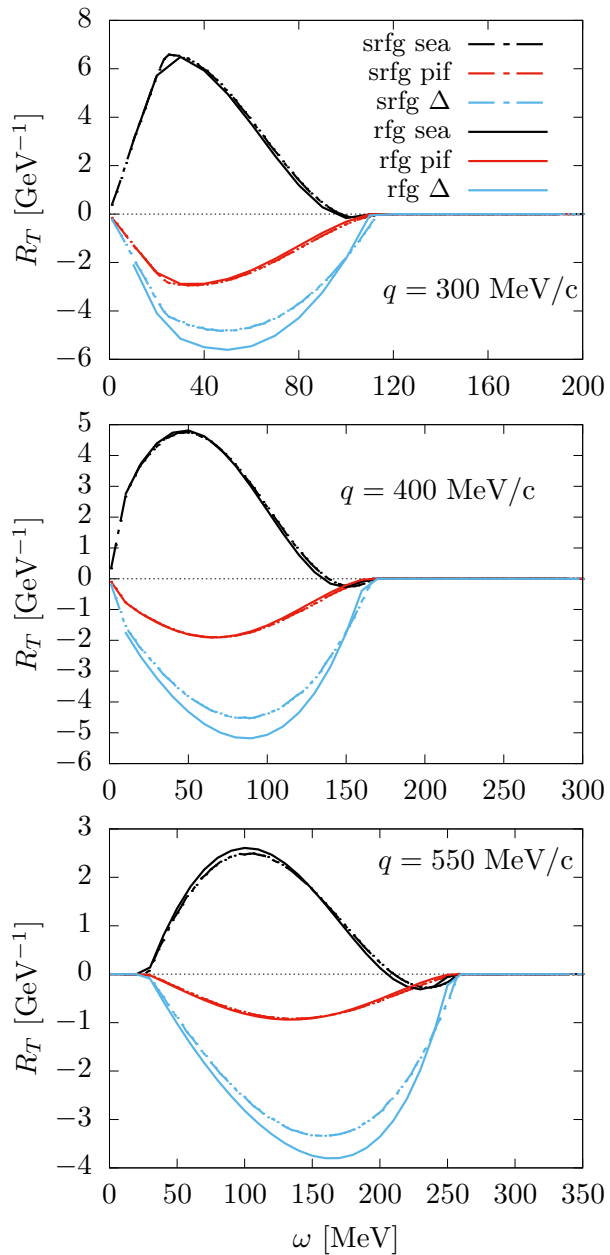


Figure 4.7: The same as Fig. 4.2 but showing two models: RFG and semirelativistic Fermi gas (SRFG). The comparison illustrates the differences between the relativistic and semirelativistic approaches in the transverse response, for different values of q .

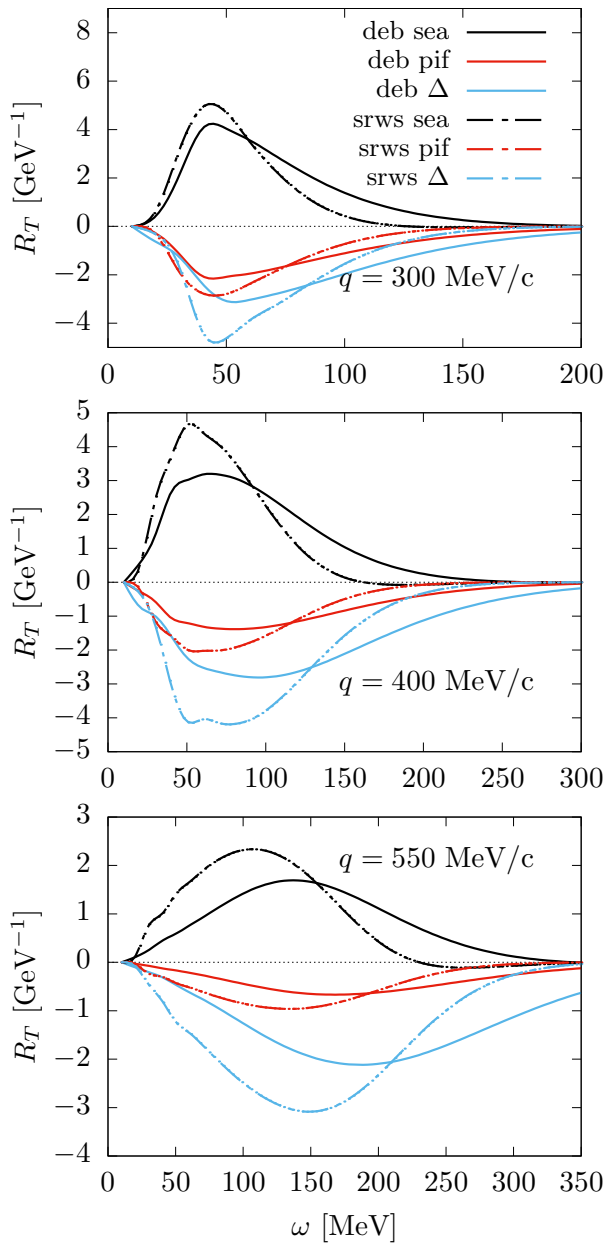


Figure 4.8: The same as Figure 4.2, but now comparing the models: relativistic mean field with DEB potential (deb) and semi-relativistic mean field with Woods-Saxon potential (srws) for different values of momentum transfer q .

This shift can be understood as a consequence of the energy imbalance between the initial and final states. In the initial state, the nucleon has both kinetic and potential energy, whereas in the final state, only kinetic energy remains, since the potential is neglected. This energy mismatch propagates to the energy-conserving delta function, altering the position of the response peak. The shift in the response function can be qualitatively understood using a back-of-the-envelope estimate. First we assume that the matrix element of the current in PWA is approximately equal to the matrix element in the Woods-Saxon model, $\langle J^\mu \rangle_{PW} \simeq \langle J^\mu \rangle_{WS}$. Second, we approximate the potential energy of the final-state nucleon as a constant, $V_p \simeq -V < 0$. Thus, the total energy of the outgoing particle can be written as the sum of its kinetic and potential energy: $\epsilon_p = t_p - V$. Using this, the transverse response function in PWA can be expressed as

$$\begin{aligned} R_{PW}^T(q, \omega) &= \sum_{ph} |\langle J_T \rangle_{PW}|^2 \delta(t_p - \epsilon_h - \omega) \\ &\simeq \sum_{ph} |\langle J_T \rangle_{WS}|^2 \delta(\epsilon_p + V - \epsilon_h - \omega) \\ &= R_{WS}^T(q, \omega - V) \end{aligned} \quad (4.82)$$

This expression shows that the response function is effectively shifted due to the neglect of the potential in the final state.

From Figure 4.9, we observe again that the low-momentum proposition for the 1b-MEC interference response remains valid in both the plane-wave approximation and the Woods-Saxon potential.

4.2.7. Spectral function model

In this subsection, we present results using the spectral function (SF) model, which employs the one-hole spectral function, $S(\mathbf{p}, E)$, that depends on the missing momentum and missing energy. In the SF model, the transverse response is computed assuming factorization of the single-nucleon response and the one-hole spectral function for one-particle emission.

$$R_T(q, \omega) = \int d^3 p w_T(\mathbf{p}, \mathbf{p} - \mathbf{q}) S(\mathbf{p} - \mathbf{q}, \omega - T_p) \quad (4.83)$$

where the single nucleon response is $w^T = w^{11} + w^{22}$, while $w^{\mu\mu}$ is defined in Eq. (4.50).

Unlike the single-particle model that assumes holes with definite energy, the SF approach accounts for a continuous distribution of hole energies. It provides the probability that the system contains a hole state with momentum $\mathbf{h} = \mathbf{p} - \mathbf{q}$ and a missing energy $E = \omega - T_p$, where $T_p = \mathbf{p}^2/(2m_N)$. The basic theory of the SF approach to QE electron scattering is summarized in Appendix F.

We use the spectral function, $S(p, E)$, for ^{12}C taken from Ref. [28] for both protons and neutrons, as shown in Fig. 4.10. This spectral function exhibits peaks around $E \simeq 19$ MeV and $E \simeq 39$ MeV as a function of energy. These values are close to the binding energies of

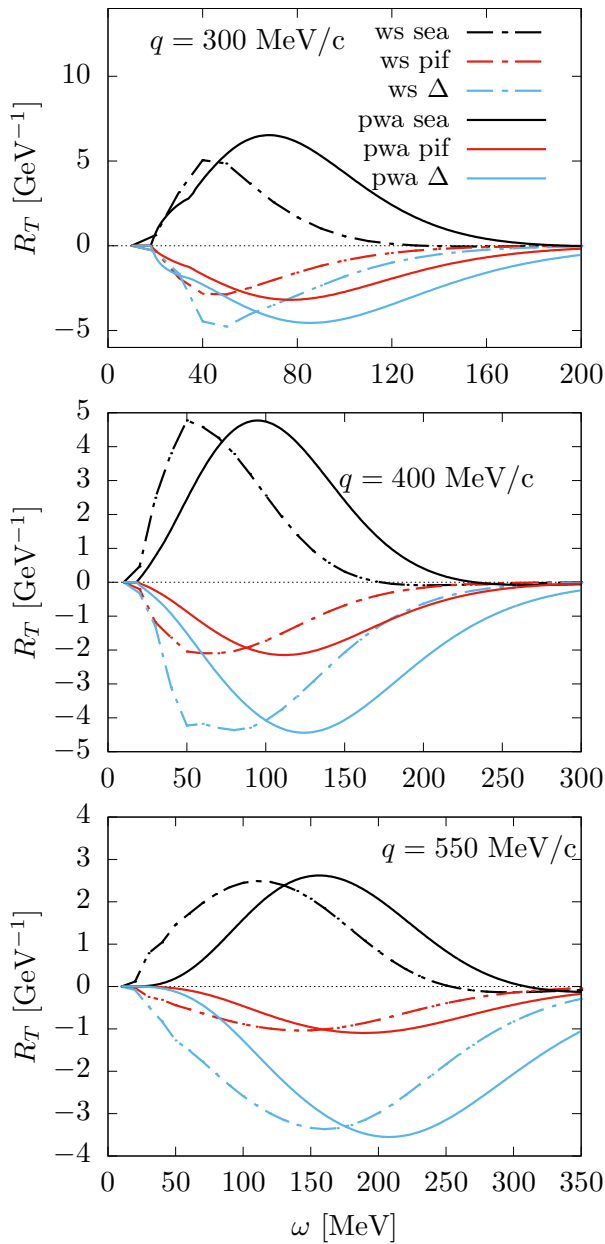


Figure 4.9: The same as Figure 4.2, but now comparing the models: mean field with Woods-Saxon potential (ws) and mean field in plane-wave approximation for the final state (pwa) for different values of momentum transfer q .

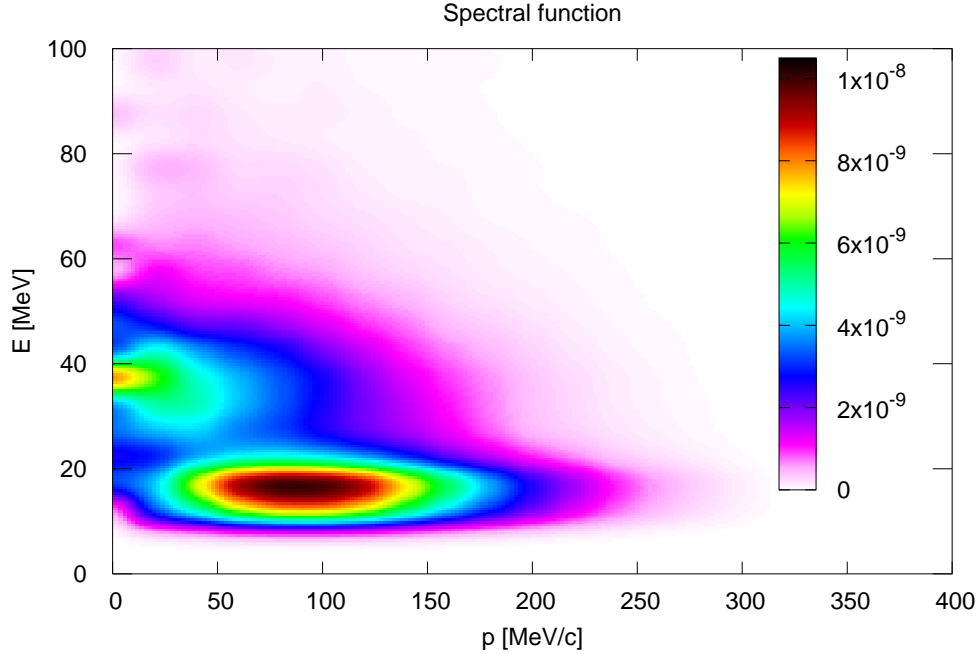


Figure 4.10: Spectral function of ^{12}C in units of $\text{MeV}^{-4}c^3$

the $1p_{3/2}$ and $1s_{1/2}$ shells in the extreme shell model, where the nuclear wave function is described by a Slater determinant.

In the shell model, the spectral function is given by

$$S(p, E) = \sum_{nlj} (2j+1) |\tilde{R}_{nlj}(p)|^2 \delta(E + \epsilon_{nlj}) \quad (4.84)$$

where the sum runs over occupied shells, and $\tilde{R}_{nlj}(p)$ are the shell radial wave functions in momentum space, with single-particle energy ϵ_{nlj} . In the more realistic spectral function of Fig. 4.10, the energy dependence is smeared around the shell binding energies, resulting in a continuous energy distribution instead of discrete shell levels.

In Fig. 4.11, we show the proton momentum distribution $n(p)$ obtained by integrating the spectral function over the missing energy. This distribution is compared with the constant momentum distribution of the Fermi gas model. Additionally, we present the radial momentum distribution, $4\pi n(p)p^2$, which highlights the probability density of nucleons as a function of momentum. The missing energy distribution, obtained by integrating the spectral function over momentum, is also displayed. The normalization follows $\int d^3p n(p) = 6$ for ^{12}C , reflecting that the proton and neutron distributions are identical in this model.

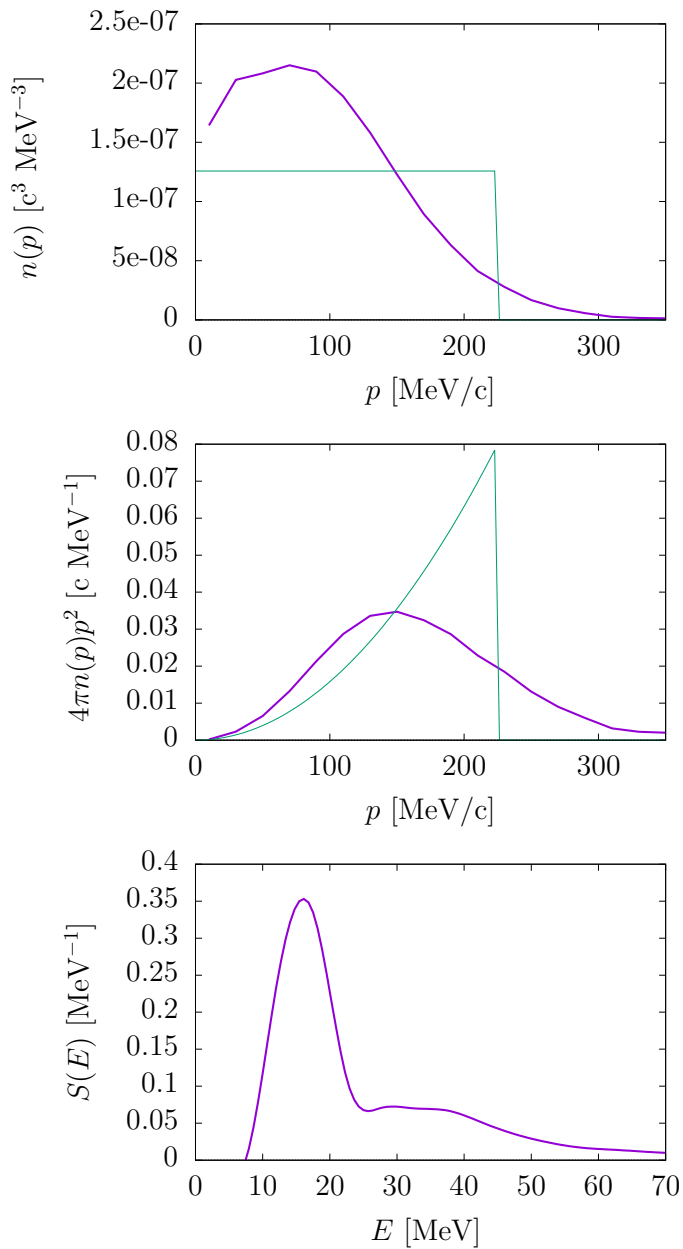


Figure 4.11: Proton momentum distribution of ^{12}C , the radial momentum distribution, and missing energy distribution, obtained from the spectral function by integration.

It is worth noting that the response function in the SF model, Eq. (4.83), is expressed as an integral over the final nucleon momentum p . To evaluate this integral, it is convenient to first integrate over the missing energy and missing momentum. The missing energy is given by

$$E = \omega - T_p = \omega - \frac{p^2}{2m_N}. \quad (4.85)$$

Differentiating, we obtain $dE = -p dp/m_N$, and the volume element in spherical coordinates is

$$d^3p = m_N p dE d\Omega$$

where θ and ϕ are the nucleon emission angles. The response function can then be rewritten as

$$R_T(q, \omega) = m_N \int dE d\Omega p w_T(\mathbf{p}, \mathbf{p} - \mathbf{q}) S(\mathbf{p} - \mathbf{q}, E) \quad (4.86)$$

Next, we define $\mathbf{h} = \mathbf{p} - \mathbf{q}$, leading to the relation $h^2 = p^2 + q^2 - 2pq \cos \theta$, where θ is the angle between \mathbf{p} and \mathbf{q} , with \mathbf{q} chosen along the z -axis. Differentiating with respect to θ , we obtain $h dh = -pq d \cos \theta$.

Substituting this into the integral (4.86), we can express the transverse response as

$$R_T(q, \omega) = 2\pi \frac{m}{q} \int_0^\omega dE \int_{|p-q|}^{p+q} dh S(h, E) w_T(\mathbf{h} + \mathbf{q}, \mathbf{h}), \quad (4.87)$$

where $p = \sqrt{2m_N(\omega - E)}$. Note that $E < \omega$ ensures that p is well defined. The factor 2π arises from the integration over ϕ , and the integration limits in h correspond to nucleon emission in the direction of $\pm \mathbf{q}$.

The effect of MEC is estimated by treating the spectator nucleon as an on-shell plane-wave with momentum \mathbf{k} , therefore we replace the single-nucleon response by the effective single nucleon including MEC, in Eq. (4.50). This approximation has been done in the past in previous calculations by the Pavia group for $(e, e'p)$ reactions [177], and in recent RMF-based calculations [46], where the spectator nucleon is described using an effective mass and vector energy. A similar approach to MEC was also adopted in the spectral function model of Ref. [47]. Thus the transverse response is evaluated using the effective single nucleon, Eq. (4.50), which includes the MEC contribution, effectively decoupling it from the spectral function.

In the spectral function model, the interference MEC-OB responses are presented in Fig. 4.12 for the separate contributions from the seagull, pion-in-flight, and Δ currents. The figure compares the SF results with those obtained using the PW model from the previous subsection. Both models yield quite similar results. This similarity arises from the fact that both models assume plane waves for the final-state nucleon. In the PW model, the response is obtained by summing the contributions from each shell separately, while in the SF model, the shell contributions are smeared according to the spectral function's energy distribution. However, this smearing effect is barely noticeable in the inclusive response, as the information about the hole energy is lost. Furthermore, the agreement between the SF and PWIA models reinforces the validity of the approximation that treats the spectator

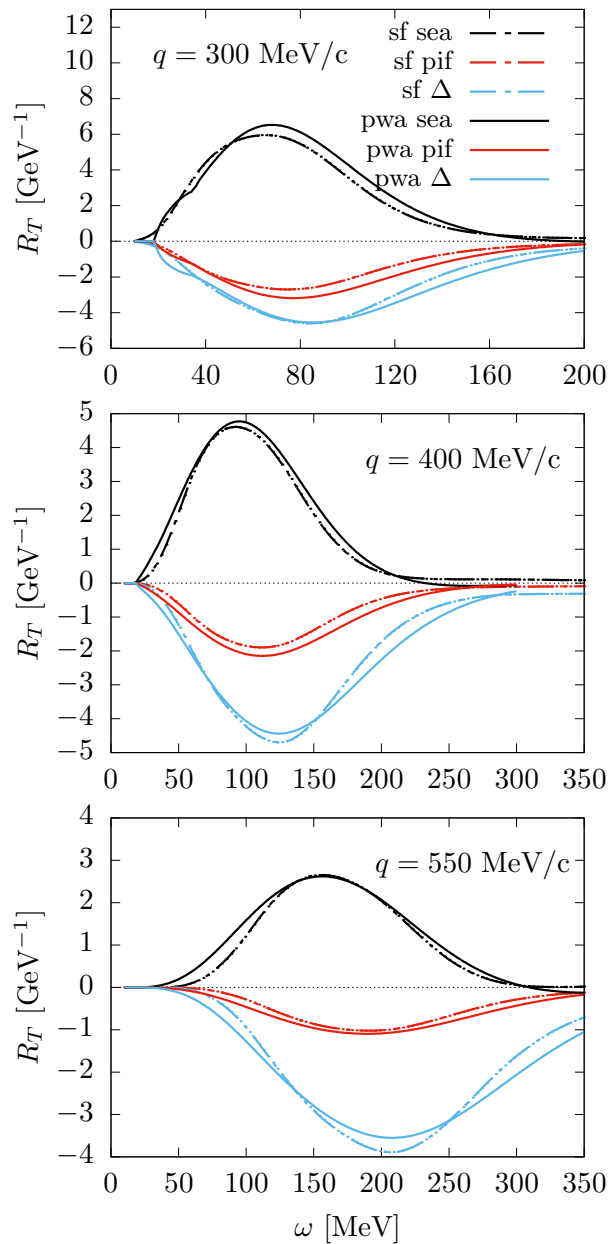


Figure 4.12: The same as Figure 4.2, but now comparing the models: spectral function (SF) and mean field with plane-wave approximation (PWA) for different values of momentum transfer q .

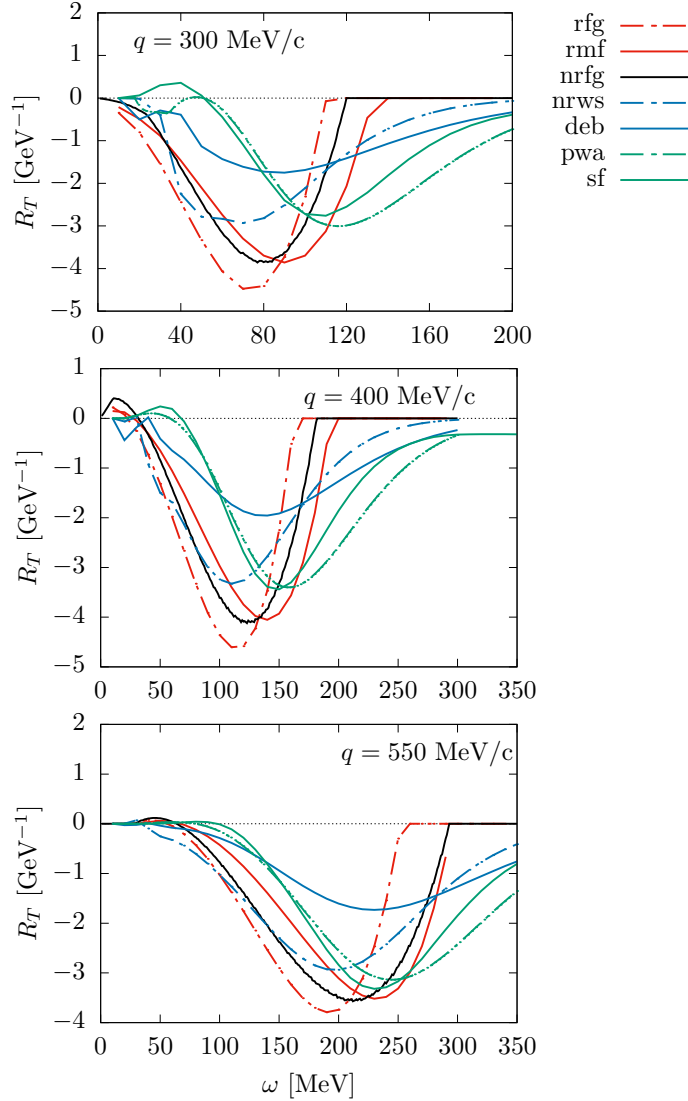


Figure 4.13: Total interference OB-MEC compared across all different models considered in this work for all values of q . The πNN form factor is not included.

nucleon as a plane wave. While this approximation is not explicitly made in the PW model, it is assumed in the SF model. In conclusion, the SF model, as applied here, fully adheres to the low-momentum proposition, consistent with all the models analyzed in this work.

4.2.8. Total interference response.

To conclude the results section, we present a comprehensive comparison of most of the models discussed in this chapter to assess the overall impact of MEC and the theoretical uncertainties. In Fig. 4.13, we display the total 1b-MEC interference for a selection of seven models. All models consistently predict a negative interference, although there are significant quantitative differences in the position of the peak and the width of the distribution. Despite these variations, the overall magnitude remains comparable, with

differences up to a factor of two. Importantly, the key takeaway from this comparison, and one of the main objectives of this chapter, is that the low-momentum proposition holds across all models analyzed. None of the models considered in this chapter exhibit a qualitative deviation, such as a sign change in the interference term.

To end we list here the models considered in this chapter:

1. Non relativistic Fermi gas (NRFG)
2. Relativistic Fermi gas (RFG)
3. Mean field with Woods-Saxon potential (WS)
4. Mean field with Dirac-equation based potential (DEB)
5. Relativistic mean field of nuclear matter with effective mass (RMF)
6. Mean field with plane wave approximation (PWA)
7. Semirelativistic mean field with Woods-Saxon (SRWS)
8. Semirelativistic Fermi gas (SRFG)
9. Superscaling model with effective mass (SuSAM*).
10. Spectral function (SF)

4.3. Final remarks

In this chapter, we have conducted a detailed reexamination of the OB-MEC interference in the one-particle emission transverse response, focusing on the low-momentum proposition. We compared various models, obtaining qualitatively consistent results. A key aspect of our analysis was the derivation of the low-momentum proposition within the non-relativistic Fermi gas framework, ensuring full transparency and reproducibility in our approach. The proposition clearly establishes that the sign of the interference with the pionic and Δ currents is negative, which refers to the Riska current, considered here as the standard. Once this current is fixed, its sign does not present ambiguities. Our results show that all models considered adhere to the low-momentum proposition. The common feature among these models is that they are based on independent-particle descriptions, either relativistic or non-relativistic, or extensions thereof, such as the one-hole spectral function for one-particle emission in electron scattering. Crucially, these models do not include explicit two-body correlations beyond mean-field approximations. Consequently, in all cases, the MEC particle-hole matrix element only retains the exchange contribution involving the spectator nucleon, without additional contributions. Given these results, it does not seem possible to explain any enhancement in the transverse response in one-particle emission using models that do not include fundamentally different ingredients that would violate the low-momentum proposition. A clear candidate for producing such an

enhancement, as suggested by previous studies, is the inclusion of SRC correlations, as in the microscopic calculation of [35]. These correlations could introduce contributions that do not adhere to the low-momentum proposition, thus altering the dynamics beyond what is captured by the models analyzed here. We will study the SRC in chapters 6 and 7.

Chapter 5

CCQE neutrino-nucleus scattering with Meson exchange currents

In the preceding chapters, we have discussed the electromagnetic scattering processes. The present chapter focuses on neutrino-nucleus scattering. The effect of meson-exchange currents on CCQE neutrino scattering with single-nucleon emission is computed and analyzed within the simplest possible framework: the RFG model. This serves as a first step towards more elaborate approaches, such as the RMF model for nuclear matter and the SuSAM* model, both of which yield qualitatively similar results. The calculations obtained show a reduction of the vector, axial and vector-axial transverse response functions and, consequently, a decrease in the total neutrino cross section. A comparison with the NR limit is also presented. More details can be found in Ref. [178].

5.1. Charge-changing quasielastic neutrino scattering

We will begin by summarizing the CCQE formalism in neutrino scattering (ν_μ, μ^-) and ($\bar{\nu}_\mu, \mu^+$). Our approach is based on previous works that have addressed charged-current (CC) reactions in nuclei [160, 7]. We assume that the four-momentum transfer is given by $k^\mu - k'^\mu = Q^\mu = (\omega, \mathbf{q})$ with $Q^2 = \omega^2 - q^2 < 0$. The energy transfer is ω , \mathbf{q} is the momentum transfer along the z-axis, and \mathbf{k} and \mathbf{k}' are the momenta of the incoming neutrino and the outgoing muon, respectively. Their corresponding energies are $\epsilon = E_\nu$ for the neutrino and $\epsilon' = m_\mu + T_\mu$ for the muon. In this way, assuming that θ is the scattering angle between \mathbf{k} and \mathbf{k}' , the double-differential cross section is written as follows,

$$\frac{d^2\sigma}{dT_\mu d\Omega_\mu} = \frac{G^2 \cos^2 \theta_c}{4\pi^2} \frac{k'}{\epsilon} \frac{v_0}{2} (V_{CC} R_{CC} + 2V_{CL} R_{CL} + V_{LL} R_{LL} + V_T R_T \pm 2V_{T'} R_{T'}) \quad (5.1)$$

where $G = 1.666 \times 10^{-11} \text{ MeV}^{-2}$ is the Fermi weak constant and θ_c is the Cabibbo angle. We define the factor $v_0 = (\epsilon + \epsilon')^2 - q^2$. The coefficients V_K are obtained from the

components of the leptonic tensor

$$\begin{aligned}
 V_{CC} &= 1 + \delta^2 \frac{Q^2}{v_0}, \\
 V_{CL} &= \frac{\omega}{q} - \frac{\delta^2}{\rho'} \frac{Q^2}{v_0}, \\
 V_{LL} &= \frac{\omega}{q^2} + \left(1 + \frac{2\omega}{q\rho'} + \rho\delta^2\right) \delta^2 \frac{Q^2}{v_0}, \\
 V_T &= \frac{Q^2}{v_0} + \frac{\rho}{2} - \frac{\delta^2}{\rho'} \left(\frac{\omega}{q} + \frac{1}{2}\rho\rho'\delta^2\right) \frac{Q^2}{v_0}, \\
 V_{T'} &= \frac{1}{\rho'} \left(1 - \frac{\omega\rho'}{q}\delta^2\right) \frac{Q^2}{v_0},
 \end{aligned} \tag{5.2}$$

with the dimensionless factors

$$\delta = \frac{m_\mu}{\sqrt{|Q^2|}}, \quad \rho = \frac{|Q^2|}{q^2}, \quad \rho' = \frac{q}{\epsilon + \epsilon'}. \tag{5.3}$$

The five nuclear responses R_K , which only depend on (q, ω) , arise from various combinations of the components of the hadronic tensor,

$$\begin{aligned}
 R_{CC} &= W^{00}, \\
 R_{CL} &= -\frac{1}{2}(W^{03} + W^{30}), \\
 R_{LL} &= W^{33}, \\
 R_T &= W^{11} + W^{22}, \\
 R_{T'} &= -\frac{i}{2}(W^{12} - W^{21}).
 \end{aligned} \tag{5.4}$$

In the case of charged-current weak interactions, the nuclear current operator is the sum of a vector and an axial-vector component. As a result, the response functions CC, CL, LL, and T, can each be written as the sum of two separate contributions: one arising from the vector-vector (VV) part of the current, and the other from the axial-axial (AA) part:

$$R_K = R_K^{VV} + R_K^{AA}, \quad K = CC, CL, LL, T. \tag{5.5}$$

On the other hand, the T' response originates from the interference between the vector and axial components of the current, and can be written as

$$R_{T'} = R_{T'}^{VA} + R_{T'}^{AV}. \tag{5.6}$$

The hadronic tensor for the 1p1h channel is calculated for a RFG and is constructed from the formalism that follows in parallel with the case of electron scattering of previous chapters. The main differences are the presence of an axial component in the charged current and the modified structure of the isospin operators. The inclusive hadronic tensor for the 1p1h channel is given by

$$W^{\mu\nu} = \sum_{ph} \langle ph^{-1} | \hat{J}^\mu | F \rangle^* \langle ph^{-1} | \hat{J}^\nu | F \rangle \delta(E_p - E_h - \omega) \theta(p - k_F) \theta(k_F - h), \tag{5.7}$$

where $|F\rangle$ is the Fermi ground state. Additionally, the theta functions ensure that the initial nucleons have a momentum below the Fermi level $h < k_F$ and that the final nucleons, after the interaction, have a momentum $p > k_F$.

The nuclear current is taken as the sum of one-body and two-body operators

$$\hat{J}^\mu = \hat{J}_{1b}^\mu + \hat{J}_{2b}^\mu. \quad (5.8)$$

The 1p1h matrix element of these operators in the RFG is given by

$$\langle ph^{-1} | \hat{J}_{1b}^\mu | F \rangle = \langle p | \hat{J}_{1b}^\mu | h \rangle, \quad (5.9)$$

$$\langle ph^{-1} | \hat{J}_{2b}^\mu | F \rangle = \sum_{k < k_F} \left[\langle pk | \hat{J}_{2b}^\mu | hk \rangle - \langle pk | \hat{J}_{2b}^\mu | kh \rangle \right]. \quad (5.10)$$

Note that the matrix element of the MEC, being a two-body operator, involves a transition between pairs of nucleons; however, in a 1p1h excitation, one of the nucleons, $|k\rangle = |\mathbf{k}, s_k, t_k\rangle$, remains in its initial state and acts merely as a spectator.

The next step is to write the elementary matrix elements of the one-body and two-body current operators between plane-wave states, using momentum conservation

$$\langle p | \hat{J}_{1b}^\mu | h \rangle = \frac{(2\pi)^3}{V} \delta^3(\mathbf{q} + \mathbf{h} - \mathbf{p}) j_{1b}^\mu(\mathbf{p}, \mathbf{h}), \quad (5.11)$$

$$\langle p'_1 p'_2 | \hat{J}_{2b}^\mu | p_1 p_2 \rangle = \frac{(2\pi)^3}{V^2} \delta^3(\mathbf{p}_1 + \mathbf{p}_2 + \mathbf{q} - \mathbf{p}'_1 - \mathbf{p}'_2) j_{2b}^\mu(\mathbf{p}'_1, \mathbf{p}'_2, \mathbf{p}_1, \mathbf{p}_2). \quad (5.12)$$

The current functions $j_{1b}^\mu(\mathbf{p}, \mathbf{h})$ and $j_{2b}^\mu(\mathbf{p}'_1, \mathbf{p}'_2, \mathbf{p}_1, \mathbf{p}_2)$ implicitly depend on spin and isospin indices. Inserting Eqs. (5.11) and (5.12) in Eqs. (5.9) and (5.10), respectively, we can write the total current matrix element in the form

$$\langle ph^{-1} | \hat{J}^\mu | F \rangle = \frac{(2\pi)^3}{V} \delta^3(\mathbf{q} + \mathbf{h} - \mathbf{p}) j^\mu(\mathbf{p}, \mathbf{h}), \quad (5.13)$$

where

$$j^\mu(\mathbf{p}, \mathbf{h}) \equiv j_{1b}^\mu(\mathbf{p}, \mathbf{h}) + j_{2b}^\mu(\mathbf{p}, \mathbf{h}), \quad (5.14)$$

and

$$j_{2b}^\mu(\mathbf{p}, \mathbf{h}) \equiv \frac{1}{V} \sum_{k < k_F} [j_{2b}^\mu(\mathbf{p}, \mathbf{k}, \mathbf{h}, \mathbf{k}) - j_{2b}^\mu(\mathbf{p}, \mathbf{k}, \mathbf{k}, \mathbf{h})]. \quad (5.15)$$

This effective current, $j_{2b}^\mu(\mathbf{p}, \mathbf{h})$, accounts for the fact that the two-body current operator, when acting on a nucleon pair in the Fermi sea, can lead to a 1p1h excitation if one of the nucleons remains a spectator. This mechanism is responsible for the interference contribution in the 1p1h channel. Then the total current function $j^\mu(\mathbf{p}, \mathbf{h})$ incorporates the contribution of the 1b and the 2b currents.

To evaluate the hadronic tensor (5.7) in the RFG we insert the matrix element (5.13), and take the thermodynamic limit by replacing the discrete sum over hole states with an integral over momentum space,

$$\sum_h \rightarrow \frac{V}{(2\pi)^3} \int d^3 h \sum_{s_h t_h} \quad (5.16)$$

The integration over the final particle state can then be performed using the momentum-conserving delta function, which fixes the particle momentum to $\mathbf{p} = \mathbf{h} + \mathbf{q}$

$$W^{\mu\nu} = \frac{V}{(2\pi)^3} \int d^3h \delta(E_p - E_h - \omega) 2w^{\mu\nu}(\mathbf{p}, \mathbf{h}) \theta(p - k_F) \theta(k_F - h), \quad (5.17)$$

where

$$w^{\mu\nu}(\mathbf{p}, \mathbf{h}) \equiv \frac{1}{2} \sum_{s_p s_h} j^\mu(\mathbf{p}, \mathbf{h})^* j^\nu(\mathbf{p}, \mathbf{h}) \quad (5.18)$$

is the single-nucleon hadronic tensor. The sums over isospin t_p, t_h no longer appear because we have already imposed the condition that, in the case of neutrino scattering, the hole state h corresponds to a neutron and the particle p to a proton, while the opposite holds for antineutrino scattering.

The single-nucleon tensor contains the square of the sum of the one-body and two-body currents. By expanding this square, one obtains

$$w^{\mu\nu} = w_{1b}^{\mu\nu} + w_{2b}^{\mu\nu} + w_{1b2b}^{\mu\nu}, \quad (5.19)$$

where $w_{1b}^{\mu\nu}$ and $w_{2b}^{\mu\nu}$ are the pure one-body and two-body contributions, respectively, and $w_{1b2b}^{\mu\nu}$ is the interference term.

$$w_{1b}^{\mu\nu} = \frac{1}{2} \sum_{s_p s_h} (j_{1b}^\mu)^* j_{1b}^\nu \quad (5.20)$$

$$w_{2b}^{\mu\nu} = \frac{1}{2} \sum_{s_p s_h} (j_{2b}^\mu)^* j_{2b}^\nu \quad (5.21)$$

$$w_{1b2b}^{\mu\nu} = \frac{1}{2} \sum_{s_p s_h} [(j_{1b}^\mu)^* j_{2b}^\nu + (j_{2b}^\mu)^* j_{1b}^\nu] \quad (5.22)$$

And the response functions also decompose accordingly:

$$R^K = R_{1b}^K + R_{2b}^K + R_{1b2b}^K \quad (5.23)$$

From calculations in electron scattering in chapter 3, it has been observed that the pure two-body MEC contribution, R_{2b}^K , is generally small and can often be neglected when compared to the interference term R_{1b2b}^K , which tends to dominate the MEC effects in the 1p1h channel [42]. This justifies our focus on the interference term, which captures the leading MEC effect in the 1p1h sector.

The one-body current operator consist of two terms: $j_{1b}^\mu(\mathbf{p}, \mathbf{h}) = j_{1bV}^\mu(\mathbf{p}, \mathbf{h}) + j_{1bA}^\mu(\mathbf{p}, \mathbf{h})$. The vector current is

$$j_{1bV}^\mu(\mathbf{p}, \mathbf{h}) = \bar{u}(\mathbf{p}) \left(F_1^V \gamma^\mu + i \frac{F_2^V}{2m_N} \sigma^{\mu\nu} Q_\nu \right) u(\mathbf{h}), \quad (5.24)$$

where the isovector nucleon form factors are defined as $F_{1,2}^V = F_{1,2}^p - F_{1,2}^n$. The axial current is

$$j_{1bA}^\mu(\mathbf{p}, \mathbf{h}) = -\bar{u}(\mathbf{p}) \left(G_A \gamma^\mu \gamma_5 + G_P \frac{Q^\mu}{2m_N} \gamma_5 \right) u(\mathbf{h}), \quad (5.25)$$

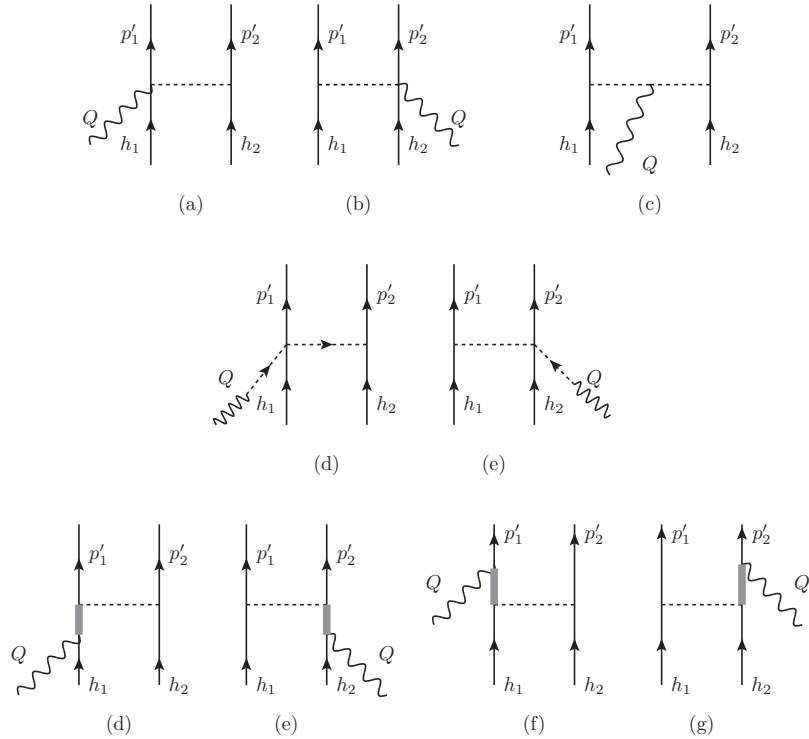


Figure 5.1: Feynman diagrams for the electroweak MEC model used in this work.

where G_A is the nucleon axial-vector form factor and G_P is the pseudo-scalar form factor, given by

$$G_A = \frac{g_A}{1 - \frac{Q^2}{M_A^2}} \quad (5.26)$$

$$G_P = \frac{4m_N^2}{m_\pi^2 - Q^2} G_A \quad (5.27)$$

with $g_A = 1.26$ and $M_A = 1032$ MeV.

Note that the minus sign in the axial one-body current (5.25) arises from our convention of defining the total current as the sum of the vector and axial parts, $J^\mu = J_V^\mu + J_A^\mu$, whereas it is often written in the literature as $V - A$. We adopt this convention for consistency with the meson-exchange currents, which are also defined as the sum $V + A$. Of course, physical results are independent of this choice.

5.2. Weak CC Meson exchange currents

We present the MEC for CC neutrino scattering considered in this work, corresponding to the Feynman diagrams shown in Figure 5.1. They were derived in [160] from the pion weak production model of ref. [165]. Similarly to the 1b current, the weak MEC are the

sum of vector and axial currents. The different current operators are: the seagull current (diagrams a and b), the pion-in-flight current (diagram c), the pion-pole current (diagrams d and e), and the Δ forward (f,g) and backward currents (diagrams h-i):

$$j_2^\mu(\mathbf{p}'_1, \mathbf{p}'_2, \mathbf{p}_1, \mathbf{p}_2) = j_{sea}^\mu + j_\pi^\mu + j_{pole}^\mu + j_\Delta^\mu, \quad (5.28)$$

The weak MEC operators exhibit a structure closely related to that of the electromagnetic case of chapters 3 and 4, reflecting their common origin in the underlying meson-nucleon dynamics. In particular, they involve the same V-function defined in Eq. (3.23)

$$V_{s'_1 s_1}(p'_1, p_1) \equiv F_{\pi NN}(k_1^2) \frac{\bar{u}_{s'_1}(p'_1) \gamma^5 k_1 u_{s_1}(p_1)}{k_1^2 - m_\pi^2}, \quad (5.29)$$

where $k_1 = p'_1 - p_1$, is the momentum transfer to the individual nucleon (and the momentum carried by the pion), the spinors $u_s(p)$ are the solutions of the Dirac equation with momentum \mathbf{p} , m_π is the pion mass, and $F_{\pi NN}(k^2)$ is a strong form factor [162, 163, 179]

$$F_{\pi NN}(k^2) = \frac{\Lambda^2 - m_\pi^2}{\Lambda^2 - k^2}, \quad \Lambda_\pi = 1300 \text{ MeV} \quad (5.30)$$

Seagull current

The seagull current is given as the sum of the vector and axial operators,

$$j_{sea}^\mu = (j_{sea}^\mu)_V + (j_{sea}^\mu)_A, \quad (5.31)$$

$$(j_{sea}^\mu)_V = i[\boldsymbol{\tau}^{(1)} \times \boldsymbol{\tau}^{(2)}]_\pm \frac{f^2}{m_\pi^2} F_1^V F_{\pi NN}(k_1^2) V_{s'_1 s_1}(p'_1, p_1) \bar{u}_{s'_2}(p'_2) \gamma^5 \gamma^\mu u_{s_2}(p_2) + (1 \leftrightarrow 2) \quad (5.32)$$

$$(j_{sea}^\mu)_A = i[\boldsymbol{\tau}^{(1)} \times \boldsymbol{\tau}^{(2)}]_\pm \frac{f^2}{m_\pi^2} \frac{F_\rho(k_2^2)}{g_A} F_{\pi NN}(k_1^2) V_{s'_1 s_1}(p'_1, p_1) \bar{u}_{s'_2}(p'_2) \gamma^\mu u_{s_2}(p_2) + (1 \leftrightarrow 2), \quad (5.33)$$

where $f^2 = 1$ is the πNN coupling constant, $\boldsymbol{\tau}^{(i)}$ is the isospin operator of nucleon i , $F_1^V(Q^2) = F_1^p - F_1^n$ is the isovector form factor of the nucleon, and F_ρ is the ρ meson form factor. Note that the current has been written as proportional to an isospin raising operator. The sign \pm in the isospin matrix elements of Eqs. (5.32–5.40) refers to neutrino (+) or antineutrino (−) scattering. The isospin matrix elements are computed in Appendix G.

Pion-in-flight current

The pion-in-flight has only vector part

$$(j_\pi^\mu)_V = i[\boldsymbol{\tau}^{(1)} \times \boldsymbol{\tau}^{(2)}]_\pm F_1^V \frac{f^2}{m_\pi^2} V_{s'_1 s_1}(p'_1, p_1) V_{s'_2 s_2}(p'_2, p_2) (k_1^\mu - k_2^\mu) \quad (5.34)$$

$$(j_\pi^\mu)_A = 0 \quad (5.35)$$

Pion-Pole current

The pion-pole current is purely axial

$$(j_{pole}^\mu)_V = 0 \quad (5.36)$$

$$(j_{pole}^\mu)_A = i[\boldsymbol{\tau}^{(1)} \times \boldsymbol{\tau}^{(2)}]_\pm \frac{f^2}{m_\pi^2} \frac{F_\rho(k_1^2)}{g_A} F_{\pi NN}(k_2^2) \frac{Q^\mu \bar{u}_{s'_1}(p'_1) Q u_{s_1}(p_1)}{Q^2 - m_\pi^2} V_{s'_2 s_2}(p'_2, p_2) + (1 \leftrightarrow 2) \quad (5.37)$$

Note that since this current contains the term Q^μ , only contributes to the longitudinal and time components of the hadronic tensor.

Delta (Δ) current

The Δ excitation current operator has both vector and axial parts,

$$j_\Delta^\mu = (j_\Delta^\mu)_V + (j_\Delta^\mu)_A. \quad (5.38)$$

corresponding to the vertices $\Gamma_V^{\beta\mu}$ and $\Gamma_A^{\beta\mu}$, respectively, in the $N \rightarrow \Delta$ transition, given in Eq. (5.42) below. The Δ current is further divided into forward and backward operators

$$\begin{aligned} j_{\Delta F}^\mu &= [U_F(1, 2)_\pm] \frac{f^* f}{m_\pi^2} F_{\pi N \Delta}(k_2^2) V_{s'_2 s_2}(p'_2, p_2) \bar{u}_{s'_1}(p'_1) k_2^\alpha G_{\alpha\beta}(p_1 + Q) \Gamma^{\beta\mu}(Q) u_{s_1}(p_1) \\ &+ (1 \leftrightarrow 2), \end{aligned} \quad (5.39)$$

$$\begin{aligned} j_{\Delta B}^\mu &= [U_B(1, 2)_\pm] \frac{f^* f}{m_\pi^2} F_{\pi N \Delta}(k_2^2) V_{s'_2 s_2}(p'_2, p_2) \bar{u}_{s'_1}(p'_1) k_2^\beta \hat{\Gamma}^{\mu\alpha}(Q) G_{\alpha\beta}(p'_1 - Q) u_{s_1}(p_1) \\ &+ (1 \leftrightarrow 2) \end{aligned} \quad (5.40)$$

where the $\pi N \Delta$ coupling constant is $f^* = 2.13f$. The $\gamma N \Delta$ vertices are

$$\Gamma^{\beta\mu}(Q) = \Gamma_V^{\beta\mu}(Q) + \Gamma_A^{\beta\mu}(Q), \quad (5.41)$$

$$\Gamma_V^{\beta\mu}(Q) = \frac{C_3^V}{m_N} (g^{\beta\mu} Q - Q^\beta \gamma^\mu) \gamma_5 \quad (5.42)$$

$$\Gamma_A^{\beta\mu}(Q) = C_5^A g^{\beta\mu}. \quad (5.43)$$

$$\hat{\Gamma}^{\beta\mu}(Q) = \hat{\Gamma}_V^{\beta\mu}(Q) + \hat{\Gamma}_A^{\beta\mu}(Q), \quad (5.44)$$

$$\hat{\Gamma}_V^{\beta\mu}(Q) = -\Gamma_V^{\mu\beta}(Q), \quad \hat{\Gamma}_A^{\beta\mu}(Q) = \Gamma_A^{\beta\mu}(Q). \quad (5.45)$$

The vector and axial form factors are taken from [165]:

$$C_3^V(Q^2) = \frac{2.13}{(1 - \frac{Q^2}{M_V^2})^2} \frac{1}{1 - \frac{Q^2}{4M_V^2}}, \quad (5.46)$$

$$C_5^A(Q^2) = \frac{1.2}{(1 - \frac{Q^2}{M_{A\Delta}^2})^2} \frac{1}{1 - \frac{Q^2}{4M_{A\Delta}^2}}, \quad (5.47)$$

with $M_V = 0.84$ GeV and $M_{A\Delta} = 1.05$ GeV. The $\pi N \Delta$ form factor is taken as [162, 163]

$$F_{\pi NN}(k^2) = F_{\pi N\Delta}(k^2) \quad (5.48)$$

The forward Δ current corresponds to processes where the Δ resonance is produced and then decays back to a nucleon, while the backward Δ current involves the exchange of a pion, leading to the creation of a Δ resonance in the intermediate state. The charge dependence of these processes is embedded in the isospin operators $U_F(1, 2)_\pm = U_F(1, 2)_x \pm iU_F(1, 2)_y$ for the forward term and $U_B(1, 2)_\pm = U_B(1, 2)_x \pm iU_B(1, 2)_y$ for the backward term, where

$$U_F(1, 2)_i = \sqrt{\frac{3}{2}} \sum_{j=1}^3 T_j^{(1)} T_i^{(1)\dagger} \tau_j^{(2)}, \quad (5.49)$$

$$U_B(1, 2)_i = \sqrt{\frac{3}{2}} \sum_{j=1}^3 T_i^{(1)} T_j^{(1)\dagger} \tau_j^{(2)}. \quad (5.50)$$

The operator T_i^\dagger is the isospin raising operator that connects isospin-1/2 states to isospin-3/2 states and satisfies the condition $T_i T_j^\dagger = \frac{2}{3} \delta_{ij} - \frac{i}{3} \epsilon_{ijk} \tau_k$. Using this property it can be written

$$U_F(1, 2)_\pm = \frac{2}{\sqrt{6}} \tau_\pm^{(2)} - \frac{i}{\sqrt{6}} [\boldsymbol{\tau}^{(1)} \times \boldsymbol{\tau}^{(2)}]_\pm \quad (5.51)$$

$$U_B(1, 2)_\pm = \frac{2}{\sqrt{6}} \tau_\pm^{(2)} + \frac{i}{\sqrt{6}} [\boldsymbol{\tau}^{(1)} \times \boldsymbol{\tau}^{(2)}]_\pm. \quad (5.52)$$

Finally, the Δ propagator is as in chapter 3

$$G_{\alpha\beta}(P) = \frac{\mathcal{P}_{\alpha\beta}(P)}{P^2 - m_\Delta^2 + im_\Delta\Gamma(P^2) + \frac{\Gamma(P^2)^2}{4}} \quad (5.53)$$

where m_Δ and Γ are the Δ mass and width respectively. The projector $\mathcal{P}_{\alpha\beta}(P)$ over spin-3/2 is

$$\begin{aligned} \mathcal{P}_{\alpha\beta}(P) &= -(P + M_\Delta) \\ &\times \left[g_{\alpha\beta} - \frac{\gamma_\alpha \gamma_\beta}{3} - \frac{2P_\alpha P_\beta}{3m_\Delta^2} + \frac{P_\alpha \gamma_\beta - P_\beta \gamma_\alpha}{3m_\Delta} \right]. \end{aligned} \quad (5.54)$$

The vector part of the weak meson-exchange currents reduces to the electromagnetic MEC of chapter 3 when the isospin-raising operators are replaced by their third components [158]. The isospin sums over t_k that appear in the two-body current are provided in Appendix G. The resulting effective one-body current consist of a direct term minus an exchange term,

$$j_{2b}^\mu(\mathbf{p}, \mathbf{h}) = j_{2b}^\mu(\mathbf{p}, \mathbf{h})_{dir} - j_{2b}^\mu(\mathbf{p}, \mathbf{h})_{exch} \quad (5.55)$$

The exchange contribution corresponds to the diagrams shown in Fig. 5.2. In symmetric nuclear matter, the direct term of the vector current vanishes, similarly to the case of the

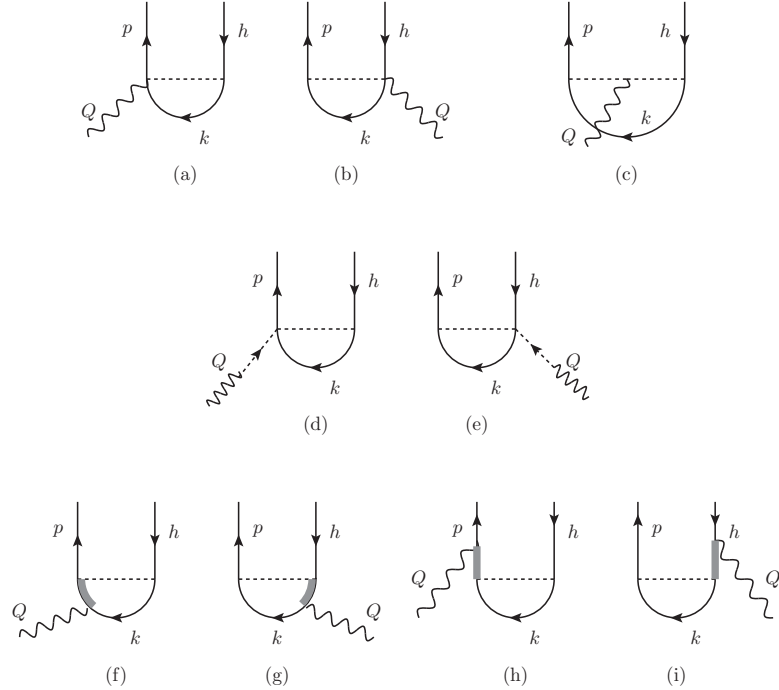


Figure 5.2: Diagrams for the 1p1h MEC matrix elements

electromagnetic exchange current, because it arises solely from the Δ current, which is transverse, and therefore vanishes upon contraction with Q^μ . When summing over spin in the direct matrix element, this contraction appears explicitly, leading to a vanishing contribution. However, for the axial Δ current, the direct term does not vanish, and in principle should be included when computing the neutrino response. Nevertheless, we have checked that this term contributes significantly only to the longitudinal response R_{LL} , which is known to be small. This behavior can be seen explicitly in the non-relativistic limit, where the structure of the current becomes more transparent. In the results section we show through explicit calculations that the LL response gives a negligible contribution to the cross section for quasielastic neutrino scattering. Since the direct axial MEC term contributes significantly only to the LL channel, and this channel plays a minor role in the kinematics of interest, it is not included in the present work.

5.3. Non-relativistic interference T-response

In this section we present the expressions for the interference responses in the NR limit, which will be compared with the corresponding relativistic results in the results section. This comparison serves several purposes: (i) to verify that relativistic and non-relativistic results agree at low momentum and energy transfer, as expected; (ii) to compare our results with known expressions for axial MEC currents in the NR literature [38]; and (iii) to test the accuracy of our numerical implementation, since the NR Fermi gas allows partial analytical

evaluation of the response functions [32, 174]. Furthermore, this limit helps identify the dominant responses and current components at moderate momentum transfer.

5.3.1. Non-relativistic weak CC one-body current

The vector part of the 1b current is the sum of magnetization and convection currents:

$$\mathbf{j}_{1b}(\mathbf{p}, \mathbf{h})_V = \mathbf{j}_{mV}(\mathbf{p}, \mathbf{h}) + \mathbf{j}_{cV}(\mathbf{p}, \mathbf{h}), \quad (5.56)$$

$$\mathbf{j}_{mV}(\mathbf{p}, \mathbf{h}) = -\frac{2G_M^V}{2m_N} i\mathbf{q} \times \boldsymbol{\sigma}_{s_p s_h}, \quad (5.57)$$

$$\mathbf{j}_{cV}(\mathbf{p}, \mathbf{h}) = \delta_{s_p s_h} \frac{2G_E^V}{m_N} \left(\mathbf{h} + \frac{\mathbf{q}}{2} \right). \quad (5.58)$$

with $\mathbf{q} = \mathbf{p} - \mathbf{h}$ by momentum conservation. Here G_M^V (G_E^V) is the isovector magnetic (electric) form factor of the nucleon. $G_E^V = (G_E^p - G_E^n)/2$.

The transverse one-body axial current at leading order is [25]

$$\mathbf{j}_{1b}^\perp(\mathbf{p}, \mathbf{h})_A = -G_A \boldsymbol{\sigma}_{s_p s_h}^\perp. \quad (5.59)$$

The time component of the axial current, j_{1b}^0 , or axial charge-density is typically not included in non-relativistic calculations because it is small at leading order; however, this suppression is not a strict consequence of the NR expansion itself. To obtain its static limit, we have considered the semi-relativistic expansion of the electroweak current introduced in Ref. [180, 25]. It can be written as the sum of a convective term and a magnetization term, in analogy with the structure of the transverse vector current [25]

$$j_{1b}^0(\mathbf{p}, \mathbf{h})_A = j_{mA}^0(\mathbf{p}, \mathbf{h}) + j_{cA}^0(\mathbf{p}, \mathbf{h}) \quad (5.60)$$

$$j_{mA}^0(\mathbf{p}, \mathbf{h}) = -\frac{G'_A}{2m_N} \mathbf{q} \cdot \boldsymbol{\sigma}_{s_p s_h} \quad (5.61)$$

$$j_{cA}^0(\mathbf{p}, \mathbf{h}) = -G_A \frac{\mathbf{h}^\perp}{m_N} \cdot \boldsymbol{\sigma}_{s_p s_h} \quad (5.62)$$

where \mathbf{h}^\perp is the transverse component of \mathbf{h} , perpendicular to the momentum transfer. The auxiliary form factor G'_A is given by

$$G'_A = G_A - \tau G_P = \left(1 - \frac{Q^2}{Q^2 - m_\pi^2} \right) G_A. \quad (5.63)$$

5.3.2. Non-relativistic weak MEC

The weak MEC operators are the sum of vector plus axial components. The vector MEC are also isovectors and closely related to the electromagnetic MEC, which are also isovectors. The key difference lies in the isospin structure: while the electromagnetic current corresponds to the third component of the isospin operator, the charged weak

current involves the raising and lowering \pm operators. Consequently, the NR expressions for electromagnetic MEC derived in chapter 4 can be directly adapted to the weak case by substituting $\tau_z \rightarrow \tau_{\pm}$, and $[\boldsymbol{\tau}^{(1)} \times \boldsymbol{\tau}^{(2)}]_z \rightarrow [\boldsymbol{\tau}^{(1)} \times \boldsymbol{\tau}^{(2)}]_{\pm}$, depending on the specific charge-changing process.

The NR expansion of the MEC is obtained by applying again standard reduction rules of chapter 4 to matrix elements involving products of gamma matrices between Dirac spinors, retaining only leading-order terms in $1/m_N$, summarized here as:

$$\gamma^0 \rightarrow 1, \quad \gamma^i \rightarrow 0, \quad \gamma_5 \gamma^0 \rightarrow 0, \quad (5.64)$$

$$\gamma_5 \gamma^i \rightarrow -\sigma_i, \quad \gamma^i \gamma^j \rightarrow -\sigma_i \sigma_j, \quad \gamma^0 \gamma^j \rightarrow 0. \quad (5.65)$$

For a nucleon momentum $p^\mu \rightarrow (m_N, p^i)$ and $\not{p} \rightarrow p_0$. For the momentum transfer to nucleon i , $k^\mu \rightarrow (0, k^i)$ and $\gamma_5 \not{k} \rightarrow \mathbf{k} \cdot \boldsymbol{\sigma}$. As a starting point, we recall the NR form of the V -function, that was already derived in chapter 4,

$$V_{s'_1 s_1}(p'_1, p_1) \rightarrow -\frac{\mathbf{k}_1 \cdot \boldsymbol{\sigma}^{(1)}}{\mathbf{k}_1^2 + m_\pi^2}. \quad (5.66)$$

The NR vector MEC are identical to the electromagnetic ones, except for the isospin operators. As a result, only the spatial components of the vector MEC survive at leading order in the non-relativistic expansion. This feature is also confirmed with the fully relativistic calculation. Then

$$\begin{aligned} j_{sV}^\mu &\xrightarrow{\text{nr}} (0, \mathbf{j}_{sV}) \\ j_{\pi V}^\mu &\xrightarrow{\text{nr}} (0, \mathbf{j}_{\pi V}) \\ j_{\Delta V}^\mu &\xrightarrow{\text{nr}} (0, \mathbf{j}_{\Delta V}) \end{aligned}$$

The axial seagull current is proportional to the matrix element of γ^μ , and in the non-relativistic limit, only its time component (proportional to γ^0) survives. On the other hand, only the spatial components of the axial Δ current remain non-zero, as shown in Appendix H. The pion-pole current, being proportional to $q_\mu \gamma^\mu$, vanishes at leading order. The surviving axial currents are

$$\begin{aligned} j_{sA}^\mu &\xrightarrow{\text{nr}} (j_{sA}^0, \vec{0}) \\ j_{\Delta A}^\mu &\xrightarrow{\text{nr}} (0, \mathbf{j}_{\Delta A}) \end{aligned}$$

The corresponding NR operators are

$$\mathbf{j}_{sV}(p'_1, p'_2, p_1, p_2) = i[\boldsymbol{\tau}^{(1)} \times \boldsymbol{\tau}^{(2)}]_+ \frac{f^2}{m_\pi^2} F_1^V \left(\frac{\mathbf{k}_1 \cdot \boldsymbol{\sigma}^{(1)}}{\mathbf{k}_1^2 + m_\pi^2} \boldsymbol{\sigma}^{(2)} - \frac{\mathbf{k}_2 \cdot \boldsymbol{\sigma}^{(2)}}{\mathbf{k}_2^2 + m_\pi^2} \boldsymbol{\sigma}^{(1)} \right). \quad (5.67)$$

$$\mathbf{j}_{\pi V}(p'_1, p'_2, p_1, p_2) = i[\boldsymbol{\tau}^{(1)} \times \boldsymbol{\tau}^{(2)}]_+ \frac{f^2}{m_\pi^2} F_1^V \frac{\mathbf{k}_1 \cdot \boldsymbol{\sigma}^{(1)}}{\mathbf{k}_1^2 + m_\pi^2} \frac{\mathbf{k}_2 \cdot \boldsymbol{\sigma}^{(2)}}{\mathbf{k}_2^2 + m_\pi^2} (\mathbf{k}_1 - \mathbf{k}_2). \quad (5.68)$$

$$\begin{aligned} \mathbf{j}_{\Delta V}(p'_1, p'_2, p_1, p_2) = & iC_\Delta^V \left\{ \frac{\mathbf{k}_2 \cdot \boldsymbol{\sigma}^{(2)}}{\mathbf{k}_2^2 + m_\pi^2} \left[4\tau_+^{(2)} \mathbf{k}_2 + [\boldsymbol{\tau}^{(1)} \times \boldsymbol{\tau}^{(2)}]_+ \mathbf{k}_2 \times \boldsymbol{\sigma}^{(1)} \right] \right. \\ & \left. + \frac{\mathbf{k}_1 \cdot \boldsymbol{\sigma}^{(1)}}{\mathbf{k}_1^2 + m_\pi^2} \left[4\tau_+^{(1)} \mathbf{k}_1 - [\boldsymbol{\tau}^{(1)} \times \boldsymbol{\tau}^{(2)}]_+ \mathbf{k}_1 \times \boldsymbol{\sigma}^{(2)} \right] \right\} \times \mathbf{q}. \end{aligned} \quad (5.69)$$

$$\mathbf{j}_{sA}^0(p'_1, p'_2, p_1, p_2) = -i[\boldsymbol{\tau}^{(1)} \times \boldsymbol{\tau}^{(2)}]_+ \frac{f^2}{m_\pi^2} \frac{1}{g_A} \left[\frac{\mathbf{k}_1 \cdot \boldsymbol{\sigma}^{(1)}}{\mathbf{k}_1^2 + m_\pi^2} - \frac{\mathbf{k}_2 \cdot \boldsymbol{\sigma}^{(2)}}{\mathbf{k}_2^2 + m_\pi^2} \right] \quad (5.70)$$

$$\begin{aligned} \mathbf{j}_{\Delta A}(p'_1, p'_2, p_1, p_2) = & -C_\Delta^A \left\{ 4\tau_+^{(1)} \frac{(\mathbf{k}_1 \cdot \boldsymbol{\sigma}^{(1)}) \mathbf{k}_1}{\mathbf{k}_1^2 + m_\pi^2} + 4\tau_+^{(2)} \frac{(\mathbf{k}_2 \cdot \boldsymbol{\sigma}^{(2)}) \mathbf{k}_2}{\mathbf{k}_2^2 + m_\pi^2} \right. \\ & \left. + [\boldsymbol{\tau}^{(1)} \times \boldsymbol{\tau}^{(2)}]_+ \left[\frac{(\mathbf{k}_2 \cdot \boldsymbol{\sigma}^{(2)}) (\mathbf{k}_2 \times \boldsymbol{\sigma}^{(1)})}{\mathbf{k}_2^2 + m_\pi^2} - \frac{(\mathbf{k}_1 \cdot \boldsymbol{\sigma}^{(1)}) (\mathbf{k}_1 \times \boldsymbol{\sigma}^{(2)})}{\mathbf{k}_1^2 + m_\pi^2} \right] \right\} \end{aligned} \quad (5.71)$$

with

$$C_\Delta^V = \sqrt{\frac{3}{2}} \frac{2}{9} \frac{ff^*}{m_\pi^2} \frac{C_3^V}{m_N} \frac{1}{m_\Delta - m_N} \quad (5.72)$$

$$C_\Delta^A = \sqrt{\frac{3}{2}} \frac{2}{9} \frac{ff^*}{m_\pi^2} C_5^A \frac{1}{m_\Delta - m_N} \quad (5.73)$$

These operators match the standard NR MEC in the literature [38] modulo differences in coupling constants and form factors.

5.3.3. Effective one-body MEC

The 1p1h matrix elements of the vector and axial MEC are

$$j_{2b}^\mu(p, h) = - \int \frac{d^3 k}{(2\pi)^3} \sum_{t_k s_k} j_{2b}^\mu(p, k, k, h) = j_s^\mu(p, h) + j_\pi^\mu(p, h) + j_\Delta^\mu(p, h), \quad (5.74)$$

where we have neglected the direct part in the axial Δ current, as previously mentioned. The results are the following for the three MEC, seagull, pionic and Δ currents

$$\mathbf{j}_{sV}(p, h) = 4 \frac{f^2}{m_\pi^2} F_1^V \int \frac{d^3 k}{(2\pi)^3} \left(\frac{\delta_{s_p s_h} \mathbf{k}_1 + i \boldsymbol{\sigma}_{ph} \times \mathbf{k}_1}{\mathbf{k}_1^2 + m_\pi^2} - \frac{\delta_{s_p s_h} \mathbf{k}_2 + i \mathbf{k}_2 \times \boldsymbol{\sigma}_{ph}}{\mathbf{k}_2^2 + m_\pi^2} \right) \quad (5.75)$$

$$\mathbf{j}_{\pi V}(p, h) = 4 \frac{f^2}{m_\pi^2} F_1^V \int \frac{d^3 k}{(2\pi)^3} \frac{\delta_{s_p s_h} \mathbf{k}_1 \cdot \mathbf{k}_2 + i (\mathbf{k}_1 \times \mathbf{k}_2) \cdot \boldsymbol{\sigma}_{ph}}{(\mathbf{k}_1^2 + m_\pi^2)(\mathbf{k}_2^2 + m_\pi^2)} (\mathbf{k}_1 - \mathbf{k}_2), \quad (5.76)$$

$$\begin{aligned} \mathbf{j}_{\Delta V}(p, h) = & \sqrt{\frac{3}{2}} \frac{8 f f^*}{9} \frac{i C_3^V}{m_\Delta^2 - m_N^2} \frac{\mathbf{q}}{m_\Delta - m_N} \\ & \times \int \frac{d^3 k}{(2\pi)^3} \left(\frac{\mathbf{k}_1^2 \boldsymbol{\sigma}_{ph} + (\boldsymbol{\sigma}_{ph} \cdot \mathbf{k}_1) \mathbf{k}_1}{\mathbf{k}_1^2 + m_\pi^2} + \frac{\mathbf{k}_2^2 \boldsymbol{\sigma}_{ph} + (\boldsymbol{\sigma}_{ph} \cdot \mathbf{k}_2) \mathbf{k}_2}{\mathbf{k}_2^2 + m_\pi^2} \right), \end{aligned} \quad (5.77)$$

$$j_{sA}^0(p, h) = -4 \frac{f^2}{m_\pi^2} \frac{1}{g_A} \int \frac{d^3 k}{(2\pi)^3} \left[\frac{\mathbf{k}_1 \cdot \boldsymbol{\sigma}_{ph}}{\mathbf{k}_1^2 + m_\pi^2} - \frac{\mathbf{k}_2 \cdot \boldsymbol{\sigma}_{ph}}{\mathbf{k}_2^2 + m_\pi^2} \right] \quad (5.78)$$

$$\begin{aligned} \mathbf{j}_{\Delta A}(p, h) = & \sqrt{\frac{3}{2}} \frac{8 f f^*}{9} \frac{C_5^A}{m_\Delta^2 - m_N^2} \\ & \times \int \frac{d^3 k}{(2\pi)^3} \left(\frac{\mathbf{k}_1^2 \boldsymbol{\sigma}_{ph} + (\boldsymbol{\sigma}_{ph} \cdot \mathbf{k}_1) \mathbf{k}_1}{\mathbf{k}_1^2 + m_\pi^2} + \frac{\mathbf{k}_2^2 \boldsymbol{\sigma}_{ph} + (\boldsymbol{\sigma}_{ph} \cdot \mathbf{k}_2) \mathbf{k}_2}{\mathbf{k}_2^2 + m_\pi^2} \right), \end{aligned} \quad (5.79)$$

with $\mathbf{k}_1 = \mathbf{p} - \mathbf{k}$ and $\mathbf{k}_2 = \mathbf{k} - \mathbf{h}$.

5.3.4. Non relativistic 1b2b interference single-nucleon responses

Here we provide separate expressions for the different contributions to the interference terms, which arise from the cross products between the various components of the one-body current and the meson exchange currents.

$$w_{CC,1b2b}^{AA} = w_{CC,ms}^{AA} + w_{CC,cs}^{AA} \quad (5.80)$$

$$w_{CC,ms}^{AA} = \text{Re} \sum_{s_p s_h} j_{mA}^0(p, h)^* j_{sA}^0(p, h) \quad (5.81)$$

$$w_{CC,cs}^{AA} = \text{Re} \sum_{s_p s_h} j_{cA}^0(p, h)^* j_{sA}^0(p, h) \quad (5.82)$$

$$w_{T,1b2b}^{VV} = w_{T,ms}^{VV} + w_{T,cs}^{VV} + w_{T,m\pi}^{VV} + w_{T,c\pi}^{VV} + w_{T,m\Delta}^{VV} \quad (5.83)$$

$$w_{T,ms}^{VV} = \operatorname{Re} \sum_{s_p s_h} \mathbf{j}_{mV}(p, h)^* \cdot \mathbf{j}_{sV}(p, h) \quad (5.84)$$

$$w_{T,cs}^{VV} = \operatorname{Re} \sum_{s_p s_h} \mathbf{j}_{cV}^T(p, h)^* \cdot \mathbf{j}_{sV}(p, h) \quad (5.85)$$

$$w_{T,m\pi}^{VV} = \operatorname{Re} \sum_{s_p s_h} \mathbf{j}_{mV}(p, h)^* \cdot \mathbf{j}_\pi(p, h) \quad (5.86)$$

$$w_{T,c\pi}^{VV} = \operatorname{Re} \sum_{s_p s_h} \mathbf{j}_{cV}^T(p, h)^* \cdot \mathbf{j}_\pi(p, h) \quad (5.87)$$

$$w_{T,m\Delta}^{VV} = \operatorname{Re} \sum_{s_p s_h} \mathbf{j}_{mV}(p, h)^* \cdot \mathbf{j}_{\Delta V}(p, h) \quad (5.88)$$

$$w_{T,1b2b}^{AA} = w_{T,1b\Delta}^{AA} = \operatorname{Re} \sum_{s_p s_h} \mathbf{j}_{1bA}^\perp(p, h)^* \cdot \mathbf{j}_{\Delta A}(p, h) \quad (5.89)$$

In the case of the T' response we separate the VA and AV contributions

$$w_{T',1b2b} = w_{T',1b2b}^{VA} + w_{T',1b2b}^{AV} \quad (5.90)$$

$$w_{T',1b2b}^{VA} = \frac{1}{2} \operatorname{Im} \sum_{s_p s_h} \left[j_{1bV}^{1*}(p, h) j_{2bA}^2(p, h) + j_{2bA}^{1*}(p, h) j_{1bV}^2(p, h) \right] \quad (5.91)$$

$$w_{T',1b2b}^{AV} = \frac{1}{2} \operatorname{Im} \sum_{s_p s_h} \left[j_{1bA}^{1*}(p, h) j_{2bV}^2(p, h) + j_{2bV}^{1*}(p, h) j_{1bA}^2(p, h) \right] \quad (5.92)$$

Then

$$w_{T',1b2b}^{VA} = w_{T',m\Delta}^{VA} \quad (5.93)$$

$$w_{T',1b2b}^{AV} = w_{T',1bs}^{AV} + w_{T',1b\pi}^{AV} + w_{T',1b\Delta}^{AV} \quad (5.94)$$

Note that in the case of the Δ current, both the vector and axial parts contribute to the response T' , whereas in the case of the seagull and pionic current, only the vector part is considered, since the axial part is longitudinal in the NR limit.

The explicit expressions for the different contributions to the single nucleon interference responses are the following (with $\mathbf{k}_1 = \mathbf{p} - \mathbf{k}$ and $\mathbf{k}_2 = \mathbf{k} - \mathbf{h}$):

$$w_{T,ms}^{VV} = 2 \frac{f^2}{m_\pi^2} F_1^V \frac{G_M^V}{m_N} \int \frac{d^3 k}{(2\pi)^3} \left(\frac{4\mathbf{q} \cdot \mathbf{k}_1}{\mathbf{k}_1^2 + m_\pi^2} + \frac{4\mathbf{q} \cdot \mathbf{k}_2}{\mathbf{k}_2^2 + m_\pi^2} \right) \quad (5.95)$$

$$w_{T,cs}^{VV} = 4 \frac{f^2}{m_\pi^2} F_1^V \frac{G_E^V}{m_N} \int \frac{d^3 k}{(2\pi)^3} \left(\frac{2\mathbf{h}_T \cdot \mathbf{k}_1}{\mathbf{k}_1^2 + m_\pi^2} - \frac{2\mathbf{h}_T \cdot \mathbf{k}_2}{\mathbf{k}_2^2 + m_\pi^2} \right) \quad (5.96)$$

$$w_{T,m\pi}^{VV} = -2 \frac{f^2}{m_\pi^2} F_1^V \frac{G_M^V}{m_N} \int \frac{d^3 k}{(2\pi)^3} \frac{4(\mathbf{q} \times \mathbf{k}_2)^2}{(\mathbf{k}_1^2 + m_\pi^2)(\mathbf{k}_2^2 + m_\pi^2)} \quad (5.97)$$

$$w_{T,c\pi}^{VV} = -4 \frac{f^2}{m_\pi^2} F_1^V \frac{G_E^V}{m_N} \int \frac{d^3 k}{(2\pi)^3} \frac{4(\mathbf{q} \cdot \mathbf{k}_2 - \mathbf{k}_2^2) \mathbf{h}_T \cdot \mathbf{k}_2}{(\mathbf{k}_1^2 + m_\pi^2)(\mathbf{k}_2^2 + m_\pi^2)} \quad (5.98)$$

$$w_{T,m\Delta}^{VV} = -2 \sqrt{\frac{3}{2}} \frac{2 f f^* C_3^V}{9 m_\pi^2 m_N m_\Delta - m_N m_N} \frac{G_M^V}{m_\Delta - m_N} \times \int \frac{d^3 k}{(2\pi)^3} 2 \left(\frac{3q^2 k_1^2 - (\mathbf{q} \cdot \mathbf{k}_1)^2}{\mathbf{k}_1^2 + m_\pi^2} + \frac{3q^2 k_2^2 - (\mathbf{q} \cdot \mathbf{k}_2)^2}{\mathbf{k}_2^2 + m_\pi^2} \right) \quad (5.99)$$

$$w_{CC,ms}^{AA} = \frac{f^2}{m_\pi^2} \frac{1}{g_A} \frac{G'_A}{m_N} \int \frac{d^3k}{(2\pi)^3} \left(\frac{4\mathbf{q} \cdot \mathbf{k}_1}{\mathbf{k}_1^2 + m_\pi^2} + \frac{4\mathbf{q} \cdot \mathbf{k}_2}{\mathbf{k}_2^2 + m_\pi^2} \right) \quad (5.100)$$

$$w_{CC,cs}^{AA} = 4 \frac{f^2}{m_\pi^2} \frac{1}{g_A} \frac{(G_A - \xi G'_A)}{m_N} \int \frac{d^3k}{(2\pi)^3} \left(\frac{2\mathbf{h}_T \cdot \mathbf{k}_1}{\mathbf{k}_1^2 + m_\pi^2} - \frac{2\mathbf{h}_T \cdot \mathbf{k}_2}{\mathbf{k}_2^2 + m_\pi^2} \right) \quad (5.101)$$

$$\begin{aligned} w_{T,1b\Delta}^{AA} = & -\sqrt{\frac{3}{2}} \frac{16}{9} \frac{ff^*}{m_\pi^2} \frac{1}{m_\Delta - m_N} \frac{C_5^A G_A}{q^2} \\ & \times \int \frac{d^3k}{(2\pi)^3} 2 \left(\frac{3q^2 k_1^2 - (\mathbf{q} \cdot \mathbf{k}_1)^2}{\mathbf{k}_1^2 + m_\pi^2} + \frac{3q^2 k_2^2 - (\mathbf{q} \cdot \mathbf{k}_2)^2}{\mathbf{k}_2^2 + m_\pi^2} \right) \end{aligned} \quad (5.102)$$

$$w_{T',1bs}^{AV} = 2 \frac{f^2}{m_\pi^2} \frac{G_A F_1^V}{q} \int \frac{d^3k}{(2\pi)^3} \left(\frac{4\mathbf{q} \cdot \mathbf{k}_1}{\mathbf{k}_1^2 + m_\pi^2} + \frac{4\mathbf{q} \cdot \mathbf{k}_2}{\mathbf{k}_2^2 + m_\pi^2} \right) \quad (5.103)$$

$$w_{T',1b\pi}^{AV} = -4 \frac{f^2}{m_\pi^2} F_1^V \frac{G_A}{q} \int \frac{d^3k}{(2\pi)^3} \frac{4(\mathbf{q} \times \mathbf{k}_2)^2}{(\mathbf{k}_1^2 + m_\pi^2)(\mathbf{k}_2^2 + m_\pi^2)} \quad (5.104)$$

$$\begin{aligned} w_{T',1b\Delta}^{AV} = & -\sqrt{\frac{3}{2}} \frac{4}{9} \frac{ff^*}{m_\pi^2} \frac{G_A C_3^V}{m_N q} \frac{1}{m_\Delta - m_N} \\ & \times \int \frac{d^3k}{(2\pi)^3} 2 \left(\frac{3q^2 k_1^2 - (\mathbf{q} \cdot \mathbf{k}_1)^2}{\mathbf{k}_1^2 + m_\pi^2} + \frac{3q^2 k_2^2 - (\mathbf{q} \cdot \mathbf{k}_2)^2}{\mathbf{k}_2^2 + m_\pi^2} \right) \end{aligned} \quad (5.105)$$

$$\begin{aligned} w_{T',m\Delta}^{VA} = & -\sqrt{\frac{3}{2}} \frac{4}{9} \frac{ff^*}{m_\pi^2} \frac{G_M^V C_5^A}{m_N q} \frac{1}{m_\Delta - m_N} \\ & \times \int \frac{d^3k}{(2\pi)^3} 2 \left(\frac{3q^2 k_1^2 - (\mathbf{q} \cdot \mathbf{k}_1)^2}{\mathbf{k}_1^2 + m_\pi^2} + \frac{3q^2 k_2^2 - (\mathbf{q} \cdot \mathbf{k}_2)^2}{\mathbf{k}_2^2 + m_\pi^2} \right) \end{aligned} \quad (5.106)$$

5.4. Results

In this section, we present numerical results for the effect of two-body MEC on the CC neutrino response functions in the 1p1h channel. We consider three nuclear models: the RFG, the RMF in nuclear matter, and the Superscaling Approach with a Relativistic Effective Mass. These results allow us to assess the model dependence of the MEC contributions. We illustrate the impact of these effects on neutrino cross sections with selected examples. To this end, we will first examine in detail the interference terms between the one-body and two-body currents, which provide the dominant MEC contribution, and later compare them with the pure one-body responses.

We begin by analyzing the dominant response functions to leading order in the non-relativistic Fermi gas (NRFG), and comparing them with the fully relativistic results obtained within the RFG model. As previously discussed, this comparison serves as a consistency test of the calculation, since the NRFG and RFG models are implemented in different ways. In the non-relativistic case, we integrate the effective single-nucleon responses derived in the previous section. Following the method of Refs. [32, 174], the integrals over the momentum of the intermediate nucleon are performed analytically except for the pion-in-flight current, where they reduce to one-dimensional integrals. In addition, the spin traces

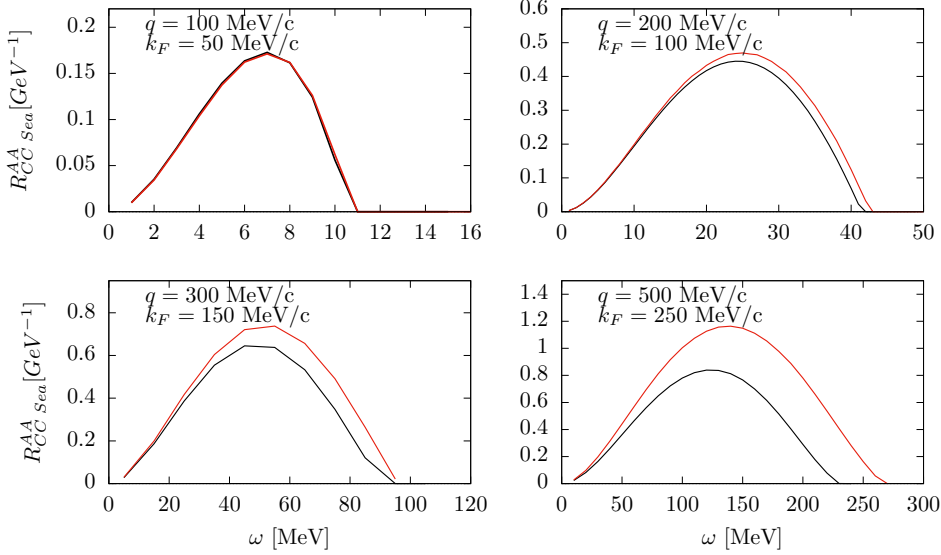


Figure 5.3: Interference response R_{CC}^{AA} between the one-body axial current and the seagull current, for increasing values of the momentum transfer q , with $k_F = q/2$. In each panel, the non-relativistic results (red lines) are compared with the relativistic ones (black lines).

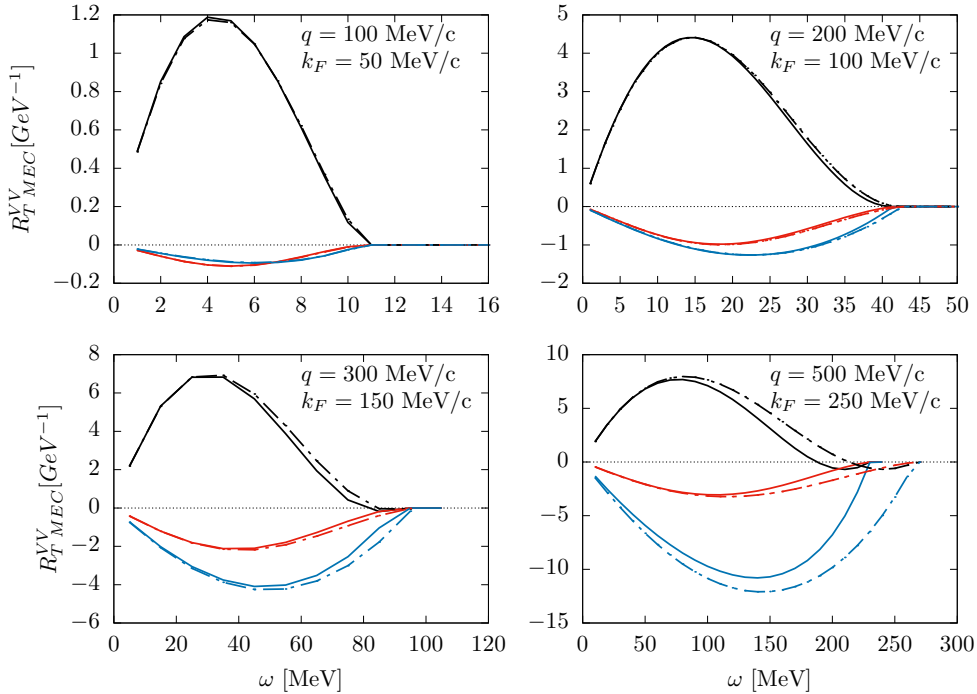


Figure 5.4: Non-relativistic (dot-dashed lines) versus relativistic (solid lines) transverse interference response $R_{T MEC}^{VV}$ between the 1b current and the seagull (black), pion-in-flight (red), and Δ -excitation (blue) two-body currents, for increasing values of q and with $k_F = q/2$.

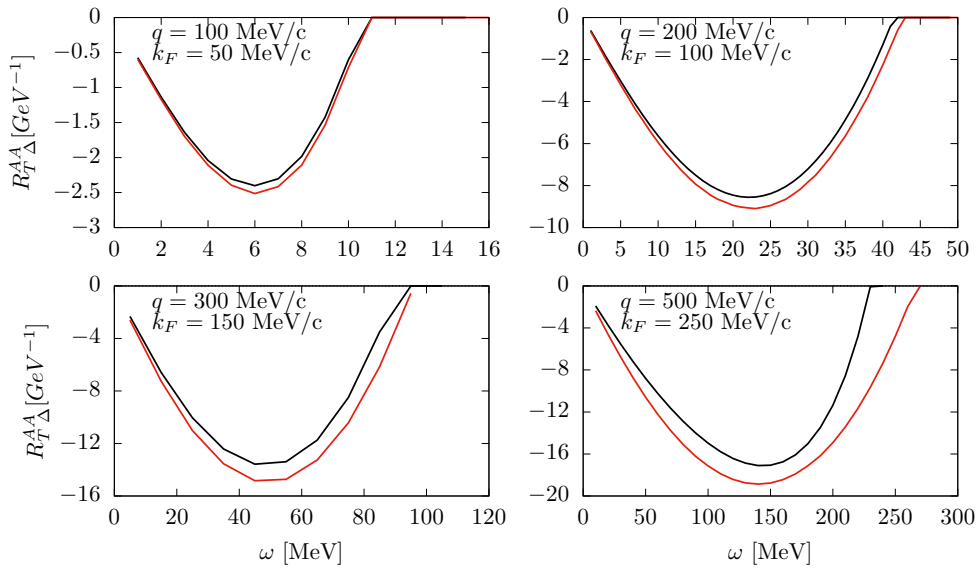


Figure 5.5: The same as Fig. 5.3 for the Interference response R_T^{AA} between the axial 1b and Δ currents

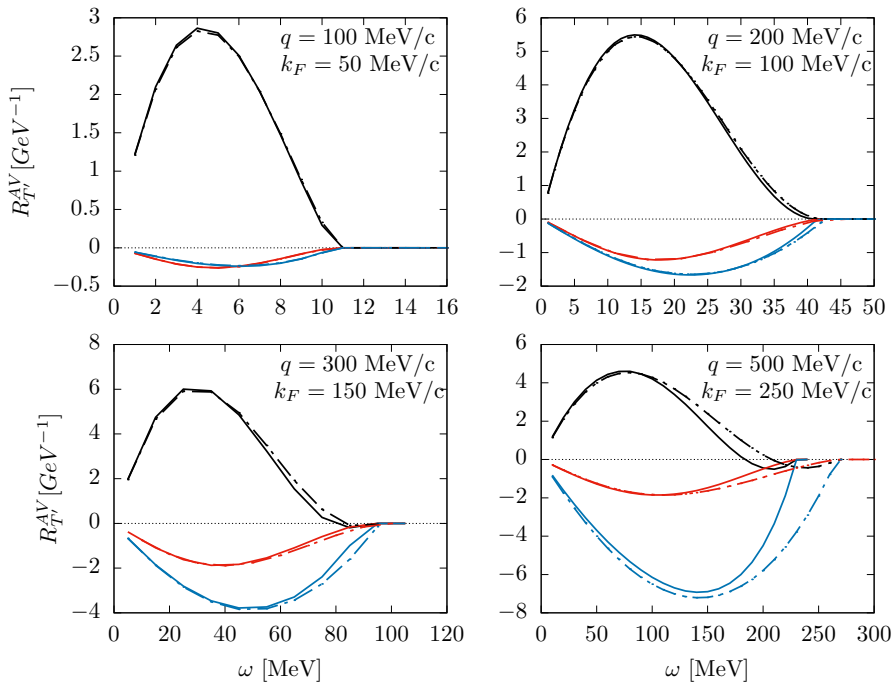


Figure 5.6: The same as fig. 5.4 for the interference response $R_{T'1b2b}^{AV}$ between the axial 1b current and the vector seagull (black), pionic (red) and Δ (blue) currents.

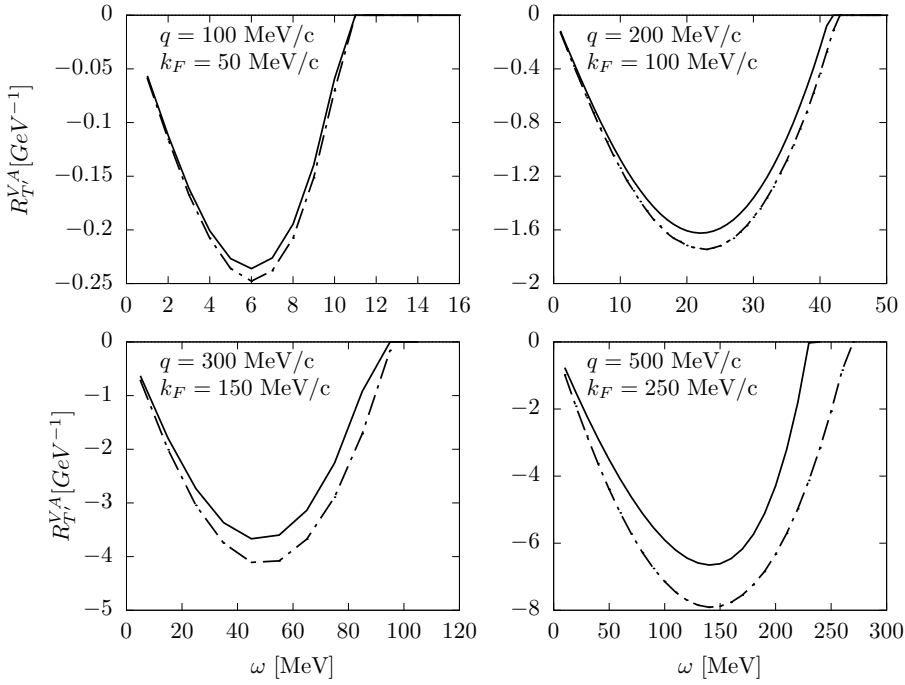


Figure 5.7: The same as fig. 5.3 for the $R_{T'1b\Delta}^{VA}$ interference response.

have been computed explicitly in the NR case. On the other hand, the RFG responses are evaluated fully numerically. As expected, the RFG results approach those of the NRFG in the low- q , low- ω region, as we explicitly demonstrate below.

In Fig. 5.3 we show the interference response $R_{CC,1b}^{AA}$, which corresponds to the interference between the axial one-body current and the axial seagull two-body current in the CC channel. This is the dominant MEC contribution to the CC responses at low momentum transfer. To examine how the relativistic response approaches the non-relativistic one as q becomes small, we present results for several values of the momentum transfer: $q = 100, 200, 300$, and $500 \text{ MeV}/c$. In each panel we set the Fermi momentum to $k_F = q/2$, so that the momenta of the initial nucleons are also small when q is small. This choice also minimizes the effects of Pauli blocking in the comparison. As expected, we observe that the relativistic and non-relativistic responses are nearly identical for $q = 100 \text{ MeV}/c$, and begin to differ progressively as q increases.

In Fig. 5.4 we show the interference contributions to the R_T^{VV} response, separating the effects of the seagull, pion-in-flight, and Δ currents. These vector-vector responses are exactly twice the corresponding electromagnetic responses, as proven in Appendix G. We observe that the seagull contribution is positive, while the pion-in-flight and Δ contributions are negative, leading to a partial cancellation. The Δ term increases with q more rapidly than the seagull term, and becomes the dominant contribution at $q = 500 \text{ MeV}/c$. This behavior is consistent with the electromagnetic response results.

In Fig. 5.5 we present the axial transverse interference response R_T^{AA} . At $q = 100 \text{ MeV}/c$, the relativistic and non-relativistic results are nearly identical, serving as a triple consistency check: first, of the non-relativistic reduction of the Δ current; second, of the numerical implementation of the RFG and NRFG frameworks; and third, of the analytic and

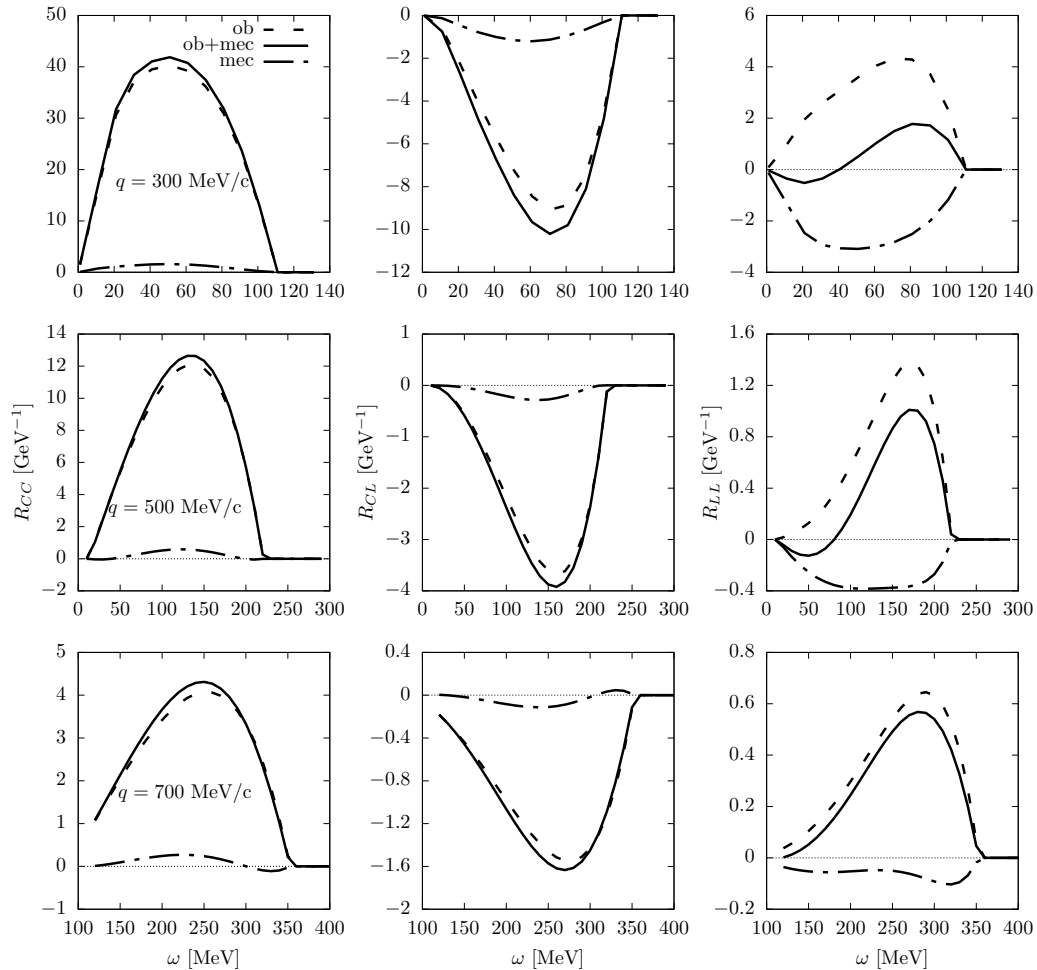


Figure 5.8: Response functions R_{CC} , R_{CL} , and R_{LL} computed in the RFG model for different values of q . We compare one-body responses with the interference MEC contribution and the total result (full lines).

numerical procedures used in each model. The response is negative and its absolute value increases with q , becoming slightly larger than the corresponding vector Δ contribution.

In Fig. 5.6 we show the interference responses $R_{T',1b-2b}^{AV}$ between the axial one-body current and the vector MEC, separating the contributions of the vector seagull, pionic, and Δ currents. These responses exhibit a behavior very similar to the corresponding $R_{T,1b-2b}^{VV}$ ones. In fact, by inspecting the expressions for the non-relativistic single-nucleon responses, one finds that $w_{T,m-2b}^{VV}$ (interference with magnetization current) and $w_{T',1b-2b}^{AV}$ involve exactly the same integrals over the intermediate nucleon momentum \mathbf{k} . The difference lies in the coupling factors between the axial current and the magnetization current. Since the convection current has little impact on the transverse responses, the resulting behavior is nearly identical in both cases.

Finally, in Fig. 5.7 we show the $R_{T',1b-\Delta}^{VA}$ interference response. Once again, we observe a close similarity between this response and both $R_{T',1b-\Delta}^{AV}$ and $R_{T,1b-\Delta}^{VV}$, for the same reasons discussed previously. This similarity originates from the fact that the structure of the Δ current and the magnetization current is nearly the same in the axial and vector sectors. The main difference lies in a vector product with \vec{q} , while the spin operator is identical in both cases, except for different coupling constants associated with the axial and vector currents. This can also be seen by inspecting the corresponding single-nucleon tensors, which involve the same integrals in all three cases.

The negative sign of the one-body- Δ interference responses can be clearly understood by inspecting the expressions of the single-nucleon response functions, Eqs. (5.99), (5.102), (5.105) and (5.106). All of them carry an overall minus sign and are proportional to the same integral, which is positive since the integrand contains terms of the form $3q^2k_1^2 - (\mathbf{q} \cdot \mathbf{k}_1)^2 > 0$. This result for the sign of the $1b-\Delta$ interference was already discussed in chapter 4 for the electromagnetic transverse response. Therefore here the low- q momentum theorem is extended to the vector-axial CC Δ responses. A similar argument applies to the $R_{T,m\pi}^{VV}$ and $R_{T',1b\pi}^{AV}$ responses, which are also negative. Although these sign arguments are strictly valid in the non-relativistic limit, numerical calculations show that they remain valid in the relativistic case, except at very large q , where sign changes can occur for high ω .

We now introduce the results obtained within the RFG model. In this section, we apply the formalism to the case of ^{12}C , using a Fermi momentum $k_F = 225$ MeV/c.

In Fig. 5.8 we show the longitudinal responses R_{CC} , R_{CL} , and R_{LL} , while in Fig. 5.9 we display the transverse responses R_T and $R_{T'}$. For each response, we present three curves: the pure one-body (1b) contribution, the full result including MEC (1b+2b), and the interference term between one-body and two-body currents.

It is observed that the effect of MEC in the R_{CC} response is negligible. In the R_{CL} response, MEC introduce a visible modification, and in the R_{LL} response they are of the same order of magnitude as the one-body part. Nevertheless, this will have little or no impact on neutrino cross sections, since R_{LL} is very small and the longitudinal responses in general contribute less significantly to the total cross section.

Figure 5.9 shows the transverse responses R_T and $R_{T'}$ in the relativistic Fermi gas model for ^{12}C . The results include the one-body (1b) contribution, the full result with

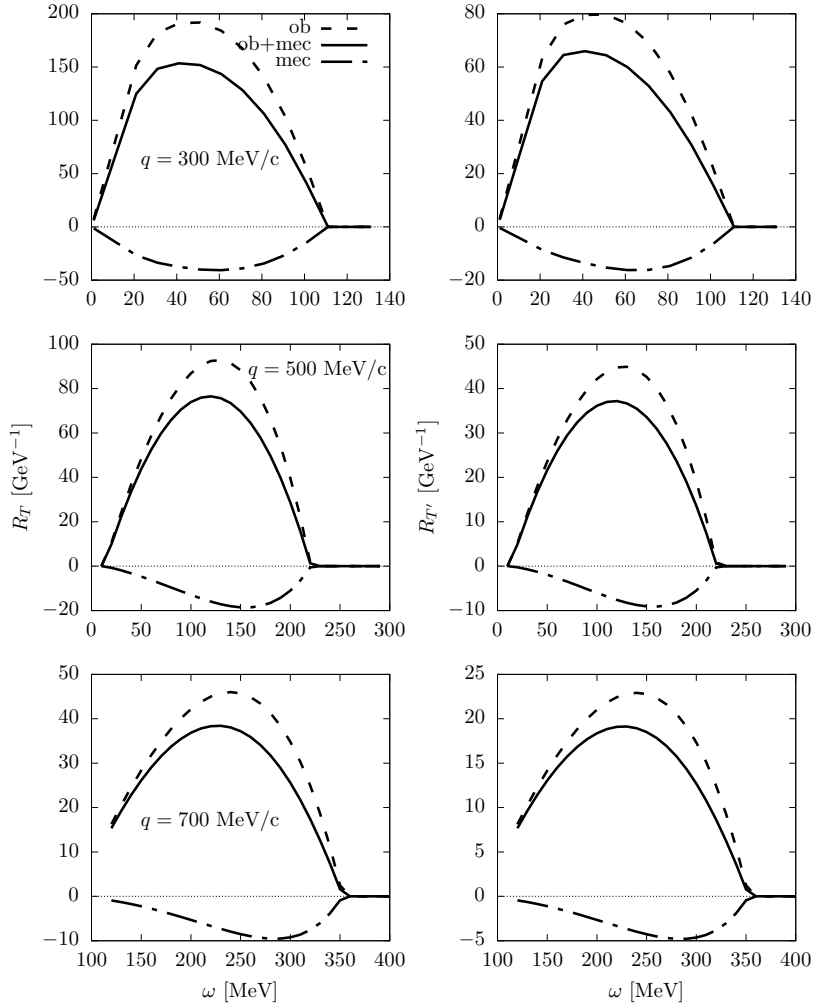


Figure 5.9: The same as in Fig. 5.8 for the transverse responses R_T and $R_{T'}$

meson exchange currents (1b+2b), and the interference term between 1b and 2b currents. The interference is negative and leads to a significant reduction of both responses. This reduction is also found in the vector transverse response R_T^{VV} , and its size is comparable to that observed in the axial R_T^{AA} and the axial-vector R_T^{VA} responses. This behavior is due to the interference with the Δ current, whose structure is similar in both the vector and axial channels and gives a dominant contribution in the relevant kinematics. As a result, the MEC-induced suppression of the transverse neutrino responses is of similar magnitude in all three cases, although slightly stronger in the axial-containing channels. To illustrate this point, in Fig. 5.10 we show separately the vector-vector (VV) and axial-axial (AA) contributions to the transverse response R_T . It can be seen that the reduction induced by MEC, relative to the one-body current, is similar in both channels. In both cases, the dominant effect is the interference between the one-body current and the Δ current, which leads to a negative contribution.

A more detailed scrutiny of the relevance of each MEC contribution to the different response functions is provided in Figs. 5.11 to 5.16 for $q = 300, 500, 700$ MeV/c, where

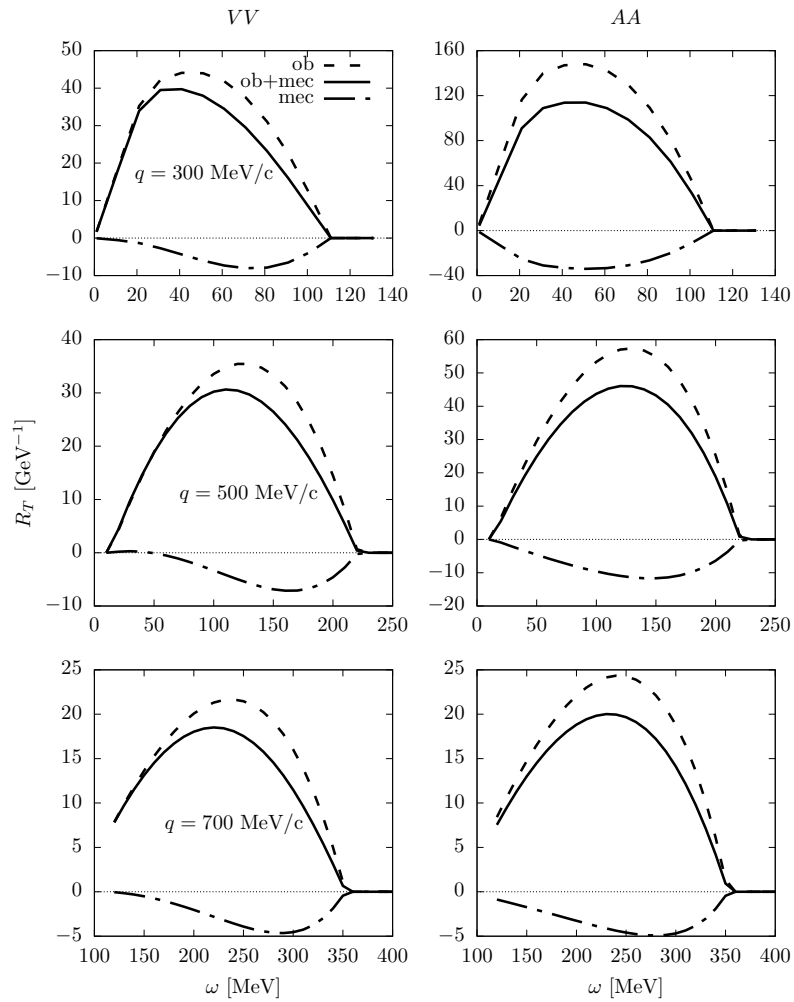


Figure 5.10: The same as Fig. 5.9 for the R_T^{VV} and R_T^{AA} response functions.

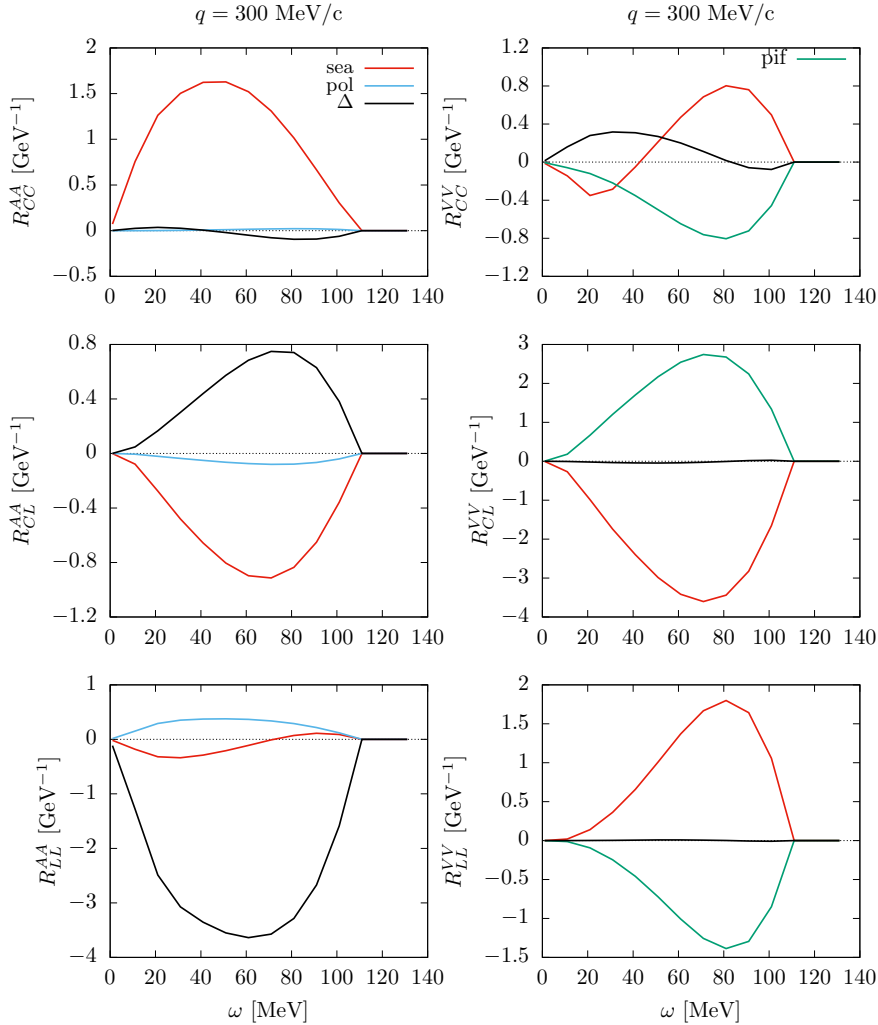


Figure 5.11: Interference longitudinal responses between the 1b current and the different MEC seagull (sea), pionic (pif), pion pole (pole) and Δ , separated in vector and axial contributions, for $q = 300$ MeV/c.

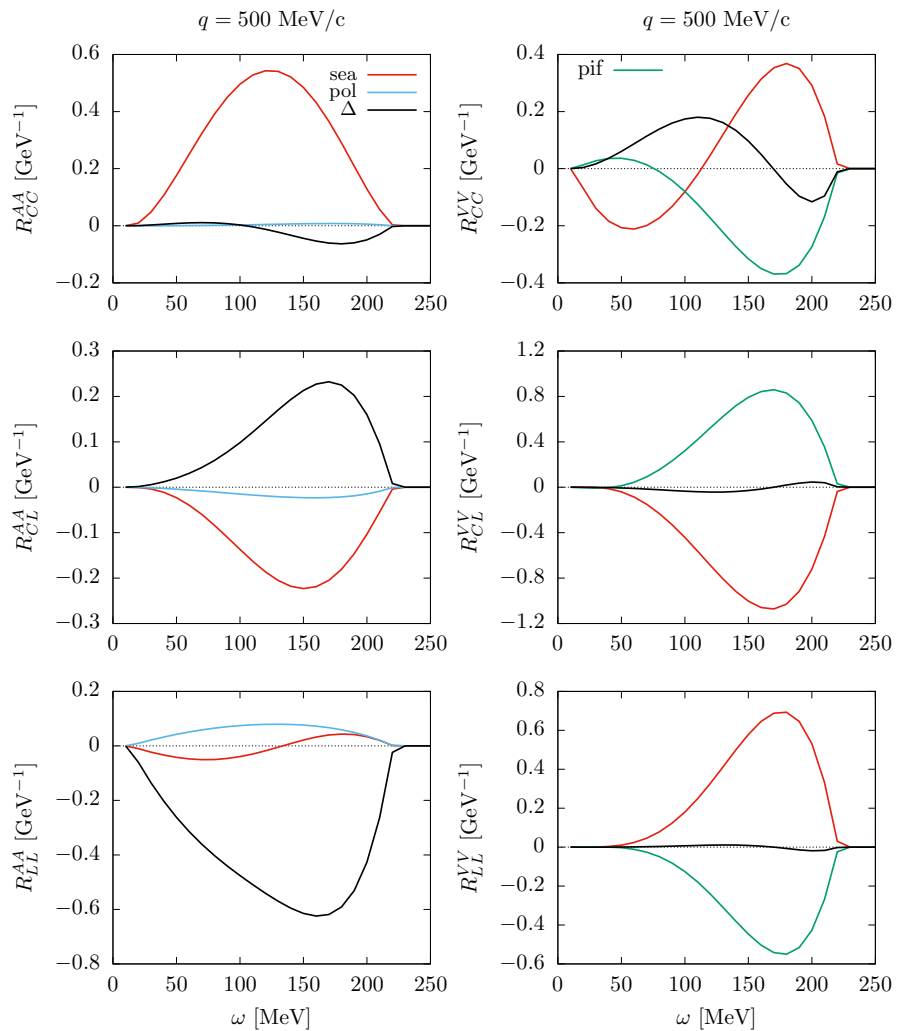


Figure 5.12: The same as in Fig. 5.11 for $q = 500$ MeV/c.

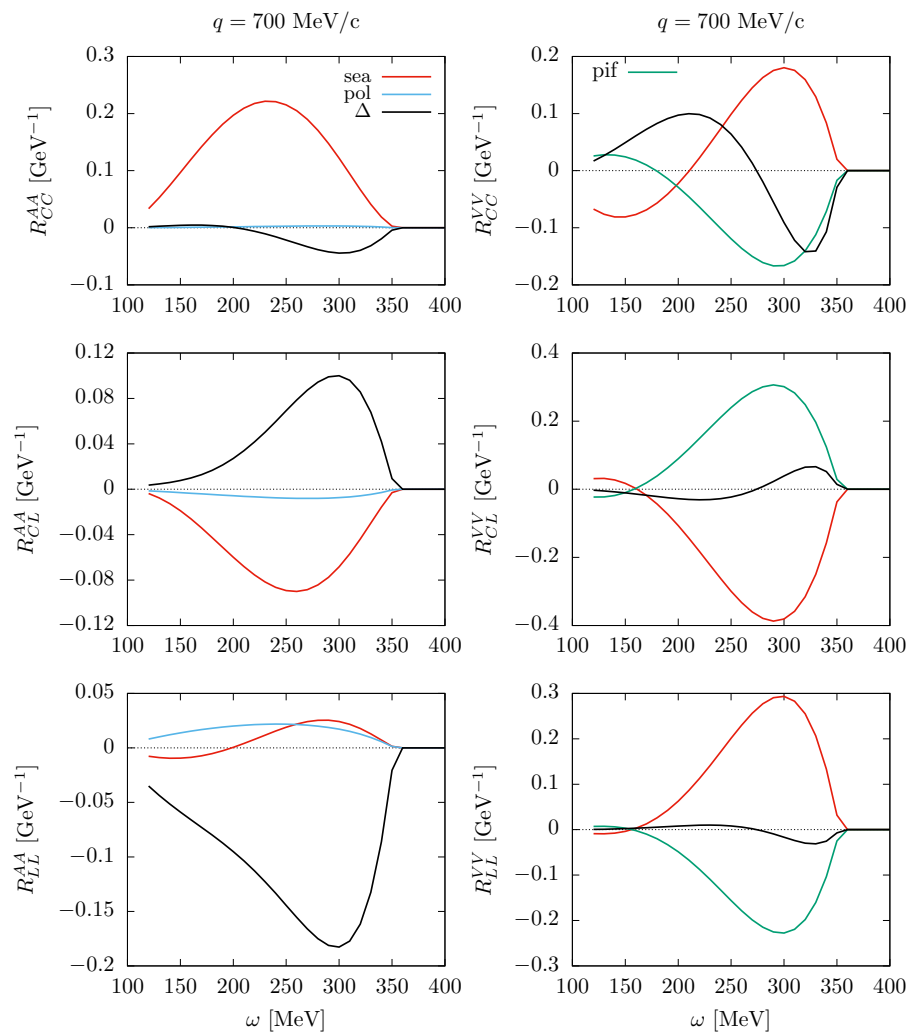


Figure 5.13: The same as in Fig. 5.11 for $q = 700$ MeV/c.

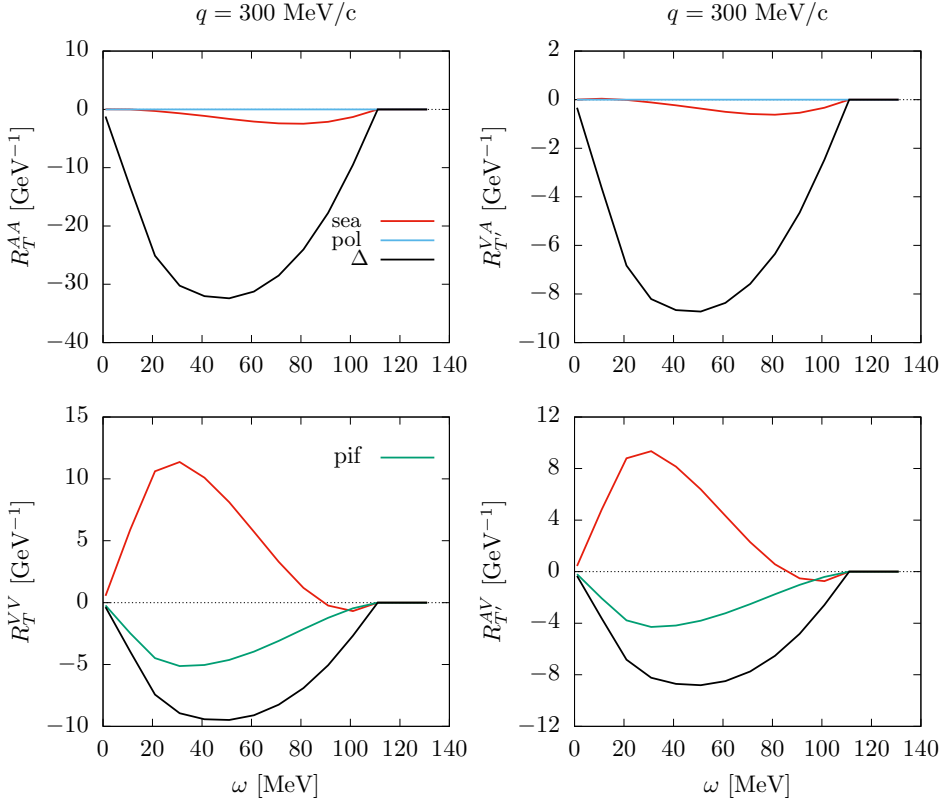


Figure 5.14: The same as Fig. 5.11 for the transverse responses for $q = 300$ MeV/c.

all the interference terms are shown separately for the seagull, pionic, pion-pole, and Δ currents. The effect of MEC on the longitudinal responses is diverse, see Figs. 5.11, 5.12, 5.13, although these interferences have a limited impact on the total responses and an even smaller one on the neutrino cross section. For example, the pionic and seagull contributions tend to cancel each other in the VV-type R_{CC} , R_{CL} , and R_{LL} responses. In the axial R_{CC} , the seagull clearly dominates, as anticipated in the non-relativistic development, while in the axial R_{CL} and R_{LL} responses a non-negligible contribution from the Δ current is observed, since the axial Δ is no longer purely transverse. The pion pole is negligible. Nevertheless, we reiterate that the overall impact of these interferences on observables is minimal. The MEC effect that plays a significant role appears in the transverse responses of Figs. 5.14, 5.15, 5.16, where the Δ current is clearly dominant and produces a sizable reduction of the response, partially compensated by the seagull contribution.

An important outcome of this analysis is the identification of a sizable negative interference between the one-body and Δ -current contributions in the axial channel, particularly in the AA transverse and AV,VA transverse responses. This effect, which to our knowledge has not been previously highlighted in the literature on quasielastic neutrino scattering, is a novel result of this work. It is especially relevant for neutrino interactions, where the axial current plays a central role. Since current neutrino event generators and models often neglect such interference terms and treat MEC contributions only a 2p2h additive term, this finding suggests that existing models may require revision in order to properly account for interference effects, especially those involving the Δ current in axial channels.

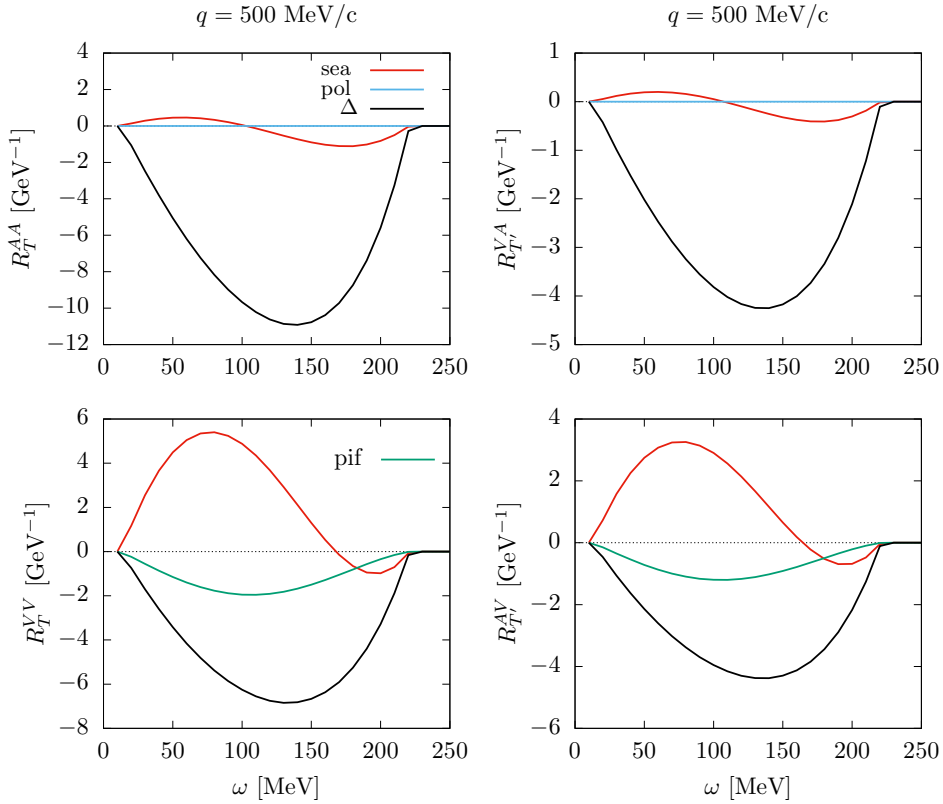


Figure 5.15: The same as Fig. 5.11 for the transverse responses for $q = 500$ MeV/c.

Now we present results obtained with two additional nuclear models beyond the RFG: the RMF model of nuclear matter and the SuSAM*. In Fig. 5.17, we compare the five response functions calculated in the RFG and RMF models for three values of the momentum transfer. The main effect of the relativistic mean field is to produce a shift in the responses due to the use of an effective mass for the nucleons. This shift effectively incorporates, through the mean field, part of the dynamical effects related to the binding and interaction energy of the nucleon in the final state.

On the other hand, in the SuSAM* approach, we use Eq. (2.21) together with the phenomenological scaling function extracted in chapter 3, Eq. (3.38). The results for the interference 1b-MEC response functions are shown in Figs. 5.18, 5.19, 5.20 and 5.21, 5.22 and 5.23 for $q = 300, 500, 700$ MeV/c, where we compare RMF and SuSAM* models. As we can see, the interference SuSAM* responses extend well beyond the allowed region of the RMF, enabling the estimation of MEC effects at large ω values. The phenomenological scaling function was parametrized as a sum of two Gaussians, which explains why some of the responses display two peaks. It is also apparent that in the transverse responses the total interference remains negative due to the Δ current.

In Fig. 5.24 we present the total response functions computed in RMF and SuSAM* models. The second peak is only visible in the longitudinal responses, which are small and contribute little to the neutrino cross section. For the dominant responses—the transverse (T) and charge-charge (CC) ones—the effect of the SuSAM* model is to introduce a high-energy tail in the responses. The relative size of the responses can be clearly seen

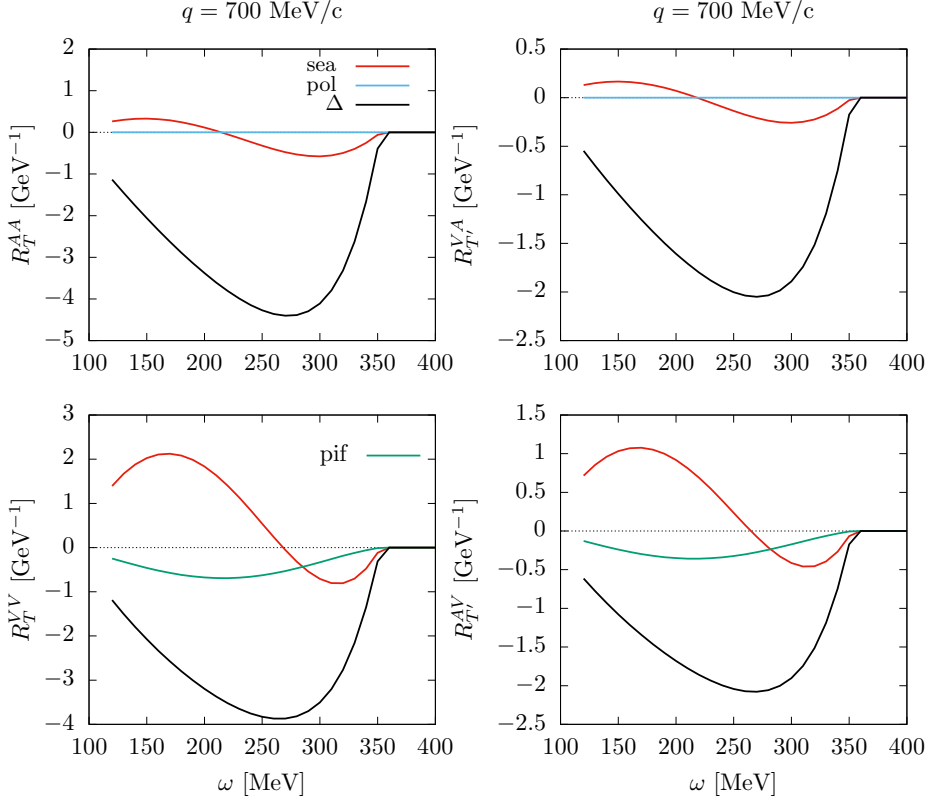


Figure 5.16: The same as Fig. 5.11 for the transverse responses for $q = 700$ MeV/c.

in this figure for $q = 500$ MeV/c: the T response reaches a maximum of approximately ~ 70 GeV $^{-1}$, T' is about half of that (~ 35 GeV $^{-1}$), CC peaks around ~ 12 , $CL \sim -4$, and $LL \sim 1.6$. This shows that the CC contribution is relatively small, CL even smaller, and LL is almost negligible. Note, however, that each response is weighted by a different kinematic factor v_K in the cross section. In particular, the LL response is so small that it becomes extremely sensitive to fine details of the model, but such differences are likely to be un-observable in the total cross section, which is largely dominated by the transverse responses and, to a lesser extent, by the CC component.

5.4.1. Cross section

To finish this section we present results for the neutrino (ν_μ, μ^-) and antineutrino ($\bar{\nu}_\mu, \mu^+$) inclusive cross sections. To compare theoretical predictions with experimental data, the double differential cross section, expressed as a function of the muon kinetic energy and the scattering angle, must be integrated over the neutrino flux. The flux-averaged cross section is defined as:

$$\frac{d^2\sigma}{dT_\mu d\cos\theta} = \frac{1}{\Phi_{tot}} \int dE_\nu \Phi(E_\nu) \frac{d^2\sigma}{dT_\mu d\cos\theta}(E_\nu) \quad (5.107)$$

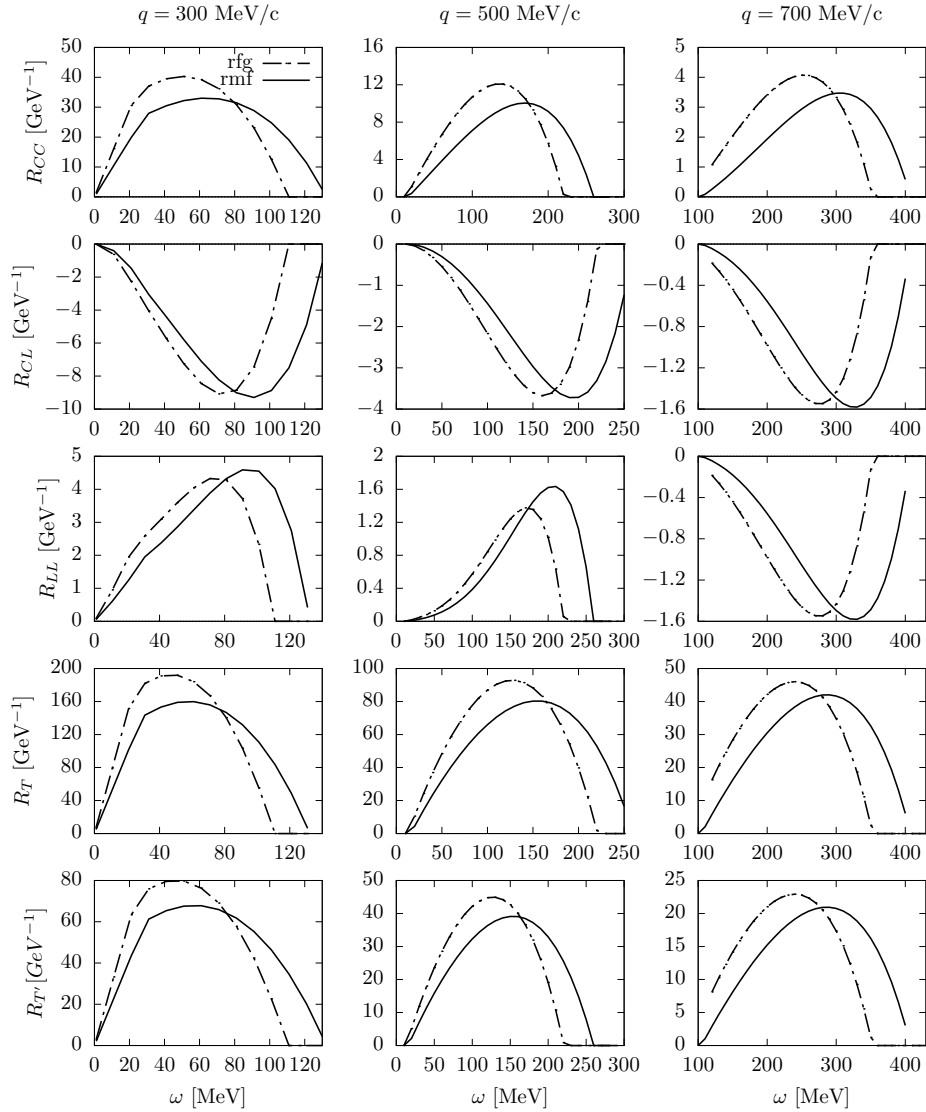


Figure 5.17: Comparison of the five total response functions R_{CC} , R_{CL} , R_{LL} , R_T , and $R_{T'}$ computed within the RFG and the RMF models for momentum transfers $q = 300$, 500 , and 700 MeV/c.

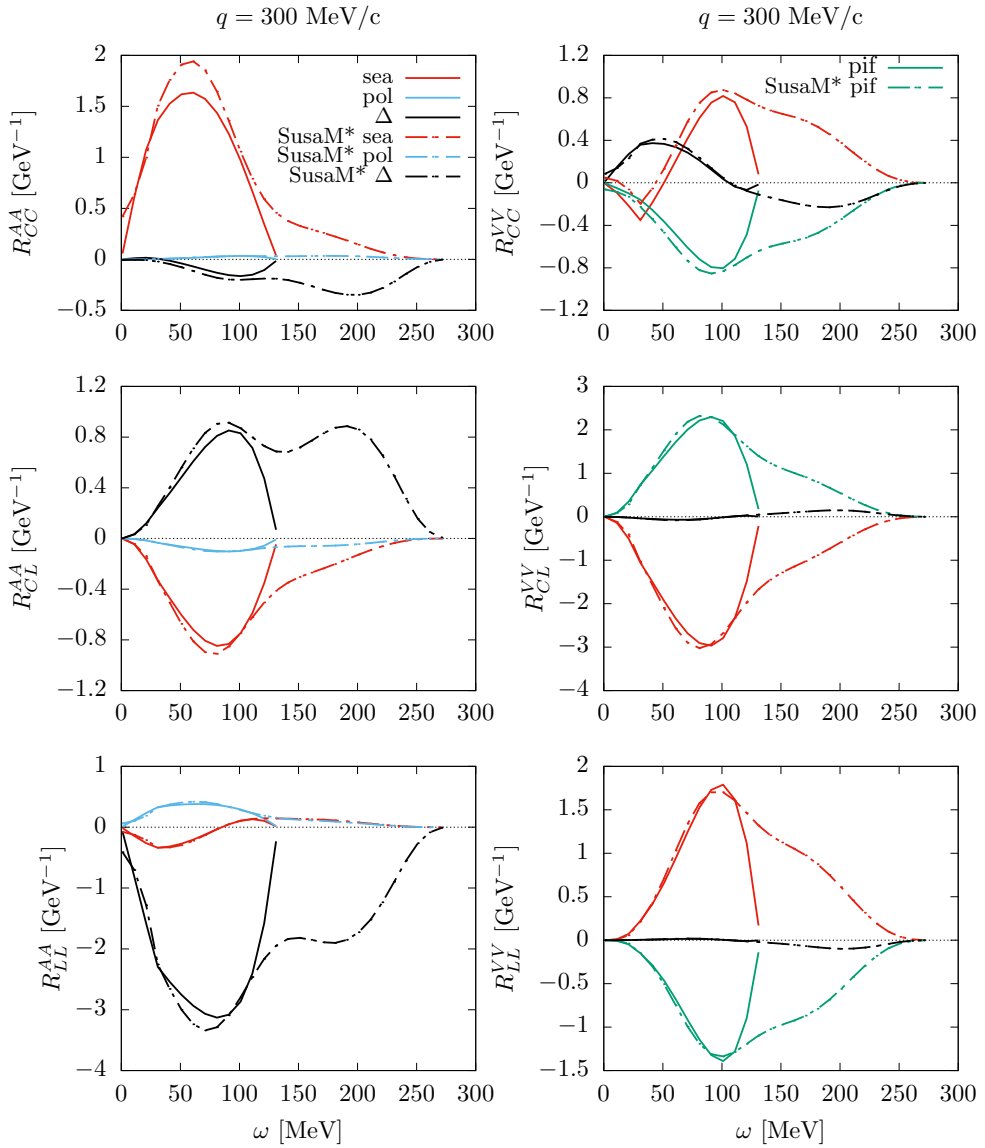
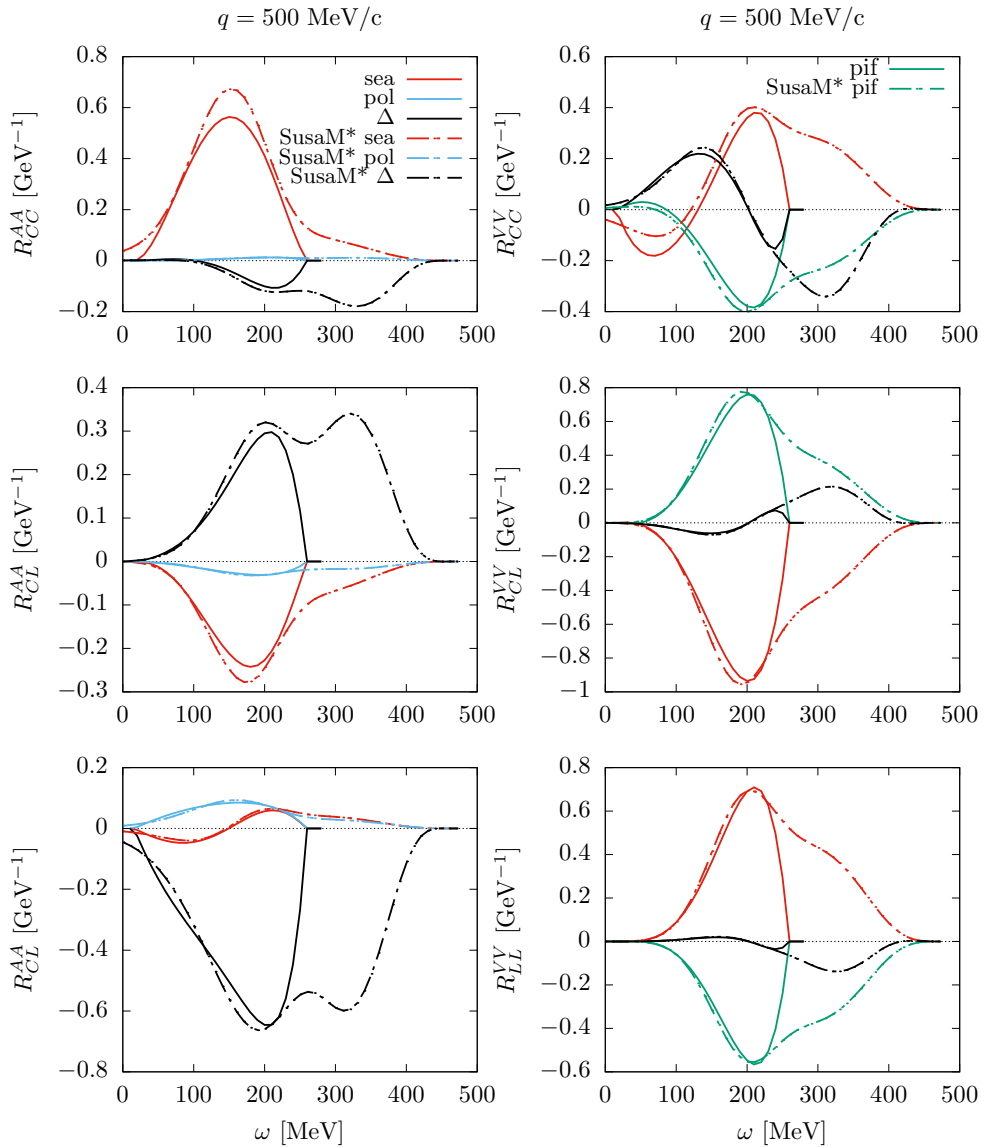


Figure 5.18: Longitudinal 1b-MEC interference responses in the SuSAM* approach compared to the RMF model for $q = 300$ MeV/c.

Figure 5.19: The same as in Fig. 5.18 for $q = 500$ MeV/c.

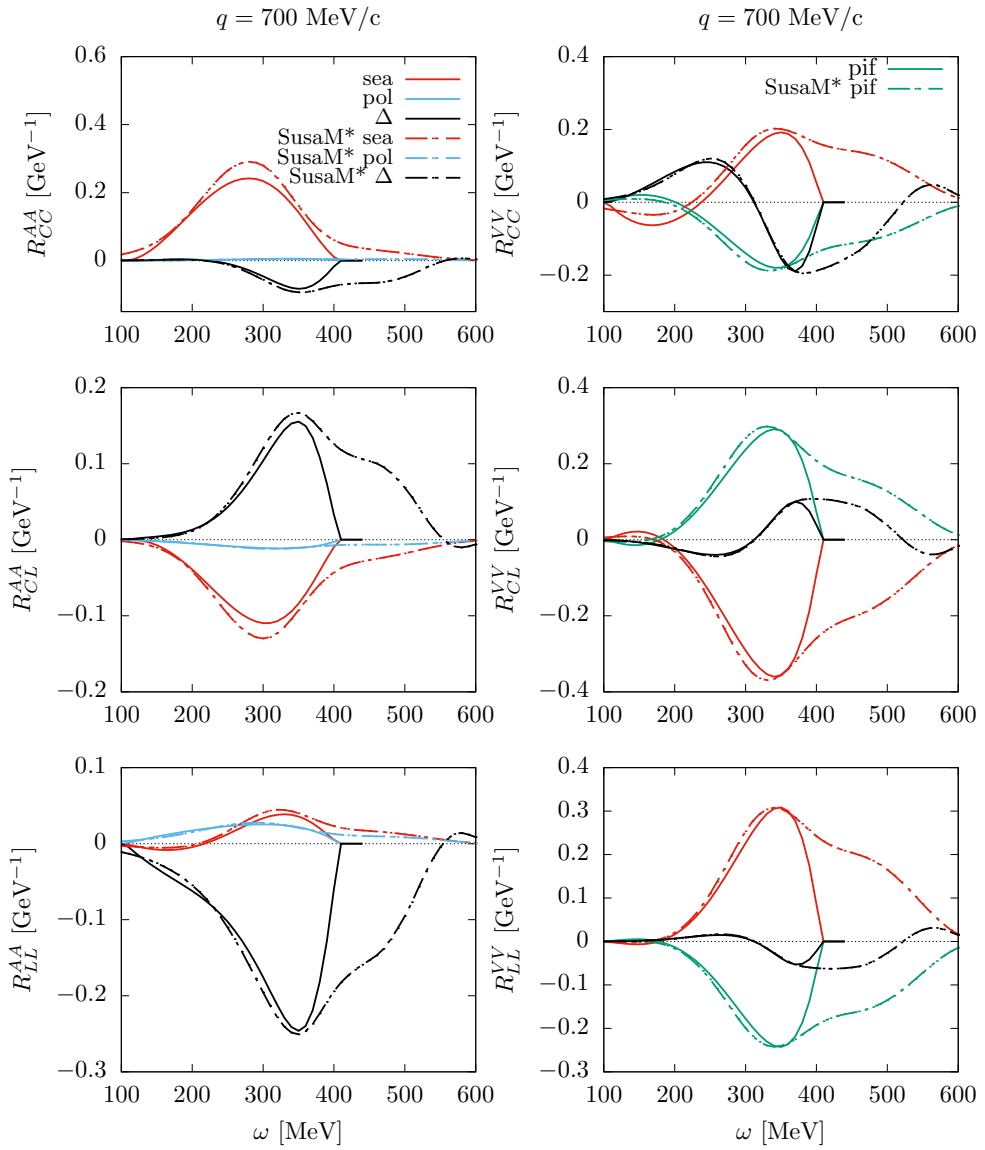


Figure 5.20: The same as in Fig. 5.18 for $q = 700 \text{ MeV}/c$.

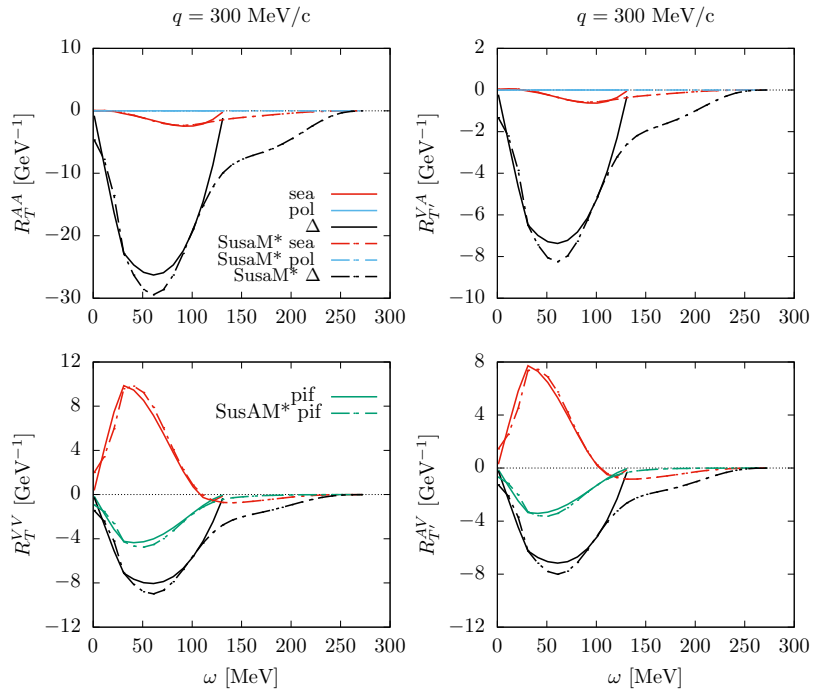


Figure 5.21: The same as in Fig. 5.18 for the transverse interference response for $q = 300 \text{ MeV}/c$.

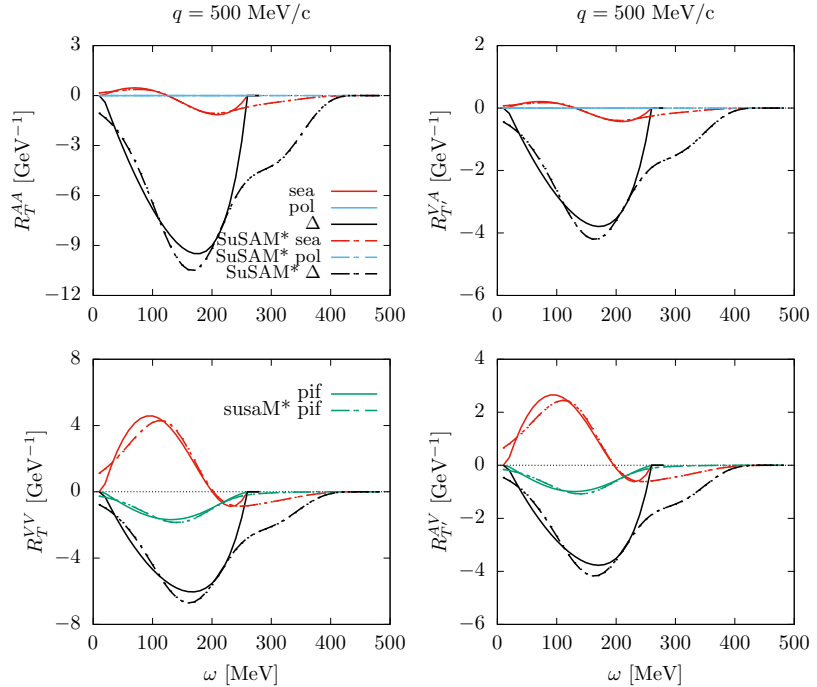


Figure 5.22: The same as in Fig. 5.21 for $q = 500 \text{ MeV}/c$.

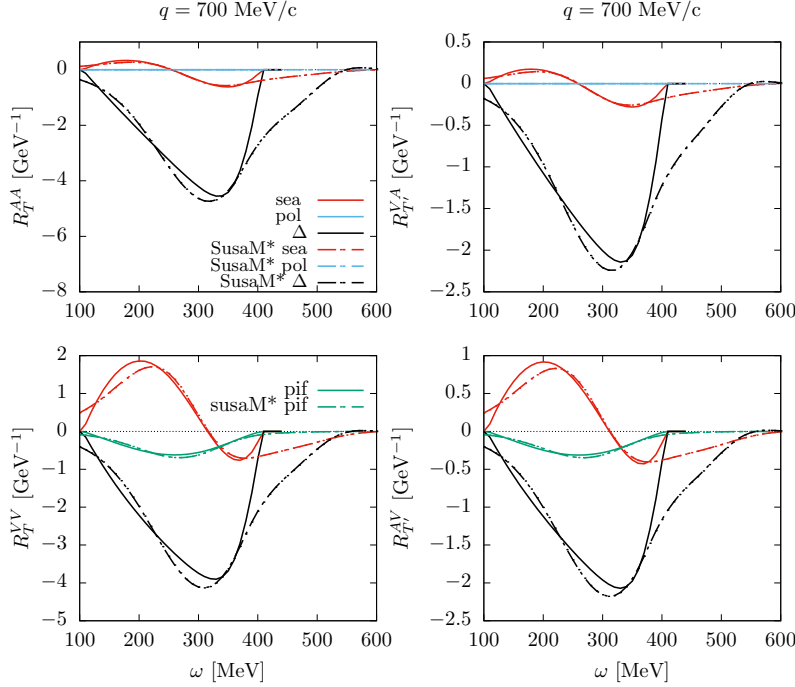


Figure 5.23: The same as in Fig. 5.21 for $q = 700$ MeV/c.

where $\Phi(E_\nu)$ is the neutrino flux, $\frac{d^2\sigma}{dT_\mu d\cos\theta}(E_\nu)$ is the cross section evaluated at a fixed neutrino energy E_ν and Φ_{tot} is the total integrated flux,

$$\Phi_{tot} = \int dE_\nu \phi(E_\nu). \quad (5.108)$$

The experimental data are typically provided in bins of $\cos\theta$, where θ is the scattering angle of the outgoing muon. For each bin, what is actually given is the cross section averaged over the bin width, which implies an integration over $\cos\theta$.

$$\left\langle \frac{d^2\sigma}{dT_\mu d\cos\theta} \right\rangle_{Bin} = \frac{1}{\Delta \cos\theta} \int_{\cos\theta_i}^{\cos\theta_f} \frac{d^2\sigma}{dT_\mu d\cos\theta}(\cos\theta) d\theta \quad (5.109)$$

However, for large angles (i.e., low values of $\cos\theta$), the variation of the cross section within the bin is generally small, and one can approximate the averaged cross section by evaluating it at the midpoint of the bin.

In Figs. 5.25 and 5.26 we present results for the double-differential charged-current neutrino and antineutrino cross sections, respectively, corresponding to the kinematics and flux of the MiniBooNE experiment [181, 183]. Each panel shows the cross section for a given $\cos\theta$ bin, with bin width $\Delta \cos\theta = 0.1$, as a function of the kinetic energy of the outgoing muon. A broad peak is observed, which arises from an average over many cross sections corresponding to different values of the incident neutrino energy E_ν , weighted with the flux. This averaging produces a much broader shape than what would be expected from a quasielastic cross section at fixed E_ν .

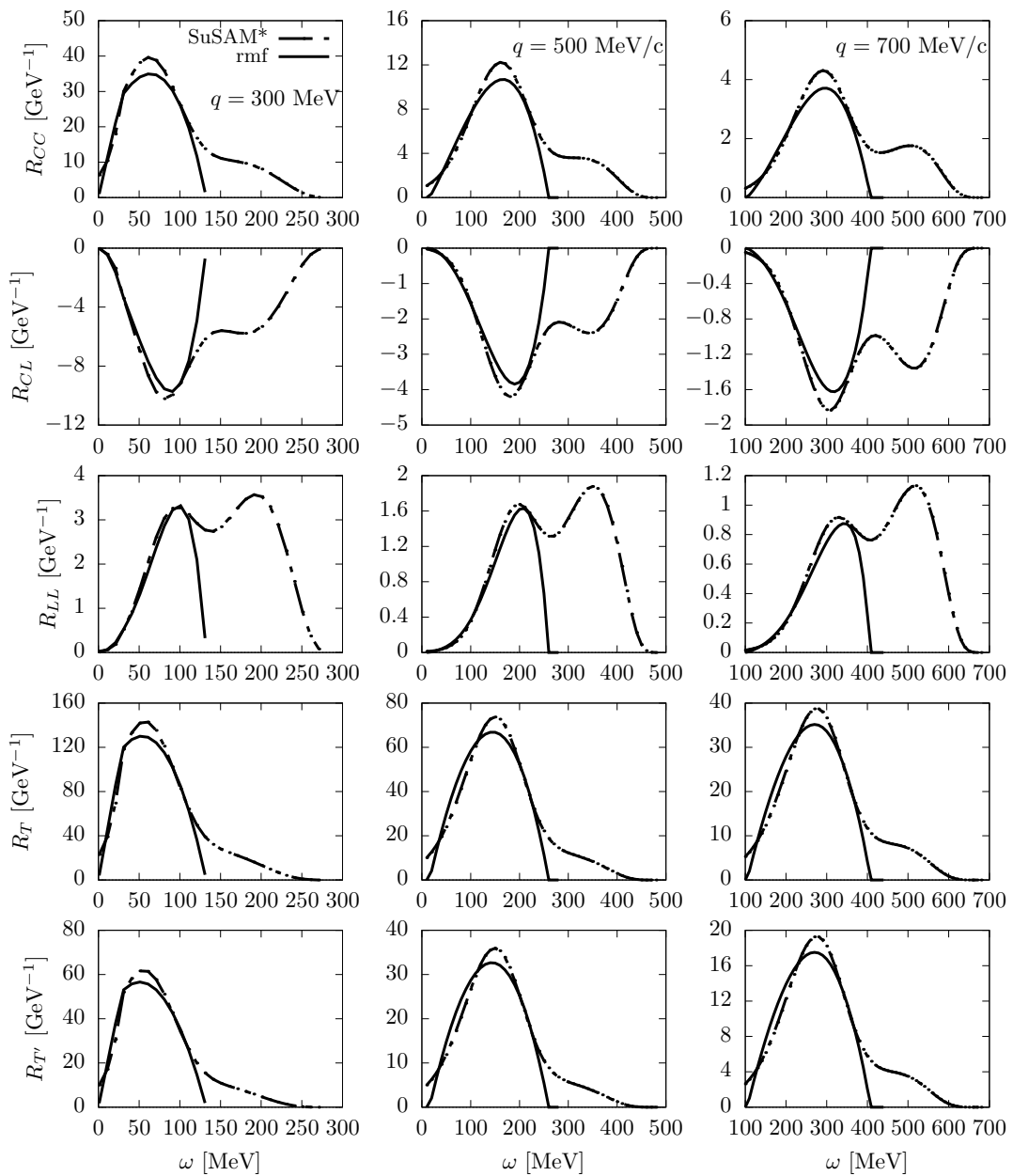


Figure 5.24: Total responses in the RMF and SuSAM* models for momentum transfers $q = 300, 500, 700$ MeV/c.

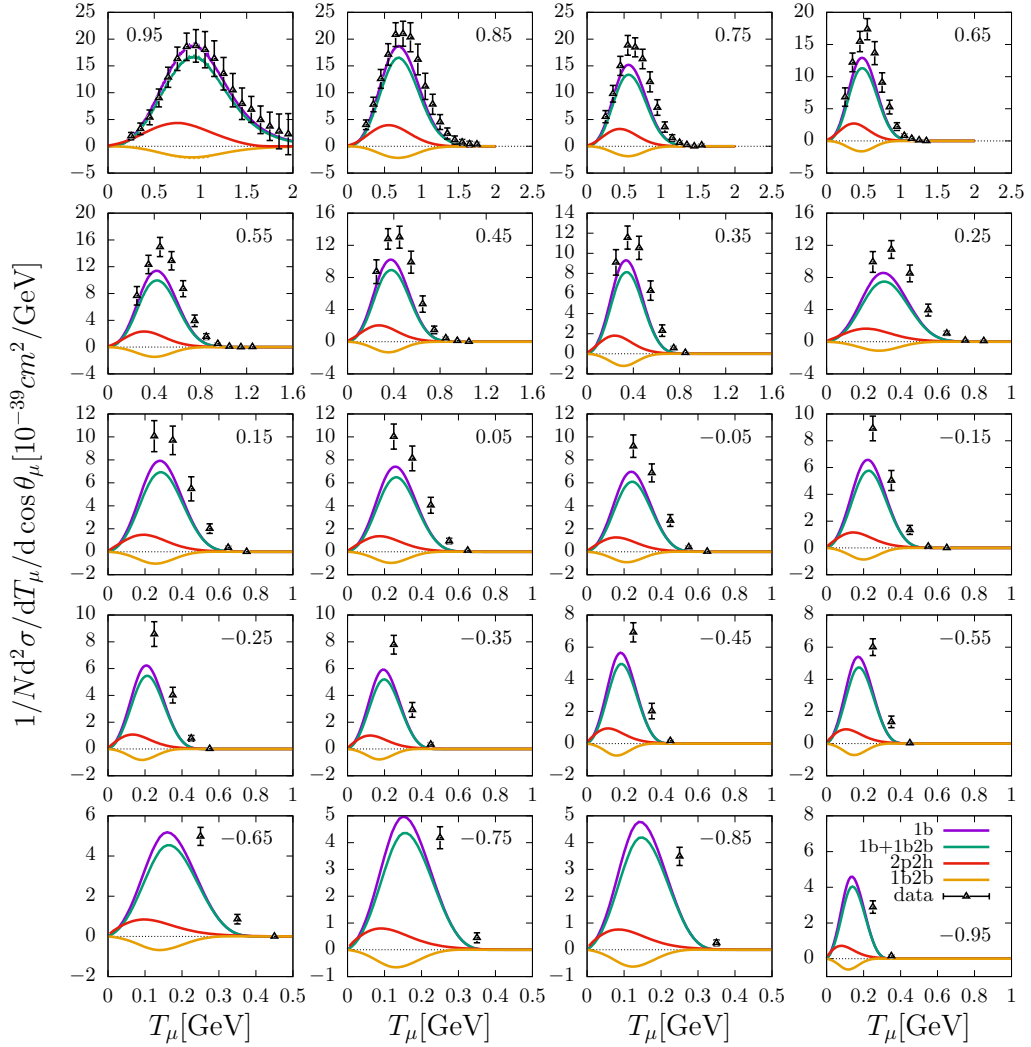


Figure 5.25: Flux-integrated double-differential cross section per neutron for CC neutrino scattering on ^{12}C in the RMF model. The experimental points are the inclusive CCQE measurements from MiniBooNE [181]. Shown are the one-body (1b) results, the one-body two-body interference (1b2b), their sum (1b+1b2b), and the 2p2h contribution from Ref. [182] computed within the same RMF model.

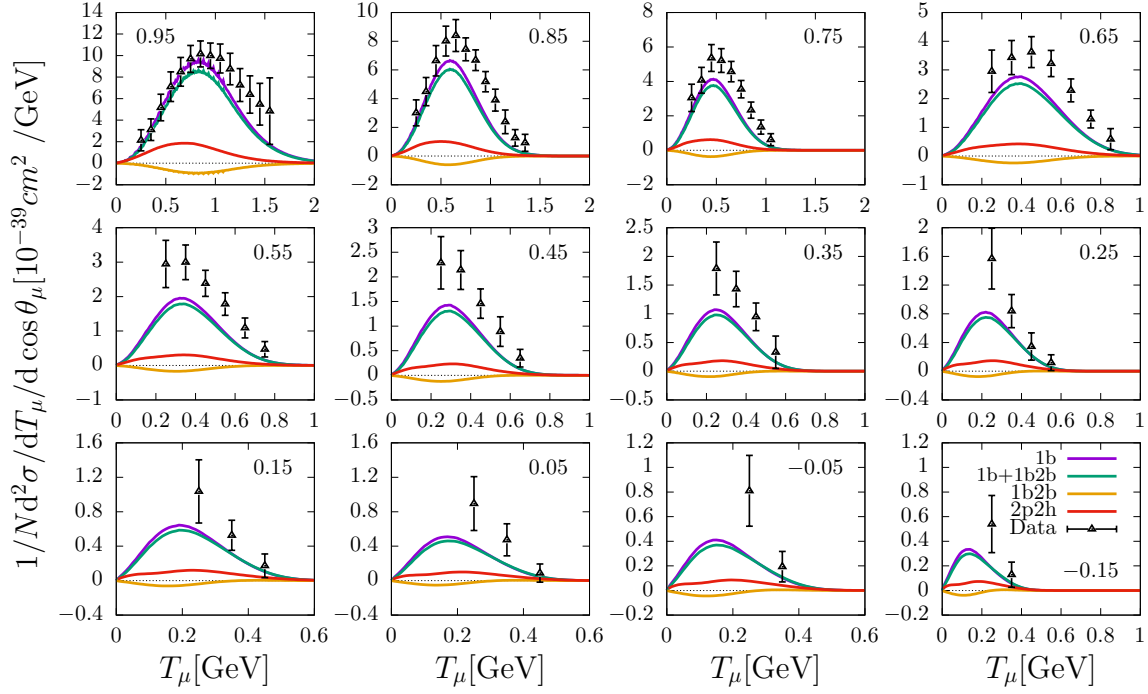


Figure 5.26: The same as in Fig. 5.25 for the antineutrino cross section. Experimental data are the CCQE antineutrino measurements from MiniBoone [183].

The theoretical calculations have been performed using the RMF model with effective mass $M^* = 0.8$ and Fermi momentum $k_F = 225$ MeV/c, corresponding to ^{12}C .

In Figs. 5.25 and 5.26 we show the one-body (1b) results together with the sum of 1b and the 1b–2b interference. One observes that the interference with MEC produces a reduction of the cross section of about 10%. For antineutrinos the effect is smaller due to the partial cancellation between the T and T' responses. In the same figures we also show separately the 1b–2b interference and the 2p2h contributions for comparison. The 2p2h responses, computed in Ref. [182], are positive, somewhat larger than the interference, and display their maximum at lower energy transfer. As a consequence, the two contributions partially cancel each other, although the 2p2h still dominates. Therefore, one expects that when both are summed the net effect would be an enhancement smaller than that produced by the 2p2h contribution alone. We have not included this sum in the figure, since the focus of the present work is on the interference, but it is clear that both effects, 2p2h and 1b–2b interference, are of comparable size.

Other models in the literature often neglect the interference between one-body and two-body currents, and their predictions vary significantly among them, contributing to the theoretical systematic uncertainties in neutrino oscillation experiments. Our results indicate that the 1b–2b interference constitutes an additional source of uncertainty that should also be taken into account.

In order to gain deeper insight into the flux-folded results of Figs. 5.25 and 5.26, in Fig. 5.27 we show the impact of the interference term on double-differential cross sections

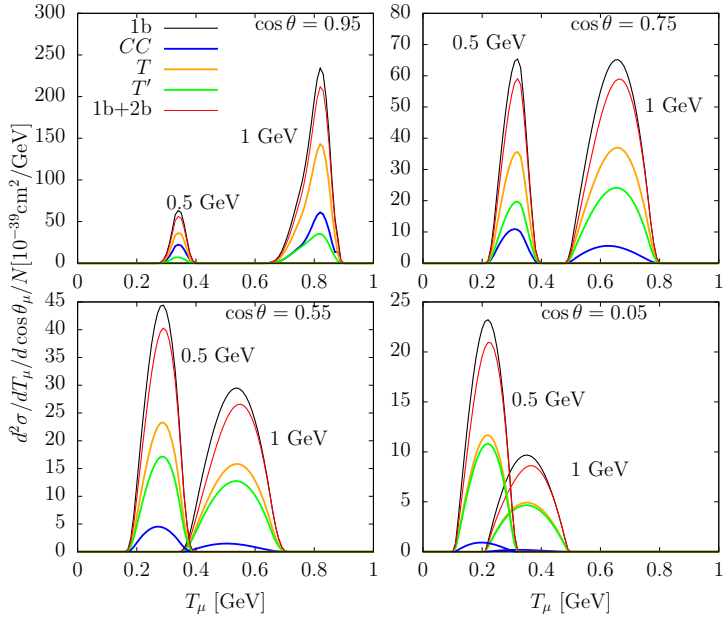


Figure 5.27: Double-differential cross sections for CC neutrino scattering on ^{12}C in the RMF model at fixed neutrino energies $E_\nu = 0.5$ and 1 GeV. Results are shown for different scattering angles corresponding to $\cos \theta = 0.95, 0.75, 0.55$, and 0.05 . For the most forward bin, $\cos \theta = 0.95$, the cross section is averaged over $\cos \theta \in [0.9, 1]$, corresponding to angles between 0° and 25° . In each panel we display the results with the one-body current alone (1b) and including the interference contribution (1b+1b2b). The 1b contributions of the CC, T, and T' responses are also shown separately.

at fixed neutrino energies and different scattering angles. Specifically, results are presented for $\cos \theta = 0.95, 0.75, 0.55$ and 0.05 . Because the cross section varies rapidly at forward angles, the case $\cos \theta = 0.95$ is averaged over the bin $\cos \theta \in [0.9, 1]$, corresponding to scattering angles between 0° and 25° . For larger angles the cross section varies smoothly within the bin, and it is sufficient to show the result at the midpoint, corresponding to 41° , 57° and 87° , respectively. Each panel displays results for incident neutrino energies of 0.5 and 1 GeV, which approximately span the region where the flux is most intense. For each kinematics we show the cross section obtained with the 1b current and after including the interference (1b+2b). The results indicate that the interference effect depends only weakly on kinematics, consistent with the behavior observed in Figs. 5.25 and 5.26.

One might expect that the transverse response becomes more relevant at larger angles, thereby increasing the relative effect of MEC. This is also illustrated in Fig. 5.27, where the separated contributions of the CC, T, and T' responses are shown (the CL and LL components are not displayed because they are smaller). For forward angles the CC response is larger than T', but the T response dominates. This arises because in neutrino scattering the axial current contributes significantly to T, while its role in CC is minor. With increasing angle the CC contribution decreases relative to T and T' and the T' component

becomes more important. In summary, except for very small angles, the neutrino cross section is dominated by the transverse response, which explains why the relative impact of MEC does not vary strongly with kinematics.

5.5. Final Remarks

In this chapter we have presented a detailed study of meson exchange currents in the 1p1h channel of CC neutrino and antineutrino scattering on nuclei. Our analysis focused on the interference between one-body and two-body currents, an effect neglected in neutrino event generators but that, as it have been shown, can be sizable and may contribute to the systematic uncertainties in oscillation experiments.

The formalism employed was developed starting from the RFG model, including 1p1h excitations produced by one-body and two-body current operators. In this context, we computed the five nuclear response functions (CC , CL , LL , T , and T') including the interference between the 1b current and the seagull, pion-in-flight, pion-pole and Δ currents. The non-relativistic limit of the response functions has been carefully examined as a preliminary step to validate the relativistic model; in this limit, the spin sums can be calculated analytically, allowing us to understand the signs and relative importance of the dominant terms. In particular, it has been found that the Δ current gives rise to a strong negative interference in the transverse responses T and T' . This is a new and important result, which is absent in existing neutrino models and calls for a careful reevaluation of the role of 1b2b interference terms in neutrino-nucleus scattering. The analysis is extended beyond the RFG by employing two additional nuclear models: the RMF in nuclear matter and the SuSAM* approach.

Although this chapter employs some of the most elementary nuclear models, this choice was necessary to formulate the problem rigorously and within a fully reproducible framework. This strategy provides a solid baseline that enables more realistic models to incorporate and test the effects identified. It is expected that this study will serve as a starting point for deeper investigations and help indicate the direction in which further theoretical efforts should proceed.

Chapter 6

Analysis of the SRC with the Bethe-Goldstone equation

In this chapter we examine an important phenomenon occurring in nuclei: short-range correlations. These correlations arise when two nucleons interact strongly in the presence of the surrounding medium, generating high-momentum components in the nuclear wave function. The ultimate goal of this analysis is to compute the wave function of a correlated nucleon pair, which will then be incorporated into our model of MEC responses. This provides the necessary foundation for chapter 7, where we will investigate in detail the combined effect of MEC and SRC on the transverse response of nuclei.

Short-range correlations are described in the independent pair approximation by solving the Bethe–Goldstone (BG) equation [184, 185, 186], which may be regarded as the in–medium two–body Schrödinger equation. Within Brueckner theory of nuclear matter [187, 188, 189] it defines the G –matrix, which encodes the effective nucleon–nucleon interaction in the medium [190, 191, 192, 193, 194, 195, 196]. We employ the coarse-grained Granada 2013 potential [197], written as a sum of Dirac deltas in each partial wave, which reduces the integral equation to a simple algebraic system. The resulting correlated wave functions are analyzed in position and momentum space via a multipole expansion, with particular emphasis on their dependence on the center-of-mass (CM) motion of the pair. Unlike the traditional back-to-back picture, correlated nucleons can carry arbitrary CM momenta, extending previous studies [198, 199] by the Granada group. The novelty of this work is the explicit inclusion of CM motion, which is required for the following chapter. See more details in Ref. [171].

6.1. The Bethe-Goldstone equation

We consider two particles with momenta \mathbf{p}_1 and \mathbf{p}_2 in the Fermi gas, with $p_1, p_2 < k_F$. In the absence of interaction they are described as independent plane waves,

$$\langle \mathbf{r}_1 | \mathbf{p}_1 \rangle = \frac{1}{(2\pi)^{3/2}} e^{i\mathbf{p}_1 \cdot \mathbf{r}_1}, \quad \langle \mathbf{r}_2 | \mathbf{p}_2 \rangle = \frac{1}{(2\pi)^{3/2}} e^{i\mathbf{p}_2 \cdot \mathbf{r}_2}$$

If we allow them to interact through a two-body potential V , the wave function of the pair $|\Psi_0\rangle = |\mathbf{p}_1\mathbf{p}_2\rangle$ is modified. Since the interaction takes place in the medium and not in the vacuum, the particles cannot scatter into states already occupied in the Fermi sea. Consequently, due to the effect of the medium, scattering is only possible into momenta above the Fermi surface, and the pair acquires virtual high-momentum components. We thus seek the solution of the Schrödinger equation for a pair of correlated nucleons in the form

$$\Psi = \Psi_0 + Q\Psi \quad (6.1)$$

where $\Psi_0 = |\mathbf{p}_1\mathbf{p}_2\rangle$ is the uncorrelated two-particle and the second term represents the high-momentum components induced by correlations. We've imposed the Pauli-Blocking condition using the operator Q , which ensures our pair scatters only into unoccupied states above k_F . This operator is defined as,

$$Q|\mathbf{p}'_1\mathbf{p}'_2\rangle = \begin{cases} |\mathbf{p}'_1\mathbf{p}'_2\rangle & \text{if } |\mathbf{p}'_i| > k_F \\ 0 & \text{otherwise} \end{cases} \quad (6.2)$$

The equation that describes this process is the Bethe-Goldstone equation, which is the Schrödinger equation for a pair of correlated nucleons in the nuclear medium. To deduce it, we need to determine the condition that the state Ψ must satisfy in order to fulfill the Schrödinger equation in the presence of Pauli blocking. Starting with the correlated wave function in Eq. (6.1), we want this function to satisfy the Schrödinger equation in the presence of an interaction,

$$(T + V)\Psi = E\Psi. \quad (6.3)$$

At the same time, the free wave satisfies,

$$T\Psi_0 = E\Psi_0 \quad (6.4)$$

Substituting the full wave function into the Schrödinger equation, we isolate the term $Q\Psi$. After some algebra, this leads to:

$$Q\Psi = \frac{Q}{E - T}V\Psi, \quad (6.5)$$

so finally, the BG equation is

$$\Psi = \Psi_0 + \frac{Q}{E - T}V\Psi. \quad (6.6)$$

We now write the Bethe-Goldstone equation in the form of an integral equation by substituting the Pauli projector Q with its representation as an integral over intermediate states,

$$Q = \int_{\mathbf{p}'_1\mathbf{p}'_2 > k_F} d^3\mathbf{p}'_1 d^3\mathbf{p}'_2 |\mathbf{p}'_1\mathbf{p}'_2\rangle\langle\mathbf{p}'_1\mathbf{p}'_2|. \quad (6.7)$$

The BG equation then reads

$$|\Psi\rangle = |\mathbf{p}_1\mathbf{p}_2\rangle + \int d^3p'_1 d^3p'_2 \frac{\theta(p'_1 - k_F)\theta(p'_2 - k_F)}{E - E'} |\mathbf{p}'_1\mathbf{p}'_2\rangle\langle\mathbf{p}'_1\mathbf{p}'_2|V|\Psi\rangle. \quad (6.8)$$

where $E' = E'_1 + E'_2 = (p'_1{}^2 + p'_2{}^2)/(2m_N)$. Note that the energy E' in the denominator is always larger than the energy E of the correlated pair, since \mathbf{p}'_1 and \mathbf{p}'_2 correspond to unoccupied states above the Fermi surface. Thus one has $E' > 2E_F$ while $E < 2E_F$. The only problematic case arises when $E = 2E_F$ and $E' \rightarrow 2E_F$. To avoid this issue we introduce an infinitesimal energy gap so that E never coincides exactly with E_F .

Since the NN potential conserves the total momentum of the two-nucleon system, it is convenient to switch from single-particle coordinates $\mathbf{r}_1, \mathbf{r}_2$ to relative, \mathbf{r} , and center-of-mass, \mathbf{R} , coordinates. Correspondingly, the momenta are expressed in terms of the total momentum, \mathbf{P} , and the relative momentum, \mathbf{p} :

$$\begin{aligned} \mathbf{R} &= \frac{1}{2}(\mathbf{r}_1 + \mathbf{r}_2), & \mathbf{P} &= \mathbf{p}_1 + \mathbf{p}_2, \\ \mathbf{r} &= \mathbf{r}_1 - \mathbf{r}_2, & \mathbf{p} &= \frac{1}{2}(\mathbf{p}_1 - \mathbf{p}_2). \end{aligned} \quad (6.9)$$

Up to this point we have omitted the spin indices for simplicity, but we now include them explicitly since the potential depends on the spin degrees of freedom. We do not introduce isospin at this stage, since the interaction we employ is charge independent. Isospin will be relevant when discussing the different symmetry properties of pp/nn and np pairs. The uncorrelated and correlated wave functions are then written

$$\langle \mathbf{r}_1 \mathbf{r}_2 | p_1 p_2 \rangle = \frac{1}{(2\pi)^3} e^{i\mathbf{P} \cdot \mathbf{R}} e^{i\mathbf{p} \cdot \mathbf{r}} | \frac{1}{2} s_1 \frac{1}{2} s_2 \rangle \equiv |\mathbf{P}\rangle \otimes |\mathbf{p} s_1 s_2\rangle \quad (6.10)$$

$$\langle \mathbf{r}_1 \mathbf{r}_2 | \Psi \rangle = \frac{1}{(2\pi)^{3/2}} e^{i\mathbf{P} \cdot \mathbf{R}} \psi_{\mathbf{P}, \mathbf{p}}^{s_1 s_2}(\mathbf{r}) \equiv |\mathbf{P}\rangle \otimes |\psi_{\mathbf{P}, \mathbf{p}}^{s_1 s_2}\rangle \quad (6.11)$$

Here $|\mathbf{p} s_1 s_2\rangle$ denotes the relative wave function of the uncorrelated pair of nucleons with spin projections s_1 and s_2 , while $|\psi_{\mathbf{P}, \mathbf{p}}^{s_1 s_2}\rangle$ represents the corresponding correlated relative wave function. Note that the center-of-mass wave function $|\mathbf{P}\rangle$ remains unaffected by the interaction because,

$$\langle \mathbf{P}', \mathbf{p}' | V | \Psi \rangle = \delta(\mathbf{P}' - \mathbf{P}) \langle \mathbf{p}' | V | \psi_{\mathbf{P}, \mathbf{p}}^{s_1 s_2} \rangle. \quad (6.12)$$

Since the NN potential commutes with S^2 and therefore conserves the total spin $S = 0, 1$ of the two nucleons, it is also convenient to express both the uncorrelated and correlated relative states in the coupled spin basis

$$|\mathbf{p} s_1 s_2\rangle = \sum_{SM_S} \langle \frac{1}{2} s_1 \frac{1}{2} s_2 | SM_S \rangle |\mathbf{p}; SM_S\rangle, \quad (6.13)$$

$$|\psi_{\mathbf{P}, \mathbf{p}}^{s_1 s_2}\rangle = \sum_{SM_S} \langle \frac{1}{2} s_1 \frac{1}{2} s_2 | SM_S \rangle |\psi_{\mathbf{P}, \mathbf{p}}^{SM_S}\rangle. \quad (6.14)$$

The state $\psi_{\mathbf{P}, \mathbf{p}}^{SM_S}$ denotes the relative correlated wave function obtained from the uncorrelated relative state $|\mathbf{p}; SM_S\rangle$, where the two nucleons are coupled to total spin S with projection M_S . Exploiting the conservation of both the total momentum \mathbf{P} and the total spin S , the center-of-mass wave function appears as a common factor $|\mathbf{P}\rangle$ on both sides of the BG equation (6.8), and therefore cancels out. In the energy denominator we write the energies of the pair as the sum of center-of-mass and relative contributions,

$E = \mathbf{P}^2/4m_N + \mathbf{p}^2/m_N$ and $E' = \mathbf{P}^2/4m_N + \mathbf{p}'^2/m_N$. The center-of-mass terms also cancel, so that only the relative energies of the pair remain, leaving an equation for the relative correlated wave function $|\psi_{\mathbf{P}, \mathbf{p}}^{SM_S}\rangle$:

$$|\psi_{\mathbf{P}, \mathbf{p}}^{SM_S}\rangle = |\mathbf{p}; SM_S\rangle + \int d^3p' \frac{Q(\mathbf{P}, \mathbf{p}')}{p^2 - p'^2} \sum_{M'_S} |\mathbf{p}'; SM'_S\rangle \langle \mathbf{p}'; SM'_S| m_N V |\psi_{\mathbf{P}, \mathbf{p}}^{SM_S}\rangle, \quad (6.15)$$

where now the Pauli-blocking function is

$$Q(\mathbf{P}, \mathbf{p}) = \theta\left(\left|\frac{\mathbf{P}}{2} + \mathbf{p}\right| - k_F\right) \theta\left(\left|\frac{\mathbf{P}}{2} - \mathbf{p}\right| - k_F\right). \quad (6.16)$$

Since the nucleon-nucleon potential does not conserve the value of the spin projection M_S , the correlated wave function for $S = 1$ in general contains admixtures of all three components $M_S = -1, 0, 1$. The wave function $\psi_{\mathbf{P}, \mathbf{p}}^{SM_S}(\mathbf{r})$ depends on the relative coordinate \mathbf{r} , the initial relative momentum \mathbf{p} , and also on the total momentum \mathbf{P} of the pair, since the Pauli-blocking operator Q carries an explicit (\mathbf{P}, \mathbf{p}) -dependence. Actually Q depends on the moduli P , p , and on the angle between them. This angular dependence breaks rotational invariance in Eq. (6.15) even for a central N-N potential [134], causing a mixing among different angular momenta in a partial-wave expansion. In this work we adopt an approximation first proposed by Brueckner [187], in which $Q(\mathbf{P}, \mathbf{p}')$ is replaced by its angular average around the direction of the center-of-mass momentum. This amounts to the substitution

$$Q(\mathbf{P}, \mathbf{p}') \longrightarrow \bar{Q}(P, p') \equiv \frac{1}{4\pi} \int d\Omega Q(\mathbf{P}, \mathbf{p}') \quad (6.17)$$

in Eq. (6.15). With this replacement, the angle-averaged Pauli-blocking function $\bar{Q}(P, p')$ depends only on the magnitudes of the CM and relative momenta, and not on the angle between them. The functional form of $\bar{Q}(P, p')$ for $P < 2k_F$ has been well known since the early work of Brueckner [187].

$$\bar{Q}(P, p') = \begin{cases} 0 & \text{if } 0 \leq p' \leq \sqrt{k_F^2 - \frac{P^2}{4}} \\ \frac{1}{Pp'} \left(\frac{P^2}{4} + p'^2 - k_F^2 \right) & \text{if } \sqrt{k_F^2 - \frac{P^2}{4}} < p' \leq k_F + \frac{P}{2} \\ 1 & \text{if } p' > k_F + \frac{P}{2}. \end{cases} \quad (6.18)$$

The use of the angle-averaged projector ensures that the correlated wave functions depend only on the magnitude of the total momentum, which simplifies the solution of the BG equation in a partial-wave expansion. Although a few works have treated the general case [200, 201, 202, 203, 204, 205], the angle-averaging approximation is standard and accurate in nuclear matter calculations [206], and is essential in this work for numerical feasibility. The resulting BG equation is:

$$|\psi_{\mathbf{P}, \mathbf{p}}^{SM_S}\rangle = |\mathbf{p}; SM_S\rangle + \int d^3p' \frac{\bar{Q}(P, p')}{p^2 - p'^2} \sum_{M'_S} |\mathbf{p}'; SM'_S\rangle \langle \mathbf{p}'; SM'_S| m_N V |\psi_{\mathbf{P}, \mathbf{p}}^{SM_S}\rangle. \quad (6.19)$$

6.2. Multipole expansion of the BG equation

The solution of the BG equation is expanded in multipoles with total angular momentum JM , obtained by coupling the orbital angular momentum l with the total spin S of the pair. This reduces the original integral equation to a set of coupled equations for the radial components. As a motivation, we first write the multipole expansion of the relative plane wave with total spin S in terms of the coupled states $\mathcal{Y}_{lSJ}(\hat{\mathbf{r}})$

$$\langle \mathbf{r} | \mathbf{p}, S m_S \rangle = A \sum_{JM} \sum_{lm_l} i^l Y_{lm_l}^* (\hat{\mathbf{p}}) \langle lm_l S m_s | JM \rangle j_l (pr) \mathcal{Y}_{lSJ}(\hat{\mathbf{r}}), \quad (6.20)$$

with $A = \frac{4\pi}{(2\pi)^{3/2}} = \sqrt{2/\pi}$, and

$$\mathcal{Y}_{lSJ}(\hat{\mathbf{r}}) = \sum_{m\mu} \langle lm S \mu | JM \rangle Y_{lm}(\hat{\mathbf{r}}) | S \mu \rangle \quad (6.21)$$

The solution of the Bethe–Goldstone equation can be expressed in a similar multipole expansion, but with coupling between different orbital angular momenta, since the potential V does not conserve l . We therefore propose the following ansatz for the relative wave function

$$|\psi\rangle = A \sum_{JM} \sum_{ll'm} i^{l'} Y_{l'm}^* (\hat{\mathbf{p}}) \langle l'm S m_s | JM \rangle \phi_{ll'}^{SJ}(r) \mathcal{Y}_{lSJ}(\hat{\mathbf{r}}), \quad (6.22)$$

In Appendix I it is shown that this ansatz satisfies the Bethe–Goldstone equation if and only if the radial functions $\phi_{ll'}^{SJ}(r)$ fulfill the coupled system of equations

$$\phi_{ll'}^{SJ}(r) = j_l(pr) \delta_{ll'} + \int_0^\infty dr' r'^2 G_l(r, r') \sum_{l_1} U_{l_1, l}^{SJ}(r') \phi_{l_1 l'}^{SJ}(r'). \quad (6.23)$$

Here, $U_{l', l}^{SJ}(r) = m_N V_{l', l}^{SJ}(r)$ is the reduced nucleon–nucleon potential connecting the corresponding partial waves, and the radial Green’s function is defined as

$$G_l(r, r') = \frac{2}{\pi} \int dp' p'^2 \frac{\bar{Q}(P, p')}{p^2 - p'^2} j_l(p'r) j_l(p'r'). \quad (6.24)$$

Note that $G_l(r, r')$ also depends implicitly on the momenta P and p .

The same multipole expansion also applies to the defect function, $\Delta\psi$, which carries the high-momentum components and is defined as

$$|\psi\rangle = |\mathbf{p}, S m_S\rangle + |\Delta\psi\rangle, \quad (6.25)$$

with

$$|\Delta\psi\rangle = A \sum_{JM} \sum_{ll'm} i^{l'} Y_{l'm}^* (\hat{\mathbf{p}}) \langle l'm S m_s | JM \rangle \Delta\phi_{ll'}^{SJ}(r) \mathcal{Y}_{lSJ}(\hat{\mathbf{r}}), \quad (6.26)$$

$$\Delta\phi_{ll'}^{SJ}(r) = \int_0^\infty dr' r'^2 G_l(r, r') \sum_{l_1} U_{l_1, l}^{SJ}(r') \phi_{l_1 l'}^{SJ}(r'), \quad (6.27)$$

In Ref. [199] the case $P = 0$ was studied using the same formalism. Therefore, the present work can be regarded as an extension of that formalism to the general case $P \neq 0$. In the cited reference, only two functions appeared in the coupled-channel case with $S = 1$ and $l = J - 1, J + 1$, whereas in the present formalism there are four functions. This should not be viewed as a shortcoming of Ref. [199], since there the coupled equations were derived from the corresponding NN scattering equations, where the initial momentum is usually chosen along the z -axis. It can be shown that if the initial momentum \mathbf{p} is along the z -axis, only two radial functions are needed in the multipole expansion. Thus the results of Ref. [199] are correct for that particular case, while our equations have general validity.

Finally, it is customary to express the partial-wave equations in terms of the reduced radial functions and the reduced Green's function, defined as

$$\phi_{l,l'}^{SJ}(r) = \frac{u_{l,l'}^{SJ}(r)}{pr}, \quad j_l(pr) = \frac{\hat{j}_l(pr)}{pr}, \quad G_l(r, r') = \frac{\hat{G}_l(r, r')}{rr'} \quad (6.28)$$

where the reduced Green's function is given by,

$$\hat{G}_l(r, r') = \frac{2}{\pi} \int_0^\infty dp' \hat{j}_l(p'r) \frac{\bar{Q}(P, p')}{p^2 - p'^2} \hat{j}_l(p'r'). \quad (6.29)$$

The Bethe-Goldstone equations for the partial waves then take the form

$$u_{l,l'}^{SJ}(r) = \hat{j}_l(pr) \delta_{ll'} + \int_0^\infty dr' \hat{G}_l(r, r') \sum_{l_1} U_{l_1,l}^{SJ}(r') u_{l_1,l'}^{SJ}(r'). \quad (6.30)$$

Additionally, note that the functions $u_{l,l'}^{SJ}(r)$ also depend implicitly on the center-of-mass momentum P and the initial relative momentum p , although this dependence is omitted in the notation for brevity.

6.3. Application to the Granada 2013 potential

In the previous section we have presented the general formalism for solving the BG equation for any nucleon-nucleon potential that can be expressed in a partial-wave expansion. We now specialize to the case of the Granada 2013 potential, a coarse-grained interaction that greatly simplifies the solution of the integral equations. This potential was fitted in a partial-wave analysis of pp and np scattering data below the pion-production threshold with high precision. Here, we apply it directly to the study of short-range correlations in nuclear matter.

The potential is defined as a sum of delta-shells for each channel, specified by the total spin S and total angular momentum J :

$$U_{l,l'}^{SJ}(r) = \sum_{i=1}^{N_\delta} (\lambda_i)_{l,l'}^{SJ} \delta(r - r_i), \quad (6.31)$$

λ_1 [fm $^{-1}$]	λ_2 [fm $^{-1}$]	λ_3 [fm $^{-1}$]	λ_4 [fm $^{-1}$]	λ_5 [fm $^{-1}$]	Partial Waves
1.31	-0.723	-0.187	0.000	-0.024	1S_0
0.0	1.19	0.000	0.076	0.000	1P_1
0.0	-0.23	-0.199	0.000	-0.0195	1D_2
0.0	0.000	0.130	0.091	0.000	1F_3
0.0	1.00	-0.339	-0.054	0.025	3P_0
0.0	1.361	0.000	0.0579	0.000	3P_1
0.0	-1.06	-0.140	-0.243	-0.019	3D_2
0.0	0.52	0.000	0.000	0.000	3D_3
1.58	-0.44	0.000	-0.073	0.000	3S_1
0.0	-1.65	-0.34	-0.233	-0.020	ϵ_1
0.0	0.000	0.35	0.104	0.014	3D_1
0.0	-0.483	0.000	-0.0280	-0.0041	3P_2
0.0	0.28	0.200	0.046	0.0138	ϵ_2
0.0	3.52	-0.232	0.000	-0.0139	3F_2

Table 6.1: Parameters λ_i used for each partial wave. For coupled channels, ϵ_1 and ϵ_2 refer to partial waves $^3D_1/ ^3S_1$, $^3S_1/ ^3D_1$ for $J = 1$ and $^3F_2/ ^3P_2$, $^3P_2/ ^3F_2$ for $J = 2$.

In the potential the number of delta-shells is fixed to $N_\delta = 5$, with $r_i = i \Delta r$ and $\Delta r = 0.6$ fm. The values of the delta-shells strengths $(\lambda_i)_{l,l'}^{SJ}$ are given in Table (6.1). The chosen value of Δr provides the optimal resolution allowed by the data. As shown in Ref. [197], adding more delta-shells does not improve the description of the elastic NN scattering data. On the contrary, from a statistical point of view, the quality of the fits does not increase, while correlations among fitting parameters become stronger, rendering the additional deltas largely redundant.

In this calculation we neglect the one-pion exchange (OPE) contribution, which starts at distances larger than 3 fm. While this contribution is essential to describe the physical scattering data with a high quality fit (particularly for the peripheral waves), its influence becomes marginal for the study of short distance correlations and makes the calculation unnecessarily more cumbersome.

6.3.1. Solutions in coordinate space

With the potential given in Eq. (6.31), the integration over the radial coordinate in Eq. (6.30) can be carried out analytically. One then obtains the following algebraic equation:

$$u_{l,l'}^{SJ}(r) = \hat{j}_l(pr) \delta_{ll'} + \sum_i \hat{G}_l(r, r_i) \sum_{l_1} (\lambda_i)_{l_1 l}^{SJ} u_{l_1 l'}^{SJ}(r_i), \quad (6.32)$$

This allows us to transform the coupled integral equation for the radial wave functions, Eq. (6.30), into a linear system of algebraic equations for the values of radial wave functions at the *grid points* r_i . In fact, by evaluating Eq. (6.32) at $r = r_j$ with $j = 1, 2, \dots, N_\delta$, one

obtains the coupled linear system:

$$u_{ll'}^{SJ}(r_j) = \hat{j}_l(pr_j)\delta_{ll'} + \sum_i \hat{G}_l(r_j, r_i) \sum_{l_1} (\lambda_i)_{l_1 l}^{SJ} u_{l_1 l'}^{SJ}(r_i). \quad (6.33)$$

By solving these equations for fixed S and J , one obtains the values of $u_{ll'}^{SJ}(r_i)$ at the grid points r_i . Then, by inserting these values into Eq. (6.32), the wave function can be reconstructed at any arbitrary point r , thus providing the complete solution of the problem.

We now proceed to write the explicit equations for each channel, classified according to the value of S and J , taking into account that the interaction conserves parity and therefore does not couple states with orbital angular momenta of opposite parity, i.e. odd l with even l' .

Case (a): $S = 0$, $J = 0, 1, 2, 3$, and $l = l' = J$. Partial waves: 1S_0 , 1P_1 , 1D_2 , and 1F_3 .

Since $\mathbf{J} = \mathbf{L} + \mathbf{S}$, for $S = 0$ the only allowed orbital angular momentum is $l = J$, so there is a single radial function $u^{0J}(r) \equiv u_J^{0J}(r) \equiv u_{JJ}^{0J}(r)$. Hence, for each J one obtains an independent set of 5 algebraic equations for the values of the radial functions $u_{JJ}^{0J}(r_i)$ at the points r_i .

$$u_{JJ}^{0J}(r_j) = \hat{j}_J(pr_j) + \sum_i \hat{G}_J(r_j, r_i) (\lambda_i)_{JJ}^{0J} u_{JJ}^{0J}(r_i). \quad (6.34)$$

Case (b): $S = 1$, $J = 0$, and $l = l' = 1$. Partial wave: 3P_0 .

Since $J = 0$, for $S = 1$ the only allowed orbital angular momentum is $l = 1$, so there is a single radial function $u^{10}(r) \equiv u_1^{10}(r) \equiv u_{11}^{10}(r)$.

$$u_{11}^{10}(r_j) = \hat{j}_1(pr_j) + \sum_i \hat{G}_1(r_j, r_i) (\lambda_i)_{11}^{10} u_{11}^{10}(r_i). \quad (6.35)$$

Case (c): $S = 1$, $J = 1, 2$, and $l = l' = J$. Partial waves: 3P_1 , 3D_2 .

When $S = 1$ and $J > 0$, there are three possibilities, $l = J-1, J, J+1$. But due to parity conservation, the partial waves with angular momenta $l = l' = J$ (parity $P = (-1)^J$) are decoupled from those with $l, l' = J \pm 1$ (parity $P = (-1)^{J+1}$). In the former case, $l = l' = J$, there is again a single radial function $u^{1J}(r) \equiv u_J^{1J}(r) \equiv u_{JJ}^{1J}(r)$, and the corresponding equations are

$$u_{JJ}^{1J}(r_j) = \hat{j}_J(pr_j) + \sum_i \hat{G}_J(r_j, r_i) (\lambda_i)_{JJ}^{1J} u_{JJ}^{1J}(r_i). \quad (6.36)$$

Case (d): $S = 1$, $J = 1, 2$, and $l, l' = J \pm 1$. Partial waves: 3S_1 , 3D_1 , $^3D_1/{}^3S_1$, ${}^3S_1/{}^3D_1$, and 3P_2 , 3F_2 , ${}^3F_2/{}^3P_2$, ${}^3P_2/{}^3F_2$

The partial waves $u_{J\pm 1, J\pm 1}^{1J}(r)$ are coupled due to the tensor part of the NN interaction, which has off-diagonal components in the orbital angular momentum basis. The

corresponding equations are

$$u_{J+1,J+1}^{1J}(r_j) = \hat{j}_{J+1}(pr_j) + \sum_i \hat{G}_{J+1}(r_j, r_i)[(\lambda_i)_{J+1,J+1}^{1J} u_{J+1,J+1}^{1J}(r_i) + (\lambda_i)_{J-1,J+1}^{1J} u_{J-1,J+1}^{1J}(r_i)] \quad (6.37)$$

$$u_{J-1,J+1}^{1J}(r_j) = \sum_i \hat{G}_{J-1}(r_j, r_i)[(\lambda_i)_{J+1,J-1}^{1J} u_{J+1,J+1}^{1J}(r_i) + (\lambda_i)_{J-1,J-1}^{1J} u_{J-1,J+1}^{1J}(r_i)] \quad (6.38)$$

$$u_{J-1,J-1}^{1J}(r_j) = \hat{j}_{J-1}(pr_j) + \sum_i \hat{G}_{J-1}(r_j, r_i)[(\lambda_i)_{J+1,J-1}^{1J} u_{J+1,J-1}^{1J}(r_i) + (\lambda_i)_{J-1,J-1}^{1J} u_{J-1,J-1}^{1J}(r_i)] \quad (6.39)$$

$$u_{J+1,J-1}^{1J}(r_j) = \sum_i \hat{G}_{J+1}(r_j, r_i)[(\lambda_i)_{J+1,J+1}^{1J} u_{J+1,J-1}^{1J}(r_i) + (\lambda_i)_{J-1,J+1}^{1J} u_{J-1,J-1}^{1J}(r_i)] \quad (6.40)$$

Upon closer inspection, we find that there are in fact two independent systems of coupled equations: one for the pairs $u_{J\pm 1,J\pm 1}^{1J}$, Eqs. (6.37,6.38), and another for the pairs $u_{J\pm 1,J-1}^{1J}$, Eqs. (6.39,6.40). Thus, the problem reduces to solving two linear systems of 10 equations each, instead of a single system of 20 equations for the grid-point values.

Case (e): $S = 1$, $J = 3$, and $l = l' = 2$. Partial wave: 3D_3 .

In fact, this is a particular case of (d) with $J = 3$ and $l, l' = 2, 4$, but where the $l = 4$ components vanish, i.e., the 3H_3 wave is absent. This happens because partial waves with higher orbital angular momentum ($l \geq 4$) were not needed to reproduce the scattering data in the partial-wave analysis. Consequently, the equations for this wave reduce to those of the previous uncoupled case.

$$u_{22}^{13}(r_j) = \hat{j}_2(pr_j) + \sum_i \hat{G}_2(r_j, r_i)(\lambda_i)_{22}^{13} u_{22}^{13}(r_i). \quad (6.41)$$

To compute the correlated wave function of a pair with total momentum (P) and relative momentum (p), one must solve the linear systems described above: five equations for uncoupled waves and (10+10) equations for coupled waves in all the (S,J) channels considered. This requires only the λ_i parameters of the potential from the table and the Green's function values $G_l(r_i, r_j)$, the latter being computed with the method outlined in Appendix J.

6.4. Solutions in momentum space

The probability amplitude to find the correlated state with relative momentum \mathbf{p}' and spin projection m'_S is

$$\langle \mathbf{p}' Sm'_s | \psi \rangle = \frac{2}{\pi} \left\langle \sum_{J_1 M_1} \sum_{l_1 m_1} i^{l_1} Y_{l_1 m_1}^*(\hat{\mathbf{p}'}) \langle l_1 m_1 Sm'_s | J_1 M_1 \rangle j_{l_1}(p' r) \mathcal{Y}_{l_1 S J_1 M_1}(\hat{\mathbf{r}}) \right| \\ \times \left| \sum_{JM} \sum_{ll'm} i^{l'} Y_{l'm}^*(\hat{\mathbf{p}}) \langle l'm Sm_s | JM \rangle \phi_{ll'}^{SJ}(r) \mathcal{Y}_{l S J M}(\hat{\mathbf{r}}) \right\rangle. \quad (6.42)$$

By exploiting the orthonormality of the spin-coupled spherical harmonics,

$$\langle \mathcal{Y}_{l_1 S J_1 M_1}(\hat{\mathbf{r}}) | \mathcal{Y}_{l S J M}(\hat{\mathbf{r}}) \rangle = \delta_{l_1 l} \delta_{J_1 J} \delta_{M_1 M},$$

we obtain

$$\langle \mathbf{p}' Sm'_s | \psi \rangle = \frac{2}{\pi} \sum_{JM} \sum_{m_1} \sum_{l, l', m} i^{l' - l} Y_{l m_1}(\hat{\mathbf{p}'}) Y_{l'm}^*(\hat{\mathbf{p}}) \langle l m_1 Sm'_s | JM \rangle \langle l'm Sm_s | JM \rangle \\ \times \int_0^\infty dr r^2 j_l(p' r) \phi_{ll'}^{SJ}(r). \quad (6.43)$$

We identify the radial partial wave function in momentum representation as

$$\tilde{\phi}_{ll'}^{SJ}(p') = \sqrt{\frac{2}{\pi}} \int_0^\infty dr r^2 j_l(p' r) \phi_{ll'}^{SJ}(r) \quad (6.44)$$

or, in terms of the reduced partial waves $u_{ll'}^{SJ}(r)$,

$$\tilde{\phi}_{ll'}^{SJ}(p') = \sqrt{\frac{2}{\pi}} \frac{1}{pp'} \int_0^\infty dr r^2 \hat{j}_l(p' r) u_{ll'}^{SJ}(r). \quad (6.45)$$

Using that

$$\langle Sm'_s | \mathcal{Y}_{l S J M}(\hat{\mathbf{p}'}) \rangle = \sum_{m_1} Y_{l m_1}(\hat{\mathbf{p}'}) \langle l m_1 Sm'_s | JM \rangle \quad (6.46)$$

we can write

$$\langle \mathbf{p}' Sm'_s | \psi \rangle = \sqrt{\frac{2}{\pi}} \sum_{JM} \sum_{l, l', m} i^{l' - l} Y_{l'm}^*(\hat{\mathbf{p}}) \langle l'm Sm_s | JM \rangle \tilde{\phi}_{ll'}^{SJ}(p') \langle Sm'_s | \mathcal{Y}_{l S J M}(\hat{\mathbf{p}'}) \rangle. \quad (6.47)$$

Then the correlated wave function in momentum space expands into the multipole series

$$\langle \mathbf{p}' | \psi \rangle = \sqrt{\frac{2}{\pi}} \sum_{JM} \sum_{l, l', m} i^{l' - l} Y_{l'm}^*(\hat{\mathbf{p}}) \langle l'm Sm_s | JM \rangle \tilde{\phi}_{ll'}^{SJ}(p') \mathcal{Y}_{l S J M}(\hat{\mathbf{p}}) \quad (6.48)$$

To obtain an explicit form of the radial wave function $\tilde{\phi}_{ll'}^{SJ}(p')$, one substitutes the coordinate-space function $u_{ll'}^{SJ}(r)$ from Eq. (6.33) into Eq. (6.45), employs the Green's function $\hat{G}_l(r, r')$

of Eq. (6.29), and performs the radial integration. The orthogonality of the reduced spherical Bessel functions must also be used:

$$\int_0^\infty dr \hat{j}_l(pr) \hat{j}_l(p'r) = \frac{\pi}{2} \delta(p - p'), \quad (6.49)$$

The final result is:

$$\tilde{\phi}_{ll'}^{SJ}(p') = \sqrt{\frac{\pi}{2}} \frac{1}{pp'} \delta_{ll'} \delta(p - p') + \Delta \tilde{\phi}_{ll'}^{SJ}(p'), \quad (6.50)$$

where

$$\Delta \tilde{\phi}_{ll'}^{SJ}(p') = \sqrt{\frac{2}{\pi}} \frac{1}{pp'} \overline{Q}(P, p') \sum_{i=1}^{N_\delta} \hat{j}_l(p'r_i) \sum_{l_1} (\lambda_i)_{l_1, l}^{SJ} u_{l_1 l'}^{SJ}(r_i). \quad (6.51)$$

The first term of Eq. (6.50) corresponds to the unperturbed radial component of the state $|\psi\rangle$ of Eq. (6.15), while the second term, given explicitly in Eq. (6.51), corresponds genuinely to the high momentum components induced in the perturbed relative wave function by the N-N interaction and the medium. The angle-averaged Pauli projector $\overline{Q}(P, p')$ ensures that low-momentum components are excluded, so that only high-momentum states contribute. The explicit dependence on p' appears both in the denominator $1/[p'(p^2 - p'^2)]$ and in the spherical Bessel functions $\hat{j}_l(p'r_i)$, which in the asymptotic limit behave as

$$\hat{j}_l(p'r) \xrightarrow[p' \rightarrow \infty]{} \sin(p'r - l\pi/2). \quad (6.52)$$

Consequently, the overall asymptotic behavior of the high-momentum wave function is

$$\Delta \tilde{\phi}_{ll'}^{SJ}(p') \sim \frac{1}{p'^3}, \quad p' \rightarrow \infty. \quad (6.53)$$

6.4.1. High-momentum distribution

We consider a nucleon pair with total spin S , total momentum \mathbf{P} , and relative momentum \mathbf{p} . The high-momentum distribution is computed by integrating over the angles the square of the high-momentum wave function and summing over the final spin projections μ' , while averaging over the initial projections μ . This procedure yields the angle-averaged radial high-momentum distribution of the nucleon pair induced by SRC:

$$\begin{aligned} \rho_{P,p}^S(p') &= \frac{1}{2S+1} \sum_{\mu\mu'} \int d\Omega' |\langle \mathbf{p}' S \mu' | \psi \rangle|^2 \\ &= \sum_{\mu\mu'} \int d\Omega' \left[\sqrt{\frac{2}{\pi}} \sum_{JM} \sum_{l,l',m} i^{l'-l} Y_{l'm}^*(\hat{\mathbf{p}}) \langle l'm S \mu | JM \rangle \tilde{\phi}_{ll'}^{SJ}(p') \langle S \mu' | \mathcal{Y}_{lSJ}(\hat{\mathbf{p}}') \rangle \right]^* \\ &\times \sqrt{\frac{2}{\pi}} \sum_{J_1 M_1} \sum_{l_1, l'_1, m_1} i^{l'_1 - l_1} Y_{l'_1 m_1}^*(\hat{\mathbf{p}}) \langle l'_1 m_1 S \mu | J_1 M_1 \rangle \tilde{\phi}_{l_1 l'_1}^{SJ}(p') \langle S \mu' | \mathcal{Y}_{l_1 S J_1 M_1}(\hat{\mathbf{p}}') \rangle. \end{aligned} \quad (6.54)$$

Where Ω' refers to the angles of \mathbf{p}' . We use the orthogonality property of the spin-coupled spherical harmonics $\mathcal{Y}_{lSJM}(\hat{\mathbf{p}})$ to perform the integration:

$$\sum_{\mu'} \int d\Omega' \langle \mathcal{Y}_{lSJM}(\hat{\mathbf{p}}') | S\mu' \rangle \langle S\mu' | \mathcal{Y}_{l_1SJ_1M_1}(\hat{\mathbf{p}}') \rangle = \delta_{l,l_1} \delta_{J,J_1} \delta_{M,M_1}. \quad (6.55)$$

Upon summation over l_1, J_1, M_1 we arrive at

$$\begin{aligned} \rho_{P,p}^S(p') &= \frac{2}{\pi} \frac{1}{2S+1} \sum_{\mu} \sum_{JM} \sum_{ll'm} \sum_{l_1'm_1} i^{l_1'-l'} Y_{l'm}(\hat{\mathbf{p}}) Y_{l_1'm_1}^*(\hat{\mathbf{p}}) \\ &\quad \times \langle l'mS\mu | JM \rangle \langle l_1'm_1S\mu | JM \rangle \tilde{\phi}_{ll'}^{SJ}(p') \tilde{\phi}_{ll_1'}^{SJ}(p') \end{aligned} \quad (6.56)$$

Using the symmetry properties of the coupling coefficients under the interchange of angular momenta l' and J ,

$$\begin{aligned} \langle l'mS\mu | JM \rangle &= (-1)^{S+m_s} \sqrt{\frac{2J+1}{2l'+1}} \langle J, -MS\mu | l', -m \rangle. \\ \langle l_1'm_1S\mu | JM \rangle &= (-1)^{S+m_s} \sqrt{\frac{2J+1}{2l'+1}} \langle J, -MS\mu | l_1', -m_1 \rangle. \end{aligned} \quad (6.57)$$

we can perform the sum over M, μ of the product of two CG coefficients:

$$\sum_{\mu M} \langle l'mS\mu | JM \rangle \langle l_1'm_1S\mu | JM \rangle = \frac{2J+1}{2l'+1} \delta_{l'l_1'} \delta_{mm_1} \quad (6.58)$$

After carrying out the sums over l_1' and m_1 , the momentum distribution (6.56) takes the form

$$\rho_{P,p}^S(p') = \frac{2}{\pi} \frac{1}{2S+1} \sum_J \sum_{ll'm} |Y_{l'm}(\hat{\mathbf{p}})|^2 \frac{2J+1}{2l'+1} \tilde{\phi}_{ll'}^{SJ}(p')^2 \quad (6.59)$$

In the last step, we make use of the property that the sum over m of the squared spherical harmonics, $\sum_m |Y_{lm}(\hat{\mathbf{p}})|^2$, has a simple analytical expression.

$$\sum_m |Y_{l'm}(\hat{\mathbf{p}})|^2 = \frac{2l'+1}{4\pi}, \quad (6.60)$$

thus obtaining the final result

$$\rho_{P,p}^S(p') = \frac{1}{2S+1} \sum_J \frac{2J+1}{4\pi} \sum_{l,l'} \frac{2}{\pi} \left| \tilde{\phi}_{l,l'}^{SJ}(p') \right|^2. \quad (6.61)$$

The high-momentum components of the correlated nucleon pair wave functions arise from short-range correlations in the nuclear medium. From the defect function defined in Eq. (6.51), for large relative momenta p' one finds $\tilde{\phi}_{ll'}^{SJ}(p') = \Delta \tilde{\phi}_{ll'}^{SJ}(p') \sim 1/p'^3$, so that the square of the wave function scales as $|\Delta \tilde{\phi}_{ll'}^{SJ}(p')|^2 \sim 1/p'^6$ for large values of p' . Including the phase-space factor p'^2 , the corresponding momentum distribution of the pair given by Eq. (6.61), exhibits a characteristic $1/p'^4$ tail [207, 208].

6.5. Results

In this section we present the results obtained for SRC from the solution of the BG equation with the Granada 2013 interaction. We display the correlated radial wave functions both in coordinate and momentum space, for the different channels arising in the multipole expansion. In addition, we analyze the associated correlation functions and momentum distributions, which provide direct insight into the role of SRC in generating high-momentum components in nuclear matter. In particular, we investigate the dependence of the results on the center-of-mass momentum \mathbf{P} , in order to assess whether the short-range correlations are significantly affected by \mathbf{P} , considering that correlated pairs are typically back-to-back (i.e., $\mathbf{P} = 0$). We show the results for a Fermi momentum of $k_F = 250$ MeV/c and an initial relative momentum of the pair of $p = 140$ MeV/c, in order to compare with what was done in the previous study of Ref. Ref. [199] for $P = 0$. For definiteness, we present results for a relative momentum of $p = 140$ MeV/c, roughly half the Fermi momentum; we have verified, however, that our conclusions regarding the dependence on the center-of-mass momentum \mathbf{P} are largely insensitive to the particular choice of p .

6.5.1. Uncoupled waves in coordinate space

In Fig. 6.1 we present the reduced radial wave functions $u_{ll'}^{SJ}(r)$ for the uncoupled partial waves, obtained as solutions of Eq. (6.32). Each panel displays several curves corresponding to different total center-of-mass momenta of the nucleon pair, $P = 0, 100, 200, 300$, and 400 MeV/c. These values are consistent with a fixed relative momentum $p = 140$ MeV/c, while ensuring that both initial single-nucleon momenta remain below the Fermi momentum k_F . The figure also includes the unperturbed wave function for comparison.

We observe that the effect of SRC is to modify the wave function at short distances ($r < 3$ fm), enhancing its curvature, whereas at large distances all correlated curves converge to the uncorrelated one. The stronger impact of SRCs on low- l partial waves arises both from the strength parameters of the delta-shell potential, $(\lambda_i)_{l,l'}^{SJ}$, and from the centrifugal barrier, which increases with l and hinders the nucleons from approaching each other. Consequently, SRC effects are most visible at short distances in S- and P-waves, while they are strongly suppressed in higher partial waves such as D or F.

Figure 6.1 shows that the effect of the two-nucleon CM motion on the radial wave functions is generally small, with the correlated waves largely independent of the CM momentum. Small differences are slightly more visible at short distances in low-lying partial waves (S and P) and in the triplet 3D_2 compared to the singlet 1D_2 , reflecting the stronger attraction of the first delta-shell parameter.

To highlight the effect of SRCs, Fig. 6.2 shows the defect wave functions, defined as

$$\Delta u_{ll'}^{SJ}(r) \equiv u_{ll'}^{SJ}(r) - \hat{j}_l(pr), \quad (6.62)$$

which quantify the distortion of the radial waves due to SRCs. The defect generally decreases with increasing orbital angular momentum l , reflecting the centrifugal barrier that

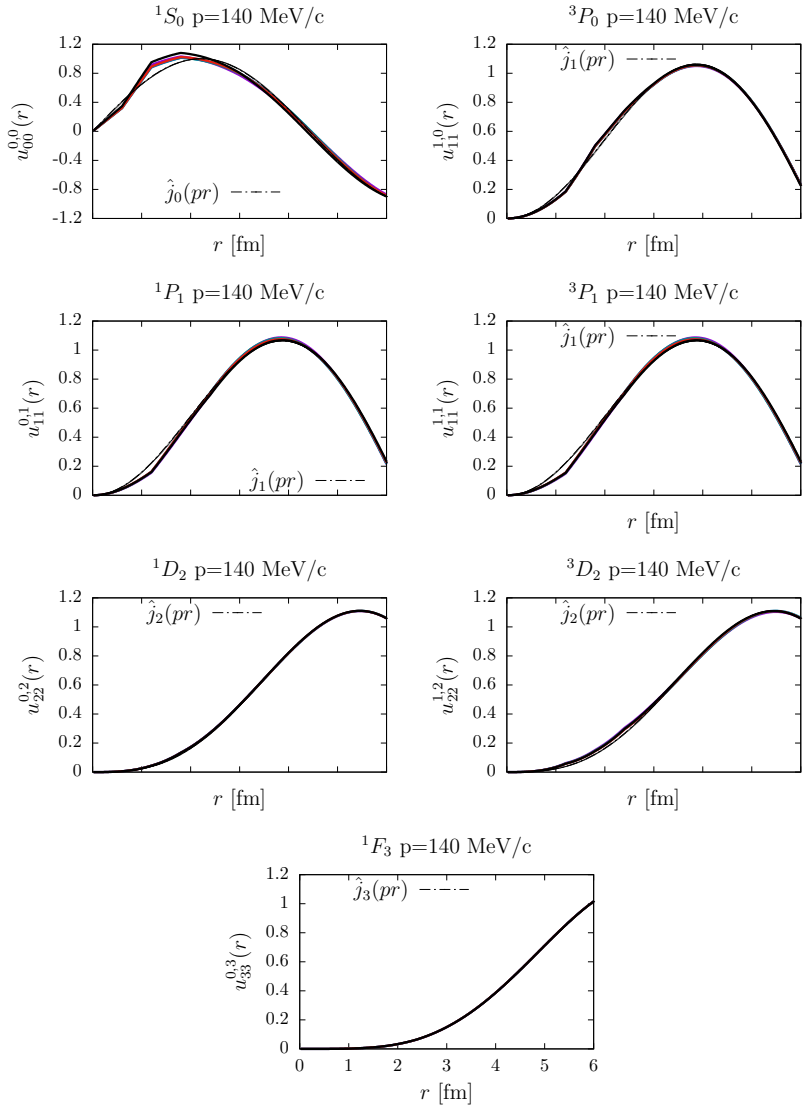


Figure 6.1: Reduced radial wave functions $u_{ll'}^{SJ}(r)$ for the uncoupled N-N partial waves ($l = l'$) at relative momentum $p = 140 \text{ MeV}/c$. For each partial wave, both the free solution $\hat{j}_l(pr)$ and the correlated waves for various CM momenta are shown.

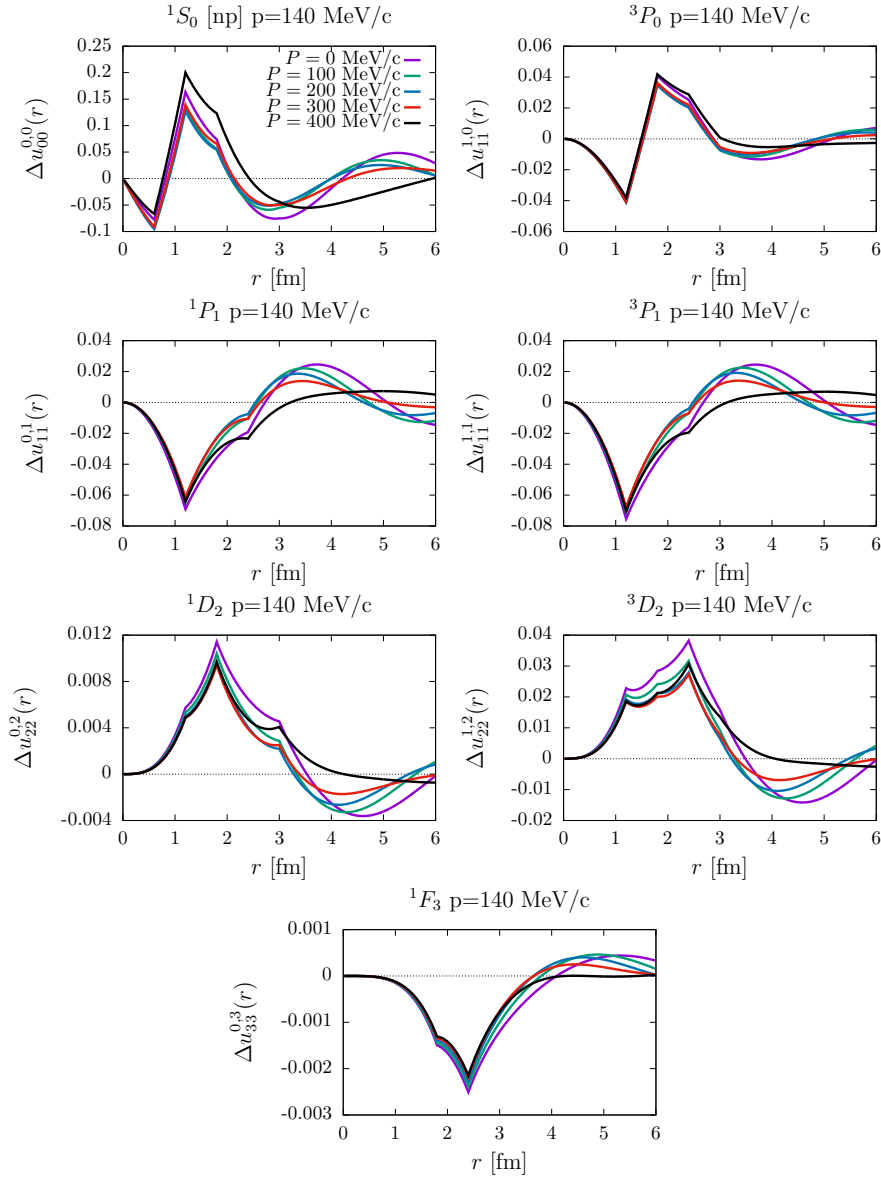


Figure 6.2: Defect wave functions $\Delta u_{ll'}^{SJ}(r) \equiv u_{ll'}^{SJ}(r) - \hat{j}_l(pr)$ for the uncoupled N-N partial waves ($l = l'$) at relative momentum $p = 140$ MeV/c. Results are shown for several values of the CM momentum.

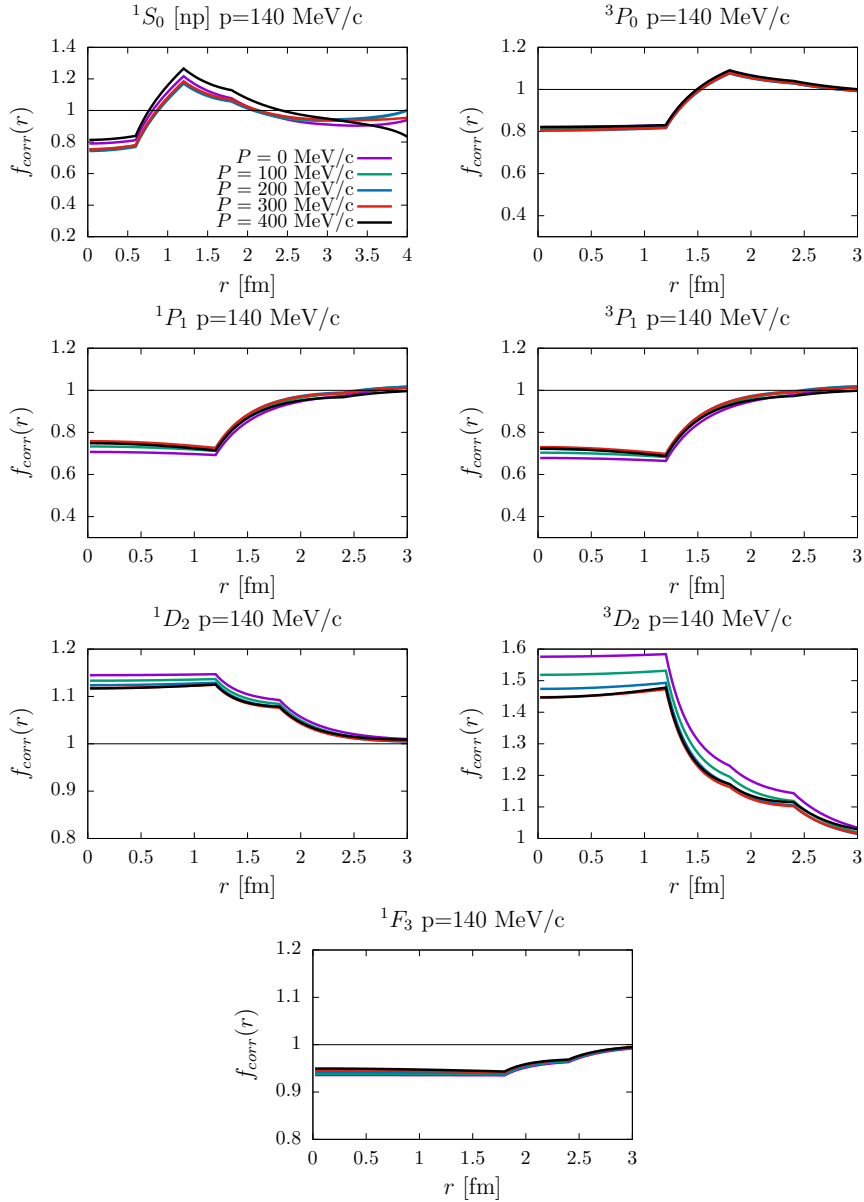


Figure 6.3: Correlation functions $f_{\text{corr}}(r) \equiv u_{ll'}^{SJ}(r)/\hat{j}_l(pr)$ for the uncoupled N-N partial waves ($l = l'$) at relative momentum $p = 140$ MeV/c. Results are shown for several CM momenta.

limits the nucleons' approach to short distances, although the delta-shell strength parameters also contribute. In contrast, the magnitude of the distortion is largely insensitive to the CM momentum. We anticipate that the amplitudes of these distortions are directly related to the high-momentum components of the wave function, which will be reflected in the relative momentum distributions discussed later.

Figure 6.3 shows the correlation functions for each uncoupled N-N partial wave,

$$f_{\text{corr}}(r) \equiv \frac{u_{ll'}^{SJ}(r)}{\hat{j}_l(pr)}, \quad (6.63)$$

which deviate from unity only at short distances, illustrating the “healing” property of the BG equation: correlations, or “wounds” in the unperturbed wave, are confined to short relative distances [206]. The correlation functions show little sensitivity to the CM momentum, with the largest variations near the origin in the 3D_2 partial wave.

In the literature, correlation functions are often defined such that $f(r) \rightarrow 1$ at large distances (beyond the healing distance). With the BG solutions, one might be concerned if the zeros of the correlated wave do not exactly coincide with those of the free wave when forming the quotient. However, this is not an issue here, since we compute the correlated wave function directly from the BG equation, rather than as a product of a correlation function and the free wave. Any differences at the nodes are infinitesimal and do not affect the physical content of the wave functions. For example, the 1S_0 correlation function in Fig. 6.3 is plotted only up to 4 fm, since the corresponding node for the chosen p lies between 4 and 5 fm in Fig. 6.1.

6.5.2. Coupled waves in coordinate space

Results for the radial wave functions of the coupled partial waves are shown in Fig. 6.4 for $J = 1$ and in Fig. 6.5 for $J = 2$. We present results for different values of the CM momentum of the two-nucleon system and for a relative momentum of $p = 140$ MeV/c.

In the case $S = J = 1$ (Fig. 6.4), the four wave functions split into two independent pairs, each arising from a distinct set of coupled equations. The first pair, $u_{00}^{11}(r)$ and $u_{20}^{11}(r)$, obtained from Eqs. (6.39,6.40), correspond to the 3S_1 (top left) and to the interference $^3D_1/^3S_1$ (bottom left) components. The second pair, $u_{22}^{11}(r)$ and $u_{02}^{11}(r)$, obtained from Eqs. (6.37,6.38), correspond to the 3D_1 (top right) and the interference $^3S_1/^3D_1$ (bottom right) components.

Correlations strongly modify the 3S_1 wave, much more than in the 1S_0 channel. They also generate a non-vanishing $^3D_1/^3S_1$ interference, entirely produced by the tensor force, which couples partial waves with $l \pm 1$ and drives the dynamics in the coupled channel. The effect of the CM momentum is limited to small quantitative changes in the correlated wave functions. Overall, the dependence on P is weak, with only minor deviations from the $P = 0$ case of back-to-back nucleons.

For the second pair of solutions in the $J = 1$ channel, namely 3D_1 and $^3S_1/^3D_1$, the 3D_1 wave remains almost indistinguishable from the uncorrelated solution. This behavior

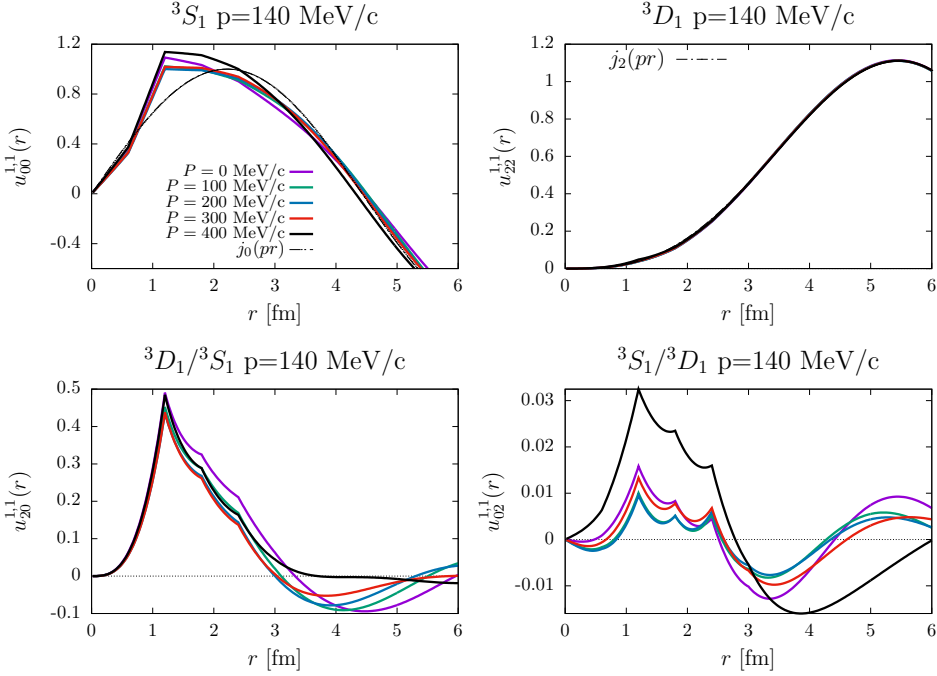


Figure 6.4: Radial wave functions $u_{ll'}^{SJ}(r)$ for the coupled partial waves with $S = J = 1$ and $l, l' = 0, 2$, at relative momentum $p = 140$ MeV/c. The corresponding uncorrelated waves $j_l(pr)$ are also shown. Results are presented for CM momenta $P = 0, 100, 200, 300, 400$ MeV/c. Top panels: diagonal components ($l = l'$); bottom panels: off-diagonal components ($l \neq l'$).

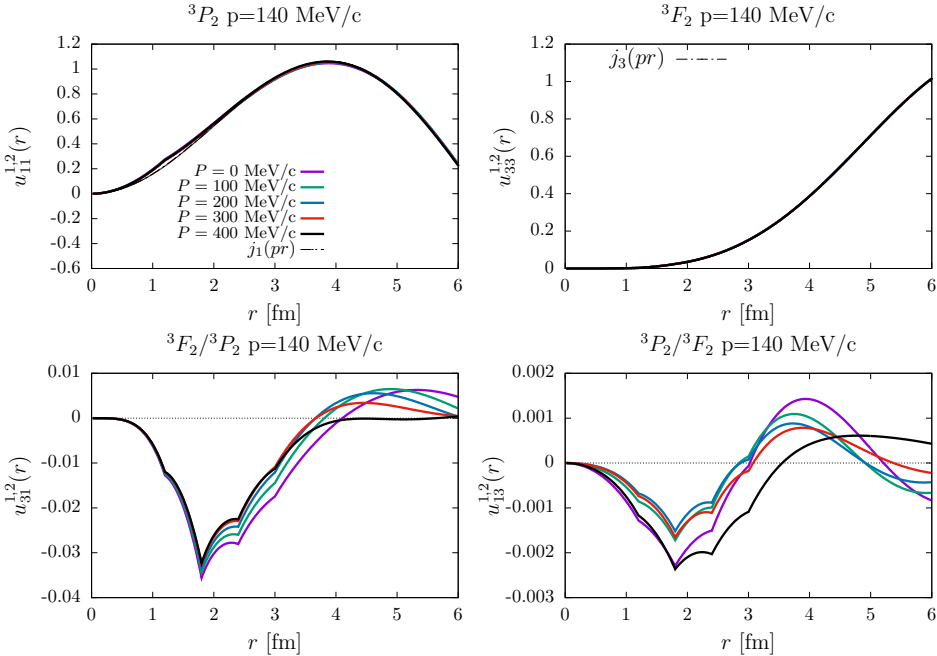


Figure 6.5: The same as fig. 6.4 but for $l, l' = 1, 3$ and $J = 2$

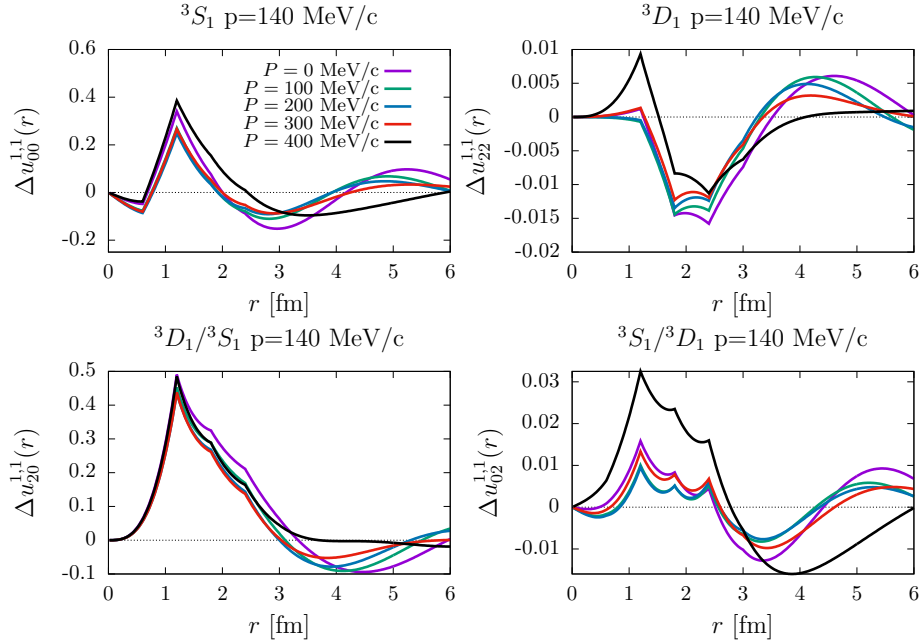


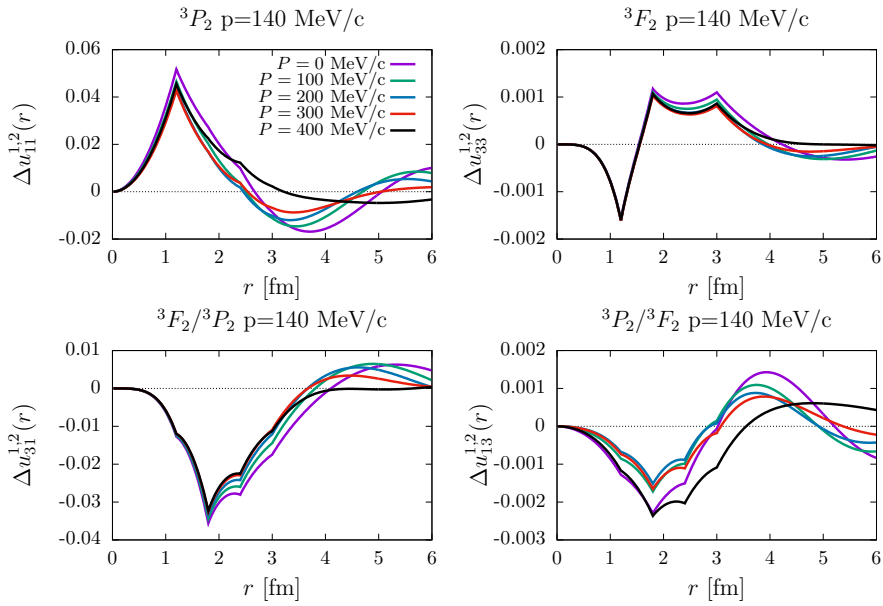
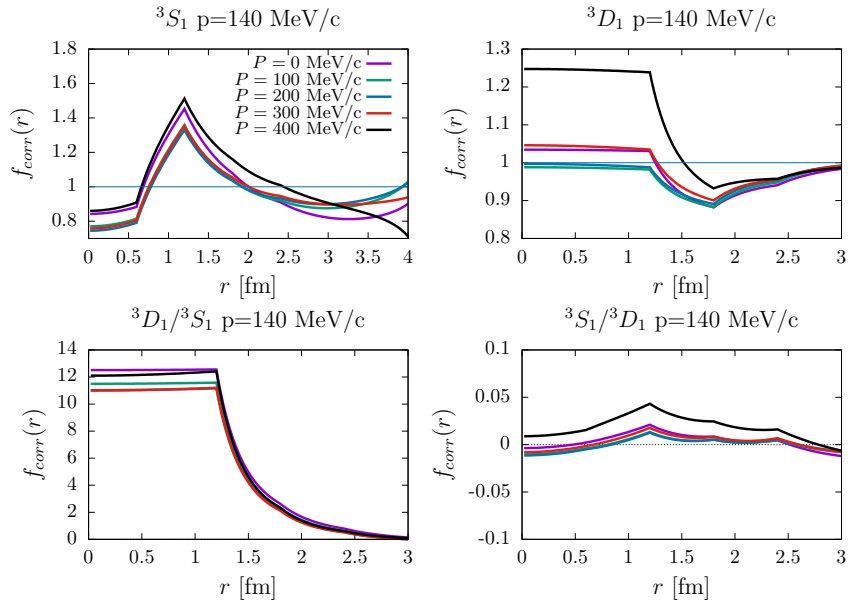
Figure 6.6: Defect wave functions for the coupled channel with $J = 1$. The top panels display the diagonal components, $\Delta u_{ll}^{SJ}(r) \equiv u_{ll}^{SJ}(r) - \hat{j}_l(pr)$, while the bottom panels show the off-diagonal components, $\Delta u_{ll'}^{SJ}(r) \equiv u_{ll'}^{SJ}(r)$ for $l \neq l'$. Results are given for relative momentum $p = 140$ MeV/c and for several values of the CM momentum.

is mainly due to the centrifugal barrier, which prevents the nucleons from approaching short distances at higher orbital angular momentum, together with the fact that in the 3D_1 channel the first two delta-shell strengths vanish. On the other hand, the mixing with the 3S_1 component, shown in the bottom-right panel, is visible but comparatively small, especially when contrasted with the much stronger $^3D_1/^3S_1$ interference discussed earlier. Of course, in the case of the small $^3S_1/^3D_1$ interference, the relative effect of the CM momentum appears amplified. However, this is simply because one is examining a very small effect on a quantity that is itself already small.

In the coupled-channel case $J = 2$, shown in Fig. 6.5, the effect of SRCs is extremely small. A slight bending of the radial functions can be seen between 1 and 2 fm, but the departure from the free Bessel solution is negligible, and in the 3F_2 wave no visible effect appears within the scale of the figure. Some tensor-induced mixing is observed in the $^3F_2/^3P_2$ and, to a much lesser extent, in the $^3P_2/^3F_2$ components, but overall the SRC effects in this channel are practically insignificant.

For completeness, we show in Figs. 6.6 and 6.7 the defect wave functions corresponding to the coupled channels $J = 1$ and $J = 2$, respectively. In this case we define $\Delta u_{ll}(r) \equiv u_{ll}(r) - \hat{j}_l(pr)$ for the diagonal components, and $\Delta u_{ll'}(r) \equiv u_{ll'}(r)$ for the off-diagonal ones ($l \neq l'$). The results indicate that Δu_{ll} is comparable in magnitude to its coupled partner, as can be appreciated by comparing the top and bottom panels of the figures.

In Figs. 6.8–6.9 we present the correlation functions for the coupled partial waves. This

Figure 6.7: The same as fig. 6.6 for $J = 2$ and $l, l' = 1, 3$ Figure 6.8: Correlation functions $f_{\text{corr}}(r)$ for the diagonal wave functions (top panels) and off-diagonal wave functions (bottom panels) for the coupled partial waves for $J = 1$ and $l, l' = 0, 2$.

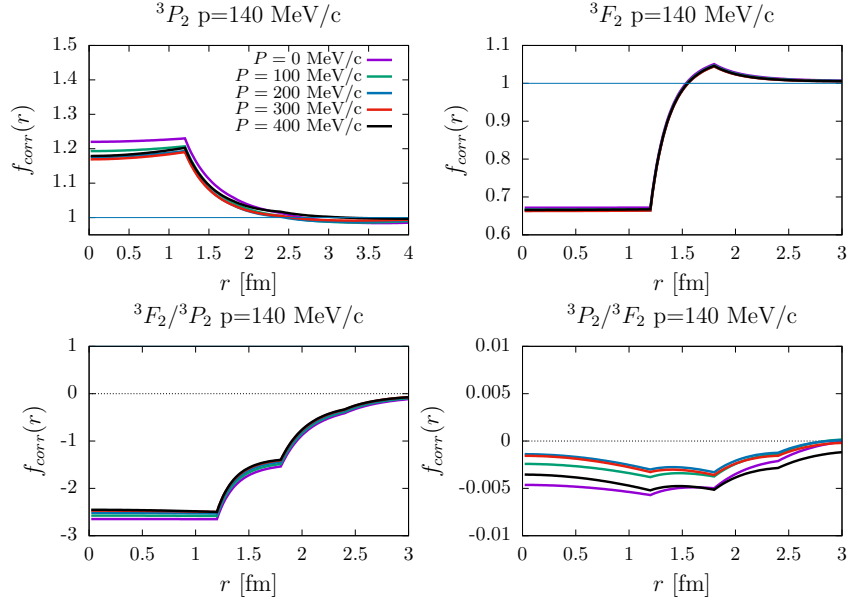


Figure 6.9: The same as fig. 6.8 for $J = 2$ and $l, l' = 1, 3$

definition only applies to the diagonal components, for which

$$f_{\text{corr}}(r) = \frac{u_{ll}(r)}{\hat{j}_l(pr)},$$

so that $f_{\text{corr}}(r) \rightarrow 1$ at large distances. As in the uncoupled case, one should keep in mind the mismatch of the nodes between numerator and denominator, although this does not affect the interpretation at short distances ($r \lesssim 3$ fm), where $f_{\text{corr}}(r)$ provides a clear visualization of the wound and its healing. In Fig. 6.8, the correlation function of the 3S_1 wave shows a behavior very similar to the 1S_0 case: a strong oscillation from ~ 0.8 to ~ 1.6 before relaxing back to unity around $r \sim 3$ fm. The effect of the CM motion in this channel remains small. By contrast, the 3D_1 wave displays practically no wound, except for very large CM momenta, but in any case this component is subdominant. In the case of the 3S_1 channel, the correlation function shows a clear wound at short distances: for $r \lesssim 0.6$ fm one finds $f_{\text{corr}}(r) \approx 0.8$, indicating an effective repulsion, since the correlated wave is suppressed with respect to the free one. In the intermediate region $0.6 \lesssim r \lesssim 1.8$ fm, the correlation function rises above unity, reaching values around $f_{\text{corr}}(r) \simeq 1.5$. This reflects the strong enhancement of the wave amplitude due to short-range correlations, which in turn signal the attractive part of the interaction in this channel. Beyond $r \gtrsim 3$ fm, $f_{\text{corr}}(r)$ smoothly approaches unity, as expected from the healing property.

There is no strict analogue of the correlation function for the off-diagonal coupled waves ($l \neq l'$), since these components vanish at large distances. Nevertheless, one can formally introduce the quotient

$$f_{\text{corr}}(r) = \frac{u_{ll'}(r)}{\hat{j}_l(pr)},$$

which we denote as a “non-diagonal correlation function.” The results are displayed in the bottom panels of Fig. 6.8 for $J = 1$. For the $ll' = 20$ component, corresponding to the ${}^3D_1/{}^3S_1$ interference, $f_{\text{corr}}(r)$ remains nearly constant for $r \lesssim 1.5$ fm before decreasing to zero at larger distances (with a small residual oscillation). This behavior shows that the interference acts effectively as a D wave at short distances, but with a much larger amplitude than a free D wave, reaching values of order ~ 12 . In contrast, the $ll' = 02$ component, associated with the ${}^3S_1/{}^3D_1$ interference, yields an almost vanishing $f_{\text{corr}}(r)$, reflecting the negligible strength of this mixing.

The 3P_2 channel is attractive at short distances, whereas the 3F_2 is strongly repulsive. As a consequence, the corresponding correlation functions shown in Fig. 6.9 exhibit an enhancement ($f_{\text{corr}} > 1$) for 3P_2 and a pronounced wound for 3F_2 . In both cases, the functions display a smooth and rapid healing toward unity at $r \simeq 3$ fm. The non-diagonal correlation function for the ${}^3F_2/{}^3P_2$ interference behaves in a similar way to the ${}^3D_1/{}^3S_1$ case: it remains nearly constant for $r < 1.2$ fm, indicating that the mixing acts effectively as a pure F wave at short distances. However, this clear behavior for the $J = 2$ channel is mainly of theoretical interest, serving as a didactic example, since its contribution to the total wave function is negligible in practice.

6.5.3. High-momentum distributions

To end this chapter, we present the results for the high-momentum distributions in momentum space. Figures (6.10)–(6.12) display the squared wave functions, $|\phi_{ll'}^{SJ}(p')|^2$, for different CM momenta of the nucleon pair, computed for $p = 140$ MeV/c as a function of the relative momentum p' . We only show results for $p' > k_F$, as indicated by the vertical lines in the plots. For very large CM momentum, $P = 400$ MeV/c, high-momentum components may also appear at $p' < k_F$, since in this kinematic configuration the two nucleons are nearly parallel. Nevertheless, our main interest lies in the high-momentum tail characteristic of short-range correlations, which emerges predominantly at large p' .

Now we turn to Fig. 6.10, which shows the results for the uncoupled waves. Each panel displays the squared high-momentum wave function, where characteristic oscillations appear. These oscillations originate from the structure of the defect function $\Delta\tilde{\phi}_{ll'}^{SJ}$, given in Eq. 6.51. From that expression it is clear that the momentum dependence of the wave function arises from a linear combination of Bessel functions $\hat{j}_l(p'r_i)$ evaluated at the grid points r_i . For large p' this can be written schematically as

$$\Delta\tilde{\phi}_{ll'}^{SJ}(p') = \sqrt{\frac{2}{\pi}} \frac{1}{pp'} \frac{1}{p^2 - p'^2} \sum_i a_{ll'}(r_i) \hat{j}_l(p'r_i), \quad (6.64)$$

where the coefficients are defined as

$$a_{ll'}(r_i) = \sum_{l_1} (\lambda_i)_{l_1 l}^{SJ} u_{l_1 l'}^{SJ}(r_i). \quad (6.65)$$

The oscillatory behavior thus results from the superposition of Bessel functions with different weights for each partial wave, leading to distinct positions of the zeros. The coefficients

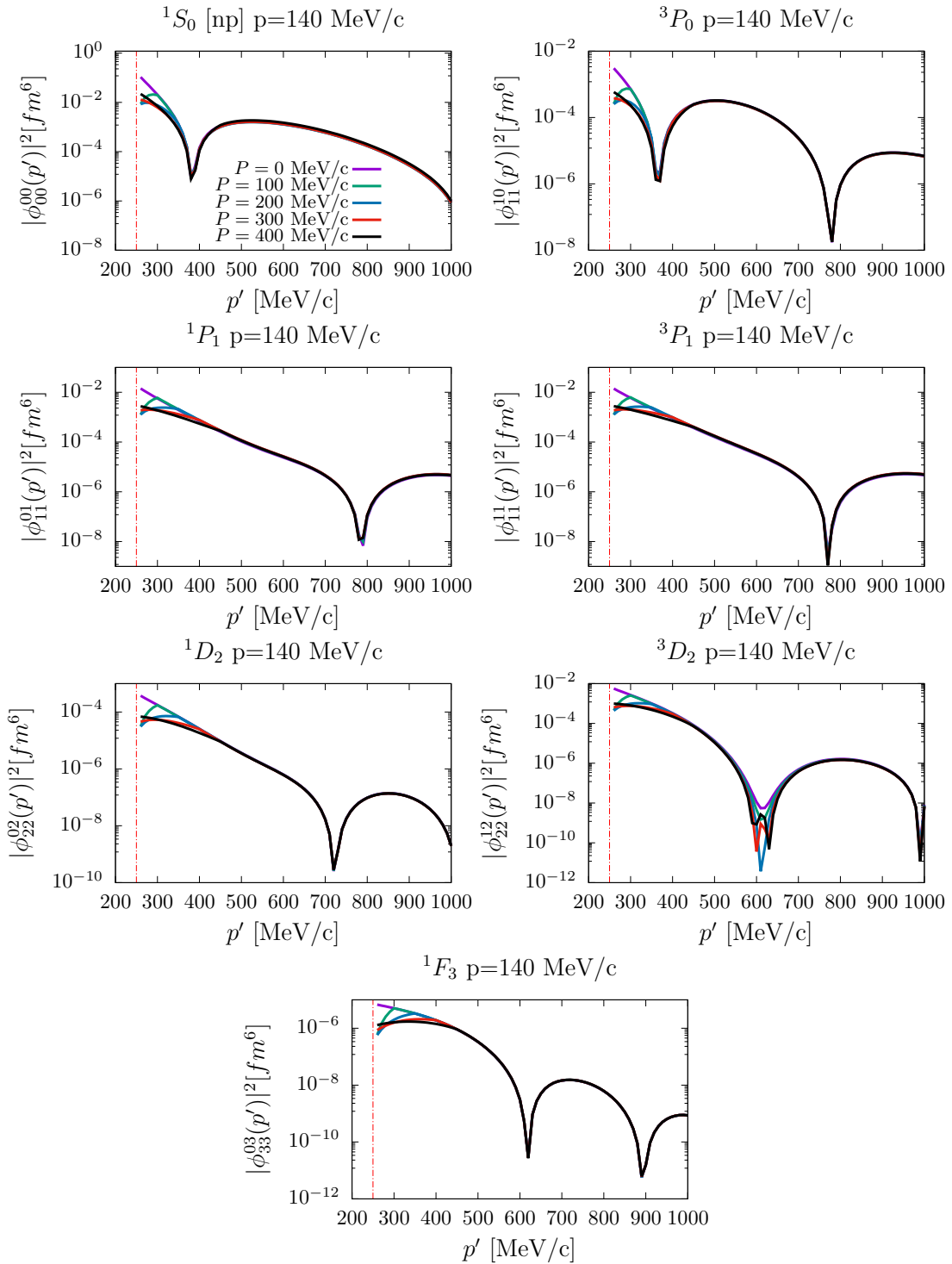


Figure 6.10: Squared radial wave functions $|\tilde{\phi}_{l,l}^{SJ}(p')|^2$ for uncoupled partial waves, plotted as a function of p' in the high-momentum region above k_F . Results are shown for a relative momentum $p = 140$ MeV/c and several values of the CM momentum.

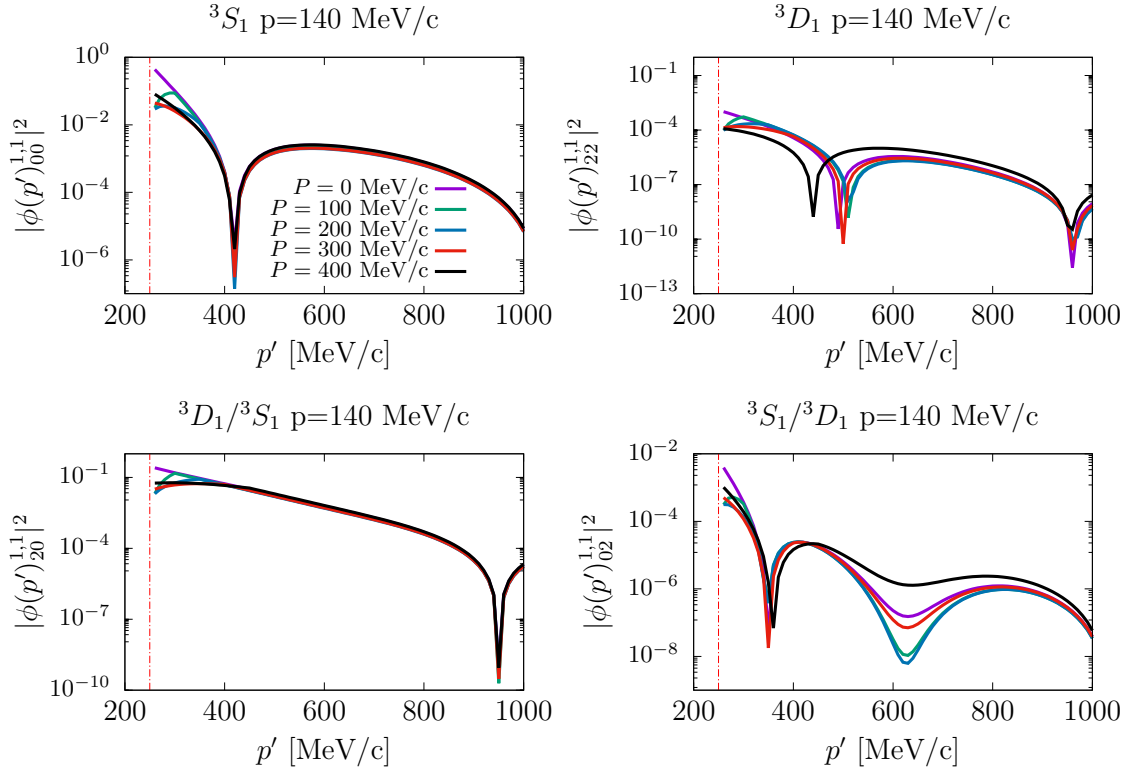


Figure 6.11: Squared radial wave functions $|\tilde{\phi}_{l,l'}^{SJ}(p)|^2$ for the coupled partial waves with $J = 1$, evaluated at relative momentum $p = 140$ MeV/c for different CM momenta.

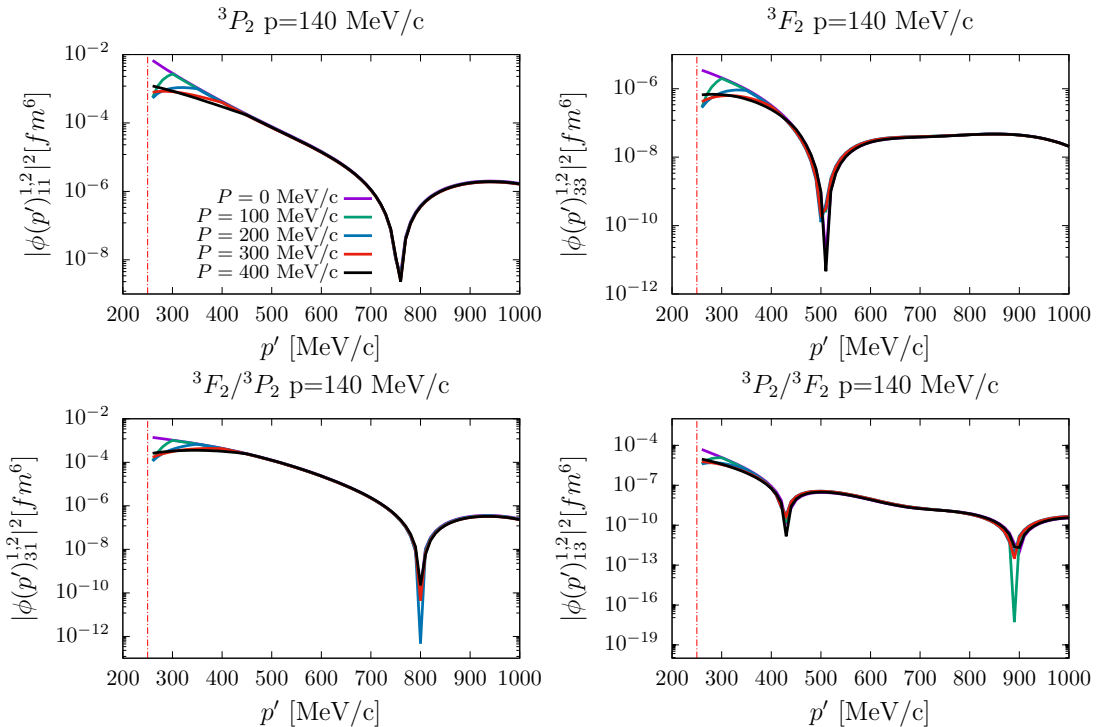


Figure 6.12: The same as fig. 6.11 for $J = 2$.

$a_{ll'}(r_i)$ depend on the product of the λ_i coefficients and the reduced wave functions in coordinate space, i.e. on the local product of the potential and the wave function at the point r_i .

From Fig. 6.10 it is apparent that the S - and P -waves tend to dominate the momentum distribution of the uncoupled channels, while the D - and F -waves are much smaller. An important feature is that, at high momentum, the dependence on the CM momentum is weak. This suggests that setting $P = 0$ provides a good approximation for evaluating these distributions.

In the case of the coupled waves with $S = 1$ and $J = 1$, shown in Fig. 6.11, the most relevant contributions come from the 3S_1 and the interference ${}^3D_1/{}^3S_1$, while the other two channels are much smaller. The 3S_1 component exhibits a zero around $p' \simeq 425$ MeV/c, whereas the non-diagonal ${}^3D_1/{}^3S_1$ wave develops a much longer tail, with its first zero only appearing beyond $p' \simeq 900$ MeV/c. This indicates that the interference term dominates the momentum distribution in the tensor-force region between 400 and 550 MeV/c. The effect of the CM momentum is negligible for the dominant waves. For the much smaller 3D_1 and ${}^3S_1/{}^3D_1$ components, the CM dependence is stronger but irrelevant due to their negligible strength.

Finally, in Fig. 6.12 we show the momentum distributions for the coupled waves with $S = 1$, $J = 2$. The same qualitative features as in the $J = 1$ case are observed: the dominant contributions are the 3P_2 and the interference ${}^3F_2/{}^3P_2$, while the other two components are negligible. The dependence on the CM momentum is again irrelevant. However, these $J = 2$ distributions are almost two orders of magnitude smaller than the 3S_1 and ${}^3D_1/{}^3S_1$ channels, making it clear that the high-momentum tail of a nucleon pair is dominated by the $J = 1$ tensor-driven components.

Figure 6.13 compares the contributions of the uncoupled partial waves to the total momentum distribution, obtained from Eq. (6.61):

$$\rho^S(p') = \sum_J \sum_{l,l'} \rho_{ll'}^{SJ} \quad (6.66)$$

where the partial momentum distributions, plotted in Fig 6.13, of the different waves are

$$\rho_{ll'}^{SJ} = \frac{1}{2S+1} \frac{2J+1}{4\pi} \frac{2}{\pi} \left| \tilde{\phi}_{l,l'}^{SJ}(p') \right|^2, \quad (6.67)$$

where $2J+1$ counts the magnetic sub-states and $1/(2S+1)$ averages over spin.

For $S = 0$ (left panel), the 1S_0 wave dominates, with the 1P_1 partially filling the depression near its zero, while the remaining waves are negligible. For $S = 1$ (right panel), the 3P_0 , 3P_1 , and 3D_2 waves have comparable magnitudes and collectively smooth the dips near the zeros of each component, complementing each other in the total distribution.

The partial momentum distributions of the coupled waves are shown in Fig. 6.14. The left panel displays the $S = 1$, $J = 1$ channel, which provides the dominant contribution to the high-momentum distribution of proton-neutron pairs. It is evident that the ${}^3D_1/{}^3S_1$ interference fills the dip around the zero of the 3S_1 wave and dominates the high-momentum

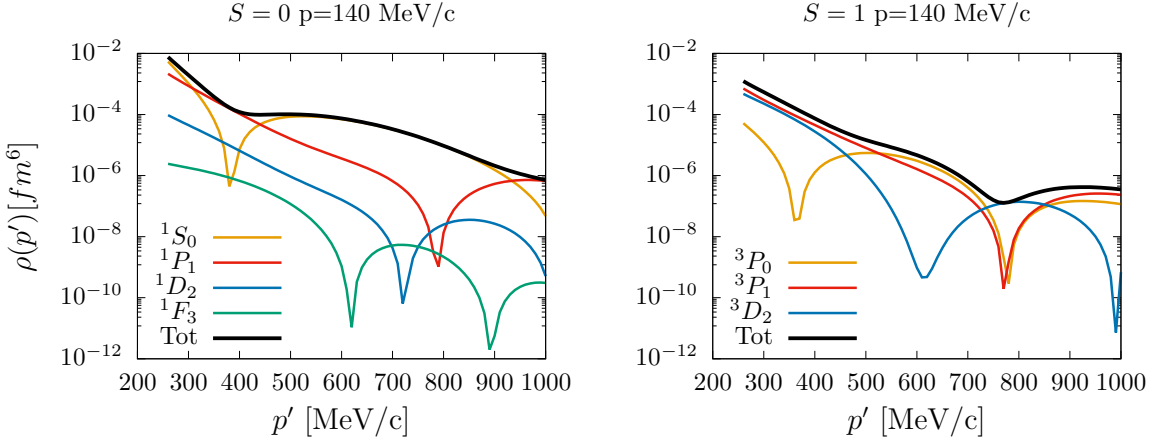


Figure 6.13: Contributions of the uncoupled partial waves to the total high-momentum distribution $\rho(p')$ for a nucleon pair with relative momentum $p = 140$ MeV/c and for $P = 0$. Left panel: $S = 0$ partial waves; right panel: $S = 1$ partial waves. The total distribution is obtained from Eq. (6.67).

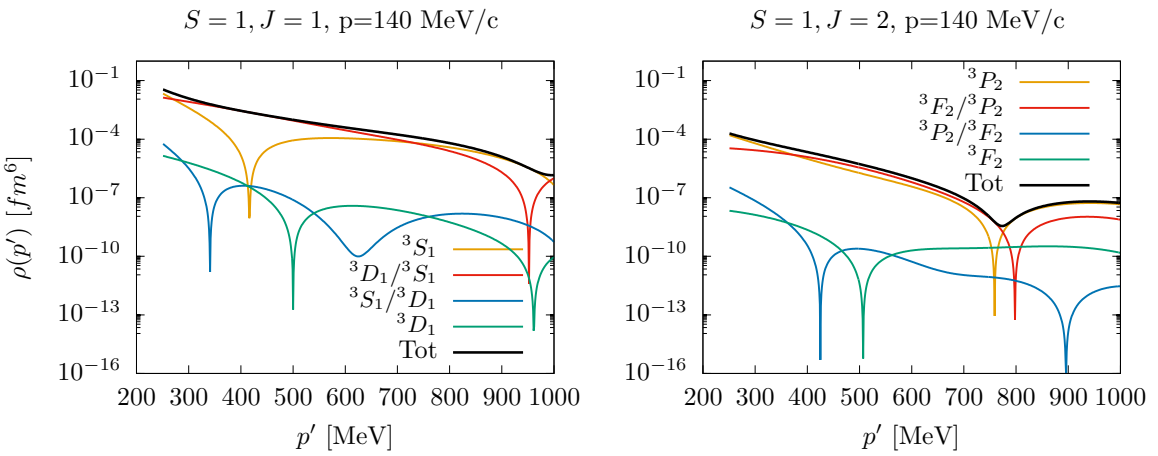


Figure 6.14: Partial high-momentum distributions $\rho_{ll'}^J(p')$ of the coupled waves for proton-neutron pairs with relative momentum $p = 140$ MeV/c. Left panel: $S = 1, J = 1$ channel; right panel: $S = 1, J = 2$ channel. The figure highlights the dominant role of the 3S_1 and ${}^3D_1/{}^3S_1$ interference in the high-momentum region associated with the tensor force, while the other components are orders of magnitude smaller and negligible.

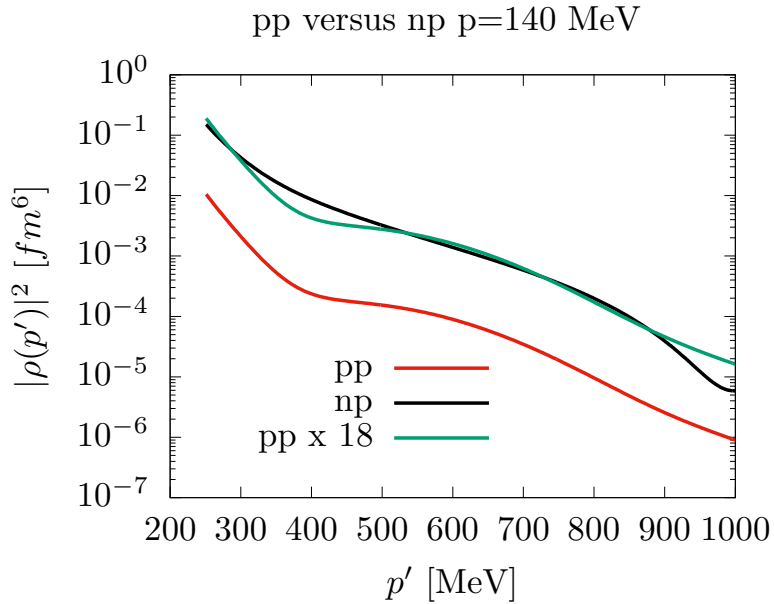


Figure 6.15: Comparison of the np and pp momentum distributions. The pp distribution multiplied by 18 is shown to agree with the np distribution, consistent with the experimental ratio of high-momentum np to pp pairs reported in Ref. [57].

region associated with the tensor force, roughly between 400 and 550 MeV/c [207]. The individual 3D_1 and $^3S_1/{}^3D_1$ components are more than two orders of magnitude smaller and can be considered negligible, as the potential in the 3D_1 channel (i.e., the values of λ_{22}^{11}) vanishes at short distances and becomes appreciable only around $r \sim 1.8$ fm. The right panel shows the $J = 2$ channel, whose partial momentum distributions are several orders of magnitude smaller than the $J = 1$ case and therefore also negligible.

Finally, in Fig. 6.15 we present the total momentum distributions for neutron-proton (np) and proton-proton (pp) pairs. In the pp case, the two-nucleon wave function must be antisymmetric under the exchange of coordinates and spins. This implies that for $S = 0$ the spatial wave function is symmetric, and therefore the relative orbital angular momentum l must be even, while for $S = 1$ the spatial wave function is antisymmetric and l must be odd. As a consequence, many partial waves do not contribute to the high-momentum distribution of pp pairs. In particular, the most relevant np channels, namely the 3S_1 and the ${}^3D_1/{}^3S_1$ interference, are absent in the pp case. In contrast, for np pairs all partial waves contribute. This explains why the momentum distribution of pp pairs is significantly suppressed compared to that of np pairs, especially in the high-momentum region.

In Ref. [57], it was experimentally found that the ratio of high-momentum np to pp pairs in ${}^{12}\text{C}$ is 18 ± 5 . This agrees with the results of Fig. 6.15, where multiplying the pp distribution by 18 brings it close to the np distribution.

6.6. Final remarks

In this chapter we have examined the effect of the short-range nucleon–nucleon interaction on the wave function of a nucleon pair in the nuclear medium, with particular attention to the role of Pauli–blocking. Within the independent pair approximation, we have shown that the two–body Schrödinger equation reduces in these conditions to the Bethe–Goldstone equation, where the Pauli principle translates into the induction of high–momentum components in the relative wave function.

We have solved the Bethe–Goldstone equation in a partial–wave expansion using the realistic Granada 2013 potential. The results show that the radial wave functions are strongly modified at short distances ($r < 3$ fm), where the short–range repulsion and tensor components of the interaction produce a wound in the wave function and new interference components. At larger distances the correlations die out and the solutions heal to the uncorrelated wave function, consistently with the physical picture of short–range correlations.

An essential feature of these correlations is the role of the tensor force, which mixes the 3S_1 and 3D_1 partial waves. This mixing, absent in the uncorrelated case, generates a new component of the wave function that is fundamental for the appearance of a long tail in the momentum distribution. In particular, the 3D_1 – 3S_1 interference dominates the so–called tensor–force region between $p = 300$ and 600 MeV/ c and extends well beyond, making it the leading contribution to the high–momentum distribution of correlated np pairs. We stress that this mechanism is absent in pp pairs, because the coupled $S = 1$, $J = 1$ channel is forbidden by the Pauli principle. As a consequence, the dominant source of high–momentum components in nuclei arises from np pairs, while the pp high-momentum distribution remains comparatively suppressed.

Finally, we note that the formalism developed here explicitly includes the center–of–mass motion of the nucleon pairs under angular-average approximation. Although we have shown that its effect on the high–momentum components is small, this treatment allowed us to compute the full correlated wave function of nucleon pairs in nuclear matter. This result will be essential in the next chapter, where we apply the formalism to evaluate the contribution of short–range correlations to an observable in electron scattering: the transverse response enhancement produced by meson–exchange currents in the presence of correlations, within the independent pair approximation.

Chapter 7

Transverse enhancement from MEC and SRC

The study of the electron and neutrino nuclear responses requires a careful consideration and have indicated the need of including mechanisms that enhance the transverse response [33, 43, 44, 209, 210, 211]. Apart from meson exchange currents, which we have seen play a significant role in the transverse response, another possible candidate responsible for this enhancement is the presence of nuclear short-range correlations.

In previous chapters, we have explored these two effects separately: first, by analyzing the effects of MEC in a relativistic framework and second, by solving the Bethe-Goldstone equation to obtain the high-momentum wave function of correlated pairs, providing a realistic description of SRC in nuclear matter. In this chapter, we focus on investigating the impact of the high momentum components in the interference transverse response including MEC. The core of this theoretical work lies in the BG wave function, solved in the previous chapter. The initial two-nucleon plane wave states are replaced with the correlated wave functions for two nucleons. This replacement allowed us to incorporate SRC explicitly into the calculation in order to compare with previous uncorrelated approaches.

The motivation behind this work comes from earlier studies where SRC played a central role. A key reference is the work of Fabrocini [35], who explored the effect of correlations on the transverse interference response between one-body and two-body currents. Fabrocini found that including tensor correlations led to an enhancement of the interference responses, shifting them from negative values (as found using Jastrow type correlations) to positive ones.

As we have seen in chapter 6, the SRC effect is also manifested clearly in the high-momentum tails of the pp and np pair distributions, which increase significantly as a result of these nuclear correlations. This behavior is in agreement with studies such as the Green Function Montecarlo (GFM) [212] and the Correlated Shell Model [213]. According to these studies, the short distance nucleon-nucleon interaction enhances the probability of finding np pairs with high relative momentum, compared to pp or nn pairs. This enhancement is often attributed to the tensor component of the NN interaction. In chapter 6 we have seen that this effect is mainly due to the dominance of the mixed $^3D_1/ ^3S_1$ wave, prevalent in np pairs at high momentum, while it is suppressed in pp configurations.

Electron scattering experiments have played a crucial role in probing short-range correlations, helping to clarify properties such as the np-pair dominance and the presence of high-momentum tails in the nuclear wave function. In the $(e, e'p)$ experiment of Subedi *et al.* [57], nucleon knockout measurements from ^{12}C revealed that about 20% of the nucleons belong to short-range correlated pairs, while the remaining 80% behave as independent particles described by the shell model. The study demonstrated that most of the correlated pairs are pn pairs, with a much smaller fraction of pp and neutron–neutron nn pairs, providing clear experimental evidence of the dominance of the tensor component of the nucleon–nucleon interaction.

In this chapter, we show that the high-momentum components of the nucleon pair wave functions also contribute to observable effects in the transverse response induced by MEC, providing additional evidence of SRC and, in particular, of the tensor force. More details can be found in Ref. [214].

7.1. Formalism

Our methodology is based on the matrix element of the two-body current operator between the ground state of the Fermi gas and a particle–hole state (1p1h). We start recalling the definition of the hadronic tensor from chapter 3. In the non-relativistic Fermi gas model it reads

$$W^{\mu\nu} = \sum_{ph} \langle ph^{-1} | \hat{J}^\mu | F \rangle^* \langle ph^{-1} | \hat{J}^\nu | F \rangle \delta(E_p - E_h - \omega) \theta(p - k_F) \theta(k_F - h). \quad (7.1)$$

Here, the index p stands for the set of quantum numbers (p, s_p, t_p) , namely momentum, spin, and isospin, and similarly for h . The final and initial states are plane-waves states for particles and holes, dependent also of spin and isospin. In our model, the total current operator \hat{J}^μ is the sum of one-body and two-body currents,

$$\hat{J}^\mu = \hat{J}_{1b}^\mu + \hat{J}_{2b}^\mu, \quad (7.2)$$

Substituting the total operator in Eq. (7.1), we obtain the many-body matrix elements of these operators:

$$\begin{aligned} \langle ph^{-1} | \hat{J}^\mu | F \rangle &= \langle ph^{-1} | \hat{J}_{1b}^\mu | F \rangle + \langle ph^{-1} | \hat{J}_{2b}^\mu | F \rangle \\ &= \langle [p] | \hat{J}_{1b}^\mu | [h] \rangle + \sum_{k < k_F} \left[\langle [pk] | \hat{J}_{2b}^\mu | [hk] \rangle - \langle [pk] | \hat{J}_{2b}^\mu | [kh] \rangle \right]. \end{aligned} \quad (7.3)$$

The first term corresponds to the one-body current matrix element, where the operator acts on a single nucleon. The second term is the matrix element of the two body current, where a sum over all occupied states $|k\rangle = |\mathbf{k}, s_k, t_k\rangle$ in the Fermi sea is included.

To avoid confusion with previous chapters, inside the matrix elements of Eq.(7.3), we have introduced the notation $|[p]\rangle$ (with brackets) to denote states normalized to unity in a finite volume V :

$$|[p]st\rangle = \frac{e^{i\mathbf{p}\cdot\mathbf{r}}}{\sqrt{V}} |\frac{1}{2}s\rangle \otimes |\frac{1}{2}t\rangle \quad (7.4)$$

In contrast, states without brackets, $|p\rangle$, refer to continuum states with spatial wave function normalized to a momentum delta function in the whole space,

$$|\mathbf{p}st\rangle = \frac{e^{i\mathbf{p}\cdot\mathbf{r}}}{(2\pi)^{3/2}} |\frac{1}{2}s\rangle \otimes |\frac{1}{2}t\rangle \quad (7.5)$$

This notation is included because in chapters 2–5 the states are normalized with V , while in chapter 6 they are normalized with $(2\pi)^3$, and in this chapter we use both normalizations.

The focus is placed exclusively on the transverse response R_T , which is more sensitive to MEC. Therefore only the $\mu = 1, 2$ components of the electromagnetic current are considered. Due to MEC contribution, an interference appears between one-body and two-body currents. Then the diagonal components of the uncorrelated hadronic tensor (7.1) are

$$\begin{aligned} W^{\mu\mu} = & \sum_{ph} \left\{ |\langle [p] | \hat{J}_{1b}^\mu | [h] \rangle|^2 + 2\text{Re} \langle [p] | \hat{J}_{1b}^\mu | [h] \rangle^* \sum_{k < k_F} \langle [pk] | \hat{J}_{2b}^\mu | [hk - kh] \rangle \right\} \\ & \times \delta(E_p - E_h - \omega) \theta(p - k_F) \theta(k_F - h), \end{aligned} \quad (7.6)$$

where the pure MEC contribution is disregarded because its effect is small, as we have seen in chapter 3.

To go beyond the uncorrelated Fermi gas model, we include the effects of SRC between two nucleons in the initial state. These correlations modify the two-nucleon wave function, introducing high-momentum components,

$$\Psi_{hk} = |hk\rangle + |\Delta\Psi_{hk}\rangle \quad (7.7)$$

$$\Psi_{kh} = |kh\rangle + |\Delta\Psi_{kh}\rangle, \quad (7.8)$$

$|hk\rangle$ and $|kh\rangle$ are the free wave functions and $\Delta\Psi_{hk}$ and $\Delta\Psi_{kh}$ are the defect functions. By replacing $|hk\rangle$ and $|kh\rangle$ with the correlated states Ψ_{hk} and Ψ_{kh} obtained from the BG equation in chapter 6,

$$\begin{aligned} W^{\mu\mu} = & \sum_{ph} \left\{ |\langle [p] | \hat{J}_{1b}^\mu | [h] \rangle|^2 + 2\text{Re} \langle [p] | \hat{J}_{1b}^\mu | [h] \rangle^* \sum_{k < k_F} \langle [pk] | \hat{J}_{2b}^\mu | [\Psi_{hk} - \Psi_{kh}] \rangle \right\} \\ & \times \delta(E_p - E_h - \omega) \theta(p - k_F) \theta(k_F - h) \end{aligned} \quad (7.9)$$

we obtain,

$$\begin{aligned} W^{\mu\mu} = & \sum_{ph} \left\{ |\langle [p] | \hat{J}_{1b}^\mu | [h] \rangle|^2 + 2\text{Re} \langle [p] | \hat{J}_{1b}^\mu | [h] \rangle^* \sum_{k < k_F} \langle [pk] | \hat{J}_{2b}^\mu | [hk - kh] \rangle \right. \\ & + 2\text{Re} \langle [p] | \hat{J}_{1b}^\mu | [h] \rangle^* \sum_{k < k_F} \langle [pk] | \hat{J}_{2b}^\mu | [\Delta\Psi_{hk} - \Delta\Psi_{kh}] \rangle \Big\} \\ & \times \delta(E_p - E_h - \omega) \theta(p - k_F) \theta(k_F - h). \end{aligned} \quad (7.10)$$

A new interference term appears, between the one-body current and two-body current acting on high-momentum nucleon pairs. The sum in k includes the spin and isospin s_k and t_k , respectively. In the thermodynamic limit, it is $1/V \sum_{s_k t_k} \int d^3k / (2\pi)^3$.

$\langle pp U_1 pp\rangle = 1$	$\langle pn U_1 pn\rangle = 1$	$\langle pn U_1 np\rangle = 0$
$\langle pp U_2 pp\rangle = 1$	$\langle pn U_2 pn\rangle = -1$	$\langle pn U_2 np\rangle = 0$
$\langle pp U_3 pp\rangle = 0$	$\langle pn U_3 pn\rangle = 0$	$\langle pn U_3 np\rangle = -2$

Table 7.1: Isospin matrix elements between two-nucleon states for proton emission.

Sum of isospin

We have seen in chapter 6 that the high-momentum components are different for np and pp pairs because of antisymmetrization. Therefore, we have to pay attention to the isospin summation that gives the contribution of np and pp pairs. It is convenient to separate explicitly the two-body isospin structure from the current operator. As in Eq. (4.40) in chapter 4, the full two body current can be decomposed into isospin channels,

$$\hat{J}_{2b}^\mu = \tau_3^{(1)} J_1^\mu + \tau_3^{(2)} J_2^\mu + i[\boldsymbol{\tau}^{(1)} \times \boldsymbol{\tau}^{(2)}]_3 J_3^\mu = \sum_{a=1}^3 U_a J_a^\mu, \quad (7.11)$$

where $U_1 = \tau_3^{(1)}$, $U_2 = \tau_3^{(2)}$ and $U_3 = i[\boldsymbol{\tau}^{(1)} \times \boldsymbol{\tau}^{(2)}]_3$. Then we can write the isospin summation as,

$$\sum_{t_k} \langle [pk] | \hat{J}_{2b}^\mu | [\Delta\Psi_{hk} - \Delta\Psi_{kh}] \rangle = \sum_{t_k} \sum_a \langle pk | U_a J_a^\mu | \Delta\Psi_{hk} - \Delta\Psi_{kh} \rangle. \quad (7.12)$$

We next perform the isospin sum for proton and neutron emission, separating the direct and exchange matrix elements.

Proton emission

- $t_p = t_h = 1/2$ and $t_k = \pm 1/2$.

Direct matrix element:

$$\begin{aligned} \sum_a \sum_{t_k} \langle t_p t_k | U_a | t_h t_k \rangle \langle pk | J_a^\mu | \Delta\Psi_{hk} \rangle &= \sum_a \langle \frac{1}{2} \frac{1}{2} | U_a | \frac{1}{2} \frac{1}{2} \rangle \langle pk | J_a^\mu | \Delta\Psi_{hk} \rangle \\ &+ \sum_a \langle \frac{1}{2} - \frac{1}{2} | U_a | \frac{1}{2} - \frac{1}{2} \rangle \langle pk | J_a^\mu | \Delta\Psi_{hk} \rangle. \end{aligned} \quad (7.13)$$

Exchange matrix element:

$$\begin{aligned} \sum_a \sum_{t_k} \langle t_p t_k | U_a | t_k t_h \rangle \langle pk | J_a^\mu | \Delta\Psi_{kh} \rangle &= \sum_a \langle \frac{1}{2} \frac{1}{2} | U_a | \frac{1}{2} \frac{1}{2} \rangle \langle pk | J_a^\mu | \Delta\Psi_{kh} \rangle \\ &+ \sum_a \langle \frac{1}{2} - \frac{1}{2} | U_a | - \frac{1}{2} \frac{1}{2} \rangle \langle pk | J_a^\mu | \Delta\Psi_{kh} \rangle. \end{aligned} \quad (7.14)$$

$\langle nn U_1 nn\rangle = 1$	$\langle np U_1 np\rangle = -1$	$\langle np U_1 pn\rangle = 0$
$\langle nn U_2 nn\rangle = -1$	$\langle np U_2 np\rangle = 1$	$\langle np U_2 pn\rangle = 0$
$\langle nn U_3 nn\rangle = 0$	$\langle np U_3 np\rangle = 0$	$\langle np U_3 pn\rangle = 2$

Table 7.2: Isospin matrix elements between two-nucleon states for neutron emission.

The combination of these two contributions gives the full result:

$$\begin{aligned} \sum_{t_k} \sum_a \langle pk|U_a J_a^\mu| \Delta\Psi_{hk} - \Delta\Psi_{kh} \rangle &= \sum_a \langle \frac{1}{2} \frac{1}{2} | U_a | \frac{1}{2} \frac{1}{2} \rangle \langle pk|J_a^\mu| \Delta\Psi_{hk} - \Delta\Psi_{kh} \rangle \\ &+ \sum_a \langle \frac{1}{2} - \frac{1}{2} | U_a | - \frac{1}{2} \frac{1}{2} \rangle \langle pk|J_a^\mu| \Delta\Psi_{hk} \rangle \\ &+ \sum_a \langle \frac{1}{2} - \frac{1}{2} | U_a | - \frac{1}{2} \frac{1}{2} \rangle \langle pk|J_a^\mu| \Delta\Psi_{kh} \rangle \end{aligned} \quad (7.15)$$

Using the explicit values of the isospin coefficients from Table 7.1, this becomes:

$$\begin{aligned} \sum_{t_k} \sum_a \langle pk|U_a J_a^\mu| \Delta\Psi_{hk} - \Delta\Psi_{kh} \rangle &= \langle pk|J_1^\mu + J_2^\mu| \Delta\Psi_{hk} - \Delta\Psi_{kh} \rangle \\ &+ \langle pk|J_1^\mu - J_2^\mu| \Delta\Psi_{hk} \rangle + 2 \langle pk|J_3^\mu| \Delta\Psi_{kh} \rangle. \end{aligned} \quad (7.16)$$

Neutron emission

- $t_p = t_h = -1/2$ and $t_k = \pm 1/2$

The derivation for neutron emission follows analogously,

$$\begin{aligned} \sum_{t_k} \sum_a \langle pk|U_a J_a^\mu| \Delta\Psi_{hk} - \Delta\Psi_{kh} \rangle &= -\langle pk|J_1^\mu + J_2^\mu| \Delta\Psi_{hk} - \Delta\Psi_{kh} \rangle \\ &- \langle pk|J_1^\mu - J_2^\mu| \Delta\Psi_{hk} \rangle - 2 \langle pk|J_3^\mu| \Delta\Psi_{kh} \rangle. \end{aligned} \quad (7.17)$$

The isospin matrix elements for neutron emission are shown in Table 7.2

7.1.1. Correlated matrix elements

We work at the non-relativistic regime as the SRC model is non relativistic. We start with the one-body matrix element between particle and hole plane wave states, which is given by

$$\langle [p] | \hat{J}_{1b}^\mu | [h] \rangle \equiv \frac{(2\pi)^3}{V} \delta^3(\mathbf{h} + \mathbf{q} - \mathbf{p}) j_{1b}^\mu(\mathbf{p}, \mathbf{h}). \quad (7.18)$$

We consider the non-relativistic reduction of the transverse response, i.e., only j_{1b}^i for $i = 1, 2$ components are involved. Then the one-body magnetization current is

$$\mathbf{j}_{1b}(\mathbf{p}, \mathbf{h}) = -i \delta_{t_p t_h} \frac{G_M^h}{2m_N} \mathbf{q} \times \boldsymbol{\sigma}_{ph}, \quad (7.19)$$

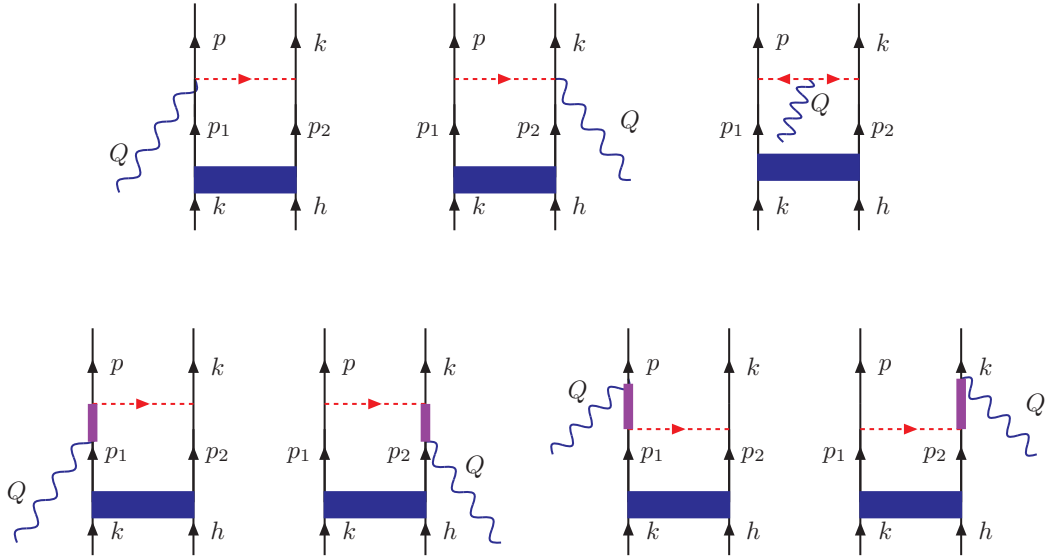


Figure 7.1: Correlation Feynman diagrams for the Seagull, Pion-in-flight and Δ resonance two body currents for the direct term. The blue square represent the correlation process and p_1 and p_2 are the high-momentum components.

where G_M^h is the magnetic form factor of a nucleon with isospin t_h .

The matrix element of the two body operator $\hat{J}_{2b}^\mu = \hat{\mathbf{J}}_{2b}$ between correlated states and 1p1h final states can be written as,

$$\langle [\mathbf{p}_s p \mathbf{k} s_k t_k] | \hat{\mathbf{J}}_{2b} | [\Delta \Psi_{\mathbf{h}\mathbf{k}}^{s_h s_k}, t_h t_k] \rangle = \int d^3 p_1 d^3 p_2 \sum_a \sum_{s_1 s_2} \langle [\mathbf{p}_s p \mathbf{k} s_k t_k] | U_a \mathbf{J}_a | \mathbf{p}_1 s_1 t_h \mathbf{p}_2 s_2 t_k \rangle \times \langle \mathbf{p}_1 s_1 t_h \mathbf{p}_2 s_2 t_k | [\Delta \Psi_{\mathbf{h}\mathbf{k}}^{s_h s_k}, t_h t_k] \rangle, \quad (7.20)$$

where \mathbf{p}_1 and \mathbf{p}_2 are the high momentum components of the correlated particles with spin s_1 and s_2 appearing in Fig. 7.1. Moreover, in Eq. (7.20), we have inserted a complete set of momentum-spin states $|\mathbf{p}_1 s_1, \mathbf{p}_2 s_2\rangle$, making the spin dependence explicit,

$$\sum_{s_1} \sum_{s_2} \int d^3 p_1 d^3 p_2 |\mathbf{p}_1 s_1 \mathbf{p}_2 s_2\rangle \langle \mathbf{p}_1 s_1 \mathbf{p}_2 s_2| = 1. \quad (7.21)$$

By applying Eq. (3.8), non-relativistic version with bracket notation, the matrix element inside the integral (7.20) can be expressed as,

$$\begin{aligned} \sum_a \langle [\mathbf{p}_s p \mathbf{k} s_k t_k] | U_a \mathbf{J}_a | \mathbf{p}_1 s_1 t_h \mathbf{p}_2 s_2 t_k \rangle &= \frac{V}{(2\pi)^3} \sum_a \langle [\mathbf{p}_s p \mathbf{k} s_k t_k] | U_a \mathbf{J}_a | [\mathbf{p}_1 s_1 t_h \mathbf{p}_2 s_2 t_k] \rangle \\ &= \frac{V}{(2\pi)^3} \frac{(2\pi)^3}{V^2} \sum_a \langle t_p t_k | U_a | t_h t_k \rangle \delta(\mathbf{p}_1 + \mathbf{p}_2 + \mathbf{q} - \mathbf{p} - \mathbf{k}) \mathbf{j}_a(\mathbf{p}, s_p, \mathbf{k}, s_k, \mathbf{p}_1, s_1, \mathbf{p}_2, s_2). \end{aligned} \quad (7.22)$$

Recalling chapter 4, the currents \mathbf{j}_1 and \mathbf{j}_2 correspond to the terms of the Δ current in Eq. (4.38) that are accompanied by the isospin factors $\tau_3^{(1)}$ and $\tau_3^{(2)}$ respectively,

$$\mathbf{j}_1(\mathbf{p}, \mathbf{k}, \mathbf{p}_1, \mathbf{p}_2) = iC_\Delta \frac{\mathbf{k}_1 \cdot \boldsymbol{\sigma}^{(1)}}{\mathbf{k}_1^2 + m_\pi^2} 4\mathbf{k}_1 \times \mathbf{q}, \quad (7.23)$$

$$\mathbf{j}_2(\mathbf{p}, \mathbf{k}, \mathbf{p}_1, \mathbf{p}_2) = iC_\Delta \frac{\mathbf{k}_2 \cdot \boldsymbol{\sigma}^{(2)}}{\mathbf{k}_2^2 + m_\pi^2} 4\mathbf{k}_2 \times \mathbf{q}, \quad (7.24)$$

with

$$C_\Delta \equiv \sqrt{\frac{3}{2}} \frac{2}{9} \frac{ff^*}{m_\pi^2} \frac{C_3^V}{m_N m_\Delta - m_N}. \quad (7.25)$$

where now $\mathbf{k}_1 = \mathbf{p} - \mathbf{p}_1$ and $\mathbf{k}_2 = \mathbf{k} - \mathbf{p}_2$. The current \mathbf{j}_3 is composed of those terms where the isospin is $i[\boldsymbol{\tau}^{(1)} \times \boldsymbol{\tau}^{(2)}]_3$. Therefore, it receives contributions from the seagull, pion in flight and Δ currents:

$$\mathbf{j}_3(\mathbf{p}, \mathbf{k}, \mathbf{p}_1 \mathbf{p}_2) = \mathbf{j}_{s3}(\mathbf{p}, \mathbf{k}, \mathbf{p}_1 \mathbf{p}_2) + \mathbf{j}_{\pi3}(\mathbf{p}, \mathbf{k}, \mathbf{p}_1 \mathbf{p}_2) + \mathbf{j}_{d3}(\mathbf{p}, \mathbf{k}, \mathbf{p}_1 \mathbf{p}_2), \quad (7.26)$$

$$\mathbf{j}_{s3}(\mathbf{p}, \mathbf{k}, \mathbf{p}_1 \mathbf{p}_2) = \frac{f^2}{m_\pi^2} F_1^V \left(\frac{\mathbf{k}_1 \cdot \boldsymbol{\sigma}^{(1)}}{\mathbf{k}_1^2 + m_\pi^2} \boldsymbol{\sigma}^{(2)} - \frac{\mathbf{k}_2 \cdot \boldsymbol{\sigma}^{(2)}}{\mathbf{k}_2^2 + m_\pi^2} \boldsymbol{\sigma}^{(1)} \right), \quad (7.27)$$

$$\mathbf{j}_{\pi3}(\mathbf{p}, \mathbf{k}, \mathbf{p}_1 \mathbf{p}_2) = \frac{f^2}{m_\pi^2} F_1^V \frac{\mathbf{k}_1 \cdot \boldsymbol{\sigma}^{(1)}}{\mathbf{k}_1^2 + m_\pi^2} \frac{\mathbf{k}_2 \cdot \boldsymbol{\sigma}^{(2)}}{\mathbf{k}_2^2 + m_\pi^2} (\mathbf{k}_1 - \mathbf{k}_2), \quad (7.28)$$

$$\mathbf{j}_{d3}(\mathbf{p}, \mathbf{k}, \mathbf{p}_1 \mathbf{p}_2) = iC_\Delta \left(\frac{\mathbf{k}_2 \cdot \boldsymbol{\sigma}^{(2)}}{\mathbf{k}_2^2 + m_\pi^2} (\mathbf{k}_2 \times \boldsymbol{\sigma}^{(1)}) - \frac{\mathbf{k}_1 \cdot \boldsymbol{\sigma}^{(1)}}{\mathbf{k}_1^2 + m_\pi^2} (\mathbf{k}_1 \times \boldsymbol{\sigma}^{(2)}) \right) \times \mathbf{q}. \quad (7.29)$$

On the other side, as in Eq. (6.12), the correlated wave function of a nucleon pair carries the same CM momentum,

$$\begin{aligned} \langle \mathbf{p}_1 s_1 \mathbf{p}_2 s_2 | [\Delta \Psi_{\mathbf{h}\mathbf{k}}^{s_h s_k}] \rangle &= \frac{(2\pi)^3}{V} \langle \mathbf{p}_1 s_1 \mathbf{p}_2 s_2 | \Delta \Psi_{\mathbf{h}\mathbf{k}}^{s_h s_k} \rangle \\ &= \frac{(2\pi)^3}{V} \delta(\mathbf{p}_1 + \mathbf{p}_2 - \mathbf{h} - \mathbf{k}) \Delta \psi_{\mathbf{h}\mathbf{k}}^{s_h s_k}(\mathbf{p}')_{s_1 s_2}, \end{aligned} \quad (7.30)$$

where $\mathbf{p}' = (\mathbf{p}_1 - \mathbf{p}_2)/2$ is the relative momentum of \mathbf{p}_1 and \mathbf{p}_2 . It is worth pointing out that the relative wave function $\Delta \psi_{\mathbf{h}\mathbf{k}}^{s_h s_k}(\mathbf{p}')$ is a bi-spinor and therefore its spinorial components are written as subscripts, $\Delta \psi_{\mathbf{h}\mathbf{k}}^{s_h s_k}(\mathbf{p}')_{s_1 s_2}$. The superscripts s_h and s_k refer to the spins of the uncorrelated pair before the interaction. Substituting this in Eq. (7.20), we finally obtain the direct matrix element

$$\begin{aligned} \langle [\mathbf{p} s_p t_p \mathbf{k} s_k t_k] | \hat{\mathbf{J}}_{2b} | [\Delta \Psi_{\mathbf{h}\mathbf{k}}^{s_h s_k} t_h t_k] \rangle &= \frac{(2\pi)^3}{V^2} \delta(\mathbf{h} + \mathbf{q} - \mathbf{p}) \sum_a \langle t_p t_k | U_a | t_h t_k \rangle \\ &\times \int d^3 p_1 \sum_{s_1 s_2} \mathbf{j}_a(\mathbf{p}, s_p, \mathbf{k}, s_k, \mathbf{p}_1, s_1, \mathbf{p}_2, s_2) \Delta \psi_{\mathbf{h}\mathbf{k}}^{s_h s_k}(\mathbf{p}_1 - \frac{\mathbf{h} + \mathbf{k}}{2})_{s_1 s_2}. \end{aligned} \quad (7.31)$$

By momentum conservation, the integral over \mathbf{p}_2 gives $\mathbf{p}_2 = \mathbf{h} + \mathbf{k} - \mathbf{p}_1$. The derivation of the exchange matrix element is conducted in a similar way. As seen in Eqs. (7.16) and

(7.17), the isospin summation leads to three distinct matrix elements:

$$\begin{aligned} \langle [\mathbf{p}_s p_t \mathbf{k}_s k_t] | \mathbf{J}_1 + \mathbf{J}_2 | [\Delta \Psi_{\mathbf{h}\mathbf{k}}^{s_h s_k} - \Delta \Psi_{\mathbf{k}\mathbf{h}}^{s_k s_h}] \rangle &= \frac{(2\pi)^3}{V^2} \delta(\mathbf{h} + \mathbf{q} - \mathbf{p}) \\ &\times \int d^3 p_1 \sum_{s_1 s_2} \mathbf{j}_+(\mathbf{p}, s_p, \mathbf{k}, s_k, \mathbf{p}_1, s_1, \mathbf{p}_2, s_2) [\Delta \psi_{\mathbf{h}\mathbf{k}}^{s_h s_k}(\mathbf{p}') - \Delta \psi_{\mathbf{k}\mathbf{h}}^{s_k s_h}(\mathbf{p}')]_{s_1 s_2} \end{aligned} \quad (7.32)$$

$$\begin{aligned} \langle [\mathbf{p}_s p_t \mathbf{k}_s k_t] | \mathbf{J}_1 - \mathbf{J}_2 | [\Delta \Psi_{\mathbf{h}\mathbf{k}}^{s_h s_k}] \rangle &= \frac{(2\pi)^3}{V^2} \delta(\mathbf{h} + \mathbf{q} - \mathbf{p}) \\ &\times \int d^3 p_1 \sum_{s_1 s_2} \mathbf{j}_-(\mathbf{p}, s_p, \mathbf{k}, s_k, \mathbf{p}_1, s_1, \mathbf{p}_2, s_2) \Delta \psi_{\mathbf{h}\mathbf{k}}^{s_h s_k}(\mathbf{p}')_{s_1 s_2} \end{aligned} \quad (7.33)$$

$$\begin{aligned} \langle [\mathbf{p}_s p_t \mathbf{k}_s k_t] | \mathbf{J}_3 | [\Delta \Psi_{\mathbf{k}\mathbf{h}}^{s_k s_h}] \rangle &= \frac{(2\pi)^3}{V^2} \delta(\mathbf{h} + \mathbf{q} - \mathbf{p}) \\ &\times \int d^3 p_1 \sum_{s_1 s_2} \mathbf{j}_3(\mathbf{p}, s_p, \mathbf{k}, s_k, \mathbf{p}_1, s_1, \mathbf{p}_2, s_2) \Delta \psi_{\mathbf{k}\mathbf{h}}^{s_k s_h}(\mathbf{p}')_{s_1 s_2} \end{aligned} \quad (7.34)$$

where we denoted by \mathbf{j}_+ and \mathbf{j}_- ,

$$\begin{aligned} \mathbf{j}_+(\mathbf{p}, s_p, \mathbf{k}, s_k, \mathbf{p}_1, s_1, \mathbf{p}_2, s_2) &= \mathbf{j}_1(\mathbf{p}, s_p, \mathbf{k}, s_k, \mathbf{p}_1, s_1, \mathbf{p}_2, s_2) + \mathbf{j}_2(\mathbf{p}, s_p, \mathbf{k}, s_k, \mathbf{p}_1, s_1, \mathbf{p}_2, s_2), \\ \mathbf{j}_-(\mathbf{p}, s_p, \mathbf{k}, s_k, \mathbf{p}_1, s_1, \mathbf{p}_2, s_2) &= \mathbf{j}_1(\mathbf{p}, s_p, \mathbf{k}, s_k, \mathbf{p}_1, s_1, \mathbf{p}_2, s_2) - \mathbf{j}_2(\mathbf{p}, s_p, \mathbf{k}, s_k, \mathbf{p}_1, s_1, \mathbf{p}_2, s_2). \end{aligned} \quad (7.35)$$

The components of the hadronic tensor defined in Eq. (7.10) determine the nuclear transverse response R_T . The first two terms correspond to the pure one-body response, R_T^{1b} , and to the uncorrelated interference between one-body and two-body currents, R_T^{1b2b} . We then focus on the third term, which represents the correlated interference response between the one-body and two-body currents.

$$(R_T^{1b2b})_{cor} = \frac{V}{(2\pi)^3} \int d^3 h \delta(E_p - E_h - \omega) w_T^{cor}(\mathbf{p}, \mathbf{h}) \theta(p - k_F) \theta(k_F - h) \quad (7.36)$$

with $\mathbf{p} = \mathbf{q} + \mathbf{h}$ after integrating over \mathbf{p} . The integrated $w_T^{cor}(\mathbf{p}, \mathbf{h})$ is the correlated single-nucleon function for the transition $p \rightarrow p$,

$$\begin{aligned} w_T^{cor}(\mathbf{p}, \mathbf{h})_{pp} &= 2Re \sum_{s_p s_h} \mathbf{j}_{1b,p}(\mathbf{p}, \mathbf{h})^* \sum_{s_k} \sum_{s_1 s_2} \int \frac{d^3 k}{(2\pi)^3} \int d^3 p_1 \\ &\times [\mathbf{j}_+(\mathbf{p}, s_p, \mathbf{k}, s_k, \mathbf{p}_1, s_1, \mathbf{p}_2, s_2) [\Delta \psi_{\mathbf{h}\mathbf{k}}^{s_h s_k}(\mathbf{p}') - \Delta \psi_{\mathbf{k}\mathbf{h}}^{s_k s_h}(\mathbf{p}')]_{s_1 s_2} \\ &+ \mathbf{j}_-(\mathbf{p}, s_p, \mathbf{k}, s_k, \mathbf{p}_1, s_1, \mathbf{p}_2, s_2) \Delta \psi_{\mathbf{h}\mathbf{k}}^{s_h s_k}(\mathbf{p}')_{s_1 s_2} \\ &+ 2\mathbf{j}_3(\mathbf{p}, s_p, \mathbf{k}, s_k, \mathbf{p}_1, s_1, \mathbf{p}_2, s_2) \Delta \psi_{\mathbf{k}\mathbf{h}}^{s_k s_h}(\mathbf{p}')_{s_1 s_2}] \end{aligned} \quad (7.37)$$

while for $n \rightarrow n$ channel is,

$$\begin{aligned} w_T^{cor}(\mathbf{p}, \mathbf{h})_{nn} &= -2Re \sum_{s_p s_h} \mathbf{j}_{1b,n}(\mathbf{p}, \mathbf{h})^* \sum_{s_k} \sum_{s_1 s_2} \int \frac{d^3 k}{(2\pi)^3} \int d^3 p_1 \\ &\times [\mathbf{j}_+(\mathbf{p}, s_p, \mathbf{k}, s_k, \mathbf{p}_1, s_1, \mathbf{p}_2, s_2) [\Delta \psi_{\mathbf{h}\mathbf{k}}^{s_h s_k}(\mathbf{p}') - \Delta \psi_{\mathbf{k}\mathbf{h}}^{s_k s_h}(\mathbf{p}')]_{s_1 s_2} \\ &+ \mathbf{j}_-(\mathbf{p}, s_p, \mathbf{k}, s_k, \mathbf{p}_1, s_1, \mathbf{p}_2, s_2) \Delta \psi_{\mathbf{h}\mathbf{k}}^{s_h s_k}(\mathbf{p}')_{s_1 s_2} \\ &+ 2\mathbf{j}_3(\mathbf{p}, s_p, \mathbf{k}, s_k, \mathbf{p}_1, s_1, \mathbf{p}_2, s_2) \Delta \psi_{\mathbf{k}\mathbf{h}}^{s_k s_h}(\mathbf{p}')_{s_1 s_2}] \end{aligned} \quad (7.38)$$

with $\mathbf{p}' = (\mathbf{p}_1 - \mathbf{p}_2)/2$ and $\mathbf{p}_2 = \mathbf{h} + \mathbf{k} - \mathbf{p}_1$. To compute the interference w_T^{cor} , it is necessary to solve a 3-dimensional integral over the spectator nucleon momentum \mathbf{k} , restricted to values below the Fermi surface, and a second 3-dimensional integral over the high-momentum component \mathbf{p}_1 , which encodes the short-range correlation effects through the defect function in momentum space. In addition to these, the T -response (7.36) also contains the integration over d^3h , which simplifies to a one-dimensional integral in the hole momentum h , yielding a total of seven dimensional numerical integration that must be carried out for each kinematical point (q, ω) .

7.1.2. High momentum wave functions

The correlated wave function in momentum space, that was obtained in previous chapter, expanded in multipoles is written as

$$\langle \mathbf{p}' s_1 s_2 | \psi \rangle \equiv \Delta \psi_{\mathbf{h}\mathbf{k}}^{S\mu}(\mathbf{p}')_{s_1 s_2} = \sqrt{\frac{2}{\pi}} \sum_{JM} \sum_{ll'm} i^{l'-l} Y_{l'm}^*(\hat{\mathbf{p}}) \langle l'm S\mu | JM \rangle \Delta \tilde{\phi}_{hk ll'}^{SJ}(p') \mathcal{Y}_{lSJ M}(\hat{\mathbf{p}})_{s_1 s_2}, \quad (7.39)$$

for the direct term. The spin-coupled spherical harmonics $\mathcal{Y}_{lSJ M}(\hat{\mathbf{p}})_{s_1 s_2}$, were defined in chapter 6 and are bi-spinors with two indices. Explicitly, they are given

$$\mathcal{Y}_{lSJ M}(\hat{\mathbf{p}})_{s_1 s_2} = \sum_{m_l m_s} \langle l m_l S m_s | JM \rangle Y_{l m_l}(\hat{\mathbf{p}}) \langle s_1 s_2 | S m_s \rangle. \quad (7.40)$$

The radial wave functions in momentum space, which are functions of the initial and final (high) relative momenta p, p' of the pair, and also of the CM momentum \mathbf{P} , are

$$\Delta \tilde{\phi}_{hk ll'}^{SJ}(p') = \sqrt{\frac{2}{\pi}} \frac{1}{p p'} \frac{\bar{Q}(P, p')}{p^2 - p'^2} \sum_{i=1}^{N_\delta} \hat{j}_l(p' r_i) \sum_{l_1} (\lambda_i)_{l_1, l}^{SJ} u_{hk l_1 l'}^{SJ}(r_i). \quad (7.41)$$

with $\mathbf{p} = (\mathbf{k} - \mathbf{h})/2$ and CM momentum $\mathbf{P} = \mathbf{k} + \mathbf{h}$. In Equations (7.32)-(7.34), we need the correlated wave function corresponding to the uncorrelated state $|\mathbf{h}, s_h, \mathbf{k}, s_k \rangle$ with uncoupled spins third components. Using Eqs. (6.13)-(6.14),

$$\Delta \psi_{\mathbf{h}\mathbf{k}}^{s_h s_k}(\mathbf{p}') = \sum_{S\mu} \langle \frac{1}{2} s_h \frac{1}{2} s_k | S\mu \rangle \Delta \psi_{\mathbf{h}\mathbf{k}}^{S\mu}(\mathbf{p}') \quad (7.42)$$

To obtain the exchange term, we change $(\mathbf{h}, s_h) \leftrightarrow (\mathbf{k}, s_k)$, and then the initial relative momentum $\hat{\mathbf{p}} \rightarrow -\hat{\mathbf{p}}$. By doing this we'll have a sign of difference in the spherical harmonic because

$$Y_{l'm}(-\hat{\mathbf{p}}) = (-)^{l'} Y_{l'm}(\hat{\mathbf{p}}). \quad (7.43)$$

The radial wave function is the same for the exchange case $\Delta \tilde{\phi}_{kh ll'}^{SJ}(p') = \Delta \tilde{\phi}_{hk ll'}^{SJ}(p')$. Then, the exchange wave function is

$$\Delta \psi_{\mathbf{k}\mathbf{h}}^{s_k s_h}(\mathbf{p}') = \sum_{S\mu} \langle \frac{1}{2} s_k \frac{1}{2} s_h | S\mu \rangle \Delta \psi_{\mathbf{k}\mathbf{h}}^{S\mu}(\mathbf{p}') \quad (7.44)$$

with

$$\Delta\psi_{\mathbf{kh}}^{S\mu}(\mathbf{p}')_{s_1s_2} = \sqrt{\frac{2}{\pi}} \sum_{JM} \sum_{ll'm} i^{l'-l} Y_{ll'm}^*(-\hat{\mathbf{p}}) \langle l'mS\mu | JM \rangle \Delta\tilde{\phi}_{kh}^{SJ}{}_{ll'}(p') \mathcal{Y}_{lSJ M}(\hat{\mathbf{p}}')_{s_1s_2} \quad (7.45)$$

Writing explicitly the singlet $S = 0$ and triplet $S = 1$ cases, we have to compute the following sums involving the partial waves:

- $S=0$ and $\mu = 0$

$$\Delta\psi_{\mathbf{hk}}^{00}(\mathbf{p}')_{s_1s_2} = \sqrt{\frac{2}{\pi}} \sum_{JM} Y^*(\hat{\mathbf{p}})_{JM} \Delta\tilde{\phi}_{hk}^{0J}(p') \mathcal{Y}_{J0JM}(\hat{\mathbf{p}}')_{s_1s_2}, \quad (7.46)$$

$$\Delta\psi_{\mathbf{kh}}^{00}(\mathbf{p}')_{s_1s_2} = \sqrt{\frac{2}{\pi}} \sum_{JM} (-1)^J Y^*(\hat{\mathbf{p}})_{JM} \Delta\tilde{\phi}_{kh}^{0J}(p') \mathcal{Y}_{J0JM}(\hat{\mathbf{p}}')_{s_1s_2}. \quad (7.47)$$

In this sum, the partial waves are: 1S_0 , 1P_1 , 1D_2 , and 1F_3 .

- $S = 1$ and $\mu = -1, 0, 1$

$$\begin{aligned} \Delta\phi_{\mathbf{hk}}^{1\mu}(\mathbf{p}')_{s_1s_2} &= \sqrt{\frac{2}{\pi}} \sum_m Y^*(\hat{\mathbf{p}})_{1m} \langle 1m1\mu | 00 \rangle \Delta\tilde{\phi}_{hk}^{10}{}_{11}(p') \mathcal{Y}_{1100}(\hat{\mathbf{p}}')_{s_1s_2} \\ &+ \sqrt{\frac{2}{\pi}} \sum_{J=1}^2 \sum_{Mm} Y^*(\hat{\mathbf{p}})_{Jm} \langle Jm1\mu | JM \rangle \Delta\tilde{\phi}_{hk}^{1J}{}_{JJ}(p') \mathcal{Y}_{J1JM}(\hat{\mathbf{p}}')_{s_1s_2} \\ &+ \sqrt{\frac{2}{\pi}} \sum_{J=2}^2 \sum_{l,l'=J\pm 1} \sum_{Mm} i^{l'-l} Y^*(\hat{\mathbf{p}})_{ll'm} \langle l'mS\mu | JM \rangle \Delta\tilde{\phi}_{hk}^{1J}{}_{ll'}(p') \mathcal{Y}_{l1JM}(\hat{\mathbf{p}}')_{s_1s_2}, \end{aligned} \quad (7.48)$$

$$\begin{aligned} \Delta\phi_{\mathbf{kh}}^{1\mu}(\mathbf{p}')_{s_1s_2} &= -\sqrt{\frac{2}{\pi}} \sum_m Y^*(\hat{\mathbf{p}})_{1m} \langle 1m1\mu | 00 \rangle \Delta\tilde{\phi}_{kh}^{10}{}_{11}(p') \mathcal{Y}_{1100}(\hat{\mathbf{p}}')_{s_1s_2} \\ &+ \sqrt{\frac{2}{\pi}} \sum_{J=1}^2 \sum_{Mm} (-1)^J Y^*(\hat{\mathbf{p}})_{Jm} \langle Jm1\mu | JM \rangle \Delta\tilde{\phi}_{kh}^{1J}{}_{JJ}(p') \mathcal{Y}_{J1JM}(\hat{\mathbf{p}}')_{s_1s_2} \\ &+ \sqrt{\frac{2}{\pi}} \sum_{J=1}^2 \sum_{l,l'=J\pm 1} \sum_{Mm} i^{l'-l} (-1)^{l'} Y^*(\hat{\mathbf{p}})_{ll'm} \langle l'mS\mu | JM \rangle \Delta\tilde{\phi}_{kh}^{1J}{}_{ll'}(p') \mathcal{Y}_{l1JM}(\hat{\mathbf{p}}')_{s_1s_2}. \end{aligned} \quad (7.49)$$

These formulas account for the computation of the partial waves 3P_0 , 3P_1 , 3D_2 , 3S_1 , ${}^3D_1/{}^3S_1$, 3D_1 , ${}^3S_1/{}^3D_1$, 3P_2 , ${}^3F_2/{}^3P_2$, 3F_2 and ${}^3P_2/{}^3F_2$. These multipole expansions are inserted into Eqs. (7.37) and (7.38) to compute the interference transverse responses.

7.2. Results

Having established the theoretical framework showing how SRC modify the 1p1h MEC matrix elements within the independent pair approximation, through their coupling to the high-momentum components of nucleon pairs in the medium, we now turn to the computation of their contribution to the interference between one-body and two-body currents in the transverse response. Specifically, the SRC correction to the transverse response is added to the previously calculated uncorrelated MEC results studied in previous chapters.

We present the results obtained for ^{12}C , using a Fermi momentum of $k_F = 250$ MeV/c. The calculation procedure requires solving the Bethe–Goldstone (BG) equation for each nucleon pair \mathbf{h}, \mathbf{k} in order to obtain the corresponding defect function $\phi_{\mathbf{h}\mathbf{k}}$ in a multipole expansion (see chapter 6). Rigorously, the integral over the high momentum \mathbf{p}_1 extends from k_F to infinity. In practice, however, the high-momentum radial functions $\phi_{ll'}^{SJ}$ decrease as a power of the relative momentum $1/p^3$, Eq. (6.53), so it is sufficient to integrate up to $|\mathbf{p}_1| \sim 800$ MeV or less to obtain convergence.

In the following, the results are obtained using the frozen- k approximation, which provides a numerically efficient procedure while preserving the accuracy of the calculation. In this approach, within the integral over \mathbf{k} , in Eq. (7.37), (7.38), one simply sets $\mathbf{k} = 0$ (frozen). With this assumption the integration reduces to a factor $4\pi k_F^3/3$. We have found that this approximation is quite accurate, introducing only a $\sim 6\%$ variation in the correlated interference transverse response. This represents a major computational advantage, since the problem is reduced from a seven-dimensional to a four-dimensional integral, and it is no longer necessary to solve the BG equation for all \mathbf{h}, \mathbf{k} pairs but only for h and $k = 0$, which are far fewer.

We begin by performing a scaling analysis of the experimental data of the longitudinal nuclear response R_L for three values of the momentum transfer: $q = 300, 380, 570$ MeV/c. To compare our results with experimental data and investigate whether an enhancement is observed in the transverse response R_T , we introduce a hybrid model, where the one-body contribution is not calculated using the Fermi gas approach, which overestimate the experimental data. Instead, we use the SuSA model. This SuSA approximation is based on a phenomenological scaling function extracted from longitudinal experimental data by dividing them by the single-nucleon factor, as in Eq. (2.22), but for the response function instead of the cross section

$$f_L(\psi') = \frac{R_L^{exp}}{r_L} \quad (7.50)$$

where r_L is given by Eq. (2.23). In this chapter we do not include the effective mass. Instead, we use $M^* = 1$ and we introduce an energy shift of 20 MeV so $\omega \rightarrow \omega - E_s$ with $E_s = 20$ MeV. The resulting longitudinal scaling function using the definition described above is shown in Figure 7.2. The black line is parametrized as a sum of two gaussians. The figure illustrates how the experimental data tend to collapse onto a single curve, particularly near the quasielastic peak, corresponding to values of the scaling variable within the interval

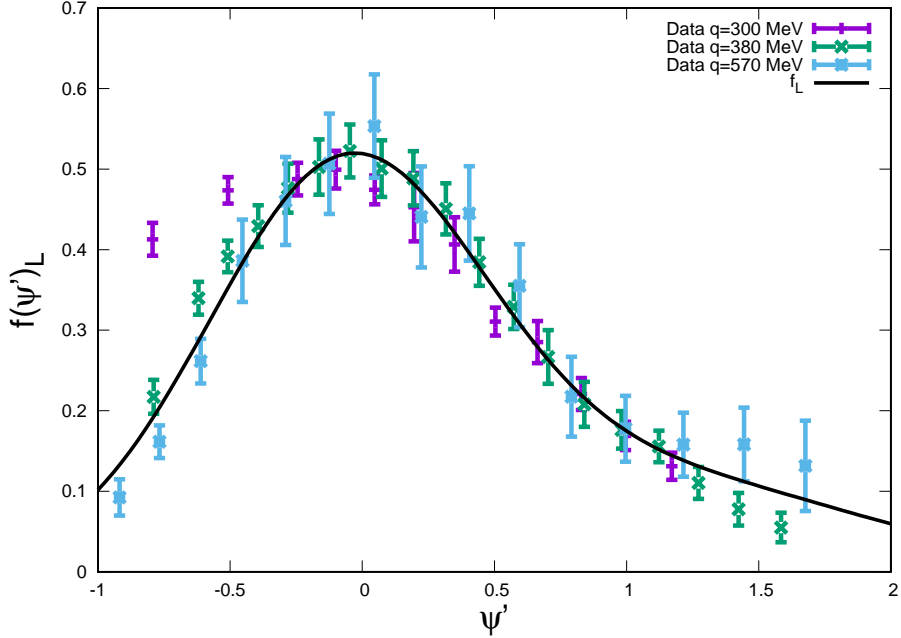


Figure 7.2: Longitudinal scaling function obtained phenomenologically for three values of $q = 300, 380, 570$ MeV/c from [44]

$-1 \leq \psi' \leq 1$. This scaling behavior supports the idea that the longitudinal response factorizes and can be used to describe the QE kinematics.

Our goal is to compute the transverse response, so we assume that the longitudinal and transverse scaling functions can be approximated as equal, ie, $f_L = f_T$. This assumption assumes zeroth kind scaling [143]. From Eq. (2.21) in chapter 2, we obtain:

$$R_T^{1b} \equiv R_T^{SuSA} = r_T(q, \omega) f_T(\psi') \quad (7.51)$$

with

$$r_T(q, \omega) = \frac{\epsilon_F - 1}{m_N \eta_F^3 \kappa} Z \bar{w}_T(q, \omega) \quad (7.52)$$

and where the $\bar{w}_T(q, \omega)$ is the averaged single nucleon tensor defined in Eq. (2.15).

In Figure 7.3, we present the longitudinal and transverse responses for ^{12}C at three values of the momentum transfer: $q = 300, 380, 570$ MeV/c. The left panel shows the one-body longitudinal response R_L obtained with the *SuSA* model, using the phenomenological longitudinal scaling function of Fig. 7.2. The comparison with experimental data demonstrates that the *SuSA* model provides a good description of the longitudinal channel. The right panel displays the corresponding transverse response R_T , including all the contributions of our model. The one-body term is computed within the *SuSA* approach, assuming $f_L = f_T$, as discussed earlier. Alongside this baseline, we show the uncorrelated 1b2b (MEC) interference $(R_T^{1b2b})_{FG}$, which yields a negative contribution, and the correlated 1b2b interference $(R_T^{1b2b})_{cor}$ from the contribution from the high momentum pairs, which is positive. The sum of these two interference terms produces a net positive contribution that enhances the *SuSA* one-body response. As a result, the total transverse

response, represented by the solid black line, is given by

$$R_T = R_T^{SuSA} + (R_T^{1b2b})_{FG} + (R_T^{1b2b})_{cor} \quad (7.53)$$

The left panel of Fig. 7.4 shows the comparison of the 1b2b uncorrelated and correlation contribution interference transverse responses $(R_T^{1b2b})_{FG}$ and $(R_T^{1b2b})_{cor}$ for seagull, pionic and Δ currents. On the other hand, in the right panel, Fig. 7.4 shows the total effect of correlations with each MEC current, given by $(R_T^{1b2b})_{FG} + (R_T^{1b2b})_{cor}$ in comparison with the non-correlated response $(R_T^{1b2b})_{FG}$. We can compare our results from Figure 7.4 with other calculations of the 1b–2b interference including correlations. The only available work of this kind is that of Fabrocini [35], who employed the correlated basis function (CBF) model in nuclear matter. A deeper comparison is possible since Fabrocini published the separate contributions of the seagull, pionic, and Δ currents. The first thing we conclude between both models is the qualitative similarity of the results. In the independent-pair approximation (the present calculation), the effect of correlations on the seagull response is very small (See right panel of Fig. 7.4), so that it practically does not change when correlations are included. The seagull response is large and positive, becoming slightly negative beyond the midpoint of the quasielastic region. Correlations have a more noticeable effect on the pionic response, which is negative in the absence of correlations and becomes positive when correlations are included. The most significant effect is observed in the interference with the Δ current: in the uncorrelated case it is negative and dominates the three contributions, while correlations render it positive. Similar results were obtained by Fabrocini using the CBF model [35]. Although our approach is based on a microscopic model, it is also worth noting the analysis by Bodek et al [44], who performed an empirical extraction of the transverse enhancement using a global fit to inclusive electron scattering data on ^{12}C and ^{16}O . Despite not being a theoretical calculation, their result also shows to an enhancement of the same size in the transverse channel, which aligns with the trend observed in our work.

A deeper insight into the effect of correlations on the 1b–2b interference response is presented in Figure 7.5, where we show the separate contributions in ^{12}C , for $q = 300, 380, 570$ MeV/c, from different multipoles, $\phi_{ll'}^{SJ}$, of the correlated wave function. Specifically, we display the contributions from the uncoupled channels with $S = 0$ and $S = 1$ (top panels), the coupled channels with $S = 1, J = 1$ (middle panels), and the coupled channels with $S = 1, J = 2$ (bottom panels). It is evident that the dominant contribution comes from the $S = 1, J = 1$ channels, i.e., the 3S_1 – 3D_1 partial waves, which exceed the other contributions by roughly a factor of 50. This dominance arises primarily from the 3D_1 / 3S_1 interference, indicating that the main effect is driven by the tensor force in the NN interaction, a feature also reported by Fabrocini in Ref. [35]. Fig. 7.5 indicates that correlations tend to generate a significant enhancement of the transverse response. Since the dominant contribution arises from the 3S_1 – 3D_1 channel, i.e. the deuteron channel, this enhancement is produced mainly by the interaction with correlated np pairs in the nuclear medium.

In Figures 7.6, 7.7 and 7.8, we present the correlated interference response $(R_T^{1b2b})_{cor}$, separated again in its partial wave contributions for each coupled channel. The notation used throughout the figures is explained in Table 7.3.

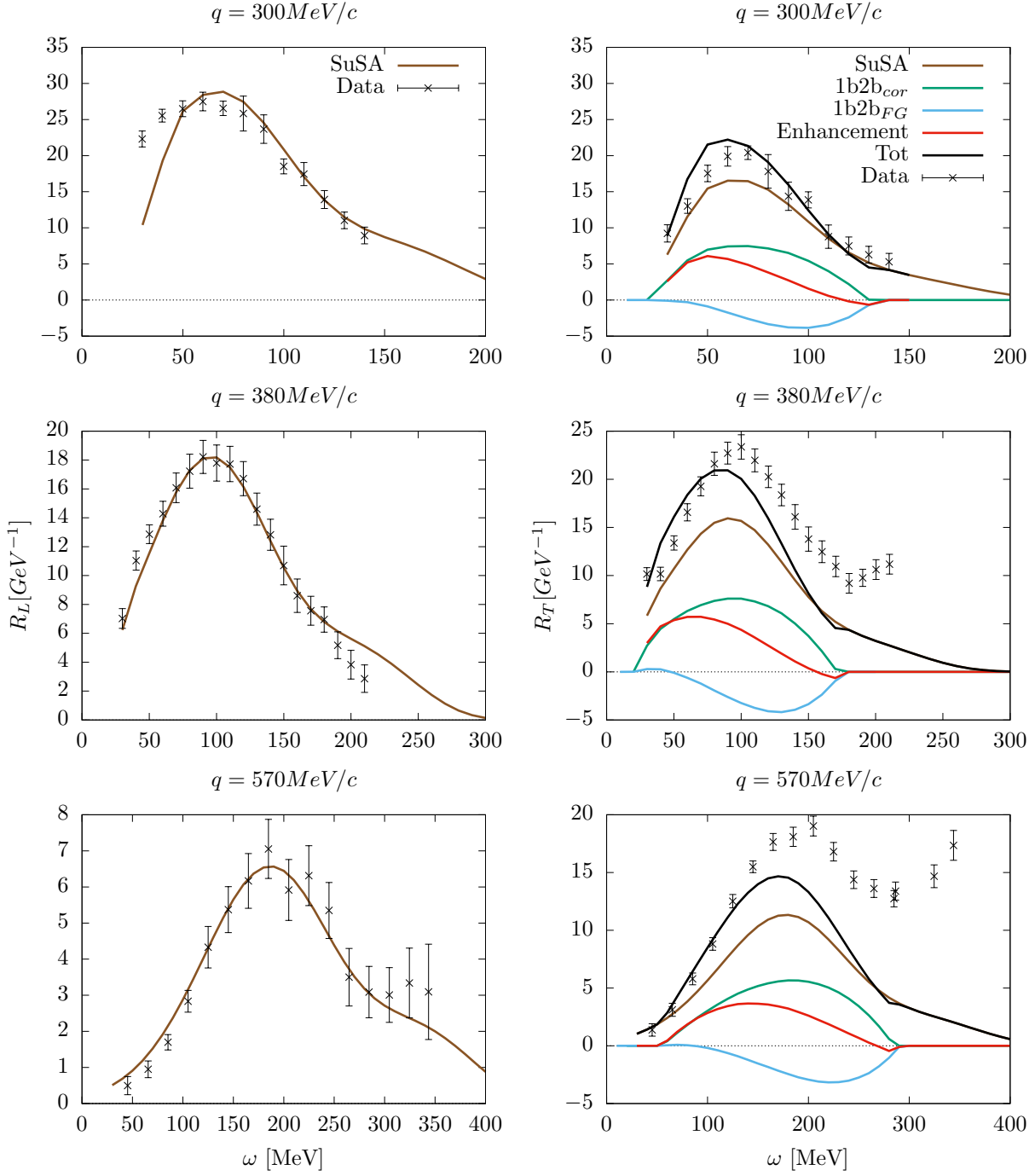


Figure 7.3: Left: Longitudinal one-body response R_L computed with the *SuSA* model and compared with experimental data for several momentum transfers $q = 300, 380, 570 \text{ MeV}/c$. Right: total transverse response function for the same q values. The latter includes the *SuSA* one-body contribution (brown line), the uncorrelated 1b2b interference ($R_T^{1b2b}_{FG}$) (blue line), the correlated 1b2b interference ($R_T^{1b2b}_{cor}$) (green line), and the net enhancement effect (red line). Experimental data are also included for comparison in both cases.

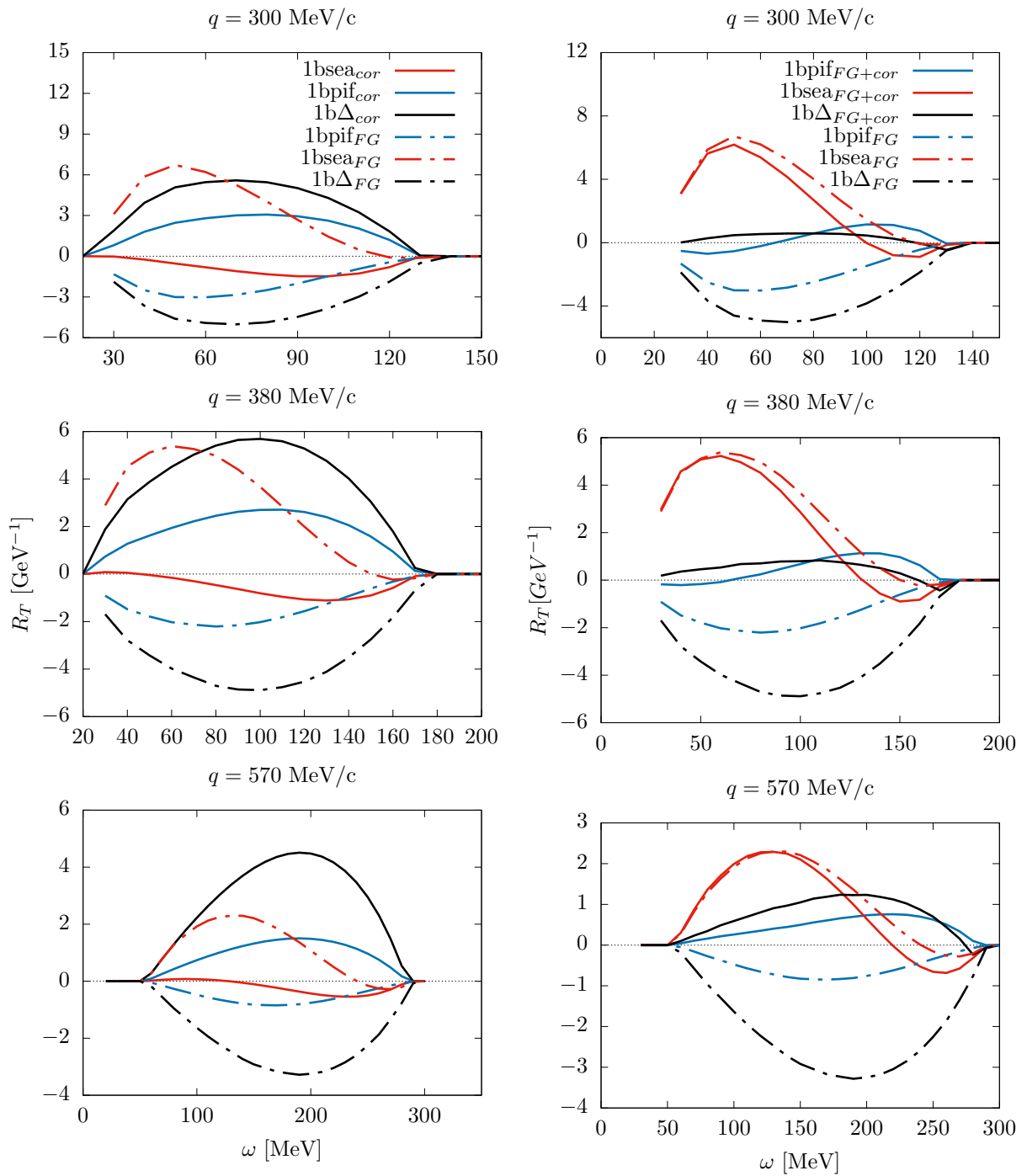


Figure 7.4: Left: Transverse 1b2b interference response at momentum transfers $q = 300, 380, 570$ MeV/c, shown separately for each MEC contribution: seagull (red), pion-in-flight (blue), and Δ (black). Dashed lines represent the uncorrelated interference $(R_T^{1b2b})_{FG}$ while the solid lines correspond to $(R_T^{1b2b})_{cor}$ with the effect of short-range correlations. Right: Comparison between the uncorrelated interference $(R_T^{1b2b})_{FG}$ (dashed lines) and the total 1b2b contribution including correlations $(R_T^{1b2b})_{FG} + (R_T^{1b2b})_{cor}$ (solid lines). Colors indicate the same MEC components as in the left panel: seagull (red), pion-in-flight (blue), and Δ (black).

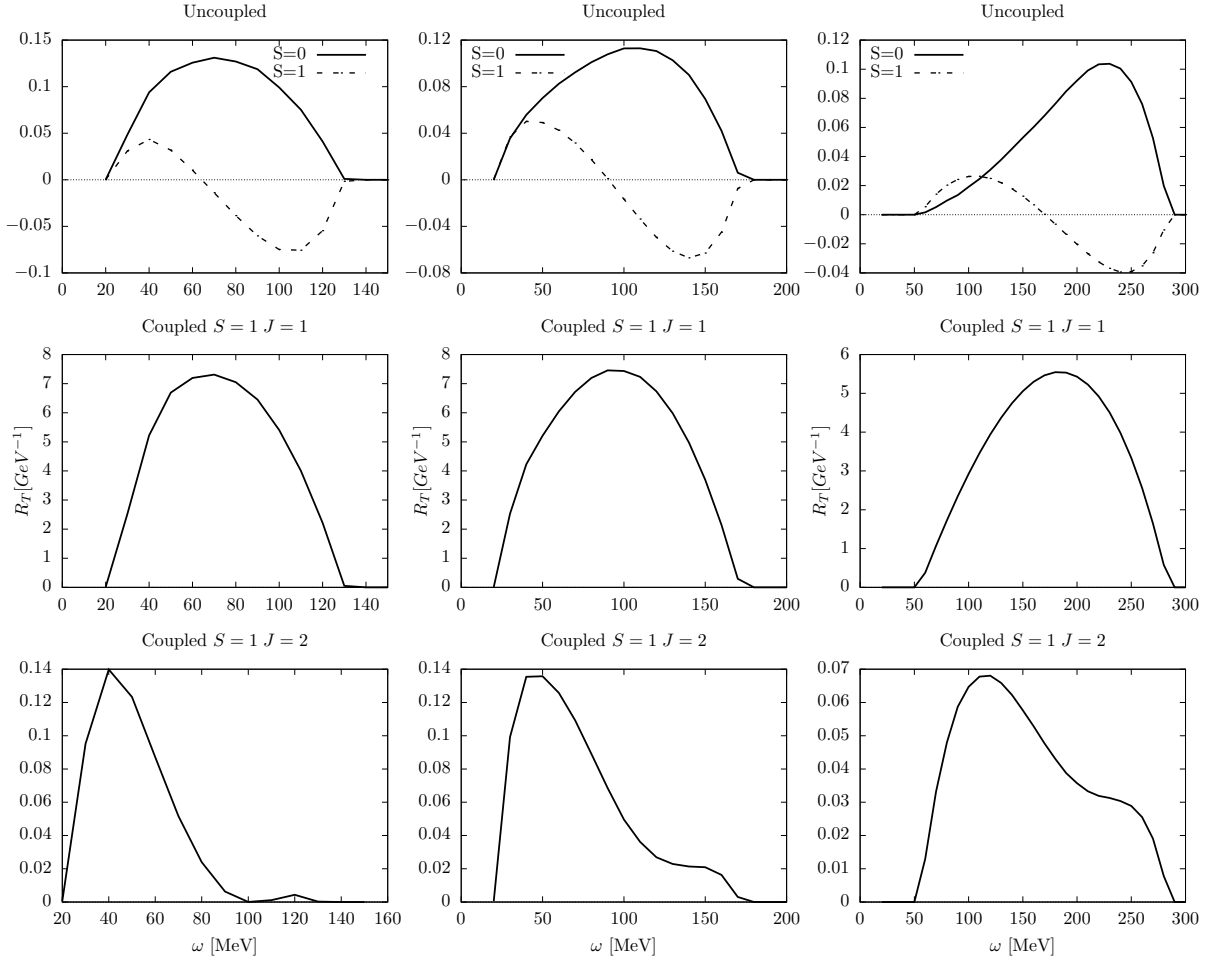


Figure 7.5: Partial wave decomposition of the correlation induced interference response $(R_T^{1b2b})_{cor}$ for $q = 300$ (left), 380 (middle) and 570 (right) MeV/c. The contributions are separated according to spin and total angular momentum: uncoupled channels with $S = 0$ and $S = 1$, and coupled channels with $S = 1$, $J = 1$ and $J = 2$.

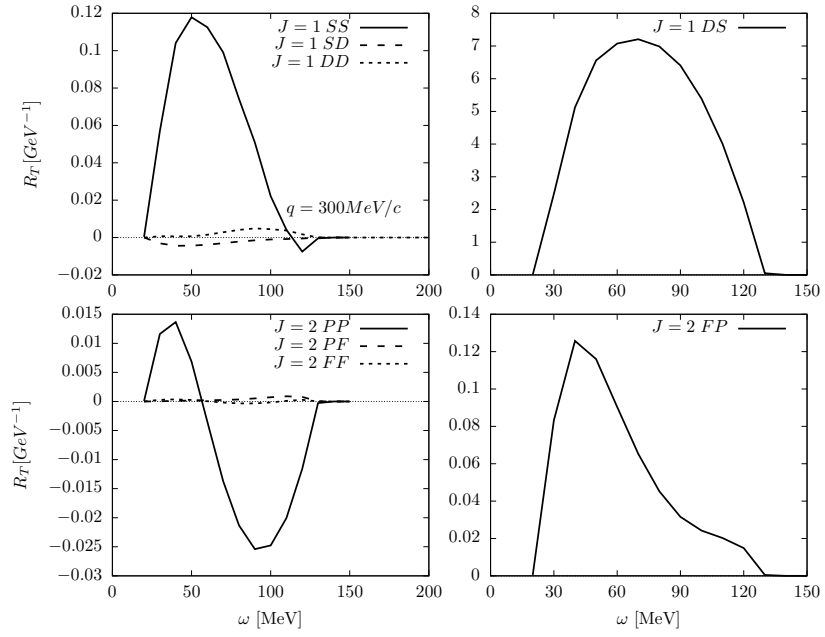


Figure 7.6: Correlated 1b2b interference response $(R_T^{1b2b})_{cor}$ for $q = 300$ MeV/c, separated in partial waves, for each coupled angular momentum channel. The upper panels correspond to the $J = 1$ channel, and the lower panels to $J = 2$. The largest contributions appear in the right-hand panels, particularly in the DS component of the $J = 1$ channel.

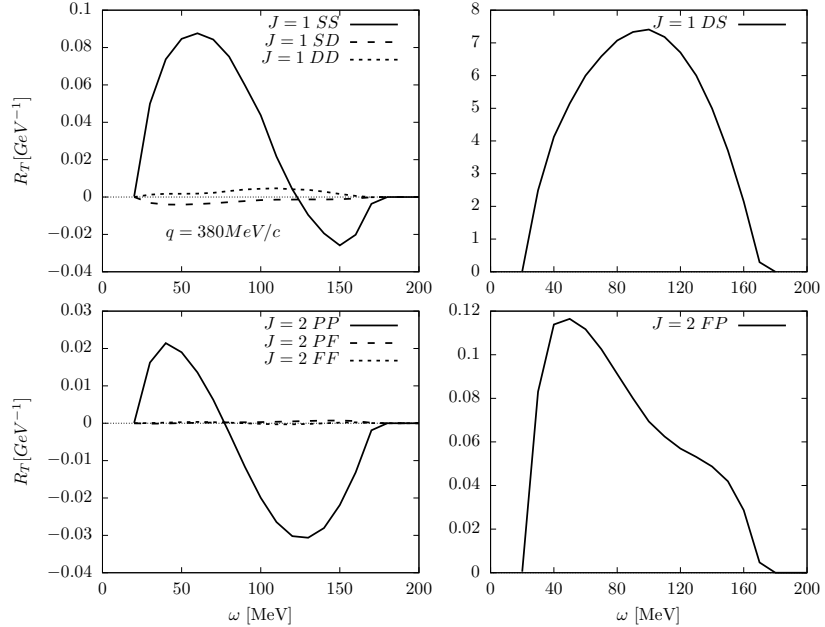


Figure 7.7: The same as Figure 7.6 but for $q = 380$ MeV/c

Partial-Wave Notation in Coupled Channels

Total Angular Momentum $J = 1$

Partial Wave	label
3S_1	SS
$^3S_1/{}^3D_1$	SD
${}^3D_1/{}^3S_1$	DS
3D_1	DD

Total Angular Momentum $J = 2$

3P_2	PP
${}^3P_2/{}^3F_2$	PF
${}^3F_2/{}^3P_2$	FP
3F_2	FF

Table 7.3: Abbreviations used for each partial wave in the coupled channels with total angular momentum $J = 1$ and $J = 2$.

Figure 7.6 shows the results for $q = 300$ MeV/c. The upper panels display the contributions to the response from the coupled $J = 1$ channel, while the lower panels correspond to $J = 2$. As we already discussed and can be seen in the top right panel, the dominant contribution clearly comes from the DS component. This behavior is consistent with what was observed in chapter 6, particularly in Figure (6.14), where it is evident that the largest contribution corresponds precisely to the partial wave mixing ${}^3D_1/{}^3S_1$ for $J = 1$. Figures 7.7 and 7.8 show the same partial wave decomposition of the correlated interference response, evaluated for momentum transfers $q = 380$ and $q = 570$ MeV/c, respectively. In both cases, the overall behavior remains consistent with the results obtained at $q = 300$ MeV/c.

7.3. Final Remarks

In this chapter we have investigated the effect of short-range correlations on the 1p1h MEC contribution to the transverse response of nuclei. Using the independent pair approximation, we have incorporated SRC by replacing the uncorrelated pair wave functions with the correlated waves obtained from the solution of the Bethe–Goldstone equation of chapter 6 with a realistic NN interaction, namely the Granada 2013 potential. This approach allows the two-nucleon wave function to acquire high-momentum components above the Fermi sea, which are absent in the uncorrelated Fermi gas.

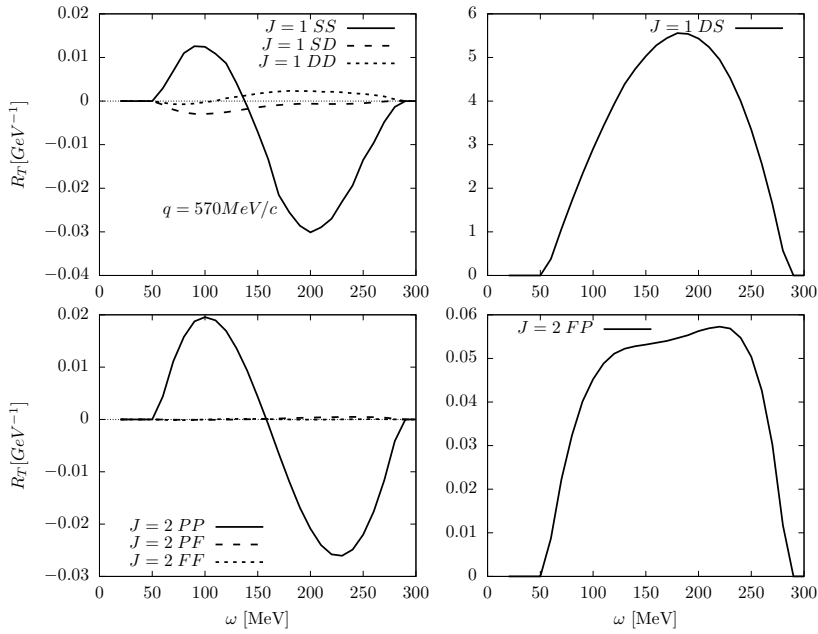


Figure 7.8: The same as Figure 7.6 but for $q = 570 \text{ MeV}/c$

The results show that SRC generate an enhancement of the transverse 1b2b interference response in the quasielastic peak region. The multipole decomposition of the correlated wave function reveals that the dominant contribution arises from the coupled $S = 1$, $J = 1$ channel, i.e., the 3S_1 – 3D_1 (deuteron-like) components. This indicates that the enhancement is primarily driven by the tensor component of the NN interaction, in agreement with previous findings from CBF calculations. Comparison with the CBF results shows a qualitative agreement despite the very different treatments of SRC: while the CBF approach applies a variational correlation operator to uncorrelated Slater determinants, our method solves the BG equation. We have combined our correlated 1b2b response with a SuSA description of the quasielastic 1b response in a hybrid model to compare with experimental transverse response data of ^{12}C . We find that the inclusion of SRC produces a net enhancement of the transverse response that brings the calculation into the correct order of magnitude to describe the data at low and intermediate momentum transfer. While at higher q additional contributions from 2p2h excitations and pion emission are missing, the present calculation highlights the essential role of SRC in generating the transverse enhancement.

Chapter 8

Conclusions

The present thesis has addressed the QE scattering of electrons and neutrinos from nuclei, with particular emphasis on the role of meson-exchange currents and short-range correlations in one-particle emission channel. The work has combined theoretical developments, model extensions, and detailed numerical analyses, aiming at a more comprehensive description of nuclear responses in this regime.

Chapter 2 is devoted to the study of the superscaling framework, revisiting the definition of single-nucleon responses within the *SuSAM** model for electron scattering. It was shown that the conventional extrapolation procedure of the averaged on-shell single nucleon responses leads to inconsistencies beyond the scaling region, occasionally producing unphysical negative responses. To overcome this limitation, a new definition is proposed, based on an average using smeared momentum distribution around the Fermi surface. This approach avoids the problem of the extrapolation while remaining consistent with data in the scaling region.

The thesis has also explored in detail the interference between one-body and two-body currents in the quasielastic regime. A method that enables the consistent inclusion of meson-exchange currents within the framework of the superscaling analysis with relativistic effective mass is presented in chapter 3. The approach is rigorously relativistic, drawing its foundation from the relativistic mean field theory of nuclear matter. The generalized scaling analysis is comprehensively illustrated and applied to the (e, e') cross-section of ^{12}C . To achieve this, we apply the new definition of the single-nucleon tensor studied in chapter 2. Calculations performed within several independent particle models like RFG, RMF and *SuSAM** confirmed the general tendency of MEC to reduce the transverse response, in line with previous findings [33],[169].

In chapter 4, we have rigorously demonstrated, within the framework of the non-relativistic Fermi gas, that the interference between one-body (1b) and two-body (2b) currents—arising from Δ -excitation and pionic mechanisms—produces a negative contribution to the transverse response. This finding has been critically evaluated through comparisons with a wide range of independent single-particle descriptions, including both relativistic and non-relativistic mean-field models, as well as spectral function approaches, all of which consistently support the conclusion of a negative interference effect.

The formalism was then extended to charged-current quasielastic neutrino and antineutrino scattering in chapter 5. The interference between one-body and two-body operators was calculated for all nuclear response functions (CC, CL, LL, T, and T'), showing that the contribution of MEC generates strong negative interference effects in the transverse responses and also in the neutrino and antineutrino cross sections for 1p1h excitations in the relativistic Fermi gas. Our results show that the 1b2b interference contributions are not negligible and may be comparable in size to other nuclear effects usually included in more sophisticated models. For instance, effects such as long-range correlations modeled via the Random Phase Approximation [36, 37], final-state interactions (FSI) in energy-dependent RMF approaches [215], finite-size shell effects in Hartree–Fock based models [216], or GiBUU transport theory [217], all modify the shape and size of the nuclear response. The presence of a non-negligible 1b2b interference is comparable to the 2p2h effect and implies that the models may need to be revisited or extended to estimate at least the order of magnitude of this contribution and its possible interplay with the aforementioned mechanisms.

It is worth mentioning the existence of some calculations that disagree with this result and suggest a different effect of MEC on the transverse response. In particular, there are two notable model calculations: the Green Function Monte Carlo (GFMC) model from Reference [54] and the RFM and spectral function models from [46, 47, 218]. In those approaches, the effect of MEC is positive in the quasielastic peak and quite significant, around 20%, in the transverse response. For GFMC model, this substantial effect is attributed to the simultaneous effect of correlations in the wave function and MEC. Conversely, the positive result of Refs. [46, 218] is due to a Δ current with a sign opposite to the standard operator, as was explicitly demonstrated in the Appendix G of Ref. [172]. A similar feature can be identified in Ref. [47], where the propagator of the Δ resonance is taken with opposite sign. On the other hand, Ref. [34] employs a fully correlated model with the standard operator, in which case the enhancement plausibly originates from the role of correlations, consistent with the findings of Fabrocini from Ref. [35].

The persistence of negative response functions across different theoretical frameworks strongly suggests that the mechanism responsible for the experimentally observed transverse enhancement [44] cannot be attributed to mean-field dynamics alone. This observation naturally points to SRC as a key ingredient that must be incorporated into the nuclear wave function to capture the correct underlying physics. Consequently, the study of SRC emerges as the natural next step, forming the focus of chapter 6.

In chapter 6, the focus shifted toward the microscopic treatment of SRC via the Bethe–Goldstone equation. The high-momentum components of the nuclear wave function of two correlated nucleons were obtained using the realistic 2013 Granada potential, which is a coarse grained interaction represented as a sum of delta functions in each partial wave. It has been observed that this coarse-grained potential reduces the problem to an algebraic linear system of five (ten) equations for uncoupled (coupled) partial waves that can be easily solved. The analysis confirmed the dominance of the 3S_1 and $^3D_1/^3S_1$ channels, which implies that the pn pairs dominate the high-momentum tail of the relative momentum distribution.

Finally, in chapter 7, these correlated wave functions were incorporated into the cal-

culation of MEC contributions within the quasielastic transverse response. The results demonstrate that the high momentum components generate an additional enhancement that cannot be accounted for within uncorrelated frameworks, reinforcing the necessity of their inclusion in any realistic description of electron and neutrino scattering. In general, this study demonstrates that the SRC mechanism incorporated via the BG equation and independent pair approximation provides a physically transparent, parameter-free, and essentially *ab initio* way to account for the observed enhancement in the 1p1h MEC transverse response. The dominance of the 3S_1 – 3D_1 channel underscores the importance of the tensor force in the nuclear medium, and the results presented suggest that SRC should be included in any realistic modeling of quasielastic transverse responses. Future investigations stemming from this work include extending the formalism to neutrino scattering, since the transverse enhancement will appear in the vector response; it is also important to determine whether the responses associated with the axial current exhibit a similar enhancement due to SRC and MEC, which would have direct implications for neutrino interaction models.

Appendix A

Single-nucleon responses

The single-nucleon hadronic tensor is computed performing the spin traces (2.9) with the current matrix elements (2.10), and can be written as

$$w^{\mu\nu} = -w_1 \left(g^{\mu\nu} - \frac{Q^\mu Q^\nu}{Q^2} \right) + w_2 V^\mu V^\nu, \quad (\text{A.1})$$

where we have defined the four-vector $V^\mu = (H^\mu + Q^\mu/2)/m_N^*$, and $H^\mu = (E, \mathbf{h})$ is the initial nucleon four-momentum with effective mass m_N^* . The four-momentum of the final nucleon is $P^\mu = H^\mu + Q^\mu$. The nucleon structure functions are given by

$$w_1(Q^2) = \tau(G_M^*)^2 > 0, \quad (\text{A.2})$$

$$w_2(Q^2) = \frac{(G_E^*)^2 + \tau(G_M^*)^2}{1 + \tau} > 0, \quad (\text{A.3})$$

where the electric and magnetic form factors for nucleons with effective mass are

$$G_E^* = F_1 - \tau \frac{m_N^*}{m_N} F_2, \quad G_M^* = F_1 + \frac{m_N^*}{m_N} F_2. \quad (\text{A.4})$$

For the F_i form factors of the nucleon, we use the Galster parametrizations [219].

Note that w_1 and w_2 are positive and depend only on Q^2 . Here we compute the longitudinal and transverse components of the hadronic tensor, $w_L = w^{00}$ and $w_T = w^{11} + w^{22}$ respectively, appearing in inclusive electron scattering.

Longitudinal single-nucleon response We use the following results for the time components of the basic tensors and vectors in terms of dimensionless variables, κ, λ, τ

$$g^{00} - \frac{Q^0 Q^0}{Q^2} = -\frac{q^2}{Q^2} = \frac{\kappa^2}{\tau}, \quad (\text{A.5})$$

$$V^0 = \frac{E + \omega/2}{m_N^*} = \epsilon + \lambda. \quad (\text{A.6})$$

Substituting the values of these time components and of the structure functions in the hadronic tensor (A.1), the longitudinal single-nucleon response function becomes

$$w_L = -\kappa^2(G_M^*)^2 + \frac{(G_E^*)^2 + \tau(G_M^*)^2}{1 + \tau}(\epsilon + \lambda)^2. \quad (\text{A.7})$$

Rearranging terms containing G_E^* and G_M^* this becomes

$$w_L = \frac{(G_M^*)^2}{1 + \tau}[\tau(\epsilon + \lambda)^2 - (1 + \tau)\kappa^2] + \frac{(G_E^*)^2}{1 + \tau}(\epsilon + \lambda)^2. \quad (\text{A.8})$$

Transverse single-nucleon response In the case of the transverse response $g^{ii} = -1$ and $V^i = h_i/m_N^* = \eta_i$, for $i = 1, 2$, where we have defined the three-vector $\boldsymbol{\eta} = \mathbf{h}/m_N^*$. Then the T response is

$$w_T = w^{11} + w^{22} = 2w_1 + w_2(\eta_1^2 + \eta_2^2). \quad (\text{A.9})$$

Note that $\eta_1^2 + \eta_2^2 = \eta^2 - \eta_3^2 = \epsilon^2 - 1 - \eta_3^2$. The value of η_3^2 is the projection of the vector $\boldsymbol{\eta}$ over the \mathbf{q} direction, which is determined by energy-momentum conservation. In fact, using Eq (2.11)

$$\eta_3 = \frac{h \cos \theta}{m_N^*} = \frac{E\omega + Q^2}{m_N^* q} = \frac{\epsilon\lambda - \tau}{\kappa}. \quad (\text{A.10})$$

Then we have

$$\eta_1^2 + \eta_2^2 = \epsilon^2 - 1 - \left(\frac{\epsilon\lambda - \tau}{\kappa}\right)^2. \quad (\text{A.11})$$

Expanding the square and using $\kappa^2 - \lambda^2 = \tau$, this gives

$$\eta_1^2 + \eta_2^2 = \frac{\tau}{\kappa^2} \left[\epsilon^2 - \frac{\kappa^2}{\tau} - \tau + 2\epsilon\lambda \right] = \frac{\tau}{\kappa^2} \left[(\epsilon + \lambda)^2 - \kappa^2 \frac{1 + \tau}{\tau} \right]. \quad (\text{A.12})$$

Inserting this result in Eq. (A.9) and using the values of w_i from Eqs. (A.2,A.3), the transverse response becomes

$$w_T = 2\tau(G_M^*)^2 + \frac{(G_E^*)^2 + \tau(G_M^*)^2}{1 + \tau} \frac{\tau}{\kappa^2} \left[(\epsilon + \lambda)^2 - \kappa^2 \frac{1 + \tau}{\tau} \right]. \quad (\text{A.13})$$

Appendix B

Isospin Summations in the 1p1h MEC Matrix Element

Here we provide the sums over the isospin index t_k of the spectator nucleon appearing in the 1p1h MEC matrix element. The isospin dependence of the MEC is of the form

$$\mathbf{j} = \tau_z^{(1)}\mathbf{j}_1 + \tau_z^{(2)}\mathbf{j}_2 + i[\boldsymbol{\tau}^{(1)} \times \boldsymbol{\tau}^{(2)}]_z\mathbf{j}_3, \quad (\text{B.1})$$

where $\boldsymbol{\tau}^{(1)}$ and $\boldsymbol{\tau}^{(2)}$ are isospin operators of the first and second particle, respectively. We begin by referencing the Pauli matrices, which also represent the isospin operators required.

$$\tau_1 = \begin{pmatrix} 0 & 1 \\ 1 & 0 \end{pmatrix}, \quad \tau_2 = \begin{pmatrix} 0 & -i \\ i & 0 \end{pmatrix}, \quad \tau_3 = \begin{pmatrix} 1 & 0 \\ 0 & -1 \end{pmatrix}. \quad (\text{B.2})$$

These matrices act on the isospin states of nucleons, $|t\rangle$, for protons ($t = +\frac{1}{2}$) and neutrons ($t = -\frac{1}{2}$). We need the basic result

$$\begin{aligned} \tau_1|p\rangle &= |n\rangle, & \tau_1|n\rangle &= |p\rangle \\ i\tau_2|p\rangle &= -|n\rangle & i\tau_2|n\rangle &= |p\rangle. \end{aligned}$$

By expanding the vector product

$$i[\boldsymbol{\tau}^{(1)} \times \boldsymbol{\tau}^{(2)}]_z = i\tau_1^{(1)}\tau_2^{(2)} - i\tau_2^{(1)}\tau_1^{(2)}, \quad (\text{B.3})$$

we obtain

$$\begin{aligned} i[\boldsymbol{\tau}^{(1)} \times \boldsymbol{\tau}^{(2)}]_z|pp\rangle &= 0, \\ i[\boldsymbol{\tau}^{(1)} \times \boldsymbol{\tau}^{(2)}]_z|nn\rangle &= 0, \\ i[\boldsymbol{\tau}^{(1)} \times \boldsymbol{\tau}^{(2)}]_z|pn\rangle &= 2|np\rangle = 4t_p|np\rangle, \\ i[\boldsymbol{\tau}^{(1)} \times \boldsymbol{\tau}^{(2)}]_z|np\rangle &= -2|pn\rangle = 4t_n|pn\rangle. \end{aligned}$$

These four equations can be written in unified form as

$$i[\boldsymbol{\tau}^{(1)} \times \boldsymbol{\tau}^{(2)}]_z|t_1t_2\rangle = 4t_1(1 - \delta_{t_1t_2})|t_2t_1\rangle. \quad (\text{B.4})$$

From these elementary results, we can compute the sums over t_k appearing in the direct and exchange matrix elements of the current.

Direct terms.

For the the direct terms we have:

$$\sum_{t_k=\pm 1/2} \langle t_p t_k | \tau_z^{(1)} | t_h t_k \rangle = \sum_{t_k} \delta_{t_p t_h} 2t_h = \delta_{t_p t_h} 4t_h, \quad (\text{B.5})$$

$$\sum_{t_k} \langle t_p t_k | \tau_z^{(2)} | t_h t_k \rangle = \sum_{t_k} \delta_{t_p t_h} 2t_k = 0, \quad (\text{B.6})$$

$$\sum_{t_k} \langle t_p t_k | i[\boldsymbol{\tau}^{(1)} \times \boldsymbol{\tau}^{(2)}]_z | t_h t_k \rangle = \sum_{t_k} \delta_{t_p t_k} \delta_{t_k t_h} 4t_k (1 - \delta_{t_h t_k}) = 0. \quad (\text{B.7})$$

Exchange terms.

For the the exchange matrix elements we have:

$$\sum_{t_k} \langle t_p t_k | \tau_z^{(1)} | t_k t_h \rangle = \sum_{t_k} \delta_{t_p t_k} \delta_{t_k t_h} 2t_k = \delta_{t_p t_h} 2t_h, \quad (\text{B.8})$$

$$\sum_{t_k} \langle t_p t_k | \tau_z^{(2)} | t_k t_h \rangle = \sum_{t_k} \delta_{t_p t_k} \delta_{t_k t_h} 2t_h = \delta_{t_p t_h} 2t_h, \quad (\text{B.9})$$

$$\begin{aligned} \sum_{t_k} \langle t_p t_k | i[\boldsymbol{\tau}^{(1)} \times \boldsymbol{\tau}^{(2)}]_z | t_k t_h \rangle &= \sum_{t_k} \langle t_p t_k | 4t_k (1 - \delta_{t_k t_h}) | t_h t_k \rangle \\ &= \sum_{t_k} \delta_{t_p t_h} 4t_k (1 - \delta_{t_k t_h}) = -\delta_{t_p t_h} 4t_h. \end{aligned} \quad (\text{B.10})$$

Null Δ diagrams.

Next, we will demonstrate that diagrams (f) and (g) corresponding to the Δ current are zero after summing over isospin. To achieve this, we must use the original form of the isospin operators, Eqs. (3.25 and 3.26). The forward current involves the operators $U_F(1, 2)$ and $U_F(2, 1)$, while the backward current contains the isospin operators $U_B(1, 2)$ and $U_B(2, 1)$. By carefully analyzing these operators, we can show that the specific contributions from diagrams (f) and (g) cancel out, leading to a net zero result for each. First, from property (4.28) we can write the following products

$$T_1 T_3^\dagger = \frac{i}{3} \tau_2 \quad T_2 T_3^\dagger = -\frac{i}{3} \tau_1 \quad (\text{B.11})$$

$$T_3 T_1^\dagger = -\frac{i}{3} \tau_2 \quad T_3 T_2^\dagger = \frac{i}{3} \tau_1 \quad (\text{B.12})$$

$$T_3 T_3^\dagger = \frac{2}{3}. \quad (\text{B.13})$$

From here, using $\tau_1\tau_2 = -\tau_2\tau_1 = i\tau_3$, we have

$$\begin{aligned} \sum_i \tau_i T_i T_3^\dagger &= \tau_1 T_1 T_3^\dagger + \tau_2 T_2 T_3^\dagger + \tau_3 T_3 T_3^\dagger = \frac{i}{3}\tau_1\tau_2 - \frac{i}{3}\tau_2\tau_1 + \frac{2}{3}\tau_3 \\ &= -\frac{1}{3}\tau_3 - \frac{1}{3}\tau_3 + \frac{2}{3}\tau_3 = 0. \end{aligned} \quad (\text{B.14})$$

In the case of the forward current, the isospin sum of the exchange matrix element of the $(1 \leftrightarrow 2)$ term is

$$\begin{aligned} \sum_{t_k} \langle pk | U_F(2, 1) | kh \rangle &= \sum_{t_k} \sqrt{\frac{3}{2}} \langle pk | \sum_i T_i^{(2)} T_3^{(2)\dagger} \tau_i^{(1)} | kh \rangle \\ &= \sqrt{\frac{3}{2}} \sum_{t_k} \sum_i \langle p | \tau_i | k \rangle \langle k | T_i T_3^\dagger | h \rangle = \\ &= \sqrt{\frac{3}{2}} \sum_i \langle p | \tau_i T_i T_3^\dagger | h \rangle = 0. \end{aligned} \quad (\text{B.15})$$

This demonstrates the result for the forward term, that diagram (f) of Fig. 3.2 is zero. Analogously, the same steps can be applied to show the result that diagram (g) for the backward term is zero. First we have

$$\sum_i T_3 T_i^\dagger \tau_i = T_3 T_1^\dagger \tau_1 + T_3 T_2^\dagger \tau_2 T_3 T_3^\dagger \tau_3 = -\frac{i}{3}\tau_2\tau_1 + \frac{i}{3}\tau_1\tau_2 + \frac{2}{3}\tau_3 = -\frac{1}{3}\tau_3 - \frac{1}{3}\tau_3 + \frac{2}{3}\tau_3 = 0. \quad (\text{B.16})$$

The diagram (g) contain the isospin operator $U_B(1, 2)$ and the isospin sum of the exchange matrix element is

$$\begin{aligned} \sum_{t_k} \langle pk | U_B(1, 2) | kh \rangle &= \sum_{t_k} \sqrt{\frac{3}{2}} \langle pk | \sum_i T_3^{(1)} T_i^{(1)\dagger} \tau_i^{(2)} | kh \rangle \\ &= \sqrt{\frac{3}{2}} \sum_{t_k} \sum_i \langle p | T_3 T_i^\dagger | k \rangle \langle k | \tau_i | h \rangle \\ &= \sqrt{\frac{3}{2}} \sum_i \langle p | T_3 T_i^\dagger \tau_i | h \rangle = 0. \end{aligned} \quad (\text{B.17})$$

Appendix C

Non relativistic reduction of the vector Δ current

Here we perform the non relativistic reduction of the four-vectors A^μ , and B^μ , Eqs. (4.21,4.22), appearing in the Δ -current. Using the definition of the $\gamma N \Delta$ vertex, Eq. (3.30) we have

$$A^\mu = \bar{u}(1') k_2^\alpha G_{\alpha\beta}(p_1 + Q) \frac{C_3^V}{m_N} (g^{\beta\mu} \not{Q} - Q^\beta \gamma^\mu) \gamma_5 u(1) \quad (C.1)$$

$$B^\mu = \bar{u}(1') k_2^\beta \frac{C_3^V}{m_N} \gamma_5 (g^{\alpha\mu} \not{Q} - Q^\alpha \gamma^\mu) G_{\alpha\beta}(p_1' - Q) u(1). \quad (C.2)$$

In the last equation we have permuted the γ_5 matrix, which introduces a minus sign that cancels with the negative sign from $-Q$. We only need to perform the non-relativistic reduction of the spatial components ($\mu = i$) of the Δ current, since we are computing the transverse response. In the non relativistic limit we neglect the time components of k^μ and Q^μ , i. e.

$$k_2^\mu \simeq (0, \mathbf{k}_2), \quad Q^\mu \simeq (0, \mathbf{q}). \quad (C.3)$$

Then for the A^i components we have

$$\begin{aligned} A^i &\simeq \bar{u}(1') k_2^k G_{kj} \frac{C_3^V}{m_N} (g^{ji} \not{Q} - Q^j \gamma^i) \gamma_5 u(1), \\ &= \bar{u}(1') k_2^k G_{kj} (p_1 + Q) \Gamma^{ji}(Q) u(1). \end{aligned} \quad (C.4)$$

Hence at leading order in the non-relativistic limit, only the spatial components of the Δ propagator G_{kj} and the vertex Γ_{ji} contribute, while the time components are suppressed. Analogously, we obtain a similar result for the backward vector components B^i ,

$$\begin{aligned} B^i &\simeq \bar{u}(1') k_2^k \frac{C_3^V}{m_N} \gamma_5 (g^{ji} \not{Q} - Q^j \gamma^i) G_{jk} u(1), \\ &= \bar{u}(1') k_2^k \Gamma^{ji}(-Q) G_{jk} (p_1' - Q) u(1). \end{aligned} \quad (C.5)$$

Furthermore, the procedure we follow to compute the non-relativistic reduction of a product of matrix operators is to perform the reduction on each operator separately. This approach is valid at leading order.

Δ propagator

We begin with the Δ propagator. In the static limit, with $p^\mu + Q^\mu \simeq (p^0, 0) = (m_N, 0)$, and neglecting the lower components we have

$$\frac{\not{p} + m_\Delta}{p^2 - m_\Delta^2} \rightarrow \frac{p_0 + m_\Delta}{p_0^2 - m_\Delta^2} = \frac{1}{m_N - m_\Delta} \quad (\text{C.6})$$

Then the Δ propagator is written as

$$\begin{aligned} G_{ij} &\simeq -\frac{1}{m_N - m_\Delta} \left(g_{ij} - \frac{1}{3} \gamma_i \gamma_j \right) \\ &\simeq -\frac{1}{m_N - m_\Delta} \left(-\delta_{ij} + \frac{1}{3} \sigma_i \sigma_j \right) \\ &= \frac{1}{m_N - m_\Delta} \left(\frac{2}{3} \delta_{ij} - i \frac{1}{3} \epsilon_{ijk} \sigma_k \right) \end{aligned} \quad (\text{C.7})$$

where we have used the property

$$\sigma_i \sigma_j = i \epsilon_{ijk} \sigma_k \quad (\text{C.8})$$

and ϵ_{ijk} is the Levi-Civita tensor.

$\gamma N \Delta$ vertex

To obtain the non-relativistic reduction of the vertex

$$\Gamma^{ji}(Q) = \frac{C_3^V}{m_N} (g^{ji} \not{Q} - Q^j \gamma^i) \gamma_5, \quad (\text{C.9})$$

in the low energy limit, we have $Q^\mu \simeq (0, q^i)$. Then

$$\begin{aligned} (g^{ji} \not{Q} - Q^j \gamma^i) \gamma_5 &\simeq \delta_{ji} q^k \gamma^k \gamma_5 - q^j \gamma^i \gamma_5 \\ &\simeq \delta_{ji} q^k \sigma_k - q^j \sigma_i \\ &= q^k \sigma_l (\delta_{ij} \delta_{kl} - \delta_{il} \delta_{kj}) \end{aligned} \quad (\text{C.10})$$

This expression can be rewritten using the contraction of two Levi-Civita tensors

$$\epsilon_{ikm} \epsilon_{jlm} = \delta_{ij} \delta_{kl} - \delta_{il} \delta_{kj}. \quad (\text{C.11})$$

Therefore we have the non relativistic reduction

$$\Gamma^{ji}(Q) \simeq \frac{C_3^V}{m_N} (\epsilon_{ikm} q^k) (\epsilon_{jlm} \sigma_l) \quad (\text{C.12})$$

Forward vector A^i

From Eq. (C.4) we have (we do not write the spinors, just the spin operators):

$$\begin{aligned} A^i &\simeq k_2^k G_{kj} \frac{C_3^V}{m_N} (\epsilon_{inm} q^n) (\epsilon_{jlm} \sigma_l) \\ &= \frac{C_3^V}{m_N} \epsilon_{inm} q^n a_m, \end{aligned} \quad (\text{C.13})$$

where we have defined the vector

$$a_m \equiv \epsilon_{jlm} k_2^k G_{kj} \sigma_l. \quad (\text{C.14})$$

(note that G_{kj} and σ_l do not commute). Therefore we can write, in vector form

$$\mathbf{A} \simeq \frac{C_3^V}{m_N} (\mathbf{q} \times \mathbf{a}). \quad (\text{C.15})$$

Hence \mathbf{A} is purely transverse.

Backward vector B^i

Similarly, from Eq. (C.5),

$$\begin{aligned} B^i &\simeq -k_2^k \frac{C_3^V}{m_N} (\epsilon_{inm} q^n) (\epsilon_{jlm} \sigma_l) G_{jk} \\ &= \frac{C_3^V}{m_N} \epsilon_{inm} q^n b_m, \end{aligned} \quad (\text{C.16})$$

where we have defined the vector

$$b_m \equiv -\epsilon_{jlm} k_2^k \sigma_l G_{jk}. \quad (\text{C.17})$$

In vector form we have

$$\mathbf{B} \simeq \frac{C_3^V}{m_N} (\mathbf{q} \times \mathbf{b}). \quad (\text{C.18})$$

Vectors a^i and b^i

Next, we perform the necessary contractions to derive the explicit expressions for the vectors \mathbf{a} and \mathbf{b} in the non relativistic limit. Using Eq. (C.7) for the static Δ -propagator, we have

$$a_m \simeq \frac{\epsilon_{jlm} k_2^k}{m_N - m_\Delta} \left(\frac{2}{3} \delta_{kj} - i \frac{1}{3} \epsilon_{kjn} \sigma_n \right) \sigma_l \quad (\text{C.19})$$

$$b_m \simeq \frac{-\epsilon_{jlm} k_2^k}{m_N - m_\Delta} \sigma_l \left(\frac{2}{3} \delta_{kj} - i \frac{1}{3} \epsilon_{jkn} \sigma_n \right). \quad (\text{C.20})$$

Hence

$$(m_N - m_\Delta)a_m \simeq \frac{2}{3}\epsilon_{jlm}k_2^j\sigma_l - \frac{i}{3}k_2^k\epsilon_{kjn}\epsilon_{jlm}\sigma_n\sigma_l \quad (C.21)$$

$$(m_N - m_\Delta)b_m \simeq -\frac{2}{3}\epsilon_{jlm}k_2^j\sigma_l + \frac{i}{3}k_2^k\epsilon_{jkn}\epsilon_{jlm}\sigma_l\sigma_n \quad (C.22)$$

To compute the contractions in the second term, we employ again the property (C.11) of the Levi-Civita tensor

$$\epsilon_{jnk}\epsilon_{jlm} = \delta_{nl}\delta_{km} - \delta_{nm}\delta_{kl} \quad (C.23)$$

Then we have

$$\begin{aligned} k_2^k\epsilon_{kjn}\epsilon_{jlm}\sigma_n\sigma_l &= k_2^k(\delta_{nl}\delta_{km} - \delta_{nm}\delta_{kl})\sigma_n\sigma_l \\ &= k_2^m\sigma_n\sigma_n - k_2^l\sigma_m\sigma_l \\ &= 3k_2^m - k_2^l(\delta_{ml} + i\epsilon_{mln}\sigma_n) \\ &= 2k_2^m - i\epsilon_{mln}k_2^l\sigma_n \\ &= (2\mathbf{k}_2 - i\mathbf{k}_2 \times \boldsymbol{\sigma})^m, \end{aligned} \quad (C.24)$$

and

$$\begin{aligned} k_2^k\epsilon_{jkn}\epsilon_{jlm}\sigma_l\sigma_n &= k_2^k(\delta_{lk}\delta_{mn} - \delta_{ln}\delta_{mk})\sigma_l\sigma_n \\ &= k_2^l\sigma_l\sigma_m - k_2^m\sigma_l\sigma_l \\ &= -3k_2^m + k_2^l(\delta_{lm} + i\epsilon_{lmn}\sigma_n) \\ &= -2k_2^m - i\epsilon_{mln}k_2^l\sigma_n \\ &= (-2\mathbf{k}_2 - i\mathbf{k}_2 \times \boldsymbol{\sigma})^m. \end{aligned} \quad (C.25)$$

Then we can write in vector form \mathbf{a} and \mathbf{b} as

$$\begin{aligned} (m_N - m_\Delta)\mathbf{a} &\simeq \frac{2}{3}(\mathbf{k}_2 \times \boldsymbol{\sigma}) - \frac{i}{3}(2\mathbf{k}_2 - i\mathbf{k}_2 \times \boldsymbol{\sigma}) \\ &= -\frac{2}{3}i\mathbf{k}_2 + \frac{1}{3}\mathbf{k}_2 \times \boldsymbol{\sigma} \end{aligned} \quad (C.26)$$

$$\begin{aligned} (m_N - m_\Delta)\mathbf{b} &\simeq -\frac{2}{3}(\mathbf{k}_2 \times \boldsymbol{\sigma}) + \frac{i}{3}(-2\mathbf{k}_2 - i\mathbf{k}_2 \times \boldsymbol{\sigma}) \\ &= -\frac{2}{3}i\mathbf{k}_2 - \frac{1}{3}\mathbf{k}_2 \times \boldsymbol{\sigma}. \end{aligned} \quad (C.27)$$

Using this result in Eqs. (C.15,C.18) finally we find

$$\mathbf{A} \simeq \frac{C_3^V}{m_N m_N - m_\Delta} \mathbf{q} \times \left[-\frac{2}{3}i\mathbf{k}_2 + \frac{1}{3}\mathbf{k}_2 \times \boldsymbol{\sigma} \right] \quad (C.28)$$

$$\mathbf{B} \simeq \frac{C_3^V}{m_N m_N - m_\Delta} \mathbf{q} \times \left[-\frac{2}{3}i\mathbf{k}_2 - \frac{1}{3}\mathbf{k}_2 \times \boldsymbol{\sigma} \right] \quad (C.29)$$

from where Eqs. (4.23) and (4.24) follow.

Appendix D

Spin summations in the 1p1h MEC matrix elements

Here we perform the spin summations appearing in the exchange matrix element, given by

$$\sum_{t_k s_k} \mathbf{j}_{2b}(p, k, k, h) = \delta_{t_p t_h} 2t_h \sum_{s_k} [\mathbf{j}_1(p, k, k, h) + \mathbf{j}_2(p, k, k, h) - 2\mathbf{j}_3(p, k, k, h)] \quad (\text{D.1})$$

Seagull current

In the case of the seagull current only the current \mathbf{j}_3 contribute, given by Eq. (5.67). The sum over t_k, s_k is

$$\begin{aligned} \sum_{t_k s_k} \mathbf{j}_s(p, k, k, h) &= -4t_h \delta_{t_p t_h} \sum_{s_k} \langle s_p s_k | \frac{f^2}{m_\pi^2} F_1^V \left(\frac{\mathbf{k}_1 \cdot \boldsymbol{\sigma}^{(1)}}{\mathbf{k}_1^2 + m_\pi^2} \boldsymbol{\sigma}^{(2)} - \frac{\mathbf{k}_2 \cdot \boldsymbol{\sigma}^{(2)}}{\mathbf{k}_2^2 + m_\pi^2} \boldsymbol{\sigma}^{(1)} \right) | s_k s_h \rangle \\ &= -4t_h \delta_{t_p t_h} \frac{f^2}{m_\pi^2} F_1^V \sum_{s_k} \left(\frac{\mathbf{k}_1 \cdot \boldsymbol{\sigma}_{pk}}{\mathbf{k}_1^2 + m_\pi^2} \boldsymbol{\sigma}_{kh} - \frac{\mathbf{k}_2 \cdot \boldsymbol{\sigma}_{kh}}{\mathbf{k}_2^2 + m_\pi^2} \boldsymbol{\sigma}_{pk} \right). \end{aligned} \quad (\text{D.2})$$

with $\mathbf{k}_1 = \mathbf{p} - \mathbf{k}$ and $\mathbf{k}_2 = \mathbf{k} - \mathbf{h}$. The separate spin sums are

$$\sum_{s_k} (\mathbf{k}_1 \cdot \boldsymbol{\sigma}_{pk}) \boldsymbol{\sigma}_{kh} = (\mathbf{k}_1 + i\boldsymbol{\sigma} \times \mathbf{k}_1)_{ph}, \quad \sum_{s_k} (\mathbf{k}_2 \cdot \boldsymbol{\sigma}_{kh}) \boldsymbol{\sigma}_{pk} = (\mathbf{k}_2 + i\mathbf{k}_2 \times \boldsymbol{\sigma})_{ph}. \quad (\text{D.3})$$

We obtain

$$\sum_{t_k s_k} \mathbf{j}_s(p, k, k, h) = -4t_h \delta_{t_p t_h} \frac{f^2}{m_\pi^2} F_1^V \langle s_p | \left(\frac{\mathbf{k}_1 + i\boldsymbol{\sigma} \times \mathbf{k}_1}{\mathbf{k}_1^2 + m_\pi^2} - \frac{\mathbf{k}_2 + i\mathbf{k}_2 \times \boldsymbol{\sigma}}{\mathbf{k}_2^2 + m_\pi^2} \right) | s_h \rangle. \quad (\text{D.4})$$

Pionic

In the case of the pion in flight or pionic current the sum over spin-isospin reads

$$\begin{aligned} \sum_{t_k s_k} \mathbf{j}_\pi(p, k, k, h) &= -4t_h \delta_{t_p t_h} \sum_{s_k} \langle s_p s_k | \frac{f^2}{m_\pi^2} F_1^V \frac{\mathbf{k}_1 \cdot \boldsymbol{\sigma}^{(1)}}{\mathbf{k}_1^2 + m_\pi^2} \frac{\mathbf{k}_2 \cdot \boldsymbol{\sigma}^{(2)}}{\mathbf{k}_2^2 + m_\pi^2} (\mathbf{k}_1 - \mathbf{k}_2) | s_k s_h \rangle \\ &= -4t_h \delta_{t_p t_h} \frac{f^2}{m_\pi^2} F_1^V \sum_{s_k} \frac{\mathbf{k}_1 \cdot \boldsymbol{\sigma}_{pk}}{\mathbf{k}_1^2 + m_\pi^2} \frac{\mathbf{k}_2 \cdot \boldsymbol{\sigma}_{kh}}{\mathbf{k}_2^2 + m_\pi^2} (\mathbf{k}_1 - \mathbf{k}_2) \end{aligned} \quad (\text{D.5})$$

with $k_1 = \mathbf{p} - \mathbf{k}$ and $\mathbf{k}_2 = \mathbf{k} - \mathbf{h}$. The sum over spin index s_k is performed using

$$\sum_{s_k} (\mathbf{k}_1 \cdot \boldsymbol{\sigma}_{ph})(\mathbf{k}_2 \cdot \boldsymbol{\sigma}_{kh}) = \mathbf{k}_1 \cdot \mathbf{k}_2 \delta_{s_p s_h} + i(\mathbf{k}_1 \times \mathbf{k}_2) \cdot \boldsymbol{\sigma}_{ph} \quad (\text{D.6})$$

Δ current

From the non-relativistic Eq. (5.69) we can identify the three contributions, \mathbf{j}_i to the Δ current.

$$\begin{aligned} \sum_{t_k s_k} \mathbf{j}_\Delta(p, k, k, h) &= -i \delta_{t_p t_h} 2t_h C_\Delta \mathbf{q} \times \sum_{s_k} \langle s_p s_k | \frac{\mathbf{k}_1 \cdot \boldsymbol{\sigma}^{(1)}}{\mathbf{k}_1^2 + m_\pi^2} 4\mathbf{k}_1 + \frac{\mathbf{k}_2 \cdot \boldsymbol{\sigma}^{(2)}}{\mathbf{k}_2^2 + m_\pi^2} 4\mathbf{k}_2 \\ &\quad + 2i \frac{\mathbf{k}_2 \cdot \boldsymbol{\sigma}^{(2)}}{\mathbf{k}_2^2 + m_\pi^2} (\mathbf{k}_2 \times \boldsymbol{\sigma}^{(1)}) - 2i \frac{\mathbf{k}_1 \cdot \boldsymbol{\sigma}^{(1)}}{\mathbf{k}_1^2 + m_\pi^2} (\mathbf{k}_1 \times \boldsymbol{\sigma}^{(2)}) | s_k s_h \rangle. \end{aligned} \quad (\text{D.7})$$

with $\mathbf{k}_1 = \mathbf{p} - \mathbf{k}$ and $\mathbf{k}_2 = \mathbf{k} - \mathbf{h}$. Writing explicitly the spin indices in the Pauli matrices we have

$$\begin{aligned} \sum_{t_k s_k} \mathbf{j}_\Delta(p, k, k, h) &= -i \delta_{t_p t_h} 2t_h C_\Delta \mathbf{q} \times \sum_{s_k} \left\{ \frac{\mathbf{k}_1 \cdot \boldsymbol{\sigma}_{pk}}{\mathbf{k}_1^2 + m_\pi^2} 4\mathbf{k}_1 \delta_{s_k s_h} + \frac{\mathbf{k}_2 \cdot \boldsymbol{\sigma}_{kh}}{\mathbf{k}_2^2 + m_\pi^2} 4\mathbf{k}_2 \delta_{s_p s_k} \right. \\ &\quad \left. + 2i \frac{\mathbf{k}_2 \cdot \boldsymbol{\sigma}_{kh}}{\mathbf{k}_2^2 + m_\pi^2} (\mathbf{k}_2 \times \boldsymbol{\sigma}_{pk}) - 2i \frac{\mathbf{k}_1 \cdot \boldsymbol{\sigma}_{pk}}{\mathbf{k}_1^2 + m_\pi^2} (\mathbf{k}_1 \times \boldsymbol{\sigma}_{kh}) \right\} \end{aligned} \quad (\text{D.8})$$

with $\mathbf{k}_1 = \mathbf{p} - \mathbf{k}$, and $\mathbf{k}_2 = \mathbf{k} - \mathbf{h}$. We need the following spin sums

$$\begin{aligned} \sum_{s_k} (\boldsymbol{\sigma}_{kh} \cdot \mathbf{k}_2)(\mathbf{k}_2 \times \boldsymbol{\sigma}_{pk}) &= -i [k_2^2 \boldsymbol{\sigma}_{ph} - (\boldsymbol{\sigma}_{ph} \cdot \mathbf{k}_2) \mathbf{k}_2] \\ \sum_{s_k} (\boldsymbol{\sigma}_{pk} \cdot \mathbf{k}_1)(\mathbf{k}_1 \times \boldsymbol{\sigma}_{kh}) &= i [k_1^2 \boldsymbol{\sigma}_{ph} - (\boldsymbol{\sigma}_{ph} \cdot \mathbf{k}_1) \mathbf{k}_1]. \end{aligned} \quad (\text{D.9})$$

The result for the sum over s_k is

$$\sum_{t_k s_k} \mathbf{j}_\Delta(p, k, k, h) = -4it_h \delta_{t_p t_h} C_\Delta \mathbf{q} \times \left\{ \frac{k_1^2 \boldsymbol{\sigma}_{ph} + (\boldsymbol{\sigma}_{ph} \cdot \mathbf{k}_1) \mathbf{k}_1}{k_1^2 + m_\pi^2} + \frac{k_2^2 \boldsymbol{\sigma}_{ph} + (\boldsymbol{\sigma}_{ph} \cdot \mathbf{k}_2) \mathbf{k}_2}{k_2^2 + m_\pi^2} \right\} \quad (\text{D.10})$$

Appendix E

Spin summations in the interference responses

Here we compute the spin summations in the 1b-2b interference response function.

In this appendix we use the notation $\mathbf{k}_1 = \mathbf{p} - \mathbf{k}$ and $\mathbf{k}_2 = \mathbf{k} - \mathbf{h}$. We use also the identities $\mathbf{k}_1 + \mathbf{k}_2 = \mathbf{q}$, and $\mathbf{k}_1 = \mathbf{q} - \mathbf{k}_2$.

Magnetization-seagull

Inserting Eq. (4.47) into Eq. (4.55) we have

$$w_{ms}^T = 4t_h \delta_{t_p t_h} \frac{G_M^h}{2m_N} \frac{f^2}{m_\pi^2} F_1^V \int \frac{d^3 k}{(2\pi)^3} \sum_{s_p s_h} i(\mathbf{q} \times \boldsymbol{\sigma}_{hp}) \cdot \left(\frac{\delta_{s_p s_h} \mathbf{k}_1 + i\boldsymbol{\sigma}_{ph} \times \mathbf{k}_1}{\mathbf{k}_1^2 + m_\pi^2} - \frac{\delta_{s_p s_h} \mathbf{k}_2 + i\mathbf{k}_2 \times \boldsymbol{\sigma}_{ph}}{\mathbf{k}_2^2 + m_\pi^2} \right). \quad (\text{E.1})$$

The sums involved inside the integral are of the kind:

$$\sum_{s_p s_h} i(\mathbf{q} \times \boldsymbol{\sigma}_{hp}) \cdot \delta_{s_p s_h} \mathbf{k} = \sum_{s_h} i(\mathbf{q} \times \boldsymbol{\sigma}_{hh}) \cdot \mathbf{k} = 0 \quad (\text{E.2})$$

$$\begin{aligned} \sum_{s_p s_h} i(\mathbf{q} \times \boldsymbol{\sigma}_{hp}) \cdot (i\boldsymbol{\sigma}_{ph} \times \mathbf{k}) &= - \sum_{s_p s_h} (\mathbf{q} \cdot \boldsymbol{\sigma}_{ph} \boldsymbol{\sigma}_{hp} \cdot \mathbf{k} - \mathbf{q} \cdot \mathbf{k} \boldsymbol{\sigma}_{hp} \cdot \boldsymbol{\sigma}_{ph}) \\ &= -\text{Tr}(q^i \sigma_i \sigma_j k^j - \mathbf{q} \cdot \mathbf{k} \sigma_i \sigma_i) \\ &= -\text{Tr}(q^i \delta_{ij} k^j - 3\mathbf{q} \cdot \mathbf{k}) = 4\mathbf{q} \cdot \mathbf{k} \end{aligned} \quad (\text{E.3})$$

Therefore

$$w_{ms}^T = 4t_h \delta_{t_p t_h} \frac{G_M^h}{2m_N} \frac{f^2}{m_\pi^2} F_1^V \int \frac{d^3 k}{(2\pi)^3} \left(\frac{4\mathbf{q} \cdot \mathbf{k}_1}{\mathbf{k}_1^2 + m_\pi^2} + \frac{4\mathbf{q} \cdot \mathbf{k}_2}{\mathbf{k}_2^2 + m_\pi^2} \right). \quad (\text{E.4})$$

Convection-seagull

Inserting Eq. (4.47) into Eq. (4.56) we have

$$\begin{aligned} w_{cs}^T &= 4t_h \delta_{t_p t_h} \frac{G_E^h}{m_N m_\pi^2} \frac{f^2}{F_1^V} \int \frac{d^3 k}{(2\pi)^3} \sum_{s_p s_h} \delta_{s_h s_p} \mathbf{h}_T \cdot \left(\frac{\delta_{s_p s_h} \mathbf{k}_1 + i\boldsymbol{\sigma}_{ph} \times \mathbf{k}_1}{\mathbf{k}_1^2 + m_\pi^2} - \frac{\delta_{s_p s_h} \mathbf{k}_2 + i\mathbf{k}_2 \times \boldsymbol{\sigma}_{ph}}{\mathbf{k}_2^2 + m_\pi^2} \right). \\ &= 4t_h \delta_{t_p t_h} \frac{G_E^h}{m_N m_\pi^2} \frac{f^2}{F_1^V} \int \frac{d^3 k}{(2\pi)^3} \left(\frac{\mathbf{h}_T \cdot \mathbf{k}_1}{\mathbf{k}_1^2 + m_\pi^2} - \frac{\mathbf{h}_T \cdot \mathbf{k}_2}{\mathbf{k}_2^2 + m_\pi^2} \right). \end{aligned} \quad (\text{E.5})$$

Magnetization-pionic

Inserting Eq. (4.48) into Eq. (4.57) we have

$$w_{m\pi}^T = 4t_h \delta_{t_p t_h} \frac{G_M^h}{2m_N m_\pi^2} \frac{f^2}{F_1^V} \int \frac{d^3 k}{(2\pi)^3} \sum_{s_p s_h} i(\mathbf{q} \times \boldsymbol{\sigma}_{hp}) \cdot (\mathbf{k}_1 - \mathbf{k}_2) \frac{\delta_{s_p s_h} \mathbf{k}_1 \cdot \mathbf{k}_2 + i(\mathbf{k}_1 \times \mathbf{k}_2) \cdot \boldsymbol{\sigma}_{ph}}{(\mathbf{k}_1^2 + m_\pi^2)(\mathbf{k}_2^2 + m_\pi^2)}. \quad (\text{E.6})$$

The sum over spin inside the integral is

$$\begin{aligned} \sum_{s_p s_h} i(\mathbf{q} \times \boldsymbol{\sigma}_{hp}) \cdot (\mathbf{k}_1 - \mathbf{k}_2) [\delta_{s_p s_h} \mathbf{k}_1 \cdot \mathbf{k}_2 + i(\mathbf{k}_1 \times \mathbf{k}_2) \cdot \boldsymbol{\sigma}_{ph}] &= \\ - \sum_{s_p s_h} (\mathbf{q} \times \boldsymbol{\sigma}_{hp}) \cdot (\mathbf{k}_1 - \mathbf{k}_2) (\mathbf{k}_1 \times \mathbf{k}_2) \cdot \boldsymbol{\sigma}_{ph} &= \\ - \sum_{s_p s_h} [(\mathbf{k}_1 - \mathbf{k}_2) \times \mathbf{q}] \cdot \boldsymbol{\sigma}_{hp} (\mathbf{k}_1 \times \mathbf{k}_2) \cdot \boldsymbol{\sigma}_{ph} &= \\ -2[(\mathbf{k}_1 - \mathbf{k}_2) \times \mathbf{q}] \cdot (\mathbf{k}_1 \times \mathbf{k}_2) &= -4(\mathbf{q} \times \mathbf{k}_2)^2 \end{aligned} \quad (\text{E.7})$$

where we have used that

$$\sum_{s_p s_h} (\mathbf{a} \cdot \boldsymbol{\sigma}_{hp}) (\mathbf{b} \cdot \boldsymbol{\sigma}_{ph}) = \text{Tr}(a^i \sigma_i \sigma_j b^j) = 2\mathbf{a} \cdot \mathbf{b} \quad (\text{E.8})$$

$$\mathbf{k}_1 = \mathbf{q} - \mathbf{k}_2 \quad (\text{E.9})$$

$$(\mathbf{k}_1 - \mathbf{k}_2) \times \mathbf{q} = (\mathbf{q} - 2\mathbf{k}_2) \times \mathbf{q} = 2\mathbf{q} \times \mathbf{k}_2 \quad (\text{E.10})$$

$$\mathbf{k}_1 \times \mathbf{k}_2 = (\mathbf{q} - \mathbf{k}_2) \times \mathbf{k}_2 = \mathbf{q} \times \mathbf{k}_2 \quad (\text{E.11})$$

With the result of Eq (E.7), we obtain

$$w_{m\pi}^T = 4t_h \delta_{t_p t_h} \frac{G_M^h}{2m_N m_\pi^2} \frac{f^2}{F_1^V} \int \frac{d^3 k}{(2\pi)^3} \frac{-4(\mathbf{q} \times \mathbf{k}_2)^2}{(\mathbf{k}_1^2 + m_\pi^2)(\mathbf{k}_2^2 + m_\pi^2)}. \quad (\text{E.12})$$

Convection-pionic

Inserting Eq. (4.48) into Eq. (4.58) we have

$$w_{c\pi}^T = 4t_h \delta_{t_p t_h} \frac{G_E^h}{m_N m_\pi^2} \frac{f^2}{F_1^V} \int \frac{d^3 k}{(2\pi)^3} \sum_{s_p s_h} \delta_{s_h s_p} \mathbf{h}_T \cdot (\mathbf{k}_1 - \mathbf{k}_2) \frac{\delta_{s_p s_h} \mathbf{k}_1 \cdot \mathbf{k}_2 + i(\mathbf{k}_1 \times \mathbf{k}_2) \cdot \boldsymbol{\sigma}_{ph}}{(\mathbf{k}_1^2 + m_\pi^2)(\mathbf{k}_1^2 + m_\pi^2)}. \quad (\text{E.13})$$

Sum over spin inside the integral:

$$\begin{aligned} \sum_{s_p s_h} \delta_{s_h s_p} \mathbf{h}_T \cdot (\mathbf{k}_1 - \mathbf{k}_2) [\delta_{s_p s_h} \mathbf{k}_1 \cdot \mathbf{k}_2 + i(\mathbf{k}_1 \times \mathbf{k}_2) \cdot \boldsymbol{\sigma}_{ph}] &= \sum_{s_h} \mathbf{h}_T \cdot (\mathbf{k}_1 - \mathbf{k}_2) (\mathbf{k}_1 \cdot \mathbf{k}_2) \\ &= 2\mathbf{h}_T \cdot (\mathbf{q} - 2\mathbf{k}_2) [(\mathbf{q} - \mathbf{k}_2) \cdot \mathbf{k}_2] = -4(\mathbf{h}_T \cdot \mathbf{k}_2)(\mathbf{q} \cdot \mathbf{k}_2 - \mathbf{k}_2^2). \end{aligned} \quad (\text{E.14})$$

Then we obtain

$$w_{c\pi}^T = 4t_h \delta_{t_p t_h} \frac{G_E^h}{m_N m_\pi^2} \frac{f^2}{F_1^V} \int \frac{d^3 k}{(2\pi)^3} \frac{-4(\mathbf{h}_T \cdot \mathbf{k}_2)(\mathbf{q} \cdot \mathbf{k}_2 - \mathbf{k}_2^2)}{(\mathbf{k}_1^2 + m_\pi^2)(\mathbf{k}_1^2 + m_\pi^2)}. \quad (\text{E.15})$$

Magnetization- Δ

Inserting Eq. (4.49) into Eq. (4.59) we have

$$\begin{aligned} w_{m\Delta}^T &= 4t_h \delta_{t_p t_h} \frac{G_M^h}{2m_N} C_\Delta \int \frac{d^3 k}{(2\pi)^3} \\ &\quad \sum_{s_p s_h} i(\mathbf{q} \times \boldsymbol{\sigma}_{hp}) \cdot \left[i\mathbf{q} \times \left(\frac{\mathbf{k}_1^2 \boldsymbol{\sigma}_{ph} + (\boldsymbol{\sigma}_{ph} \cdot \mathbf{k}_1) \mathbf{k}_1}{\mathbf{k}_1^2 + m_\pi^2} + \frac{\mathbf{k}_2^2 \boldsymbol{\sigma}_{ph} + (\boldsymbol{\sigma}_{ph} \cdot \mathbf{k}_2) \mathbf{k}_2}{\mathbf{k}_2^2 + m_\pi^2} \right) \right] \end{aligned} \quad (\text{E.16})$$

We need the following spin sums. The first one is similar to Eq. (E.3)

$$\sum_{s_p s_h} (\mathbf{q} \times \boldsymbol{\sigma}_{hp}) \cdot (\mathbf{q} \times \boldsymbol{\sigma}_{ph}) = 4q^2 \quad (\text{E.17})$$

The second sum required is

$$\begin{aligned} \sum_{s_p s_h} (\mathbf{q} \times \boldsymbol{\sigma}_{hp}) \cdot (\mathbf{q} \times \mathbf{k}_1) (\boldsymbol{\sigma}_{ph} \cdot \mathbf{k}_1) &= \sum_{s_p s_h} [q^2 \boldsymbol{\sigma}_{hp} \cdot \mathbf{k}_1 - (\mathbf{q} \cdot \mathbf{k}_1)(\mathbf{q} \cdot \boldsymbol{\sigma}_{hp})] (\boldsymbol{\sigma}_{ph} \cdot \mathbf{k}_1) \\ &= q^2 \sum_{s_p s_h} (\boldsymbol{\sigma}_{hp} \cdot \mathbf{k}_1) (\boldsymbol{\sigma}_{ph} \cdot \mathbf{k}_1) - (\mathbf{q} \cdot \mathbf{k}_1) \sum_{s_p s_h} (\mathbf{q} \cdot \boldsymbol{\sigma}_{hp}) (\boldsymbol{\sigma}_{ph} \cdot \mathbf{k}_1) \\ &= 2q^2 k_1^2 - 2(\mathbf{q} \cdot \mathbf{k}_1)^2 \end{aligned} \quad (\text{E.18})$$

where we have used twice Eq. (E.8). Using these results the $m\Delta$ response function is

$$w_{m\Delta}^T = -4t_h \delta_{t_p t_h} \frac{G_M^h}{2m_N} C_\Delta \int \frac{d^3 k}{(2\pi)^3} \left(\frac{6q^2 k_1^2 - 2(\mathbf{q} \cdot \mathbf{k}_1)^2}{\mathbf{k}_1^2 + m_\pi^2} + \frac{6q^2 k_2^2 - 2(\mathbf{q} \cdot \mathbf{k}_2)^2}{\mathbf{k}_2^2 + m_\pi^2} \right). \quad (\text{E.19})$$

Appendix F

Spectral function and hadronic tensor

The spectral function is obtained by assuming plane waves for the final nucleon. This assumption leads to a factorization approximation for the response function within the impulse approximation, where the current is considered to be one-body only. In this framework, the response function can be factored into a product of the current matrix element and the spectral function, which describes the distribution of hole states in the nucleus.

We assume that the initial nuclear state is a spin-zero nucleus at rest with energy $E_i = M_A$, and wave function:

$$|i\rangle = |\Phi_0^{(A)}\rangle \quad (\text{F.1})$$

The final state correspond to a plane wave particle and a residual $A - 1$ nucleus

$$|f\rangle = |\Phi_\alpha^{(A-1)}, \mathbf{p}, s\rangle = a_{\mathbf{p},s}^\dagger |\Phi_\alpha^{(A-1)}\rangle \quad (\text{F.2})$$

The label α denotes the quantum numbers of the daughter nucleus in an excited state with excitation energy $\epsilon_\alpha^{(A-1)}$. Then the final energy, neglecting the recoil energy is,

$$E_f = m_N + T_p + M_{A-1} + \epsilon_\alpha^{(A-1)} \quad (\text{F.3})$$

where $T_p = p^2/2m_N$. Then the diagonal component of the hadronic tensor is,

$$W^{\mu\mu} = \sum_{\alpha\mathbf{p}s} |\langle \Phi_\alpha^{(A-1)}, \mathbf{p}, s | J^\mu(\mathbf{q}) | \Phi_0^{(A)} \rangle|^2 \delta(E_i + \omega - E_f) \quad (\text{F.4})$$

Assuming that the current is a one-body operator and ignoring the final nucleon spin for simplicity we have,

$$\begin{aligned} W^{\mu\mu} &= \\ &\sum_{\alpha\mathbf{p}} |\langle \Phi_\alpha^{(A-1)} | a_{\mathbf{p}} \int d^3k J^\mu(\mathbf{q} + \mathbf{k}, \mathbf{k}) a_{\mathbf{q}+\mathbf{k}}^\dagger a_{\mathbf{k}} | \Phi_0^{(A)} \rangle|^2 \\ &\delta(M_A + \omega - m_N - T_p - M_{A-1} - \epsilon_\alpha^{(A-1)}) \end{aligned} \quad (\text{F.5})$$

Using the commutation properties of the creation and annihilation operators,

$$a_{\mathbf{p}} a_{\mathbf{q}+\mathbf{k}}^\dagger = \delta(\mathbf{p} - \mathbf{q} - \mathbf{k}) - a_{\mathbf{q}+\mathbf{k}}^\dagger a_{\mathbf{p}}, \quad (\text{F.6})$$

and assuming that the final particle momentum is large enough to neglect high-momentum components in the initial wave function (as the dominant contribution comes from momenta below the Fermi momentum), $a_{\mathbf{p}} |\Phi_0^{(A)}\rangle \simeq 0$, then the hadronic tensor is

$$\begin{aligned} W^{\mu\mu} = & \sum_{\alpha} \int d^3 p |\langle \Phi_{\alpha}^{(A-1)} | J^{\mu}(\mathbf{p}, \mathbf{p} - \mathbf{q}) a_{\mathbf{p}-\mathbf{q}} | \Phi_0^{(A)} \rangle|^2 \\ & \delta(M_A + \omega - m_N - T_p - M_{A-1} - \epsilon_{\alpha}^{(A-1)}) \end{aligned} \quad (\text{F.7})$$

Introducing the separation energy $S = M_{A-1} + m_N - M_A > 0$ and the missing energy $E_m = \omega - T_p$ then

$$W^{\mu\mu} = \int d^3 p |J^{\mu}(\mathbf{p}, \mathbf{p} - \mathbf{q})|^2 S(\mathbf{p} - \mathbf{q}, E_m)$$

where the one-hole spectral function is defined as,

$$S(\mathbf{h}, E) = \sum_{\alpha, s} |\langle \Phi_{\alpha}^{(A-1)} | a_{\mathbf{h}, s} | \Phi_0^{(A)} \rangle|^2 \delta(E - S - \epsilon_{\alpha}^{(A-1)}).$$

Appendix G

Isospin Summations in CCQE matrix element

Here we provide the sums over the isospin index t_k of the appearing in the 1p1h MEC matrix element. We first note that the MEC can be written as a linear combination of $\tau_{\pm}^{(1)}$ and $\tau_{\pm}^{(2)}$ and $i[\boldsymbol{\tau}^{(1)} \times \boldsymbol{\tau}^{(2)}]_{\pm}$

$$j_{2b}^{\mu} = \tau_{\pm}^{(1)} j_1^{\mu} + \tau_{\pm}^{(2)} j_2^{\mu} + i[\boldsymbol{\tau}^{(1)} \times \boldsymbol{\tau}^{(2)}]_{\pm} j_3^{\mu}, \quad (\text{G.1})$$

where the 2b currents j_1^{μ} , j_2^{μ} , and j_3^{μ} are isospin-independent. To be specific, we will consider the case of the (+) component of the isospin current, corresponding to $N \rightarrow P$ transitions.

$$\tau_{+} = \tau_1 + i\tau_2 = \begin{pmatrix} 0 & 2 \\ 0 & 0 \end{pmatrix}, \quad (\text{G.2})$$

$$i[\boldsymbol{\tau}^{(1)} \times \boldsymbol{\tau}^{(2)}]_{+} = \tau_{+}^{(1)} \tau_3^{(2)} - \tau_3^{(1)} \tau_{+}^{(2)}, \quad (\text{G.3})$$

from where we obtain

$$\tau_{+}|P\rangle = 0, \quad \tau_{+}|N\rangle = 2|P\rangle \quad (\text{G.4})$$

$$\begin{aligned} i[\boldsymbol{\tau}^{(1)} \times \boldsymbol{\tau}^{(2)}]_{+}|NP\rangle &= 2|PP\rangle, \\ i[\boldsymbol{\tau}^{(1)} \times \boldsymbol{\tau}^{(2)}]_{+}|NN\rangle &= -2|PN\rangle + 2|NP\rangle, \\ i[\boldsymbol{\tau}^{(1)} \times \boldsymbol{\tau}^{(2)}]_{+}|PP\rangle &= 0 \\ i[\boldsymbol{\tau}^{(1)} \times \boldsymbol{\tau}^{(2)}]_{+}|PN\rangle &= -2|PP\rangle \end{aligned} \quad (\text{G.5})$$

From these elementary results, it is straightforward to compute the isospin sums. The results are the following.

Direct terms.

$$\sum_{t_k=\pm 1/2} \langle Pt_k | \tau_{+}^{(1)} | Nt_k \rangle = 4, \quad (\text{G.6})$$

$$\sum_{t_k} \langle Pt_k | \tau_z^{(2)} | Pt_k \rangle = 0, \quad (G.7)$$

$$\sum_{t_k} \langle Pt_k | i[\boldsymbol{\tau}^{(1)} \times \boldsymbol{\tau}^{(2)}]_+ | Nt_k \rangle = 0. \quad (G.8)$$

Exchange terms.

$$\sum_{t_k} \langle Pt_k | \tau_+^{(1)} | t_k N \rangle = 2, \quad (G.9)$$

$$\sum_{t_k} \langle Pt_k | \tau_+^{(2)} | t_k N \rangle = 2, \quad (G.10)$$

$$\sum_{t_k} \langle Pt_k | i[\boldsymbol{\tau}^{(1)} \times \boldsymbol{\tau}^{(2)}]_+ | t_k N \rangle = -4. \quad (G.11)$$

Similar results are obtained for the $P \rightarrow N$ transition with the $(-)$ isospin components.

After performing this sums the effective one-body matrix element $j_{2b}(\mathbf{p}, \mathbf{h})$ induced by the two-body current, Eq. (5.15), can be written as sum of direct minus exchange currents

$$j_{2b}^\mu(\mathbf{p}, \mathbf{h}) = j_{2b}^\mu(\mathbf{p}, \mathbf{h})_{\text{dir}} - j_{2b}^\mu(\mathbf{p}, \mathbf{h})_{\text{ex}}, \quad (G.12)$$

where

$$j_{2b}^\mu(\mathbf{p}, \mathbf{h})_{\text{dir}} = \frac{1}{V} \sum_{\mathbf{k}} \sum_{s_k} 4j_1^\mu(\mathbf{p}, \mathbf{k}, \mathbf{h}, \mathbf{k}) \quad (G.13)$$

$$j_{2b}^\mu(\mathbf{p}, \mathbf{h})_{\text{ex}} = \frac{1}{V} \sum_{\mathbf{k}} \sum_{s_k} [2j_1^\mu(\mathbf{p}, \mathbf{k}, \mathbf{k}, \mathbf{h}) + 2j_2^\mu(\mathbf{p}, \mathbf{k}, \mathbf{k}, \mathbf{h}) - 4j_3^\mu(\mathbf{p}, \mathbf{k}, \mathbf{k}, \mathbf{h})]. \quad (G.14)$$

Relation between CC and EM interference responses in the vector sector

We demonstrate that the interference responses between the one-body and two-body currents in CC neutrino scattering in the vector sector are exactly twice the corresponding electromagnetic responses when both proton and neutron emission are summed. This relation holds in symmetric nuclear matter and follows from the isovector nature of both the CC and the electromagnetic two-body currents.

Indeed, the one-body electromagnetic and CC vector currents written as isospin operators are

$$j_{1b,e}^\mu = s^\mu + f^\mu \tau_z \quad (G.15)$$

$$j_{1b,V}^\mu = f^\mu \tau_+ \quad (G.16)$$

where s^μ and f^μ are the isoscalar and isovector 1b currents, respectively. Therefore the electromagnetic current in a 1p1h excitation between isospin states $|t_h\rangle$ and $|t_p\rangle$ is

$$\langle t_p | j_{1b,e}^\mu(\mathbf{p}, \mathbf{h}) | t_h \rangle = \delta_{t_p t_h} [s^\mu(\mathbf{p}, \mathbf{h}) + 2t_h f^\mu(\mathbf{p}, \mathbf{h})] \quad (\text{G.17})$$

and the CC vector current in a neutron-to-proton transition is

$$\langle P | j_{1b,V}^\mu(\mathbf{p}, \mathbf{h}) | N \rangle = 2t_h f^\mu(\mathbf{p}, \mathbf{h}). \quad (\text{G.18})$$

The two-body MEC currents are written in a similar way

$$j_{2b,e}^\mu = \tau_z^{(1)} j_1^\mu + \tau_z^{(2)} j_2^\mu + i[\boldsymbol{\tau}^{(1)} \times \boldsymbol{\tau}^{(2)}]_z j_3^\mu \quad (\text{G.19})$$

$$j_{2b,V}^\mu = \tau_\pm^{(1)} j_1^\mu + \tau_\pm^{(2)} j_2^\mu + i[\boldsymbol{\tau}^{(1)} \times \boldsymbol{\tau}^{(2)}]_\pm j_3^\mu \quad (\text{G.20})$$

where the 2b vector currents j_1^μ , j_2^μ and j_3^μ are isospin- independent. Since the two-body current $j_{2b,V}^\mu$ has no axial component, the corresponding effective one-body current contains only the exchange term, as given in (G.14). Thus in a transition where h is neutron and p is proton, we have

$$\langle P | j_{2b,V}^\mu(\mathbf{p}, \mathbf{h}) | N \rangle = -j_{2b}^\mu(\mathbf{p}, \mathbf{h})_{ex} \quad (\text{G.21})$$

where $j_{2b}^\mu(\mathbf{p}, \mathbf{h})_{ex}$ is given in Eq. (G.14) with only the vector part. On the other hand the electromagnetic current for a transition from isospin t_h to t_p is given by

$$\langle t_p | j_{2b,e}^\mu(\mathbf{p}, \mathbf{h}) | t_h \rangle = -\delta_{t_p t_h} t_h j_{2b}^\mu(\mathbf{p}, \mathbf{h})_{ex} \quad (\text{G.22})$$

Let us compute a generic contribution to the interference tensor $w_{1b2b}^{\mu\nu}$ of Eq. (5.22), such as $j_{1b}^\mu j_{2b}^\mu$, with the one-body and two-body currents. In the case of neutrino scattering the vector part is

$$\langle P | j_{1b,V}^\mu(\mathbf{p}, \mathbf{h}) | N \rangle^* \langle P | j_{2b,V}^\nu(\mathbf{p}, \mathbf{h}) | N \rangle = 2f^{\mu*}(j_{2b}^\nu)_{ex} \quad (\text{G.23})$$

In the em case it is

$$\langle t_p | j_{1b,e}^\mu(\mathbf{p}, \mathbf{h}) | t_h \rangle^* \langle t_p | j_{2b,e}^\nu(\mathbf{p}, \mathbf{h}) | t_h \rangle = -\delta_{t_p t_h} (s^\mu + 2t_h f^\mu) t_h (j_{2b}^\nu)_{ex} \quad (\text{G.24})$$

Performing the sum over isospin in the em case,

$$\sum_{t_p t_h = \pm 1} \langle t_p | j_{1b,e}^\mu(\mathbf{p}, \mathbf{h}) | t_h \rangle^* \langle t_p | j_{2b,e}^\nu(\mathbf{p}, \mathbf{h}) | t_h \rangle = -f^{\mu*}(j_{2b}^\nu)_{ex} \quad (\text{G.25})$$

This factor of two between the CC (G.23) and EM (G.25) expressions thus applies to all interference response functions considered in this work.

Appendix H

Non relativistic reduction of the axial Δ current

Here we compute the non relativistic axial Δ current to leading order in the $1/m_N$ expansion. The non-relativistic reduction follows the same procedure as that used for the vector current in Appendix C. We start by writing the weak forward and backward relativistic currents (5.39, 5.40) in the form

$$J_{\Delta F}^\mu = U_F A^\mu \quad (H.1)$$

$$J_{\Delta B}^\mu = U_B B^\mu \quad (H.2)$$

where,

$$A^\mu = \bar{u}(p'_2)\gamma^5 \not{k}_2 u(p_2) \bar{u}_{s'_1}(p'_1) k_2^\alpha G_{\alpha\beta}(p_1 + Q) C_5^A(Q) g^{\beta\mu} u_{s_1}(p_1) + (1 \leftrightarrow 2) \quad (H.3)$$

$$B^\mu = \bar{u}(p'_2)\gamma^5 \not{k}_2 u(p_2) \bar{u}_{s'_1}(p'_1) k_2^\beta C_5^A(Q) g^{\mu\alpha} G_{\alpha\beta}(p'_1 - Q) u_{s_1}(p_1) + (1 \leftrightarrow 2) \quad (H.4)$$

In the following, we omit the explicit spinors and reduce the expressions to leading order. The πNN vertex is common in both A^μ and B^μ tensors,

$$\gamma^5 \not{k}_2 \rightarrow -\gamma^5 \gamma^i k_2^i \rightarrow \mathbf{k}_2 \cdot \boldsymbol{\sigma}^2 \quad (H.5)$$

where we've used the non relativistic reduction of the gamma matrices: $\gamma^5 \gamma^i \rightarrow -\sigma_i$ and $\not{k}_2 = \gamma^0 k_2^0 - \gamma^i k_2^i \rightarrow -\gamma^i k_2^i$.

Foward A^μ tensor

Using $k_2^\alpha \rightarrow (0, \mathbf{k}_2)$ the $\Delta\pi N$ vertex becomes,

$$k_2^\alpha G_{\alpha\beta} g^{\beta\mu} \rightarrow k_2^k G_{kl} g^{lj} \quad (H.6)$$

Writing the Δ propagator in the static limit in the form

$$G_{ij} \rightarrow \frac{1}{m - m_\Delta} (\delta_{ij} + \frac{1}{3} \gamma_i \gamma_j) \quad (H.7)$$

and inserting the spatial components of the Δ propagator, we obtain the A^i components

$$\begin{aligned} A^i \sim k_2^k G_{kl} g^{lj} &\rightarrow k_2^k \frac{1}{m - m_\Delta} (\delta_{kl} + \frac{1}{3} \gamma_k \gamma_l) g^{lj} = \frac{-1}{m - m_\Delta} k_2^k (\frac{2}{3} \delta_{kl} - \frac{i}{3} \epsilon_{klm} \sigma_m) \delta^{lj} \\ &= \frac{-1}{m - m_\Delta} (\frac{2}{3} k_2^j + \frac{i}{3} \epsilon_{jkm} k_2^k \sigma_m) \end{aligned} \quad (\text{H.8})$$

where we have used $g_{ij} = -\delta_{ij}$, the reduction of gamma matrices

$$\gamma_k \gamma_l = \begin{bmatrix} 0 & \sigma_k \\ -\sigma_k & 0 \end{bmatrix} \begin{bmatrix} 0 & \sigma_l \\ -\sigma_l & 0 \end{bmatrix} \rightarrow -\sigma_k \sigma_l \quad (\text{H.9})$$

and

$$\delta_{kl} + \frac{1}{3} \gamma_k \gamma_l = \delta_{kl} - \frac{1}{3} \sigma_k \sigma_l = \frac{2}{3} \delta_{kl} - \frac{i}{3} \epsilon_{klm} \sigma_m. \quad (\text{H.10})$$

The A_i components can be written in vector form

$$\mathbf{A} \Rightarrow \frac{-1}{m - m_\Delta} \left(\frac{2}{3} \mathbf{k}_2 + \frac{i}{3} \mathbf{k}_2 \times \boldsymbol{\sigma}^1 \right) \quad (\text{H.11})$$

Backward B^μ tensor

Similarly, from Eq. (H.4)

$$\begin{aligned} B^i \sim k_2^k g^{il} G_{lk} &\rightarrow k_2^k g^{il} \frac{1}{m - m_\Delta} (\delta_{lk} + \frac{1}{3} \gamma_l \gamma_k) = \frac{-1}{m - m_\Delta} k_2^k \delta^{il} (\frac{2}{3} \delta_{lk} - \frac{i}{3} \epsilon_{lkm} \sigma_m) \\ &= \frac{-1}{m - m_\Delta} (\frac{2}{3} k_2^i - \frac{i}{3} \epsilon_{ikm} k_2^k \sigma_m) \end{aligned} \quad (\text{H.12})$$

Moreover, in vector notation, \mathbf{B} can be expressed as:

$$\mathbf{B} \Rightarrow \frac{-1}{m - M_\Delta} \left(\frac{2}{3} \mathbf{k}_2 - \frac{i}{3} \mathbf{k}_2 \times \boldsymbol{\sigma}^1 \right) \quad (\text{H.13})$$

Total Δ Current

Using Eqs. 5.51 and 5.52 for the isospin operators U_F and U_B we can write the axial Δ current in the form

$$\begin{aligned} \mathbf{j}_{\Delta A} &= -\frac{2}{9} \sqrt{\frac{3}{2}} \frac{f f^*}{m_\pi^2} C_5^A \frac{1}{m_\Delta - m} \left(4\tau_+^{(2)} \frac{(\mathbf{k}_2 \cdot \boldsymbol{\sigma}^2) \mathbf{k}_2}{\mathbf{k}_2^2 + m_\pi^2} + 4\tau_+^{(1)} \frac{(\mathbf{k}_1 \cdot \boldsymbol{\sigma}^1) \mathbf{k}_1}{\mathbf{k}_1^2 + m_\pi^2} \right. \\ &\quad \left. + [\boldsymbol{\tau}^{(1)} \times \boldsymbol{\tau}^{(2)}]_+ \left\{ \frac{(\mathbf{k}_2 \cdot \boldsymbol{\sigma}^2)(\mathbf{k}_2 \times \boldsymbol{\sigma}^1)}{\mathbf{k}_2^2 + m_\pi^2} - \frac{(\mathbf{k}_1 \cdot \boldsymbol{\sigma}^1)(\mathbf{k}_1 \times \boldsymbol{\sigma}^2)}{\mathbf{k}_1^2 + m_\pi^2} \right\} \right) \end{aligned} \quad (\text{H.14})$$

Appendix I

Multipole expansion of the BG equation

In this appendix we perform the multipole expansion of the Bethe-Goldstone equation presented in chapter 6, section 6.2. We start with the free wave function expansion with total angular momentum JM and a well-defined spin S is

$$\frac{1}{(2\pi)^{3/2}} e^{i\mathbf{p}\cdot\mathbf{r}} \chi_{S\mu} = A \sum_{JM} \sum_{lm_l} i^l Y_{lm_l}^*(\hat{\mathbf{p}}) \langle lm_l S\mu | JM \rangle j_l(pr) \mathcal{Y}_{lSJM}(\hat{\mathbf{r}}), \quad (\text{I.1})$$

with $A = \sqrt{2/\pi}$. The spinor functions $\mathcal{Y}_{lSJM}(\hat{\mathbf{r}})$ are obtained by coupling the angular momentum l and spin S bases through the Clebsch-Gordan coefficients,

$$\mathcal{Y}_{lSJM}(\hat{\mathbf{r}}) = \sum_{m\mu} \langle lm S\mu | JM \rangle Y_{lm}(\hat{\mathbf{r}}) | S\mu \rangle. \quad (\text{I.2})$$

The inverse relation is,

$$Y_{lm}(\hat{\mathbf{r}}) | S\mu \rangle = \sum_{JM} \langle lm S\mu | JM \rangle \mathcal{Y}_{lSJM}(\hat{\mathbf{r}}). \quad (\text{I.3})$$

The integral Bethe-Goldstone equation with well-defined momentum \mathbf{p} , coupled to total spin S with projection μ defined in Eq. (6.19) is

$$|\psi, \mathbf{p} S\mu \rangle = |\mathbf{p} S\mu \rangle + \int d^3\mathbf{p}' \frac{Q(\mathbf{P}, \mathbf{p}')}{p^2 - p'^2} \sum_{\mu'} |\mathbf{p}' S\mu' \rangle \langle \mathbf{p}' S\mu' | m_N V | \psi \rangle \quad (\text{I.4})$$

We assume that the potential commutes with S^2 , J^2 , and J_z , but not with the angular momentum L^2 . The action of this potential over the spinor functions multiplied by a radial function is

$$V j_l(pr) \mathcal{Y}_{lSJM}(\hat{\mathbf{r}}) = \sum_{l'} V_{l'l}^{SJ}(r) j_l(pr) \mathcal{Y}_{l'SJM}(\hat{\mathbf{r}}). \quad (\text{I.5})$$

If we define $U_{l'l}^{SJ}(r) = m_N V_{l'l}^{SJ}(r)$, this leads us to,

$$m_N V |\mathbf{p} S\mu \rangle = A \sum_{JM} \sum_{ll'm} i^{l'} Y_{l'm}^*(\hat{\mathbf{p}}) \langle l'm S\mu | JM \rangle U_{ll'}^{SJ}(r) j_{l'}(pr) \mathcal{Y}_{lSJM}(\hat{\mathbf{r}}) \quad (\text{I.6})$$

Looking at the multipole expansion of the free wave function, Eq. (I.1), and considering how the potential acts on these spinor-angular functions in Eq.(I.6), it becomes natural to anticipate that the solution of the Bethe-Goldstone equation should have a similar structure. Therefore, we propose the ansatz

$$|\psi\rangle = A \sum_{JM} \sum_{ll'm} i^{l'} Y_{l'm}^*(\hat{\mathbf{p}}) \langle l'mS\mu|JM\rangle \phi_{ll'}^{SJ}(r) \mathcal{Y}_{lSJM}(\hat{\mathbf{r}}). \quad (\text{I.7})$$

We calculate the matrix element of V acting on the state $\langle \mathbf{p}'S\mu' |$, that appears in Eq.(I.4)

$$\begin{aligned} \langle \mathbf{p}'S\mu' | V | \psi \rangle &= A^2 \left\langle \sum_{J_1 M_1} \sum_{l_1 l_1' m_1} i^{l_1'} Y_{l_1' m_1}^*(\hat{\mathbf{p}}') \langle l_1' m_1 S\mu' | J_1 M_1 \rangle j_{l_1'}(p'r) U_{l_1 l_1'}^{SJ}(r) \mathcal{Y}_{l_1 S J_1 M_1}(\hat{\mathbf{r}}) \right| \\ &\quad \times \left. \sum_{JM} \sum_{ll'm} i^{l'} Y_{l'm}^*(\hat{\mathbf{p}}) \langle l'mS\mu|JM\rangle \phi_{ll'}^{SJ}(r) \mathcal{Y}_{lSJM}(\hat{\mathbf{r}}) \right\rangle \end{aligned} \quad (\text{I.8})$$

Using that $\langle \mathcal{Y}_{l_1 S J_1 M_1}(\hat{\mathbf{r}}) | \mathcal{Y}_{lSJM}(\hat{\mathbf{r}}) \rangle = \delta_{l_1 l} \delta_{J_1 J} \delta_{M_1 M}$ we reduce the matrix element to

$$\begin{aligned} \langle \mathbf{p}'S\mu' | V | \psi \rangle &= A^2 \sum_{JM} \sum_{l_1' m_1} \sum_{ll'm} i^{l'-l_1'} Y_{l_1' m_1}^*(\hat{\mathbf{p}}') Y_{l'm}^*(\hat{\mathbf{p}}) \\ &\quad \langle l_1' m_1 S\mu' | JM \rangle \langle l'mS\mu|JM\rangle \int dr r^2 j_{l_1'}(p'r) U_{ll'}^{SJ}(r) \phi_{ll'}^{SJ}(r). \end{aligned} \quad (\text{I.9})$$

We use this result in Eq. (I.4), written as

$$\Delta\psi \equiv \int d^3\mathbf{p}' \frac{Q(\mathbf{P}, \mathbf{p}')}{p^2 - p'^2} \sum_{\mu'} |\mathbf{p}'S\mu'\rangle \langle \mathbf{p}'S\mu'| m_N V |\Psi\rangle = |\psi, \mathbf{p}S\mu\rangle - |\mathbf{p}S\mu\rangle. \quad (\text{I.10})$$

Then

$$\begin{aligned} \Delta\psi &= A^3 \int d^3\mathbf{p}' \frac{Q(\mathbf{P}, \mathbf{p}')}{p^2 - p'^2} \sum_{\mu'} \sum_{J_2 M_2} \sum_{l_2 m_2} i^{l_2} Y_{l_2 m_2}^*(\hat{\mathbf{p}}') \langle l_2 m_2 S\mu' | J_2 M_2 \rangle j_{l_2}(p'r) \mathcal{Y}_{l_2 S J_2 M_2}(\hat{\mathbf{r}}) \\ &\quad \sum_{JM} \sum_{l_1' m_1} \sum_{ll'm} i^{l'-l_1'} Y_{l_1' m_1}^*(\hat{\mathbf{p}}') Y_{l'm}^*(\hat{\mathbf{p}}) \langle l_1' m_1 S\mu' | JM \rangle \langle l'mS\mu|JM\rangle \\ &\quad \times \int dr' r'^2 j_{l_1'}(p'r') U_{ll'}^{SJ}(r') \phi_{ll'}^{SJ}(r'). \end{aligned} \quad (\text{I.11})$$

Using the orthonormality of the spherical harmonics

$$\int Y_{l_2 m_2}^*(\hat{\mathbf{p}}') Y_{l_1' m_1}(\hat{\mathbf{p}}') d\hat{\mathbf{p}}' = \delta_{l_2 l_1'} \delta_{m_2 m_1}. \quad (\text{I.12})$$

and the orthonormality relations of the Clebsch-Gordan coefficients,

$$\sum_{\mu} \sum_{m_1} \langle l_1' m_1 S\mu' | J_2 M_2 \rangle \langle l_1' m_1 S\mu' | JM \rangle = \delta_{J_2 J} \delta_{M_2 M}, \quad (\text{I.13})$$

equation (I.11) becomes,

$$\begin{aligned}\Delta\psi &= A^3 \sum_{JM} \sum_{l'_1} \sum_{ll'm} i^{l'} Y_{l'm}^*(\hat{\mathbf{p}}) \langle l'mS\mu | JM \rangle \mathcal{Y}_{l'_1 S JM}(\hat{\mathbf{r}}) \\ &\times \int dr' r'^2 \int dp' p'^2 \frac{Q(\mathbf{P}, \mathbf{p}')}{p^2 - p'^2} j_{l'_1}(p'r) j_{l'_1}(p'r') U_{l'_1 l}^{SJ}(r') \phi_{ll'}^{SJ}(r'),\end{aligned}\quad (I.14)$$

Finally we define the radial Green's function:

$$G_{l_1}(r, r') = A^2 \int dp' p'^2 \frac{Q(\mathbf{P}, \mathbf{p}')}{p^2 - p'^2} j_{l_1}(p'r) j_{l_1}(p'r'), \quad (I.15)$$

and Eq.(I.14), replacing l with l_1 , becomes

$$\Delta\psi = A \sum_{JM} \sum_{ll'm} i^{l'} Y_{l'm}^*(\hat{\mathbf{p}}) \langle l'mS\mu | JM \rangle \mathcal{Y}_{l S JM}(\hat{\mathbf{r}}) \sum_{l_1} \int dr' r'^2 G_{l_1}(r, r') U_{l_1 l}^{SJ}(r') \phi_{l_1 l}^{SJ}(r'). \quad (I.16)$$

Comparing with the ansatz proposed, Eq.(I.7), and the multipole expansion of the free wave from which we started, we observe that $\Delta\psi$ shares the same angular-spin structure,

$$\Delta\psi = A \sum_{JM} \sum_{ll'm} i^{l'} Y_{l'm}^*(\hat{\mathbf{p}}) \langle l'mS\mu | JM \rangle \Delta\phi_{ll'}^{SJ}(r) \mathcal{Y}_{l S JM}(\hat{\mathbf{r}}). \quad (I.17)$$

Therefore, the radial functions must satisfy the integral equation

$$\Delta\phi_{ll'}^{SJ}(r) = \int dr' r'^2 G_{l_1}(r, r') \sum_{l'_1} U_{l_1 l}^{SJ}(r') \phi_{l_1 l}^{SJ}(r'). \quad (I.18)$$

This ensures that the full wave function

$$|\psi\rangle = |\mathbf{p}S\mu\rangle + |\Delta\psi\rangle, \quad (I.19)$$

satisfies the Bethe-Goldstone equation.

Appendix J

Solution of the Green's Function integral

To solve the system of equations derived from the multipole expansion of the Bethe–Goldstone equation, it is necessary to evaluate the reduced Green's function, which we rewrite here for reference:

$$\hat{G}_l(r, r') = \frac{2}{\pi} \int_0^\infty dp' \hat{j}_l(p'r) \frac{\bar{Q}(P, p')}{p^2 - p'^2} \hat{j}_l(p'r'). \quad (\text{J.1})$$

This Green's function is symmetric and depends on spherical Bessel functions—oscillatory in nature through sine and cosine terms—as well as on the Pauli blocking function, which restricts the integration domain. Moreover, the integrand exhibits a pole at $p = p'$. To properly handle this singularity, we proceed by dividing the integral into regions according to the definition of the Pauli function:

$$\int_0^\infty = \int_0^{q_0} + \int_{q_0}^{q_1} + \int_{q_1}^\infty,$$

$$q_0 = \sqrt{k_F^2 - \frac{P^2}{4}} < q_1 = k_F + \frac{P}{2},$$

Substituting these limits, we obtain

$$\hat{G}_l(r, r') = \frac{2}{\pi} \int_{q_0}^{q_1} dp' \hat{j}_l(p'r) \frac{\bar{Q}(P, p')}{p^2 - p'^2} \hat{j}_l(p'r') + \frac{2}{\pi} \int_{q_1}^\infty dp' \frac{\hat{j}_l(p'r) \hat{j}_l(p'r')}{p^2 - p'^2} \quad (\text{J.2})$$

Since the Pauli blocking function is defined piece-wise, the integral naturally separates into three parts. The first term vanishes, as can be seen from the definition in Eq. 6.18. The second integral corresponds to the region $q_0 < p' < q_1$, while the third extends from q_1 to ∞ . Both of these integrals contain poles in the denominator. To avoid the singularity at $p' = p$, the Cauchy principal value prescription is applied to the second integral in Eq. J.2 (the first integral does not include the pole within its domain).

For convenience, we can transform the Cauchy integral as follows:

$$\begin{aligned}
\mathcal{I} &= \frac{2}{\pi} \mathcal{P} \int_{q_1}^{\infty} dp' \frac{\hat{j}_l(p'r) \hat{j}_l(p'r')}{p^2 - p'^2} \\
&= \frac{2}{\pi} \mathcal{P} \int_0^{\infty} dp' \frac{\hat{j}_l(p'r) \hat{j}_l(p'r')}{p^2 - p'^2} - \frac{2}{\pi} \mathcal{P} \int_0^{q_1} dp' \frac{\hat{j}_l(p'r) \hat{j}_l(p'r')}{p^2 - p'^2} \\
&= \frac{1}{p} \hat{j}_l(pr_<) \hat{y}_l(pr_>) - \frac{2}{\pi} \mathcal{P} \int_0^{q_1} dp' \frac{\hat{j}_l(p'r) \hat{j}_l(p'r')}{p^2 - p'^2},
\end{aligned} \tag{J.3}$$

where we define $r_< = \min(r', r)$, $r_> = \max(r', r)$ and the function \hat{y}_l is a reduced Bessel function of the second kind, also known as the Neumann function. From Eq. J.2, we are thus left with an integral that must be evaluated using the Cauchy principal value theorem, as explained below.

Principal value theorem

The principal value integral arises when evaluating integrals with singularities, such as:

$$I \equiv \mathcal{P} \int_a^b \frac{f(x)}{x - x_0} dx, \tag{J.4}$$

where $a < x_0 < b$, and $f(x)$ is a continuous function with a well-defined derivative at $x = x_0$. The singularity at $x = x_0$ prevents direct evaluation of the integral. Instead, it is defined in terms of a limiting process:

$$\mathcal{P} \int_a^b \frac{f(x)}{x - x_0} dx = \lim_{\epsilon \rightarrow 0} \left(\int_a^{x_0 - \epsilon} \frac{f(x)}{x - x_0} dx + \int_{x_0 + \epsilon}^b \frac{f(x)}{x - x_0} dx \right). \tag{J.5}$$

This definition ensures that the integral remains well-defined despite the singularity.

A suitable approach for numerical computation involves rewriting the integral in the following form by adding and subtracting $f(x_0)$ in the numerator:

$$I = \mathcal{P} \int_a^b \frac{f(x) - f(x_0) + f(x_0)}{x - x_0} dx. \tag{J.6}$$

This can be separated into two integrals:

$$I = \int_a^b \frac{f(x) - f(x_0)}{x - x_0} dx + f(x_0) \mathcal{P} \int_a^b \frac{1}{x - x_0} dx. \tag{J.7}$$

The first integral no longer has a singularity at x_0 if $f(x)$ is differentiable, making it suitable for numerical evaluation using Simpson's rule or another standard quadrature method. The second integral is the principal value of $\frac{1}{x - x_0}$, which can be computed analytically.

We assume that $0 < a < x_0 < b$. We have

$$\mathcal{P} \int_a^b \frac{1}{x - x_0} dx = \lim_{\epsilon \rightarrow 0} \int_a^{x_0 - \epsilon} \frac{1}{x - x_0} dx + \int_{x_0 + \epsilon}^b \frac{1}{x - x_0} dx \tag{J.8}$$

In the first integral $x - x_0 < 0$. To compute the first integral we change variable $t = x_0 - x > 0$. Then $dt = -dx$ and

$$\int_a^{x_0-\epsilon} \frac{1}{x-x_0} dx = \int_{x_0-a}^{\epsilon} \frac{dt}{t} = \ln \epsilon - \ln(x_0 - a) \quad (\text{J.9})$$

The second integral is directly integrable with

$$\int_{x_0+\epsilon}^b \frac{1}{x-x_0} dx = \ln(x-x_0) \Big|_{x_0+\epsilon}^b = \ln(b-x_0) - \ln \epsilon \quad (\text{J.10})$$

Then

$$\mathcal{P} \int_a^b \frac{1}{x-x_0} dx = \ln \epsilon - \ln(x_0 - a) + \ln(b - x_0) - \ln \epsilon = -\ln(x_0 - a) + \ln(b - x_0) = \ln \frac{b - x_0}{x_0 - a}. \quad (\text{J.11})$$

Finally we obtain the general formula for the principal value

$$\mathcal{P} \int_a^b \frac{f(x)}{x-x_0} dx = \int_a^b \frac{f(x) - f(x_0)}{x-x_0} dx + f(x_0) \ln \frac{b-x_0}{x_0-a}. \quad (\text{J.12})$$

Once this result is obtained using the Cauchy method, the total result for the Green's function integral in Equation J.2 is

$$\begin{aligned} \hat{G}_l(r, r') = & \frac{2}{\pi} \int_{q_0}^{q_1} dp' \hat{j}_l(p'r) \frac{\bar{Q}(P, p')}{p^2 - p'^2} \hat{j}_l(p'r') + \frac{1}{p} \hat{j}_l(pr_<) \hat{y}_l(pr_>) \\ & - \frac{2}{\pi} \left(\int_0^{q_1} \frac{f(p') - f(p)}{p - p'} dp' - f(p) \ln \left| \frac{q_1 - p}{p} \right| \right). \end{aligned} \quad (\text{J.13})$$

with

$$f(p') = \frac{\hat{j}_l(p'r) \hat{j}_l(p'r')}{p + p'} \quad (\text{J.14})$$

$$f(p) = \frac{\hat{j}_l(pr) \hat{j}_l(pr')}{2p}. \quad (\text{J.15})$$

Bibliography

- [1] L. Alvarez-Ruso, Y. Hayato, J. Nieves, *New J. Phys.* **16** (2014) 075015.
- [2] U. Mosel, *Ann. Rev. Nuc. Part. Sci.* **66** (2016), 171.
- [3] T. Katori and M. Martini, *J. Phys. G* **45** (2018) no.1, 013001.
- [4] A. M. Ankowski, C. Mariani, *J. Phys. G* **44** (2017) 054001
- [5] O. Benhar, P. Huber, C. Mariani, D. Meloni, *Phys. Rep.* **700** (2017) 1.
- [6] L. Alvarez-Ruso et al., *Progress in Particle and Nuclear Physics* **100**, 1 (2018).
- [7] J. E. Amaro, M. B. Barbaro, J. A. Caballero, R. González-Jiménez, G. D. Megias and I. Ruiz Simo, *J. Phys. G* **47** (2020) no.12, 124001
- [8] A. M. Ankowski, A. Ashkenazi, S. Bacca, J. L. Barrow, M. Betancourt, A. Bodek, M. E. Christy, L. D. S. Dyt- man, A. Friedland and O. Hen, et al. *J. Phys. G* **50**, no.12, 120501 (2023).
- [9] L. A. Russo, A. M. Ankowski, S. Bacca, A. B. Balantekin, J. Carlson, S. Gardiner, R. González-Jiménez, R. Gupta, T. J. Hobbs and M. Hoferichter, et al. *J. Phys. G* (2025) in press
- [10] O. Benhar and D. Meloni, “Total neutrino and antineutrino nuclear cross sections around 1 GeV,” *Nucl. Phys. A* **789**, 379-402 (2007).
- [11] J. Nieves, I. Ruiz Simo, and M. J. Vicente Vacas, “The nucleon axial mass and the MiniBooNE quasielastic neutrino-nucleus scattering problem,” *Phys. Lett. B* **707**, 72-75 (2012).
- [12] M. Martini, M. Ericson, G. Chanfray, and J. Marteau, “Unified approach for nucleon knock-out, coherent and incoherent pion production in neutrino interactions with nuclei,” *Phys. Rev. C* **80**, 065501 (2009).
- [13] O. Benhar, D. Day and I. Sick, arXiv:nucl-ex/0603032.
- [14] O. Benhar, D. Day, and I. Sick, <http://faculty.virginia.edu/qes-archive/>
- [15] V. Pandey, *Prog. Part. Nucl. Phys.* **134**, 104078 (2024)

[16] M. Sajjad Athar, A. Fatima and S. K. Singh, *Prog. Part. Nucl. Phys.* **129**, 104019 (2023)

[17] J. G. Morfin, J. Nieves and J. T. Sobczyk, *Adv. High Energy Phys.* **2012**, 934597 (2012)

[18] L. Alvarez-Ruso, A. M. Ankowski, A. Ashkenazi, J. Barrow, M. Betancourt, K. Borah, M. Sajjad Athar, E. Catano-Mur, P. Coloma and P. Dunne, et al. [arXiv:2503.23556 [hep-ex]].

[19] E.J.Moniz, *Phys.Rev.* **184** 1154-1161 (1969)

[20] E. J. Moniz, I. Sick, R. R. Whitney, J. R. Ficenec, R. D. Kephart and W. P. Trower, *Phys. Rev. Lett.* **26**, 445-448 (1971).

[21] R. A. Smith and E. J. Moniz, *Nucl. Phys. B* **43**, 605 (1972) [erratum: *Nucl. Phys. B* **101**, 547 (1975)].

[22] *Annals Phys.* **83**, 491-529 (1974).

[23] B.D. Serot, and J.D. Walecka, *Adv. Nucl. Phys.* **16** (1986) 1.

[24] R. Rosenfelder, *Ann. Phys. (N.Y.)* **128**, 188 (1980).

[25] J. E. Amaro, M. B. Barbaro, J. A. Caballero, T. W. Donnelly, A. Molinari and I. Sick, *Phys. Rev. C* **71**, 015501 (2005).

[26] G. D. Megias, J. E. Amaro, M. B. Barbaro, J. A. Caballero and T. W. Donnelly, *Phys. Rev. D* **94**, 013012 (2016).

[27] J. E. Amaro, V. L. Martinez-Consentino, E. Ruiz Arriola and I. Ruiz Simo, *Phys. Rev. C* **98** (2018) 024627

[28] O. Benhar, A. Fabrocini, S. Fantoni and I. Sick, *Nucl. Phys. A* **579** (1994), 493-517

[29] C. J. Horowitz, D. P. Murdock, B. D. Serot, in *Computational Nuclear Physics 1*, K. Langanke, J. A. Maruhn and S. E. Koonin (Eds.), Springer Verlag (1991), Berlin

[30] J. M. Udias, P. Sarriguren, E. Moya de Guerra, E. Garrido and J. A. Caballero, *Phys. Rev. C* **51** (1995), 3246-3255

[31] F. Capuzzi, C. Giusti and F. D. Pacati, *Nucl. Phys. A* **524** (1991), 681-705

[32] J. E. Amaro, A. M. Lallena and G. Co, *Int. Jou. Mod. Phys E* **3** (1994), 735.

[33] J. E. Amaro, A. M. Lallena and G. Co, *Nucl. Phys. A* **578** (1994), 365-396

[34] A. Lovato, S. Gandolfi, J. Carlson, S. C. Pieper, and R. Schiavilla, *Phys. Rev. C* **93**, 065504 (2016).

[35] Adelchi Fabrocini, *Phys. Rev. C* **55** (1997) 338.

- [36] J. Nieves, J. E. Amaro and M. Valverde, Phys. Rev. C **70**, 055503 (2004)
- [37] M. Martini, M. Ericson, G. Chanfray and J. Marteau, Phys. Rev. C **80**, 065501 (2009)
- [38] D.O. Riska, Phys. Rep. 181 (1989) 207.
- [39] J. E. Amaro, M. B. Barbaro, J. A. Caballero, T. W. Donnelly and C. F. Williamson, Phys. Lett. B **696**, 151-155 (2011)
- [40] M. Kohno and N. Ohtsuka, Phys. Lett. B **98** (1981), 335-339 doi:10.1016/0370-2693(81)90919-9
- [41] W. M. Alberico, T. W. Donnelly and A. Molinari, Nucl. Phys. A **512**, 541-590 (1990)
- [42] J. E. Amaro, M. B. Barbaro, J. A. Caballero, T. W. Donnelly and A. Molinari, Nucl. Phys. A **723**, 181-204 (2003)
- [43] J. Jourdan, Nucl. Phys. A **603**, 117-160 (1996)
- [44] A. Bodek and M. E. Christy, Phys. Rev. C **106** (2022) no.6, L061305
- [45] V. Van der Sluys, J. Ryckebusch and M. Waroquier, Phys. Rev. C **51**, 2664-2670 (1995) doi:10.1103/PhysRevC.51.2664
- [46] T. Franco-Munoz, J. García-Marcos, R. González-Jiménez and J. M. Udías, Phys. Rev. C **108**, no.6, 064608 (2023)
- [47] A. Lovato, N. Rocco and N. Steinberg, [arXiv:2312.12545 [nucl-th]].
- [48] O. Benhar, A. Lovato and N. Rocco, Phys. Rev. C **92**, no.2, 024602 (2015) doi:10.1103/PhysRevC.92.024602
- [49] R. Gran, J. Nieves, F. Sanchez and M. J. Vicente Vacas, Phys. Rev. D **88**, no.11, 113007 (2013) doi:10.1103/PhysRevD.88.113007
- [50] J. E. Sobczyk, J. Nieves and F. Sánchez, Phys. Rev. C **102**, no.2, 024601 (2020) doi:10.1103/PhysRevC.102.024601
- [51] G. D. Megias, M. B. Barbaro, J. A. Caballero, J. E. Amaro, T. W. Donnelly, I. Ruiz Simo and J. W. Van Orden, J. Phys. G **46**, no.1, 015104 (2019) doi:10.1088/1361-6471/aaf3ae
- [52] J. Gonzalez-Rosa, G. D. Megias, J. A. Caballero, M. B. Barbaro and J. M. Franco-Patino, Phys. Rev. D **108**, no.11, 113008 (2023) [erratum: Phys. Rev. D **111**, no.7, 079903 (2025)] doi:10.1103/PhysRevD.108.113008
- [53] J. Carlson, J. Jourdan, R. Schiavilla, and I. Sick, Phys. Rev. C **65** (2002)
- [54] A. Lovato, S. Gandolfi, J. Carlson, S. C. Pieper and R. Schiavilla, Phys. Rev. Lett. **117** (2016) no.8, 082501

- [55] W. Leidemann and G. Orlandini, *Prog. Part. Nucl. Phys.* **68**, 158 (2013)
- [56] J. Walecka, *Theoretical Nuclear and subnuclear Physics* Oxford University Press, 200 Madison Avenue, New York 10016 (1995)
- [57] R. Subedi *et al.*, *Science* **320**, 1476 (2008)
- [58] O. Hen *et al.*, *Science* **346**, 614 (2014).
- [59] H. A. Bethe, “Theory of nuclear matter,” *Ann. Rev. Nucl. Part. Sci.* **21**, 93 (1971).
- [60] J. P. Jeukenne, A. Lejeune, and C. Mahaux, “Many-body theory of nuclear matter,” *Phys. Rept.* **25**, 83 (1976).
- [61] A. Ramos, A. Polls, and W. H. Dickhoff, *Nucl. Phys. A* **A503**, 1 (1989).
- [62] Y. Dewulf, W. H. Dickhoff, D. Van Neck, E. R. Stoddard, and M. Waroquier, *Phys. Rev. Lett.* **90**, 152501 (2003).
- [63] B. E. Vonderfecht, W. H. Dickhoff, A. Polls, and A. Ramos, *Phys. Rev. C* **C44**, R1265 (1991).
- [64] S. Fantoni and V. R. Pandharipande, *Nucl. Phys. A* **A427**, 473 (1984).
- [65] H. Muther, A. Polls, and W. H. Dickhoff, *Phys. Rev. C* **C51**, 3040 (1995).
- [66] R. B. Wiringa, R. Schiavilla, S. C. Pieper, and J. Carlson, *Phys. Rev. C* **89**, 024305 (2014).
- [67] O. Benhar, C. Ciofi Degli Atti, S. Liuti, and G. Salmè, *Phys. Lett. B* **B177**, 135 (1986).
- [68] J. W. Van Orden, W. Truex, and M. K. Banerjee, *Phys. Rev. C* **C21**, 2628 (1980).
- [69] M. M. Sargsian, *Phys. Rev. C* **C89**, 034305 (2014).
- [70] H. Riffert, H. Muther, H. Herold, and H. Ruder, *Springer Tracts Mod. Phys.* **133**, 1 (1996).
- [71] L. Frankfurt, M. Sargsian, and M. Strikman, *Int. J. Mod. Phys. A* **23**, 2991 (2008).
- [72] A. Mukherjee, *Phys. Rev. C* **C79**, 045811 (2009).
- [73] G. Shen, C. J. Horowitz, and S. Teige, *Phys. Rev. C* **C83**, 035802 (2011).
- [74] G. Röpke, *Phys. Rev. C* **C92**, 054001 (2015).
- [75] O. Hen, B.-A. Li, W.-J. Guo, L. B. Weinstein, and E. Piasetzky, *Phys. Rev. C* **C91**, 025803 (2015).
- [76] D. Ding, A. Rios, H. Dussan, W. H. Dickhoff, S. J. Witte, A. Polls, and A. Carbone, *Phys. Rev. C* **94**, 025802 (2016); [Addendum: *Phys. Rev. C* **94**, 029901 (2016)].

- [77] A. Rios, A. Polls, and W. H. Dickhoff, *J. Low Temp. Phys.* **189**, 234 (2017).
- [78] W. Broniowski and M. Rybczynski, *Phys. Rev. C* **C81**, 064909 (2010).
- [79] F. Simkovic, A. Faessler, H. Muther, V. Rodin, and M. Stauf, *Phys. Rev. C* **C79**, 055501 (2009).
- [80] M. Kortelainen, O. Civitarese, J. Suhonen, and J. Toivanen, *Phys. Lett. B* **B647**, 128 (2007).
- [81] L. L. Frankfurt, M. I. Strikman, D. B. Day, and M. Sargsian, *Phys. Rev. C* **C48**, 2451 (1993).
- [82] L. B. Weinstein, E. Piasetzky, D. W. Higinbotham, J. Gomez, O. Hen, and R. Shneor, *Phys. Rev. Lett.* **106**, 052301 (2011).
- [83] C. Giusti, H. Muther, F. D. Pacati, and M. Stauf, *Phys. Rev. C* **60**, 054608 (1999).
- [84] J. Ryckebusch, M. Vanderhaeghen, K. Heyde, and M. Waroquier, *Phys. Lett. B* **350**, 1 (1995).
- [85] C. Colle, O. Hen, W. Cosyn, I. Korover, E. Piasetzky, J. Ryckebusch, and L. B. Weinstein, *Phys. Rev. C* **92**, 024604 (2015).
- [86] S. Tan, *Ann. Phys.* **323**, 2952 (2008).
- [87] S. Tan, *Ann. Phys.* **323**, 2971 (2008).
- [88] S. Tan, *Ann. Phys.* **323**, 2987 (2008).
- [89] M. Alvioli, C. Ciofi degli Atti, L. P. Kaptari, C. B. Mezzetti, H. Morita, and S. Scopetta, *Phys. Rev. C* **85**, 021001 (2012).
- [90] M. Alvioli, C. Ciofi Degli Atti, L. P. Kaptari, C. B. Mezzetti, and H. Morita, *Int. J. Mod. Phys. E* **22**, 1330021 (2013).
- [91] R. Weiss, B. Bazak, and N. Barnea, *Phys. Rev. C* **92**, 054311 (2015).
- [92] M. Alvioli, C. Ciofi degli Atti, and H. Morita, *Phys. Rev. C* **94**, 044309 (2016).
- [93] R. Weiss, R. Cruz-Torres, N. Barnea, E. Piasetzky, and O. Hen, *Phys. Lett. B* **780**, 211 (2018).
- [94] R. Weiss and N. Barnea, *Phys. Rev. C* **96**, 041303 (2017).
- [95] R. Jastrow, *Phys. Rev.* **98**, 1479 (1955).
- [96] S. Fantoni and S. Rosati, *Nuovo Cim.* **A20**, 179 (1974).
- [97] S. Fantoni and S. Rosati, *Nuovo Cim.* **A25**, 593 (1975).
- [98] R. Guardiola, A. Polls, and J. Ros, *Nuovo Cim.* **A59**, 419 (1980).

[99] R. Guardiola, A. Faessler, H. Müther, and A. Polls, *Nucl. Phys.* **A371**, 79 (1981).

[100] O. Benhar, A. Fabrocini, and S. Fantoni, in *Modern Topics in Electron Scattering*, eds. B. Frois and I. Sick (World Scientific, Singapore), p. 460 (1991).

[101] M. V. Stoitsov, A. N. Antonov, and S. S. Dimitrova, *Phys. Rev. C* **48**, 74 (1993).

[102] O. Benhar, A. Fabrocini, S. Fantoni, and I. Sick, *Nucl. Phys.* **A579**, 493 (1994), doi:10.1016/0375-9474(94)90920-2.

[103] R. Guardiola, P. I. Moliner, J. Navarro, R. F. Bishop, A. Puente, and N. R. Walet, *Nucl. Phys.* **A609**, 218 (1996), doi:10.1016/0375-9474(96)00315-6.

[104] R. F. Bishop, R. Guardiola, I. Moliner, J. Navarro, M. Portesi, A. Puente, and N. R. Walet, *Nucl. Phys.* **A643**, 243 (1998), doi:10.1016/S0375-9474(98)00562-4.

[105] M. Vanhalst, J. Ryckebusch, and W. Cosyn, *Phys. Rev.* **C86**, 044619 (2012), doi:10.1103/PhysRevC.86.044619.

[106] K. A. Brueckner and J. L. Gammel, *Phys. Rev.* **109**, 1023 (1958), doi:10.1103/PhysRev.109.1023.

[107] K. A. Brueckner, C. A. Levinson, and H. M. Mahmoud, *Phys. Rev.* **95**, 217 (1954), doi:10.1103/PhysRev.95.217.

[108] K. A. Brueckner, *Phys. Rev.* **97**, 1353 (1955), doi:10.1103/PhysRev.97.1353.

[109] H. A. Bethe, *Phys. Rev.* **103**, 1353 (1956), doi:10.1103/PhysRev.103.1353.

[110] J. Goldstone, *Proc. Roy. Soc. Lond.* **A239**, 267 (1957), doi:10.1098/rspa.1957.0037.

[111] G. Dahll, E. Østgaard, and B. Brandow, *Nucl. Phys.* **A124**, 481 (1969), doi:10.1016/0375-9474(69)90649-6.

[112] H. S. Köhler, *Ann. Phys.* **16**, 375 (1961), doi:10.1016/0003-4916(61)90113-0.

[113] M. I. Haftel and F. Tabakin, *Nucl. Phys.* **A158**, 1 (1970), doi:10.1016/0375-9474(70)90047-3.

[114] J. P. Jeukenne, A. Lejeune, and C. Mahaux, *Phys. Rev. C* **10**, 1391 (1974), doi:10.1103/PhysRevC.10.1391.

[115] K. Nakayama, S. Krewald, J. Speth, and W. G. Love, *Nucl. Phys.* **A431**, 419 (1984), doi:10.1016/0375-9474(84)90117-9.

[116] A. Hosaka, K. I. Kubo, and H. Toki, *Nucl. Phys.* **A444**, 76 (1985), doi:10.1016/0375-9474(85)90292-1.

[117] K. Nakayama, S. Drozdz, S. Krewald, and J. Speth, *Nucl. Phys.* **A470**, 573 (1987), doi:10.1016/0375-9474(87)90588-4; Erratum: *Nucl. Phys.* **A484**, 685 (1988), doi:10.1016/0375-9474(88)90316-8.

[118] H. F. Boersma and R. Malfliet, Phys. Rev. C49, 233 (1994), doi:10.1103/PhysRevC.49.233; Phys. Rev. C50, 1253 (1994), doi:10.1103/PhysRevC.50.1253.

[119] S. K. Bogner, R. J. Furnstahl, and R. J. Perry, Phys. Rev. C75, 061001 (2007), doi:10.1103/PhysRevC.75.061001.

[120] V. S. Timoteo, S. Szpigel, and E. Ruiz Arriola, Phys. Rev. C86, 034002 (2012), doi:10.1103/PhysRevC.86.034002.

[121] T. Neff, H. Feldmeier, and W. Horiuchi, Phys. Rev. C92, 024003 (2015), doi:10.1103/PhysRevC.92.024003.

[122] J. Carlson, V. R. Pandharipande, and R. Schiavilla, Phys. Rev. C47, 484 (1993), doi:10.1103/PhysRevC.47.484.

[123] J. L. Forest, V. R. Pandharipande, J. Carlson, and R. Schiavilla, Phys. Rev. C52, 576 (1995), doi:10.1103/PhysRevC.52.576.

[124] S. Quaglioni and P. Navratil, Phys. Rev. C79, 044606 (2009), doi:10.1103/PhysRevC.79.044606.

[125] G. Hagen, T. Papenbrock, D. J. Dean, and M. Hjorth-Jensen, Phys. Rev. C82, 034330 (2010), doi:10.1103/PhysRevC.82.034330.

[126] W. Leidemann and G. Orlandini, Prog. Part. Nucl. Phys. 68, 158 (2013), doi:10.1016/j.ppnp.2012.09.001.

[127] B. R. Barrett, P. Navratil, and J. P. Vary, Prog. Part. Nucl. Phys. 69, 131 (2013), doi:10.1016/j.ppnp.2012.10.003.

[128] R. D. Viollier and J. D. Walecka, Acta Phys. Polon. B8, 25 (1977).

[129] I. Ruiz Simo, R. Navarro Pérez, J. E. Amaro, and E. Ruiz Arriola, Phys. Rev. C95, 054003 (2017a), doi:10.1103/PhysRevC.95.054003.

[130] I. Ruiz Simo, R. Navarro Pérez, J. E. Amaro, and E. Ruiz Arriola, Phys. Rev. C96, 054006 (2017b), doi:10.1103/PhysRevC.96.054006.

[131] R. Navarro Pérez, J. E. Amaro, and E. Ruiz Arriola, Phys. Rev. C88, 024002 (2013a), doi:10.1103/PhysRevC.88.024002 [Erratum: Phys. Rev. C88, 069902 (2013)].

[132] P. C. Bhargava and D. W. Sprung, Ann. Phys. 42, 222 (1967), doi:10.1016/0003-4916(67)90070-X.

[133] A. Kallio and B. D. Day, Nucl. Phys. A124, 177 (1969), doi:10.1016/0375-9474(69)90527-2.

[134] E. Werner, Nuclear Physics 10, 688 (1959).

[135] T. Cheon and E. F. Redish, Phys. Rev. C39, 331 (1989), doi:10.1103/PhysRevC.39.331.

[136] E. Schiller, H. Muther, and P. Czerski, Phys. Rev. C59, 2934 (1999), [Erratum: Phys. Rev. C60, 059901 (1999)], doi:10.1103/PhysRevC.59.2934.

[137] K. Suzuki, R. Okamoto, M. Kohno, and S. Nagata, Nucl. Phys. A665, 92 (2000), doi:10.1016/S0375-9474(99)00399-1.

[138] F. Sammarruca, X. Meng, and E. J. Stephenson, Phys. Rev. C62, 014614 (2000), doi:10.1103/PhysRevC.62.014614.

[139] E. J. Stephenson, R. C. Johnson, and F. Sammarruca, Phys. Rev. C71, 014612 (2005), doi:10.1103/PhysRevC.71.014612.

[140] L. White and F. Sammarruca, Phys. Rev. C90, 044607 (2014), doi:10.1103/PhysRevC.90.044607.

[141] R. Schiavilla, R. B. Wiringa, S. C. Pieper, and J. Carlson, Phys. Rev. Lett. 98, 132501 (2007).

[142] T. W. Donnelly and I. Sick, Phys. Rev. Lett. **82**, 3212-3215 (1999)

[143] T. W. Donnelly and I. Sick, Phys. Rev. C **60**, 065502 (1999)

[144] J. E. Amaro, M. B. Barbaro, J. A. Caballero, T. W. Donnelly, A. Molinari and I. Sick, Phys. Rev. C **71**, 015501 (2005)

[145] P. R. Casale, J. E. Amaro, V. L. Martinez-Consentino and I. Ruiz Simo, Universe **9**, no.4, 158 (2023)

[146] W. M. Alberico, A. Molinari, T. W. Donnelly, E. L. Kronenberg and J. W. Van Orden, Phys. Rev. C **38**, 1801-1810 (1988)

[147] R. Cenni, T. W. Donnelly and A. Molinari, Phys. Rev. C **56**, 276-291 (1997)

[148] D Drechselt and M M Giannini, Rep. Prog. Phys. 52 (1989) 1083.

[149] K. Wehrberger, Phys. Rep. 225 (1993) 273.

[150] G. B. West, Phys. Rept. **18**, 263-323 (1975)

[151] A. M. Saruis, Phys. Rept. **235**, 57-188 (1993)

[152] V. L. Martinez-Consentino, I. Ruiz Simo, J. E. Amaro and E. Ruiz Arriola, Phys. Rev. C **96**, no. 6, 064612 (2017).

[153] I. Ruiz Simo, V. L. Martinez-Consentino, J. E. Amaro and E. Ruiz Arriola, Phys. Rev. D **97**, 116006 (2018).

[154] V. L. Martinez-Consentino, I. R. Simo and J. E. Amaro, Phys. Rev. C **104**, no.2, 025501 (2021)

- [155] V. L. Martinez-Consentino, J. E. Amaro and I. Ruiz Simo, Phys. Rev. D **104**, no.11, 113006 (2021)
- [156] V. L. Martinez-Consentino, J. E. Amaro, P. R. Casale and I. Ruiz Simo, Phys. Rev. D **108** (2023) no.1, 013007
- [157] J. E. Amaro, M. B. Barbaro, J. A. Caballero, T. W. Donnelly and A. Molinari, Nucl. Phys. A **697**, 388-428 (2002)
- [158] P. R. Casale, J. E. Amaro and M. B. Barbaro, Symmetry **15**, no.9, 1709 (2023)
- [159] J. E. Amaro, M. B. Barbaro, J. A. Caballero, T. W. Donnelly and A. Molinari, Phys. Rept. **368**, 317-407 (2002)
- [160] I. Ruiz Simo, J. E. Amaro, M. B. Barbaro, A. De Pace, J. A. Caballero and T. W. Donnelly, J. Phys. G **44**, no.6, 065105 (2017)
- [161] Pascalutsa and O. Scholten, Nucl. Phys. A 591 658 (1995).
- [162] W. M. Alberico, M. Ericson and A. Molinari, Annals Phys. **154**, 356 (1984)
- [163] B. Sommer, Nucl. Phys. A **308** (1978)
- [164] C. H. Llewellyn Smith, Phys. Rept. **3**, 261-379 (1972)
- [165] E. Hernandez, J. Nieves and M. Valverde, Phys. Rev. D **76**, 033005 (2007)
- [166] J.J. Quiros, C. Barbero, D.E. Jaramillo, A. Mariano, J. Phys. G: Nucl. Part. Phys. **44** (2017) 045112.
- [167] H. C. Kim, S. Schramm and C. J. Horowitz, Phys. Rev. C **53**, 2468-2473 (1996)
- [168] J. Hockert, D.O. Riska, M. Gari, A. Huffman, Nucl. Phys. **A217** (1973) 14.
- [169] J. E. Amaro, M. B. Barbaro, J. A. Caballero, T. W. Donnelly, C. Maieron and J. M. Udias, Phys. Rev. C **81**, 014606 (2010)
- [170] J. E. Amaro, M. B. Barbaro, J. A. Caballero and F. Kazemi Tabatabaei, Phys. Rev. C **68**, 014604 (2003).
- [171] P. R. Casale, J. E. Amaro, E. Ruiz Arriola and I. Ruiz Simo, Phys. Rev. C **108** (2023) no.5, 054001
- [172] P.R. Casale, J.E. Amaro, V. Belocchi, M.B. Barbaro, A. De Pace, and M. Martini, Phys. Rev. C **112**, 024603 (2025).
- [173] R. Schiavilla, V. R. Pandharipande and D. O. Riska, Phys. Rev. C **40** (1989), 2294-2309
- [174] J. E. Amaro, A. M. Lallena and G. Co, Nucl. Phys. A **578** (1994), 365-396.

[175] J. E. Amaro, M. B. Barbaro, J. A. Caballero, T. W. Donnelly and C. Maieron, Phys. Rev. C **71** (2005), 065501

[176] J.E. Amaro, C. Maieron, M.B. Barbaro, J.A. Caballero and T.W. Donnelly Phys. Rev. C82 (2010) 044601

[177] S. Boffi, C. Giusti, F. D. Pacati and M. Radici, Nucl. Phys. A **518** (1990), 639-657

[178] P. R. Casale, J. E. Amaro, V. Belocchi, M. B. Barbaro and M. Martini, Phys. Rev. C, to be published [arXiv:2507.20246 [hep-ph]].

[179] R. Machleidt, K. Holinde, and Ch. Elster, Phys. Rep. 149 (1987) 1.

[180] J. E. Amaro, J. A. Caballero, T. W. Donnelly, A. M. Lallena, E. Moya de Guerra and J. M. Udias, Nucl. Phys. A **602**, 263-307 (1996)

[181] A. Aguilar-Arevalo et al. (MiniBooNE Collaboration), Phys. Rev. D 81, 092005 (2010).

[182] V. L. Martinez-Consentino, J. E. Amaro Phys. Rev. D **108** (2023) no.11, 113006

[183] A. A. Aguilar-Arevalo et al. [MiniBooNE Collaboration], Phys. Rev. D 88, 032001 (2013),

[184] H. A. Bethe, Phys. Rev. 103 (1956), 1353.

[185] J. Goldstone, Proc. R. Soc. London A 239 (1957), 267.

[186] G. Dahll, E. Ostgaard, and B. Brandow, Nucl. Phys. A 124 (1969), 481.

[187] K. A. Brueckner and J. L. Gammel, Phys. Rev. 109, 1023 (1958).

[188] K. A. Brueckner, C. A. Levinson, and H. M. Mahmoud, Phys. Rev. 95, 217 (1954).

[189] K. A. Brueckner, Phys. Rev. 97, 1353 (1955)

[190] H. S. Köhler, Ann. Phys. (NY) 16 (1961) 375.

[191] M. I. Haftel and F. Tabakin, Nucl. Phys. A 158 (1970), 1.

[192] J. P. Jeukenne, A. Lejeune, and C. Mahaux, Phys. Rev. C 10 (1974) 1391.

[193] K. Nakayama, S. Krewald, J. Speth, and W.G. Love, Nucl. Phys. A 431 (1984), 419.

[194] A. Hosaka, K. I Kubo, and H. Toki, Nucl. Phys. A 444 (1985), 76.

[195] K. Nakayama, S. Drozdz, S Krewald and J. Speth, Nucl. Phys. A 470 (1987), 573.

[196] H. F. Boersma, and R. Malflied, Phys. Rev. C 49 (1994), 233.

[197] R. Navarro Perez, J. E. Amaro, and E. Ruiz Arriola Phys. Rev. C **88**, 024002 (2013), [Erratum: Phys.Rev.C88,no.6,069902(2013)]

- [198] I. Ruiz Simo, R. Navarro Perez, J. E. Amaro, E. Ruiz Arriola Phys. Rev. C **95**, 054003 (2017)
- [199] I. Ruiz Simo, R. Navarro Perez, J. E. Amaro, E. Ruiz Arriola Phys. Rev. C **96**, 054006 (2017)
- [200] T. Cheon and E. F. Redish, Phys. Rev. C39, 331 (1989).
- [201] E. Schiller, H. Muther, and P. Czerski, Phys. Rev. C59, 2934 (1999), [Erratum: Phys.Rev.C60,059901(1999)].
- [202] K. Suzuki, R. Okamoto, M. Kohno, and S. Nagata, Nucl. Phys. A665, 92 (2000).
- [203] F. Sammarruca, X. Meng, and E. J. Stephenson, Phys. Rev. C62, 014614 (2000).
- [204] E. J. Stephenson, R. C. Johnson, and F. Sammarruca, Phys. Rev. C71, 014612 (2005).
- [205] L. White and F. Sammarruca, Phys. Rev. C90, 044607 (2014)
- [206] M. A. Preston and R. K. Bhaduri, *Structure of the Nucleus*, Addison-Wesley, Reading, MA, 1975.
- [207] A. Rios, A. Polls, and W.H. Dickhoff, Phys. Rev. c 89, 044303 (2014)
- [208] Bao-Jun Cai and Bao-An Li, Phys. Rev. C 93, 014619 (2016).
- [209] A. Bodek and M. E. Christy, Phys. Rev. C **107** (2023) no.5, 054309
- [210] A. Bodek, M. E. Christy, Z. Lin, G. M. Bulugean and A. M. Delgado, [arXiv:2410.15991 [hep-ex]].
- [211] A. Bodek, M. E. Christy, Z. Lin, G. M. Bulugean, A. M. Delgado, A. M. Ankowski, G. D. Megias and J. Tena Vidal, [arXiv:2409.10637 [hep-ex]].
- [212] R. B. Wiringa, R. Schiavilla, S. C. Pieper and J. Carlson, Phys. Rev. C **89** (2014) no.2, 024305
- [213] C. Colle, W. Cosyn and J. Ryckebusch, Phys. Rev. C **93** (2016) no.3, 034608
- [214] P. R. Casale and J. E. Amaro, Jou. Phys. G (to be published), [arXiv:2510.16578 [nucl-th]].
- [215] R. González-Jiménez, N. Jachowicz, K. Niewczas, J. Nieves and M. B. Barbaro, Phys. Rev. C **95**, 065501 (2017)
- [216] N. Jachowicz, K. Heyde, J. Ryckebusch and S. Rombouts, Phys. Rev. C **65**, 025501 (2002).
- [217] U. Mosel, Ann. Rev. Nucl. Part. Sci. **66**, 171–195 (2016)
- [218] T. Franco-Munoz, R. Gonzalez-Jimenez and J. M. Udias, J. Phys. G **52** (2025) no.2, 025103.

[219] S. Galster, H. Klein, J. Moritz, K. H. Schmidt, D. Wegener and J. Bleckwenn, Nucl. Phys. B **32**, 221 (1971).